RIGA TECHNICAL UNIVERSITY

Oskars Bormanis

INCREASING RELIABILITY OF ROBOTIZED MANUFACTURING SYSTEMS

Doctoral Thesis

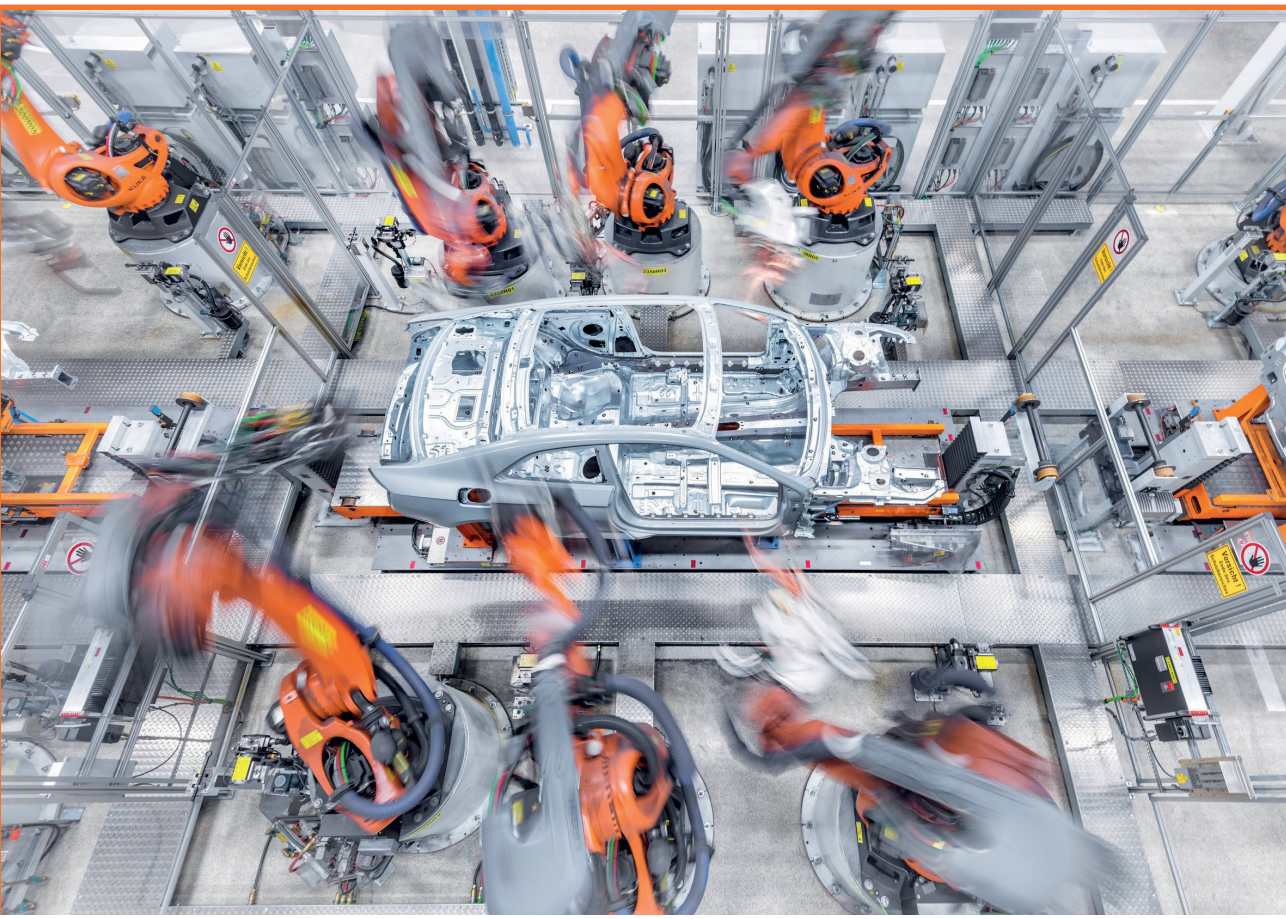

RTU Press
Riga 2022

RIGA TECHNICAL UNIVERSITY
Faculty of Electrical and Environmental Engineering
Institute of Industrial Electronics and Electrical Engineering

Oskars BORMANIS
Doctoral Student of the Study Programme "Computerized Control of Electrical Technologies"

INCREASING RELIABILITY OF ROBOTIZED MANUFACTURING SYSTEMS

Doctoral Thesis

Scientific supervisor:
Professor Dr. habil. sc. ing.
LEONĪDS RIBICKIS

RTU Press
Riga 2022

ABSTRACT

ROBOTICS, MISSION PROFILE, LIFETIME, MANUFACTURING, DC MICROGRID, RELIABILITY, VIRTUAL COMMISSIONING SOFTWARE.

The Thesis studies robotized manufacturing systems focusing the research on industrial robots. Development and production testing methods of the electronic components of industrial robot and their role in the life cycle of hardware are reviewed in the Thesis. The main achievement of the Thesis is the development of a software tool for robot language code translation to lifetime consumption of robot drive inverter power electronics components. Reliability assessment for various industrial robot electrical cabinet layout and operation options is included in this study by applying the developed tool in practice.

This work is written in English. It consists of 186 pages, 157 Figures, 18 tables and an addition of 14 attachments. Information was obtained from scientific databases such as IEEE Xplore Digital Library, ScienceDirect. A total of 170 information sources were used to develop this work, published in a time period between year 1973 and 2021.

ANOTĀCIJA

ROBOTIKA, EKSPLUATĀCIJAS PROFILS, DARBMŪŽS, RAŽOŠANA, LOKĀLS LĪDZSPRIEGUMA TĪKLS, UZTICAMĪBA, VIRTUĀLĀS EKSPLUATĀCIJAS PROGRAMMATŪRA.

Promocijas darbā pētītas robotizētās ražošanas sistēmas, kuru centrā ir industriālais robots. Darba gaitā apskatītas industriālo robotu elektronikas izstrādes un ražošanas pārbaužu metodes, kā arī to loma aparatūras aprites ciklā. Būtiskākais darba sasniegums ir programmatūras rīka izstrāde robota programmēšanas valodas koda pārveidošanai par robota piedziņas invertora energoelektronikas komponentu kalpošanas laika patēriņu. Darbs iekļauj atšķirīgu industriālo robotu enerģijas apgādes veidu, kā arī to darbības režīmu uzticamības novērtējumu, kas veikts, izstrādāto rīku lietojot praksē.

Promocijas darbs rakstīts angļu valodā. Tas sastāv no 186 lapām, tai skaitā 157 attēliem, 18 tabulām un papildus – 14 pielikumiem. Informācijas avotu iegūšanai izmantotas tādas zinātniskās datubāzes kā IEEE Xplore Digital Library, ScienceDirect. Kopā darba izstrādei informācija apkopota no 170 informācijas avotiem, kas izdoti laika periodā no 1973. līdz 2021. gadam.

CONTENTS

1. INTRODUCTION

Section 1.1 provides a basic introduction and background to DC microgrid, control and reliability topics covered in this study, followed by a discussion of motivation and relevance of the study in section 1.2. The main hypothesis and objectives are highlighted in section 1.3. Results of the study are presented in section 1.4.

1.1. DC Microgrids, Control and Reliability

Industrial microgrids are a topic with high potential in industrial and research environment. Innovation supported electrical energy consumption reduction in this area has been researched in multiple projects. Previous research by Daimler AG and Riga Technical University has shown reduction of energy consumption by up to 30 % by introduction of an external energy storage to a state of the art robotized system [1]. This work continues the previos research as the demand for direct current (DC) microgrid solutions is increasing. DC microgrid in manufacturing environment is a new challenge and is included the innovations introduced by Industry 4.0.

As the focus of previous studies has been on reduction of electrical energy consumption by changing layouts, detailed analysis of suggested robotized manufacturing system layout and control improvements is a currently missing, but required addition to previous work.

Various DC microgrid applications and control methods are reviewed, evaluating reliability and other major parameters. Energy consumption computational model of industrial robots for virtual commissioning software is applied for research and extended with the addition of thermal and lifetime consumption simulation capability. Study introduces a lifetime improvement tool for specific reliability and lifetime improvements due to review of robotized equipment application types and robot programs common in automotive industry.

1.2. Motivation

Significant motivation to study the topics presented in this work is an industry standard requirement to maintain initial functionality of the robotized manufacturing hardware (see Fig. 1.1) for as long as possible, as it provides the required process continuity of the automotive environment.

Maintaining initial functionality of electronics in general reduces waste is required for sustainable manufacturing, since effective use of resources is a basis for sustainable industry.

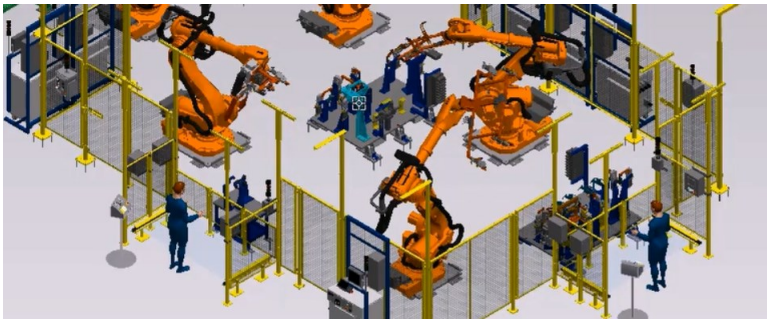

Fig. 1.1. Sample manufacturing cell with six degree of freedom industrial robots, simulated in 3D environment [2].

The trend is highlighted in the consumer electronics market, where European Union may consider enforcing seven-year smartphone lifespan and demanding improved maintenance options. It confirms that the reliability requirement and understanding of the related lifetime concepts is essential for product developers, demanded by the customer and in some cases the government.

Industrial environment has seen an increase of robotized equipment through the last decades. Operational stock of industrial robots has increased and the trend is expected to continue (see Fig. 1.2).

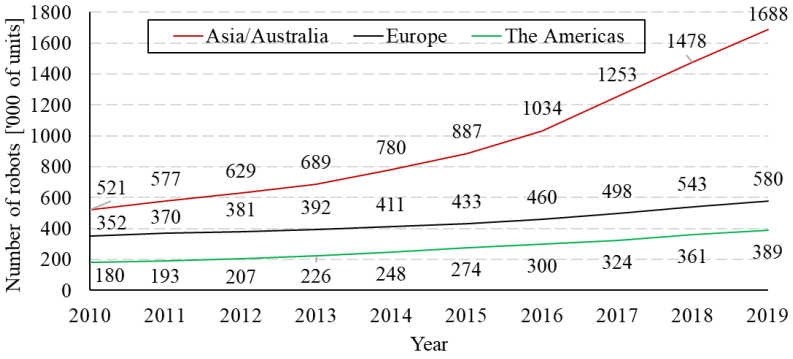

Fig. 1.2. Number of industrial robot operational units per world region [3].

A lot of manufacturing equipment design is outsourced and developed in a virtual environment before reaching the manufacturing site. Virtual models of an industrial robot have been created earlier to assist the hardware designers in decision making.

Engineering department is expected to adjust the hardware for the needs of the specific application, considering the simulated parameters and the simulation results. The developed robot programs are expected to run without major modification for up to 7 years, therefore

programmers are creating robot programs, which will be operational in production for the following years.

Computational extension introducing energy consumption and lifetime consumption in virtual commissioning environment is a novelty to support engineering team with data to design the robotized hardware in a sustainable way. Modeling toolbox with energy consumption and lifetime estimation capability presented in this study provides the required agile feedback to manufacturing equipment engineer (see Fig. 1.3).

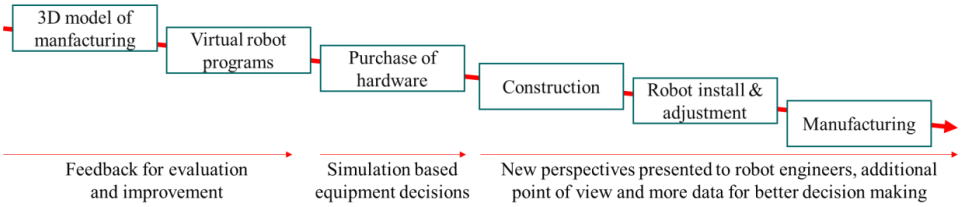

Fig. 1.3. Design, confirmation and setup of robotized manufacturing equipment.

Engineering equipment decisions can be adjusted to meet the requirements of robot program and application type early in the development. Energy and lifetime consumption differences are expected to multiply over time, increasing the cost and risks of the manufacturing.

Research begins with modeling as the state-of-the-art information about the studied use case is gathered and used through the further sections of this work. Computation model is developed to improve the scale and capability of the research. Several use-cases are simulated at device (transistors) and converter (KUKA Servo Pack inverter) level followed by analysis of the results and comparison to the previously made assumptions.

Objective of the modeling stage is to develop a computation tool for junction temperature and lifetime consumption assessment. It planned to evaluate the assumed relationship between weight of the industrial robot tool and lifetime consumption of the power electronics. As there are multiple use cases of industrial robotized systems, confirmation of the connection between robot application type and lifetime consumption is one of the objectives. Estimation tool is used to compare various of the robot electrical cabinet layouts.

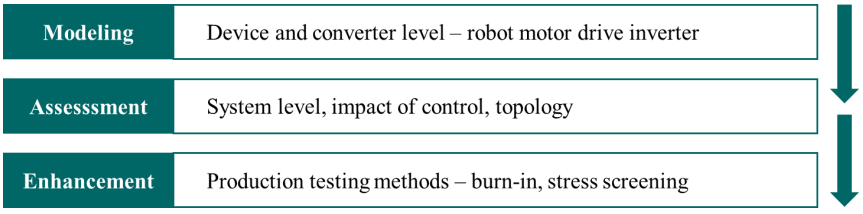

Fig. 1.4. Modeling, assessment and enhancement stages of the presented reliability improvement study.

Research (see Fig. 1.4.) is continued by enhancement stage, during which production methods and various tests, as well as screening methods are analyzed. The third part of the study reviews the established industrial robot electronic component development, production and testing methods. Analysis of the studied power electronics reliability cycle starting from development, to mass production and final use in production, by in-depth review of the development and production reliability tests is the objective of the enhancement stage.

1.3. Main Hypothesis and Objectives

Reliability of manufacturing equipment is important in European Union and worldwide. Maintaining the hardware initial functionality for as long as possible provides continuity of automated proceses and protects environment, where effective use of resources is an essential basis for sustainable manufacturing industry. Robotized manufacturing has an increasing role in production, and it is applied widely in automotive, and other industries.

Reliability in automated factories at component and material level has been well researched and documented. Often power electronics converters of industrial robots are designed with reliability margin, expecting the highest possible load. This reduces risk of manufacturing downtime due to equipment defects.

Similar to energy consumption reduction through robotic system level analysis, improvement of equipment reliability prediction accuracy depends on the application analysis as well. Power electronics equipment is the same and it does not depend on the specific robot application type – either adhesive application or material handling, although the mission profile is different for both tasks.

Missing methodology for power electronics equipment adjustment for actual load and consumption of robotized manufacturing is the main problem, solved through this work. Results of the work present new solutions with a scientific novelty.

Purpose of this PhD thesis work is *reliability improvement of equipment for automated robotized factories*, by development of new methods for development of industrial robot systems and applications.

Study is expected to improve accuracy of reliability prediction for industrial robot manufacturing systems, improving lifetime predictions and providing data for maintenance scheduling of robotized applications.

The main hypothesis is that the accuracy of automated robot manufacturing system reliability estimations can be improved by considering application-specific parameters. Robotized equipment costs can be reduced on the basis of system hardware layout and mission profile.

1.4. Dissemination of Results

Scientific novelty of the research presented through this work and the main results are listed below.

1. Evaluation of the main reliability differences between alternating current (AC) and direct current (DC) supplied industrial robot systems.
2. Development of a model for power electronics wear estimation depending on robot program and application.
3. New analysis method which expands previously researched energy efficiency study with robot power electronics modules temperature and lifetime evaluation.
4. A lifetime model has been created with an intention of integration in virtual commissioning software.

Analysis of robotized manufacturing systems should consider reliability, as repetitive load damage wear is application specific, dependent on mission profile, robot tool weight and robot hardware layout. In addition, reliability of robot motor drive inverter transistors is linked to electrical energy consumption of the mission profile.

Applications of the study results include a wider range of inverter lineup, reducing costs and increasing market share. Integration of wear estimation model in virtual commissioning software is a highly valued novelty. Predictive maintenance schedule based on mission profile analysis allow to reduce lifetime damage and recognize any hardware with especially high predicted damage.

Future work is to improve model accuracy and performance. Addition of new system components to reliability tool.

Related research of the author has been published and presented 8 times in international conferences or scientific journals. See list of related author's publications, disseminating the research results and conclusions:

1. Šenfelds, A., **Bormanis, O.**, Paugurs, A. Modelling of AC/DC Power Supply Unit for DC Microgrid. In: *2015 IEEE 3rd Workshop Advances in Information, Electronic and Electrical Engineering (AIEEE 2015) Proceedings, Riga, 2015.* Place: IEEE, 2016, pp. 1-4. ISBN 978-1-5090-1202-2. e-ISBN 978-1-5090-1201-5. Available from: doi: 10.1109/AIEEE.2015.7367294.
2. **Bormanis, O.** Development of energy consumption model for virtual commissioning software. In: *2015 56th International Scientific Conference on Power and Electrical Engineering of Riga Technical University (RTUCON) Proceedings, Riga, 2015*. Place: IEEE, 2015, pp. 1-4. ISBN 978-1-5090-0334-1. e-ISBN 978-1-4673-9752-0. Available from: doi:10.1109/RTUCON.2015.7343139.
3. Senfelds, A., Vorobjovs, M., Meike, D., **Bormanis, O.** Power smoothing approach within industrial DC microgrid with supercapacitor storage for robotic manufacturing application. In: *2015 IEEE International Conference on Automation Science and Engineering (CASE) Proceedings, Gothenburg, 2015.* Place: IEEE, 2015, pp. 1333-1338. e-ISBN 978-1-4673-

8183-3. ISSN 2161-8070. e-ISSN 2161-8089. Available from: doi: 10.1109/CoASE.2015.7294283.

4. Šenfelds, A., **Bormanis, O.**, Paugurs, A. Analytical Approach for Industrial Microgrid Infeed Peak Power Dimensioning. In: *2016 57th International Scientific Conference on Power and Electrical Engineering of Riga Technical University (RTUCON 2016) Proceedings, Riga, 2016.* Place: IEEE, 2016, pp. 1-4. ISBN 978-1-5090-3732-2. e-ISBN 978-1-5090-3731-5. Available from: doi: 10.1109/RTUCON.2016.7763140.
5. **Bormanis, O.**, Ribickis, L. Accelerated Life Testing in Reliability Evaluation of Power Electronics Assemblies. In: *2018 IEEE 59th International Scientific Conference on Power and Electrical Engineering of Riga Technical University (RTUCON 2018), Proceedings, Riga, 2018*. Place: IEEE, 2019, pp. 1-5. ISBN 978-1-5386-6904-4. e-ISBN 978-1-5386-6903-7. Available from: doi: 10.1109/RTUCON.2018.8659911.
6. **Bormanis, O.**, Ribickis, L. Review of Burn-In for Production of Reliable Power Electronic Applications. In: *2019 IEEE 60th International Scientific Conference on Power and Electrical Engineering of Riga Technical University (RTUCON 2019) Proceedings, Riga, 2019*. Place: IEEE, 2020, pp.1-7. ISBN 978-1-7281-3943-2. e-ISBN 978-1-7281-3942-5. Available from: doi: 10.1109/RTUCON48111.2019.8982357.
7. **Bormanis, O.**, Ribickis, L. Power Module Temperature in Simulation of Robotic Manufacturing Application. *Latvian Journal of Physics and Technical Sciences.* 2021, vol.5., no.4, pp.3-14. ISSN 0868-8257. e-ISSN 2255-8896. Available from: doi:10.2478/lpts-2021-0029.
8. **Bormanis, O.**, Ribickis, L. Mission Profile based Electro-Thermal Model of Robotic Manufacturing Application. In: *2021 23rd European Conference on Power Electronics and Applications (EPE'21 ECCE Europe) Proceedings, Ghent, 2021*. Place: IEEE, 2021, pp. 1-6. ISBN 978-1-6654-3384-6. e-ISBN 978-9-0758-1537-5. Available from: doi: 10.23919/EPE21ECCEEurope50061.2021.9570547.

Hypothesis of this work are supported by research presented in sections 2, 3 and 4. Section 2 is a modeling stage of the study, presenting the developed mechatronic translation from robot language code to lifetime estimation. Industrial robot electrical cabinet hardware layout options are evaluated and compared in Section 3, and Section 4 investigates various available methods to estimate reliability of the robotized manufacturing hardware.

Thesis sections align with the modeling, assessment and enhancement stages of the study. Results and conclusions are presented within each section and in a summary at the end of this work. Data tables, plots and visualizations with large dimensions are included in the appendices of this thesis.

2. LIFETIME CONSUMPTION MODEL

Parameters of electrical components are defined by operation specification of the equipment. Maximal values are selected considering required derating of the components to comply with the predicted field life stress level. Harsh environment, difficult accessibility, high downtime costs, are some of the factors which demand endurance from electronic designs.

As the customer requires reliable electronics, at the same time a requirement to decrease cost and therefore absolute maximum values of materials is existing from the manufacturer. Cost efficiency is considered during design and manufacturing, and mission profile data has high value to provide knowledge and understanding of expected field stress.

This study attempts to estimate lifetime of semiconductor switch through realistic computer model analysis of field life mission profile data. Junction temperature of isolated gate bipolar transistor (IGBT) is estimated for each of industrial robot axis drive inverters from the robot energy consumption data of model. Junction temperature swings contribute to IGBT degradation due to thermal expansion coefficient mismatch of the adjacent materials. Total fatigue damage is estimated by Palmgren-Miner linear damage hypothesis. To evaluate reliability improvement concepts, a highly detailed model of the hardware is required.

Background of the developed model and specifics of the industrial robot modeling in automotive industry and are reviewed at section 2.1. Section 2.2 contains detailed description of six degree of freedom (6-DoF) KUKA AG (KUKA) industrial robot mechatronic model, translating robot language code to energy consumption. Addition of the developed thermal and lifetime estimation model is presented in section 2.3.

2.1. Modeling Principles, Background of the Model

VCS tools from various industry leaders such as Delmia Robotics (Dassault Systemes) [4], RobotStudio (ABB) [5], Kuka.sim (KUKA) [6] enable simulation of process flow and robot trajectories during development phase of the production cell. Such virtual tools generate robot movement code from the user supplied robot program code. If the launched virtual machine plugin [7] of given VCS includes vendor-specific robot control simulation (RCS) module, then the output simulated trajectory is expected to match with actual movement trajectory and timing on site, with the same robot program code. See differences in trajectory planning between generic path planner and RCS module in Fig. 1 (b). Realistic Robot Simulation (RRS) as a product extension provides support to simulation software connection to manufacturer's RCS module, enabling connection between VCS and RCS module, as shown in Fig. 2.1 (a).

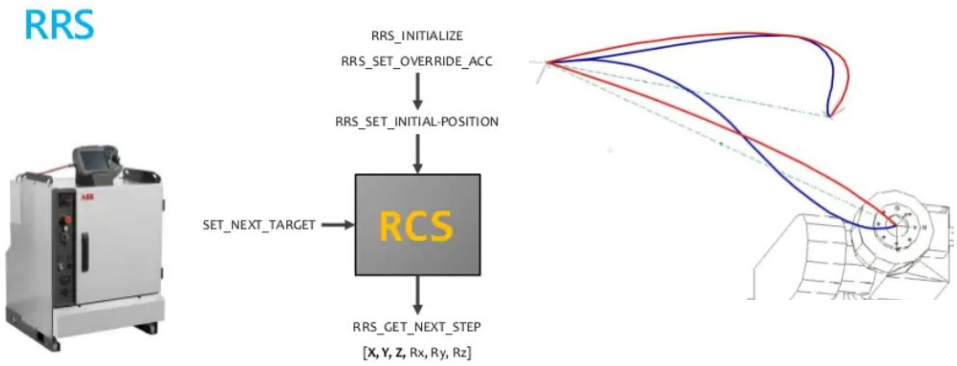

a) b)

Fig. 2.1 (a) sample RRS providing support of RCS to VCS [6], (b) example of trajectory differences, between Robcad Motion Planner (MOP) and KRC1 RCS [8].

With the support of VCS including RCS modules, simulated robot trajectory is highly realistic and can be uploaded on actual hardware with minor modifications, while the simulated mission profile can be used as an input data for further manufacturing hardware related calculations and estimations.

Availability of a realistic mission profile provides valuable input data for energy consumption models. Consumption data of industrial robots and other significant energy consumers are provided to the engineering team for analysis, for example, to adjust robot profile timings or tool application schedule in an attempt to decrease peak currents of the supply circuit.

Simulation model presented in this work is based on output trajectories of KUKA RCS module, extending the available tools not only to provide energy consumption data, but to estimate lifetime of IGBT power modules based on mission profile for each supplied program in KUKA robot language (KRL), as shown in Fig. 2.2.

```
;----- Kleber ein -----
;$VEL.CP=0.45 ; Bahngeschwindigkeit auf 0.45 m/s setzen
;LIN  {X -1197.56,Y -1306.73,Z 549.34,A 3.33,B -4.62,C 107.56,S 6,T 50} C_VEL
;LIN  {X -1090.04,Y -1326.83,Z 538.02,A 0.55,B -4.39,C 105.5,S 6,T 50} C_VEL
;LIN  {X -1017.28,Y -1345.6,Z 534.26,A -1.38,B -4.25,C 104.07,S 6,T 50} C_VEL
;----- Kleber aus -----
;LIN  {X -899.04,Y -1381.65,Z 528.97,A -5.16,B -4.27,C 101.03,S 6,T 50} C_VEL
;LIN  {X -857.19,Y -1393.04,Z 525.27,A -5.59,B -4.27,C 100.69,S 6,T 50} C_VEL
```

Fig. 2.2. KRL code example from adhesive bonding application, defining movement of robot.

In the automotive industry life cycle of industrial robot program is predicted up to 7 years within continuous production. Slight energy efficiency improvements introduce significant energy consumption reduction over long term operating period. Industrial robot energy consumption tools are valuable for cost-effective multi-robot manufacturing scheduling and trajectory planning, providing feedback to engineering team.

Data of the developed simulation tool is suited for analysis of reliability engineers, allowing to evaluate long-term performance of the system and relationship between energy efficiency o of the mission profile and reliability of hardware. Estimation of industrial robot inverter semiconductor module lifetime consumption (LC) from robot program code is a novelty presented through this work. Since mechanical and electrical data of the robot are known from verified model, and trajectory generation is supported by RCS module, junction temperature and total fatigue damage can be estimated through analysis of mission profile data.

There are several factors which affect energy consumption of an industrial robot. Robot movement is defined by kinetic energy, therefore parameters of Eq. (2.1) are significant to energy consumption. As the energy consumption of robot and remaining lifetime of hardware is expected to have a predicted relationship, there factors are estimated to impact reliability of the hardware as well.

$$E_{\mathrm{K}} = \frac{1}{2} m v^2 \tag{2.1}$$

where:

E_{K} – kinetic energy of the robot [J],

m – total mass of the robot, including tool and load [kg],

v – velocity of the robot axis [m/s].

Firstly, more agile robot programs such as handling, clinching, spot-welding, include fast acceleration to arrive at the next processing point quickly, while slower programs such as painting or adhesive bonding are limited by process quality requirements and robot is moving slower. Higher velocity and steep acceleration profile result in increased power consumption peaks, and due to increased kinetic energy, recuperated power peaks during regenerative braking are increased as well, compared to slower robot programs.

Mass is the second parameter of Eq. (2.1), and it is known that moving larger mass requires more energy, which applies for robot applications as well. While mass of the robot is defined by manufacturer, robot tool mass or mass with tool and load combined may vary significantly and is customer introduced. Higher mass will increase power consumption, while lower mass will decrease it.

As the degradation of components is expected to be energy consumption dependent, it is predicted that increased thermal loading from larger power peaks will accelerate bond wire and solder joint wear out of the power electronics modules.

2.2. Mechatronic Model of KUKA 6-DoF Industrial Manipulator

Industrial robot cabinet (see Fig. 2.3 (a)) is simulated in the model not only to provide data from mechanical operation and movement, but also to include electric circuit and electrical processes. This stage of model includes an inverter KUKA Servo Pack (KSP) and rectifier KUKA Power Pack (KPP) losses, stored energy change in DC bus capacitor capacitance, brake chopper status and dissipated power, DC bus voltage, motor current, and others. Simulated industrial robot electric hardware layout is a rectifier-inverter multiple PMSM drive system

with DC link. It includes brake chopper for overvoltage protection and optional external capacitance for storage of regenerated energy.

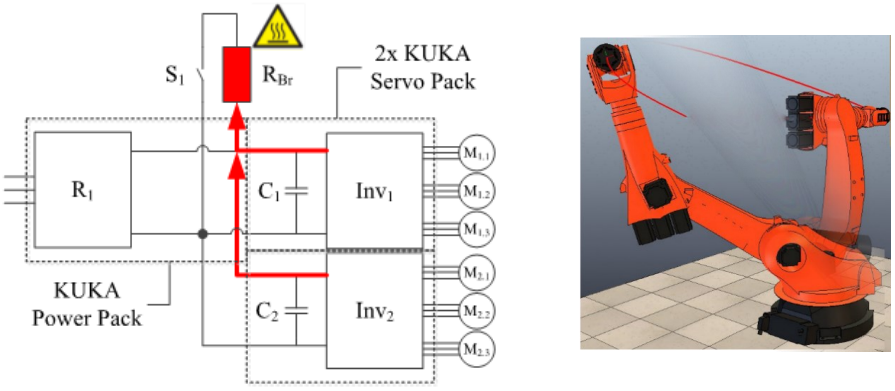

(a) (b)

Fig. 2.3. Simplified industrial robot electrical circuit layout with single power supply and brake chopper to dissipate regenerated energy (a). Model supports a 3D visualization including the robot computer aided design file provided by the manufacturer (b).

Robotics Toolbox for MATLAB [9, 10] is a software tool on which virtual model of robot mechatronic hardware and further transformations to electrical power losses is based. Toolbox supports differential motion, 3-dimensional (3D), 2-dimensional (2D) transformation functions, being involved in data processing to obtain torque values through robot movement.

While the Robotics Toolbox, which is at the core of robot mechanical model, supports simplified graphics and dynamic models, more realistic 3D visualization tool has been integrated in the model, for detailed analysis of robot movement through time and operating space. It simulates actual 3D model of robot (see Fig. 2.3 (b)) and follows the path, generated earlier by the vendor specific RCS module.

Robot cabinet current consumption profile reveal peaks during robot acceleration and periods of no consumption during regenerative braking, as robot motors supply energy to DC bus during deceleration. During spot welding (see Fig. 2.4) or other static operation point, robot axis motors hold the position with relatively small power consumption. In shorter processing times following a deceleration this consumption is expected to be completely or partially supplied from energy stored in capacitance during regeneration. Standstill current depends on load of each axis.

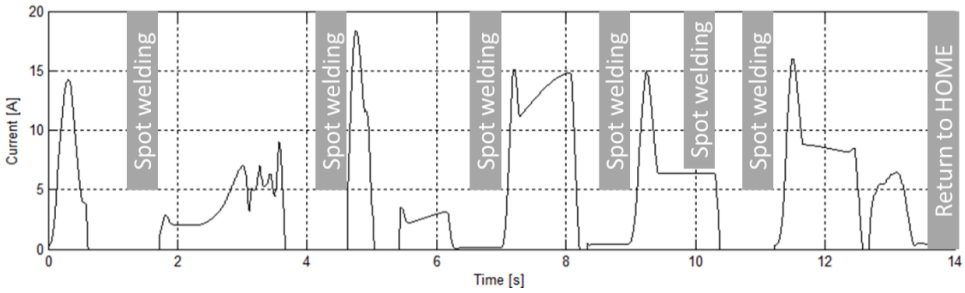

Fig. 2.4. Cabinet current consumption from AC grid during sample six processing points of sample spot-welding program.

There is one inverter circuit for each of robot axis motors, to provide electrical power for its operation, as shown in Fig. 2.5. See data of KUKA industrial robot inverters in Appendix C. Inverters are arranged by rated current through channel in two KSP units with rated current 40A for more demanding axis 1-3 and rated current 20A for less demanding motors of axis 4-6. Larger current consumption for axis 1-3 is expected, as they support most of the robot weight, while axis 4-6 mostly are considered for fine-tuning of the movement and control of approach angle.

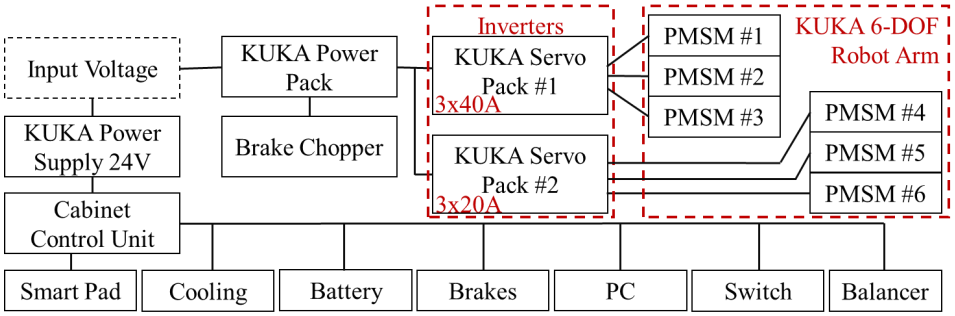

Fig. 2.5. Power supply circuit of KUKA industrial robot cabinet and robot motors.

Background mathematical model of industrial robot axis motor losses is reviewed in section 2.2.1 and section 2.2.2. It includes relevant variables, symbol descriptions and computation equation. Equations are arranged by execution order, starting from motor winding losses, torques, up to final total electrical power consumption of robot permanent magnet synchronous motors (PMSM). Rated values of the mechatronic model components are provided to the study by Daimler AG team and are considered actual or highly probable. Inverter and rectifier losses are evaluated in more detail at section 2.2.3. Final section of this chapter, section 2.2.4. provides an insight to energy flow computation of DC bus, considering previously calculated power losses.

2.2.1. Data of PMSM Torque

Robot movement trajectory for the model is generated from KRL code by RCS module, specific for KUKA robots. File with values of axis position (in degrees) is output of the robot movement path simulation. Array of motor position data for each axis through robot program is illustrated in Fig. 2.6. Derivative of the position data line in graph leads to axial velocity of the motor. Maximal and minimal values of motor axial displacement is limited through control methods.

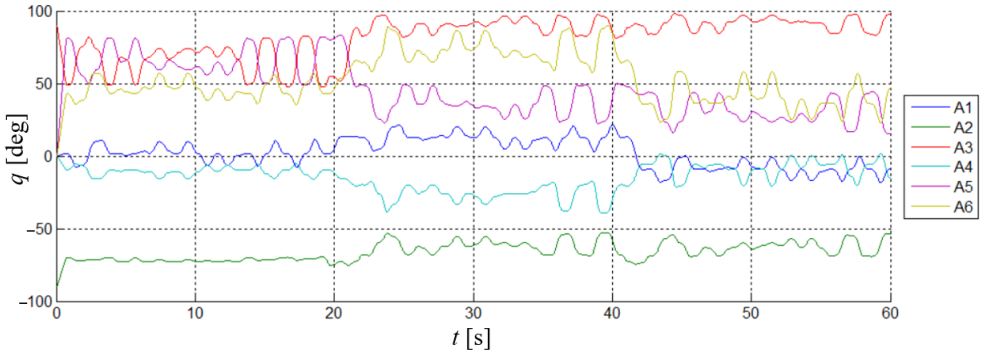

Fig. 2.6. Joint space movement of each robot axis during sample robot program, as generated by computer model.

Input data of robot trajectory is sampled with 12ms intervals, therefore 0.6 second movement includes 50 data points of robot axis angular location. Calculations are loop based, and two data points (current and subsequent) are processed during a single loop. Variables considered in this section are:

$\triangle s$ – distance change between data points [rad],
$\triangle t$ – time difference between data points [s],
$\tau_{\mathrm{fric_v}}$ – viscous friction torque [Nm],
$\tau_{\mathrm{fric_c}}$ – coulomb friction torque [Nm,]
τ_{JM} – inertia moment torque [Nm],
$\tau_{\mathrm{motor_{nofriction}}}$ – torque on motor shaft [Nm],
τ_{gear} – axis gear torque [Nm],
τ_{data} – torque data of robot motors [Nm],
data – input array of robot axis position [rad],
I_{m} – phase current of robot motors [A],
P_{m} – power consumption of robot motors [W],
$qd_{\mathrm{data_m}}$ – rotational speed of motor shaft [rad/s],
qd_{data} – average rotational speed of robot axis of each loop iteration [rad/s].

A series of parameters from the model are hardware dependent and are not affected by the robot application type, either defined as constants or calculated from the defined constant variables. There parameters are:

τ_{N} – rated motor torque [Nm],

I_{N} – rated motor current [A],

k_{t} – torque constant [Nm/A],

R_{axis} – Gear reduction ratio of each motor.

Average rotational speed of robot axis of each loop iteration is calculated as shown in Eq. (2.2).

$$qd_{\mathrm{data}} = \frac{\triangle s}{\triangle t} = \frac{(data_{\mathrm{i+1}} - data_{\mathrm{i}})}{(t_{\mathrm{i+1}} - t_{\mathrm{i}})} \tag{2.2}$$

Rotational speed of motor shaft is calculated considering gear reduction ratios of each motor, according to Eq. (2.3).

$$qd_{\mathrm{data_m}} = qd_{\mathrm{data}} * R_{\mathrm{axis}} \tag{2.3}$$

Torque data array is formed considering torque on motor shaft and various torque losses, see Eq. (2.4). Torque values are calculated through application of inverse dynamic model, output of which is a data array.

$$\tau_{\mathrm{data}} = \tau_{\mathrm{motor_{nofriction}}} + \tau_{\mathrm{fric_v}} + \tau_{\mathrm{fric_c}} + \tau_{\mathrm{JM}} + \tau_{\mathrm{gear}} \tag{2.4}$$

Multiple torque losses are included in model for improved accuracy, including mechanical stress resistance of oil in gearboxes, inertia moment, and others.

Power consumption of robot motors is calculated as a multiplication result from previously obtained motor torques and motor shaft rotational speed, see Eq.(2.5)

$$P_{\mathrm{m}} = \tau_{\mathrm{data}} * qd_{\mathrm{data_m}} \tag{2.5}$$

Sample welding program was simulated with RCS module and processed through Robotics Toolbox integrated in model. Output torque values through the robot program duration are shown in Fig. 2.7 and are input to further calculation. Axis 1-3 show higher torque values, as they support more mass through movement, while axis 4-6 (see complete Axis 1-6 data in Appendix D) support less mass of the robot and load.

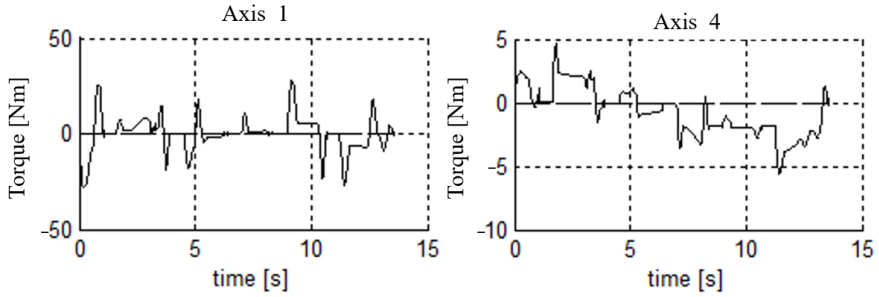

Fig. 2.7. Torque translation for each of six degree of freedom industrial robot servo motors through simulated sample welding program.

Detailed mass and dimension adjustment options for tool of the robot are available, such as mass center and tool weight. Changing these options affect the instantaneous motor torque values – increasing tool mass increase energy consumption and vice versa, as mentioned earlier.

Friction, inertia, gear losses are all considered and calculated in mechanical model of the robot, where translated torque through robot movement is an input parameter [11]. Model includes mass data for robot links of multiple robot types, therefore simulation is not limited to single robot model.

Torque constant is calculated according to Eq. (2.6).

$$k_{\mathrm{t}} = \frac{\tau_{\mathrm{N}}}{I_{\mathrm{N}}} \tag{2.6}$$

2.2.2. Data of PMSM Power Consumption

Phase current of motors is calculated as shown in Eq. (2.7). This equation translates motor torques to electrical current consumed or generated by robot motors.

$$I_{\mathrm{m}} = \frac{\tau_{\mathrm{data}}}{k_{\mathrm{t}}} = \frac{I_{\mathrm{N}}}{\tau_{\mathrm{N}}}\left(\tau_{\mathrm{motor}_{\mathrm{nofriction}}} + \tau_{\mathrm{fric_v}} + \tau_{\mathrm{fric_c}} + \tau_{\mathrm{JM}} + \tau_{\mathrm{gear}}\right) \tag{2.7}$$

Value of phase current changes dynamically through the acceleration and deceleration cycles during robot movement, as shown in Fig. 2.8. Robot is consuming current through the internal DC bus if the current value is positive, and returning recuperated energy to DC bus if the phase current is negative. Amplitude of the current value is higher for axis A1−A3, as the motors of these axis have the highest load weight, supporting the load and tool weight.

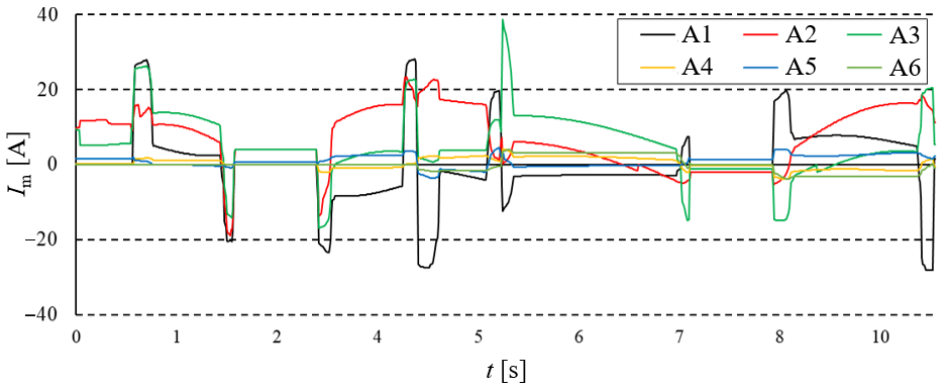

Fig. 2.8. Phase current of robot motors during sample robot program.

As presented earlier in this section, input of electrical model is torque of robot motors through movement time with included hardware mechanical losses of the selected robot. After translation from torque to current consumption, various electrical power losses are calculated. Losses considered in this stage of computation model include iron, cable and stator resistive losses of PMSM. Variables considered in this section are:

P_{R_s} – power loss of stator winding resistance [W],

P_{Fe} – power loss of iron [W],

P_{add} – power loss of additional miscellaneous losses [W],

P_{sum} – total electric power consumption of all motors [W],

$P_{M_{el}}$ – power consumption of each motor with electrical losses [W].

Parameters defined as constants or calculated from the defined constant variables are:

α_{Cu} – temperature coefficient for the stator winding material,

η_{rob} – efficiency of robot motor [%],

$\eta_{m_{add}}$ – proportion of additional losses, such as cable losses [%],

τ_N – rated torque of robot motor [Nm],

ω_N – rated rotational speed of the motor [rad/s],

$k_{\Delta_{add}}$ – coefficient of additional losses,

R_s – robot stator winding resistance [Ω],

P_{Rs_N} – rated power loss of stator winding resistance [W],

P_{m_N} – rated mechanical power of motor [W],

P_{loss_N} – rated power loss of robot motor [W],

P_{add_N} – rated value of additional motor power losses [W],

P_{Fe_N} – rated iron losses [W],

$T_{ambient}$ – ambient temperature of robot motors [°C],

T_{max} – maximal temperature of robot motor [°C].

Visual representation of the mentioned losses is shown in Fig. 2.9, where combined electrical power consumption of sample robot motor A1, during sample movement, includes motor power consumption, iron and stator resistive power losses.

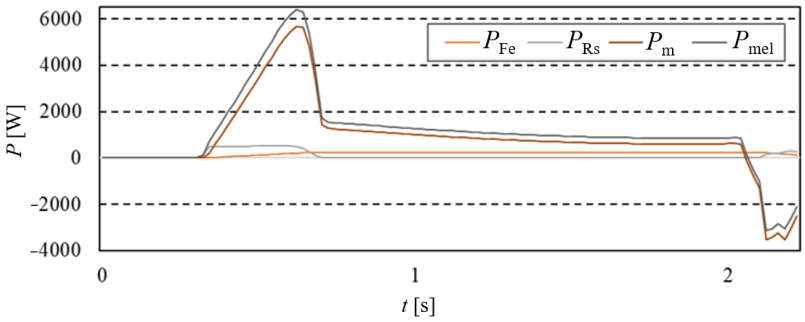

Fig. 2.9. Robot motor power consumption structure of single robot axis A1, during sample movement, including mechanical power consumption, electrical power consumption, resistive power losses of cables and power loss in iron.

Iron losses are robot movement speed dependent, and resistive power losses depends on phase current of robot motors.

Electrical losses of stator winding are calculated according to Eq. (2.8).

$$R_{\mathrm{s}} = R_{\mathrm{ref}}\big(1 + \alpha(T - T_{\mathrm{ref}})\big) = R_{\mathrm{s}_0} * \big(1 + \alpha_{\mathrm{Cu}} * (T_{\mathrm{max}} - T_{ambient})\big) \tag{2.8}$$

Power losses of stator windings are calculated as shown in Eq. (2.9).

$$P_{\mathrm{R_s}} = 3 * I_{\mathrm{m}} * R_{\mathrm{s}} \tag{2.9}$$

Rated value of stator winding power losses is calculated as shown in Eq. (2.10).

$$P_{\mathrm{Rs_N}} = 3 * I_{\mathrm{N}}^2 * R_{\mathrm{s}} \tag{2.10}$$

Rated mechanical power of motor is calculated according to Eq. (2.11).

$$P_{\mathrm{m_N}} = \tau_{\mathrm{N}} * \omega_{\mathrm{N}} \tag{2.11}$$

Rated power loss of robot motor considers rated power and efficiency, see Eq. (2.12).

$$P_{\mathrm{loss_N}} = \frac{1 - \eta_{\mathrm{rob}}}{\eta_{\mathrm{rob}}} * P_{\mathrm{m_N}} \tag{2.12}$$

Rated value of additional motor power losses is calculated as shown in Eq. (2.13)

$$P_{\mathrm{add_N}} = \frac{k_{\Delta_{\mathrm{add}}}}{\eta_{\mathrm{rob}}} * P_{\mathrm{m_N}} \tag{2.13}$$

Rated value of iron losses in robot motor core is calculated according to Eq. (2.14).

$$P_{\mathrm{Fe_N}} = P_{\mathrm{loss_N}} - P_{\mathrm{add_N}} - P_{\mathrm{Rs_N}} = \tau_{\mathrm{N}} * \omega_{\mathrm{N}} \left(\frac{1 - \eta_{\mathrm{rob}}}{\eta_{\mathrm{rob}}} - \frac{k_{\Delta_{\mathrm{add}}}}{\eta_{\mathrm{rob}}} \right) - 3 * I_{\mathrm{N}}^2 * R_{\mathrm{s}} \tag{2.14}$$

Moving forward, power losses of iron are calculated according to Eq. (2.15).

$$P_{\mathrm{Fe}} = P_{\mathrm{Fe_N}} * \left(\frac{q d_{\mathrm{data_m}}}{\omega_{\mathrm{N}}} \right) \tag{2.15}$$

Electrical power consumption of each motor with electrical losses is calculated as shown in Eq. (2.16).

$$P_{\mathrm{M_{el}}} = \big(P_{\mathrm{m}} + P_{\mathrm{R_s}} + P_{\mathrm{Fe}}\big)\big(1 - \eta_{\mathrm{m_{add}}}\big) \tag{2.16}$$

Total electrical power consumption of robot motors is calculated according to Eq. (2.17), *i* being the number of PMSM axis, from 1 to 6 according to currently developed model. Total power consumption includes mechanical and electrical power losses from previous simulation steps, combined in single variable, as all of the inverter modules are connected to the same internal DC link of robot electrical cabinet. Inverter power losses are added to the computed value of electrical power consumption in further computation steps.

$$P_{\mathrm{sum}} = \sum_{\mathrm{i}=1}^{6} P_{\mathrm{M_{el}}}(i) \tag{2.17}$$

Power consumption fluctuates as the robot is accelerating and decelerating, demanding high combined power consumption value as all of the robot motors are accelerating, and providing a significant amount of power back to DC bus during deceleration as recuperated energy, see Fig. 2.10.

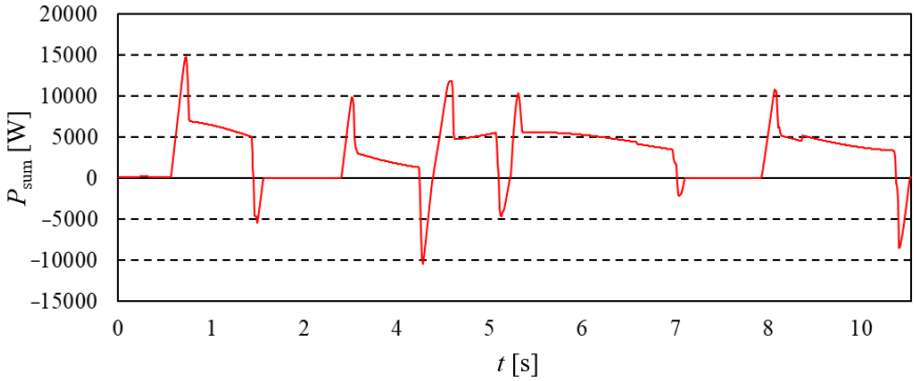

Fig. 2.10. Combined electrical power consumption of robot motors.

Output result, electrical power consumption of robot motors is ready for further simulation steps. Operation parameters and states of the internal DC link still needs to be computed and the process is described in the following sections.

2.2.3. Inverter and Rectifier Losses

Inverter and rectifier power losses are calculated considering efficiency and proportion of actual equipment load current from rated current. Related inverter and rectifier power losses are calculated for each of the robot axis separately. Computation related variables introduced in this section are:

I_{m} – motor consumed phase current [A],

$I_{\mathrm{rec_N}}$ – rated rectifier current [A],

P_{rec} – power losses of rectifier [W].

Parameters defined as constants or calculated from the defined constant variables are:

$\eta_{\mathrm{inv_{KSP}}}$ – Efficiency of inverter cooling [%],

$\eta_{\mathrm{inv_{IGBT}}}$ – Efficiency of inverter IGBT [%],

$\eta_{\mathrm{rec_{KPP}}}$ – Efficiency of rectifier cooling [%],

$\eta_{\mathrm{rec_{diode}}}$ – Efficiency of rectifier diode [%],

$I_{\mathrm{inv_N}}$ – Rated inverter current [A],

$I_{\mathrm{rec_N}}$ – Rated rectifier current [A],

$P_{\mathrm{rec_N}}$ – Rated power consumption of rectifier [W],

$P_{\mathrm{inv_N}}$ – Rated inverter power consumption [W].

Total power consumption of industrial robot includes combined inverter losses of all robot axis, as shown in Eq. (2.18). Proportion of actual inverter load and rated inverter load current is included in estimation of inverter power losses, which are separated in cooling and IGBT related efficiency losses.

$$P_{\text{sum}} = P_{\text{sum}} + \sum_{i=1}^{6} P_{\text{inv}_\text{N}} * \left(\eta_{\text{inv}_{\text{KSP}}}(i) * \left(\frac{I_{\text{m}}(i)}{I_{\text{inv}_\text{N}}} \right) + \eta_{\text{inv}_{\text{IGBT}}}(i) * \left(\frac{I_{\text{m}}(i)}{I_{\text{inv}_\text{N}}} \right)^2 \right) \quad (2.18)$$

Power losses, current consumption, rated current – inverter electrical parameters are considered per each of robot axis, as each of the axis has independent drive circuit, as shown in Fig. 2.11. Single IGBT device (see Fig. 2.11 (c)) as manufactured merges 6 integrated switches to support drive of the robot axis PMSM, and has integrated case mount for heatsink assembly, as heatsink is shared by the six integrated semiconductor switches. Three of the single-phase inverters are grouped into a single drive unit printed circuit board assembly (PCBA) as shown in Fig. 2.11 (b). KUKA Servo pack inverter (see Fig. 2.11 (a)) has a massive heatsink, to which the full bridge single phase inverters are attached with thermal compound for improved thermal contact.

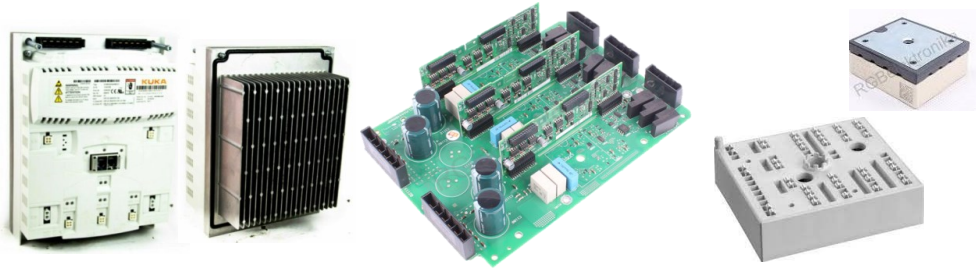

a) b) c)

Fig. 2.11. Inverter components of robot electric cabinet, including: a) front and rear view of KUKA Servo Pack inverter, b) inverter PCBA for 3 robot axes, c) IGBT device with 6 integrated switches for three phase H bridge motor drive support.

While inverter losses are considered for each axis of robot motor, rectifier losses combine the previously reviewed per robot unit and are calculated according to Eq. (2.19). Losses are proportional to load current, similar as inverter losses. Rectifier losses are reviewed later in the computational model, as DC bus operational parameters must be calculated.

$$P_{\text{rec}} = P_{\text{rec}_\text{N}} * \left(\eta_{\text{rec}_{\text{KPP}}} * \left(\frac{I_{\text{m}}}{I_{\text{inv}_\text{N}}} \right) + \eta_{\text{rec}_{\text{diode}}} * \left(\frac{I_{\text{m}}}{I_{\text{inv}_\text{N}}} \right)^2 \right) \quad (2.19)$$

2.2.4. DC Bus Energy and Power Data

Energy flow and electrical parameters in DC bus of the robot model are calculated in this section. DC bus related variables introduced in this section are:

E_{act} – actual energy state of the circuit [J],

E_{motor} – anergy consumption of motors and inverters [J],

$E_{\text{DC}_{\text{bus}}}$ – energy consumption through DC bus, including robot motors and inverters [J],

E_{total} – total energy consumption of the computation cycle in model [J],

i – incremental computation index of for-to loop,

I – DC bus current, consumed from AC grid [A],

$I(1)$ – initial current of DC bus [A],

$I_{\mathrm{m_{sum}}}$ – combined current consumption of robot motors [A],

P_{DCbus} – power consumption of the DC bus chopper and balancing resistors [W],

U – DC bus voltage [V],

$U(1)$ – initial voltage of DC bus [V],

U_{ripple} – voltage ripple of rectifier output [V].

Parameters defined as constants or calculated from the defined constant variables are:

β_{cap} – constant of capacitor passive balancing circuit resistance calculations [Ω*F],

C_{add} – capacitance connected to DC bus externally [F],

$C_{\mathrm{rob_{default}}}$ – internal capacitance of inverter input, rectifier output [F],

C – capacitance of DC bus [F],

D_{ch} – duty cycle of brake chopper connecting switch [%],

f – frequency of the rectifier output voltage AC component [Hz],

R_{ch} – resistance of brake chopper [Ω],

R_{bal} – resistance of capacitor voltage balancing [Ω],

t – time step of the computational model [s],

$U_{\mathrm{ch_h}}$ – voltage threshold of brake chopper connection [V],

U_{norm} – rated DC bus voltage [V].

DC bus voltage and current of the initial state is calculated from the total electrical power consumption of all motors, including inverter losses as shown in Eq. (2.20).

$$I(1) = \frac{P_{\mathrm{sum}}(1)}{U(1)} \tag{2.20}$$

Data of PMSM electrical power consumption was sampled with a time step of 12ms through mechanical model. This variable is an input to the electrical model and is therefore interpolated to 1ms time steps for increased accuracy. Basis of the DC bus energy model is constructed as a for-to loop, continued until the end of total electrical power consumption data, at the end of the robot mission profile. As initial state is defined with i=1, computation is continued starting from loop index *i*=2.

Actual energy of the DC bus is calculated at the beginning of each cycle, as shown in Eq. (2.21). Initial state of DC bus capacitor capacitance is fully charged, and the state of charge varies according to the voltage in previous computation cycle.

$$E_{\mathrm{act}}(i) = \frac{C * U_{\mathrm{i-1}}^2}{2} \tag{2.21}$$

Energy consumption of motors and inverters is calculated as shown in Eq. (2.22).

$$E_{\mathrm{motor}}(i) = P_{\mathrm{sum}}(i) * t \tag{2.22}$$

Operation modes of the model is controlled by DC bus voltage of the previous cycle. At initial stage motors of robot are supplied from AC grid, as the alternative energy source (capacitors) are not sufficiently charged. Combined current supplied to robot motors is calculated as shown in Eq. (2.23).

$$I_{\mathrm{m_{sum}}} = \frac{P_{\mathrm{sum}}(\mathrm{i})}{U_{\mathrm{i-1}}} \tag{2.23}$$

Total capacitance of the DC bus is a combination of internal capacitance connected at the inverter and rectifier, and an optional external capacitance connected by engineer at the production site, see Eq. (2.24).

$$C = C_{\mathrm{add}} + C_{\mathrm{rob_{default}}} \tag{2.24}$$

Value of passive balancing resistance is selected according to [12], as shown in Eq. (2.25).

$$R_{\mathrm{bal}} = \frac{\beta_{\mathrm{cap}}}{C_{\mathrm{add}}} \tag{2.25}$$

In case of additional capacitance, energy dissipated in the process of passive voltage balancing of capacitors is calculated as in Eq. (2.26).

$$E_{\mathrm{bal}}(i) = \frac{U_{\mathrm{i-1}}^2}{R_{\mathrm{bal}}} * t \tag{2.26}$$

As current consumption of robot motors is increasing, ripple voltage increases as well. It is calculated according to Eq. (2.27).

$$U_{\mathrm{ripple}} = \frac{U_{\mathrm{norm}}}{12 * f * \frac{U_{\mathrm{i-1}}}{I_{\mathrm{m_{sum}}}} * C} \tag{2.27}$$

DC bus voltage of the following computation cycle is calculated as shown in Eq. (2.28). It is a result of computations presented in previous equations, and considers various operation states of the DC bus, such as capacitor charge, discharge, brake chopper activation.

$$U(i) = U_{\mathrm{norm}} - U_{\mathrm{ripple}} \tag{2.28}$$

During operation ripple voltage is calculated, depending on motor power consumption as one of impact factors. As the robot accelerates and motor phase current is increased, ripple voltage increases as well. As the robot decelerates and recuperation energy is returned to DC bus, voltage is increasing as well. Voltage increase is limited by threshold voltage, at which brake chopper resistance is connected, resulting in a voltage decrease. DC bus voltage dynamics through computation of sample robot program is shown in Fig. 2.12.

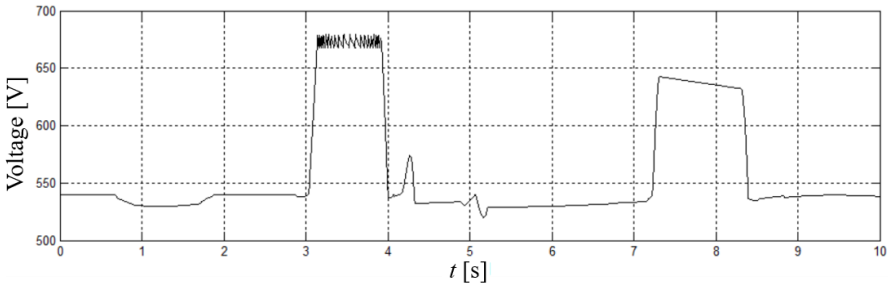

Fig. 2.12. DC bus voltage during sample movement.

As PMSMs and inverters robot are consuming from AC grid through DC bus, electrical energy consumption is calculated as in Eq. (2.29).

$$E_{\mathrm{DC_{bus}}}(i) = E_{\mathrm{motor}}(i) \tag{2.29}$$

Energy is not supplied from the AC grid either if the robot is decelerating and enters regenerative mode ($P_{\mathrm{sum}}(i)$<0) or the charge in capacitors is capable to supply the consumption of robot motors and DC bus voltage is above rated value.

If brake chopper resistance is connected it dissipates the recuperated energy of robot motors, as the resistance connection is controlled by duty cycle. Conditions of connection include completely charged capacitors and DC bus voltage above the threshold value. Dissipated energy is calculated as in Eq. (2.30) . As the dissipated energy exceeds the recuperated energy of robot motors, capacitor is slightly discharged before disconnection of brake chopper resistance.

$$E_{\mathrm{chopper}}(i) = \frac{U_{\mathrm{i-1}}^2}{R_{\mathrm{ch}}} * t * D_{\mathrm{ch}} \tag{2.30}$$

As amount of recuperated energy continue to increase above dissipation rate of fully connected brake chopper, dissipated energy is calculated as shown in Eq. (2.31).

$$E_{\mathrm{chopper}}(i) = E_{\mathrm{act}} - \frac{C * U_{\mathrm{ch_h}}^2}{2} - E_{\mathrm{motor}} - E_{\mathrm{bal}} \tag{2.31}$$

During the recuperation and energy dissipation on brake chopper no energy is supplied from AC grid, therefore energy consumption of DC bus from AC grid is as in Eq. (2.32).

$$E_{\mathrm{DC_{bus}}}(i) = 0 \tag{2.32}$$

Total energy consumption of the computation cycle is calculated as shown in Eq. (2.33).

$$E_{\mathrm{total}}(i) = E_{\mathrm{act}}(i) - E_{\mathrm{motor}}(i) - E_{\mathrm{chopper}}(i) - E_{\mathrm{bal}}(i) \tag{2.33}$$

Model DC bus voltage for the scenario of energy not being consumed from AC grid is calculated each cycle, according to Eq. (2.34).

$$U(i) = \sqrt{\frac{2 * E_{\mathrm{total}}(i)}{C}} \tag{2.34}$$

Current value supplied to DC bus through rectifier in the computation model is calculated during each iteration of the cycle, according to Eq. (2.35). It considers energy state of the DC bus, which is calculated from electrical power consumption of the motors.

$$I(i) = \frac{E_{\mathrm{DC_{bus}}}(i)}{U(i) * t} \tag{2.35}$$

Current change in time during sample robot program is shown in Fig. 2.13. As the current is inverse to voltage, higher current will correspond to a lower DC bus voltage, likely during brake chopper connection, or robot acceleration. During recuperation no current is consumed from AC grid.

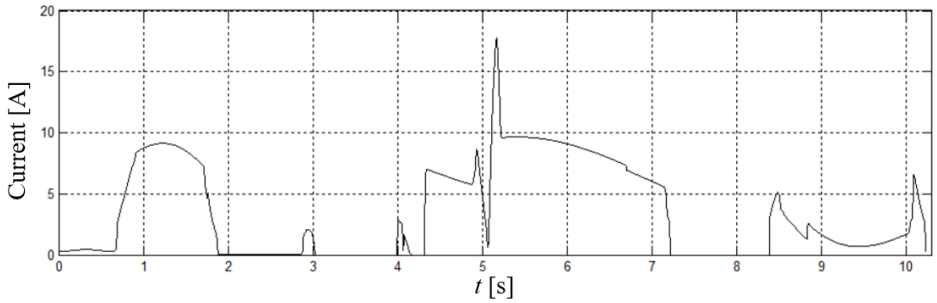

Fig. 2.13. Current supplied from AC grid to DC link through rectifier.

Power consumption of the DC bus chopper and balancing resistors is calculated according to Eq. (2.36).

$$P_{\mathrm{DC_{bus}}}(i) = \frac{E_{\mathrm{DC_{bus}}}(i)}{t} \tag{2.36}$$

Computation loop ends with addition of rectifier losses to total power consumption, see Eq. (2.37). As there is a single rectifier unit per robot, internal DC link and robot motors are supplied through it.

$$P_{\mathrm{DCbus}} = P_{\mathrm{DCbus}} + P_{\mathrm{rec}} \tag{2.37}$$

Power consumption graph (see Fig. 2.14) reveals amount of power supplied to some of the major electrical cabinet components. Rectifier, inverter and other efficiency losses form the difference of motor and grid power consumption. Electrical energy stored in capacitor reveal how recuperation energy is stored in the capacitance, and how excess power is dissipated in brake chopper resistance. Sample movement includes two standstill points at 2nd and 7th second.

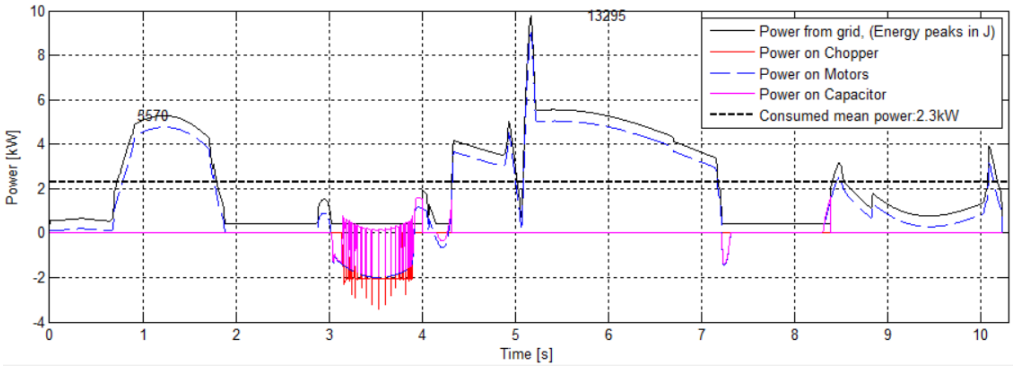

Fig. 2.14. Power consumption of motors, brake chopper resistance and capacitor through sample movement with 2 standstill points.

2.3. Estimation of Junction Temperature and Thermal Wear

Code is translated to movement, which is an input to inverse kinematics model of Robotics Toolbox, therefore providing data of robot axis placement and velocity. Mechanical losses are translated to electrical power losses. Voltage and current estimations are computed. The developed model is designed considering requirement to return computed data to virtual commissioning software (VCS), through application programming interface (API).

Translation of robot program code to IGBT module junction temperature and thermal wear data is managed through the previously described and developed computation model, as shown in Fig. 2.15.

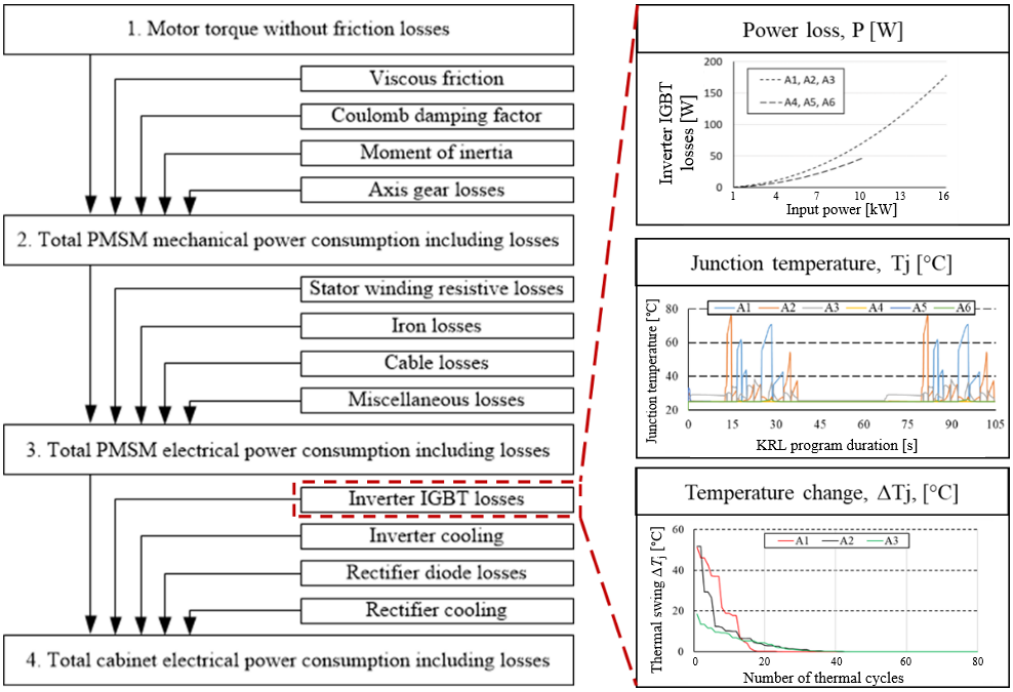

Fig. 2.15. Computation flow of translating mechanical data to electrical parameters in the computer model, extended with thermoelectrical calculations of IGBT operation

Mission profile for inverter IGBT junction temperature estimation is considered power consumption of motors including inverter power losses. Power is translated from DC bus voltage and current consumption of the robot axis motor, as the current is supplied through IGBT modules of the inverter. Power losses are input power dependent, see Fig. 2.16 (b).

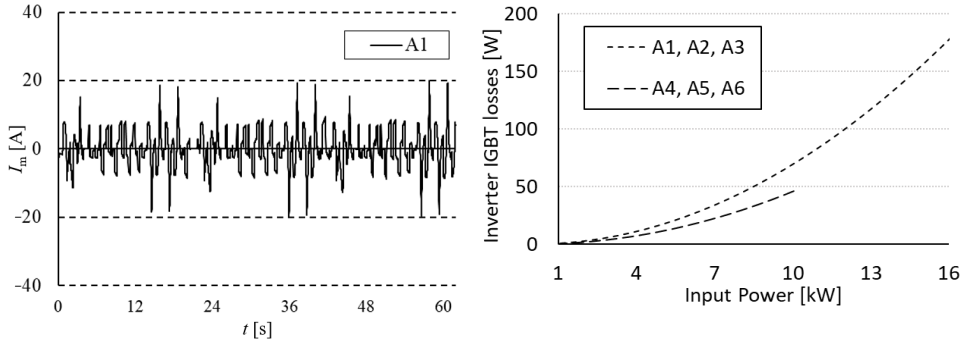

(a) (b)

Fig. 2.16. Mission profiles of inverters for six robot axis motors (a). Drive unit inverter IGBT losses as a function of input power per robot axis (b).

As the robot is following the programmed KRL code, mission profile for each of robot motors is expected to differ even through the executed program is the same. Different industrial applications of the robot change acceleration or deceleration slopes, program duration, acceleration cycles, and other factors, therefore changing the mission profile, which for sample motor current consumption of A1 robot axis is sampled with step size in milliseconds (see Fig. 2.16 (a)).

Section 2.3.1. provides an insight to computation of IGBT junction temperature in the developed model, as a translation from motor phase current mission profile. Application of fatigue estimation principles from the estimated junction temperature data is described in section 2.3.2. Factors affecting temperature and fatigue are analyzed in section 2.3.3.

2.3.1. Junction Temperature of IGBT Modules

Data of inverter performance is evaluated in current model to estimate lifetime of IGBT modules. Increased power consumption through robot operation leads to higher inverter currents, which result in higher currents and also losses at IGBT as shown in Fig. 2.16 (b).

Standards for terminology, essential ratings and other relevant information of IGBTs is specified by IEC 60747-9. In scope with this standard, junction temperature is in the junction region of a semiconductor chip. It is more correctly termed "virtual junction temperature", as it is not exact junction temperature of one of the chips in the module [13]. Junction temperature of inverter IGBT modules is estimated in this section.

Motor phase current is supplied to collector of IGBT. It is supplied through multiple parallel and redundant wire-bonds to die of the module. IGBT is controlled through gate current supplied to die, and main output is at the emitter. In the thermal resistance chain, junction temperature is the first level, where wire-bond is connected to die of semiconductor.

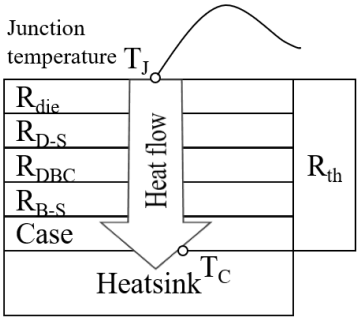

Fig. 2.17. Thermal impedances of sample IGBT module from wire-bond to heatsink.

Thermal impedance of IGBT module combines a series of internal layer impedances as shown in Fig. 2.17, heat flowing from junction temperature through stack-up of module, until

case temperature. Thermal impedance of heatsink will affect the heatsink temperature, which is considered constant in this model, due to active cooling.

In the developed model electrical power losses and temperature values are being averaged at millisecond level, as the focus of study is to provide initial feedback to robot program developers at VCS. Inverter unit is assumed to be a completed product, which parameters are not expected to be reviewed in detail during this study.

Current model does consider the anti-parallel diode integrated in IGBT module package, thermally linked to IGBT semiconductor switch. Power losses of inverter IGBT and anti-parallel diode are averaged through the switching cycles within a step of 12ms (0.012s) which may include several cooling and heating cycles of the inverter.

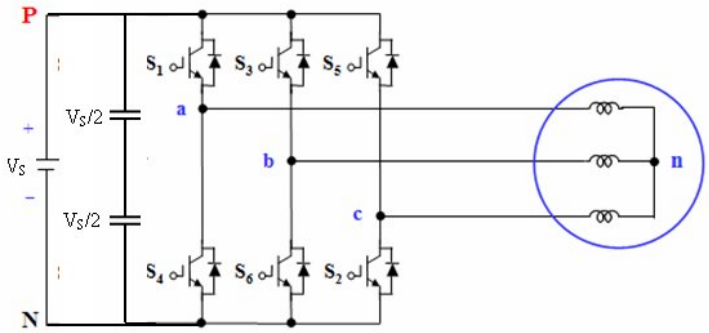

Fig. 2.18. Sample power circuit diagram of three phase bridge inverter, based on IGBT semiconductor switches [14].

Electro-thermal model of IGBT module has been developed to support further translation of mission profile data to instantaneous electrical power losses and junction temperature of the semiconductor module [15]. There are six PMSM motors for six degree of freedom industrial robot. Each of motors is supplied by three phase inverters, including a pair of IGBT modules per each phase (see Fig. 2.18). Six modules are considered equal and electrical load is applied equally between the three phases.

Junction temperature of inverter IGBT modules is estimated in this section. Variables used in computations include:

I_{m} – PMSM current supplied through inverter [A],

P – inverter semiconductor module power loss [W],

P_{inv}– inverter power consumption [W],

t_{prog} – KRL robot program duration [s],

T_{j} – inverter semiconductor power module junction temperature [°C].

Parameters defined as constants or calculated from the defined constant variables are:

β_1 – translation parameter of IGBT and anti-parallel diode thermal impedance,

β_2 – constant translating losses from 6-pack module level to a single device,

i – time sampling interval [s],

T_{a} – ambient temperature of robot hardware cabinet [°C],

$Z_{\mathrm{th_{j-c}}}$ – junction to case thermal impedance of semiconductor module [°C/W],

$Z_{\mathrm{th_{c-h}}}$ – case to heatsink thermal impedance of semiconductor module [°C/W],

$Z_{\mathrm{th_{h-a}}}$ – heatsink to ambient environment thermal impedance [°C/W].

IGBT module package must be durable and reliably dissipate the power losses, withstand high junction temperature. Power losses of each IGBT module 6-package is calculated according to Eq. (2.38). In this model switching losses and conduction losses are not considered separately.

$$P_{\mathrm{inv_{IGBT}}} = P_{\mathrm{inv_N}} * \eta_{\mathrm{inv_{IGBT}}} \left(\frac{|I_{\mathrm{m}}(i)|}{I_{\mathrm{inv_N}}} \right)^2 \tag{2.38}$$

Proportion of inverter IGBT losses related to total power losses during inverter operation is shown in Fig. 2.19. Other inverter losses include miscellaneous power losses of KSP, not related to IGBT operation.

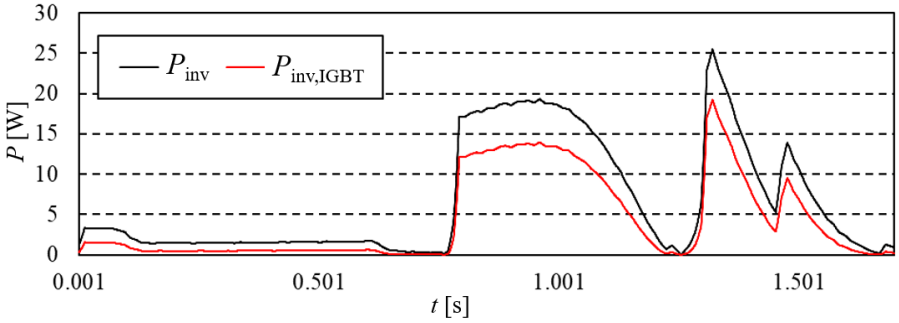

Fig. 2.19. Computed power losses of A1 robot axis inverter and power loss of IGBT module switches.

In the developed electro-thermal model, ambient environment and heatsink temperatures are stabilized by forced airflow. Thermal transient process is ignored in this computation. In this initial study, heatsink temperature is considered constant due to active cooling. Power losses of IGBT is the power which is dissipated in module and therefore directly influence junction temperature change in time, as shown in Eq. (2.39).

$$T_{\mathrm{j}}(t) = P_{\mathrm{inv_{IGBT}}}(t) \cdot (Z_{\mathrm{th_{j-c}}} + Z_{\mathrm{th_{c-h}}} + Z_{\mathrm{th_{h-a}}}) + T_{\mathrm{a}}(t) \tag{2.39}$$

As the investigated module combines six IGBT modules in single package, division of power by number of embedded IGBT modules is required, to estimate dissipated power of single-phase switches. Thermal impedances of the module from junction to ambient environment are required for junction temperature calculation. Total thermal impedance of the inverter system is calculated according to Eq. (2.40).

$$Z_{\mathrm{th_{SUM}}} = Z_{\mathrm{th_{j-c}}} + Z_{\mathrm{th_{c-h}}} + Z_{\mathrm{th_{h-a}}} \tag{2.40}$$

Model is expected to provide initial estimate of junction temperature, therefore estimation method from maximal junction temperature of IGBT is selected for computation of combined thermal resistance. Thermal resistance of the robot axis 1-3 drive inverter system is calculated from the maximal junction temperature data of IGBT semiconductor switch as in Eq. (2.41).

$$Z_{\mathrm{th_{SUM_{IGBT}}}} = \frac{T_{\mathrm{j,IGBT_{max}}} - T_{\mathrm{a}}}{P_{\mathrm{loss_{max}}}} \tag{2.41}$$

As the estimated combined thermal resistance is computed, junction temperature estimation equation is transformed to Eq. (2.42), depending on the thermal impedance, power losses and ambient temperature. Equation is adjusted to IGBT semiconductor switch and diode junction temperature, as shown later in Eq. (2.45) and Eq. (2.46).

$$T_{\mathrm{j}}(i) = P_{\mathrm{IGBT}} * Z_{\mathrm{th_{SUM}}} + T_{\mathrm{a}} \tag{2.42}$$

Hardware selection variation options is a problem for the developed model, as selection of any specific values would limit the model to use cases for specific manufacturer, specific units. Workaround for this situation is an introduction of multiplier β_1 (see Eq.2.43, Eq.2.44), averaged from IGBT and anti-parallel thermal inertia data comparison of 7 various SKiiP IGBT modules (see Table 2.1).

$$\frac{Z_{\mathrm{th_{SUM_{IGBT}}}}}{Z_{\mathrm{th_{SUM_d}}}} = \frac{1}{\beta_1} \rightarrow Z_{\mathrm{th_{SUM_d}}} = Z_{\mathrm{th_{SUM_{IGBT}}}} * \beta_1 \tag{2.43}$$

It should be noted, that using datasheet value in the computation model does not guarantee precise results, due to production process and aging effect introduced variations [16].

Table 2.1.

Parameters of Infineon SKiiP IGBT six-pack modules

		[K/W]	[K/W]	
i	P/N	$R_{\mathrm{th_{IGBT}}}(\mathrm{i})$	$R_{\mathrm{th_d}}(\mathrm{i})$	β_1
1	27AC066V1	0.75	1.2	
2	13AC12T4V1	1	1.52	
3	15AC065V1	1.05	1.5	
4	26AC126V1	0.5	0.7	
5	25AC12T4V1	0.71	0.95	
6	28AC12T7V1	0.65	0.85	
7	23AC12Y4V1	1	1.52	1.444

$$\beta_1 = \frac{1}{7}\sum_{i=0}^{7}\frac{R_{\mathrm{th_d}}(i)}{R_{\mathrm{th_{IGBT}}}(i)} \tag{2.44}$$

IGBT switch and anti-parallel diode does not conduct current simultaneously, as IGBT losses are affected during positive voltage and positive current, while diode losses are dissipated

during positive voltage and negative current periods. During current conduction, IGBT component junction temperatures are estimated as shown in Eq. (2.45) and Eq. (2.46).

$$T_{\mathrm{j_{IGBT}}}(i) = P_{\mathrm{IGBT}} * Z_{\mathrm{th_{SUM_{IGBT}}}} + T_{\mathrm{a}} \tag{2.45}$$

$$T_{\mathrm{j_d}}(i) = P_{\mathrm{IGBT}} * \beta_1 * Z_{\mathrm{th_{SUM_{IGBT}}}} + T_{\mathrm{a}} \tag{2.46}$$

As the load current is not always rated current, adjustment to range of current values is required. Load adjustment is assumed linear by absolute value of motor current and rated inverter current comparison. Junction temperature of IGBT module switch and diode with linear current adjustment is computed as shown in Eq. (2.47), Eq. (2.48).

$$T_{\mathrm{j,IGBT}}(i) = P_{\mathrm{IGBT}} * Z_{\mathrm{th_{SUM_{IGBT}}}} * \frac{\overline{I_{\mathrm{m}}(i)}}{I_{\mathrm{inv_N}}} + T_{\mathrm{a}} \tag{2.47}$$

$$T_{\mathrm{j,d}}(i) = P_{\mathrm{IGBT}} * Z_{\mathrm{th_{SUM_d}}} * \beta_1 * \frac{\overline{I_{\mathrm{m}}(i)}}{I_{\mathrm{inv_N}}} + T_{\mathrm{a}} \tag{2.48}$$

Expanding the thermal impedance and power loss expressions and shortening the repeating variables, results in junction temperature estimation equations, see Eq. (2.49) and Eq. (2.50).

$$T_{\mathrm{j,IGBT}}(i) = \frac{P_{\mathrm{inv_{N_{loss}}}}}{P_{\mathrm{inv_{max_{loss}}}}} \frac{\overline{I_{\mathrm{m}}(i)}}{I_{\mathrm{inv_N}}} \left(T_{\mathrm{j,IGBT_{max}}} - T_{\mathrm{a}}\right) + T_{\mathrm{a}} \tag{2.49}$$

$$T_{\mathrm{j,d}}(i) = \beta_1 \frac{P_{\mathrm{inv_{N_{loss}}}}}{P_{\mathrm{inv_{max_{loss}}}}} \frac{\overline{I_{\mathrm{m}}(i)}}{I_{\mathrm{inv_N}}} \left(T_{\mathrm{j,d_{max}}} - T_{a}\right) + T_{\mathrm{a}} \tag{2.50}$$

Junction temperature data output by previous calculations are further processed, introducing thermal inertia and heating time constant in the model, as shown in Eq. (2.51). Output result is a smoother, more realistic temperature profile, as extreme peak values are filtered.

$$T_{\mathrm{j}}(i) = T_{\mathrm{j_{(i-1)}}} + \left(T_{\mathrm{j_{(i)}}} - T_{\mathrm{j_{(i-1)}}}\right) * \left(1 - e^{-\frac{0.012}{\beta_2}}\right) \tag{2.51}$$

As the current is held constant for a period of time, temperature attempts to reach a stable value as well, however, there is a time delay in the process, due to thermal inertia of the hardware system acting as a thermal capacitance. Range of heatsink time constant, considering this is an active air-cooled system, is expected to be in range of several 100 seconds, while time constant for the IGBT module is estimated around 1 second [17].

Due to this difference heatsink temperature rise delay affects change of IGBT temperature to a small degree. Time constant, the delay of heatsink temperature change is not considered in the current translation model due to assumed low impact on IGBT temperature change dynamics.

As the input current is considered a mission profile for the IGBT junction temperature computation, sample plot of motor phase current and IGBT junction temperature estimation is shown in Fig. 2.20. Junction temperature is estimated both, for anti-parallel diode and the IGBT semiconductor switch. Each of the two power switching module components follow different load current to junction temperature relationship and operates at different PMSM operation states.

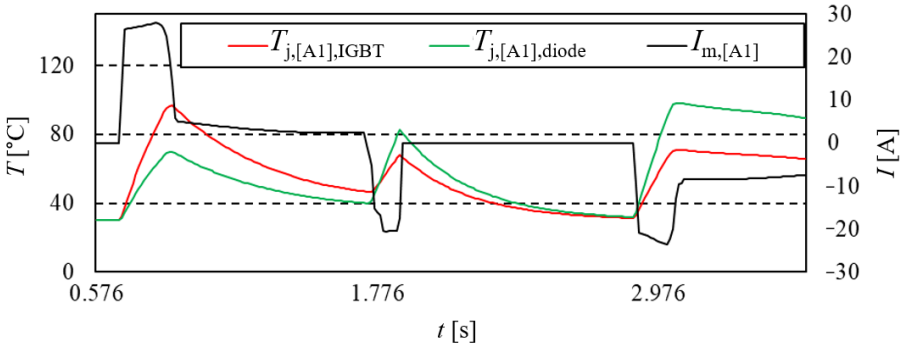

Fig. 2.20. Change of IGBT module and anti-parallel junction temperature as a function of load current

With positive voltage and positive current values (PMSM consumption) IGBT module semiconductor switch will conduct the current and its switching and conduction power losses heat up the device significantly. As current is negative during PMSM operation in generator mode, current path is closed through anti-parallel diodes and semiconductor switch power losses become insignificant. IGBT module temperature increases due to power losses of the diode.

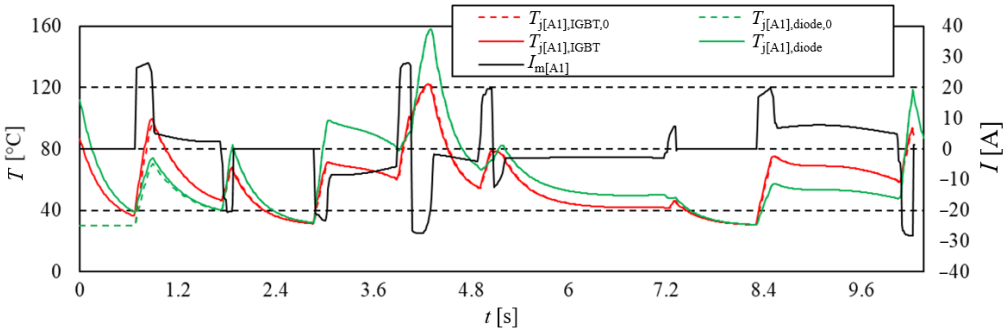

Fig. 2.21. Visualization of A1 robot axis A1 inverter anti-parallel diode and IGBT junction temperature and motor phase current relationship during sample movement. Temperature during initial and repeated cycles is different at the first part of profile.

Simulation data confirm the relationship (see Fig. 2.21), as increased motor phase current through IGBT increase the temperature. Improved accuracy of thermal impedance data will improve the accuracy of the model, which is considered as a future improvement, together with implementation of IGBT module degradation of thermal performance [18].

2.3.2. Application of Fatigue Estimation Principles

Effect of more structural damage by alternating loads than constant loads of the same magnitude was documented by German engineer August Wöhler in the 19th century. It generalizes that increased stress amplitude results in decreased number of load cycles to failure, and that specific load cycle number of fatigue crack can be found for given stress amplitude.

Junction temperature data and profile of IGBT modules is an input for further estimation of mechanical wear calculations. The main connection between junction temperature and wear is difference in thermal expansion coefficient of module materials, as shown in Fig. 2.22. These materials include aluminum, copper and others. Materials are changing volume at different rate due to heating and cooling, leading to micro-cracks and eventual failure after extensive thermal cycling.

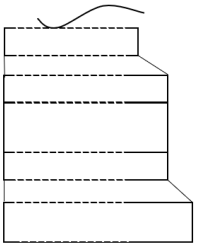

Material	CTE
Aluminum (Al)	22
Silicon (Si)	3
Solder	Compliant
Cuprum (Cu)	16.8
Al_2O_3	7
AlSiC	8

Fig. 2.22. Internal layers of sample IGBT semiconductor module with thermal expansion coefficient and material description [19].

Some of the common failure modes accelerated by thermal cycling [18] include bond-wire and die-attach solder fatigue [20-22]. Bond-wire and die separation due to shear stress (see Fig. 2.23 (a)), cracking of die-attach solder joint (see Fig. 2.23 (b)), delamination of die-attach solder layer (see Fig. 2.23 (c)), as well as rupture of bond-wire or bond-wire heel fracture (see Fig. 2.23 (d)) are some of the expected failure mechanisms, as shown in Fig. 2.23. Significantly degraded die-attach solder joint result in a bond-wire failure [23-24], as solder joint and bond-wire damage are linked. In literature R_{th} increase by 20 %, or an on-state voltage increase by 5 % is considered as a failure criterion of IGBT [25].

Time delay of heatsink temperature change is not considered in the current translation model. IGBT module wear-out is estimated from junction temperature profile. Differences in coefficient of thermal expansion of module materials is leading to microcracks and eventual failure after extensive thermal cycling.

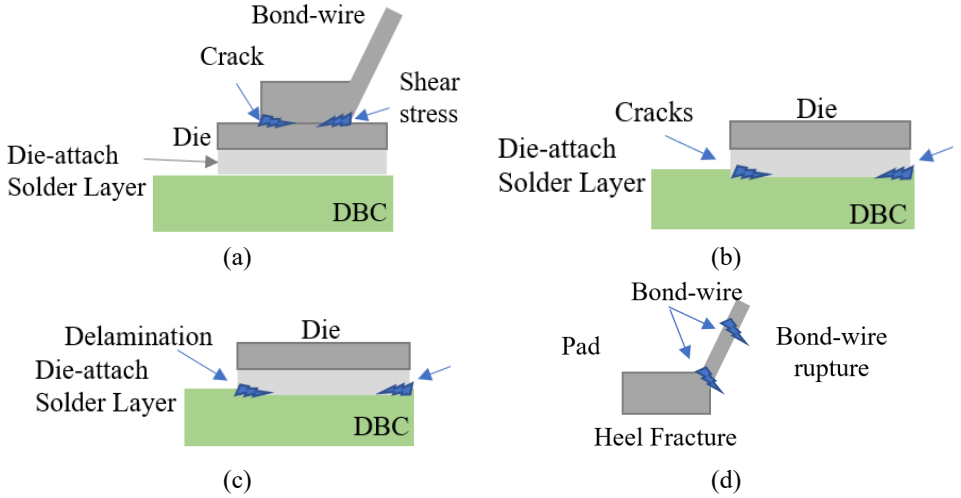

Fig. 2.23. Mechanical defects causing IGBT field failures - a) shear stress crack at bond-wire and die junction, b) cracks at die-attach solder layer, c) delamination of die-attach solder layer from direct bonded copper (DBC), d) bond wire defects - rupture and heel fracture [26].

Range, amplitude and mean are characteristics of the load cycle. Range is a subtraction of maximum and minimum cycle data point values. Amplitude value is half of the range value. Mean is a half of the maximum and minimum data point value sum. Number of cycles in each range of load signal (the load spectrum) are counted with one of typical fatigue cycle counting methods – Rainflow counting and Markov counting. Rainflow counting is selected as the fatigue cycle counting method in this research. Due to hysteresis presence, some cycles may be either partially or completely nested in other cycles. Examples of cycle counting method applications are presented further in this section.

Physical quantity defining the excitation of a system or component over time is defined as load, torques, strains, displacements, being some of the most common load types. Load half-cycle is created by a minimum extremum of the profile and a consecutive maximum extremum of the profile, or other way around – a maximum extrema followed by minimum extrema, see Fig. 2.24 (a). Two consecutive half-cycles form a full-cycle, as shown in Fig. 2.24 (b).

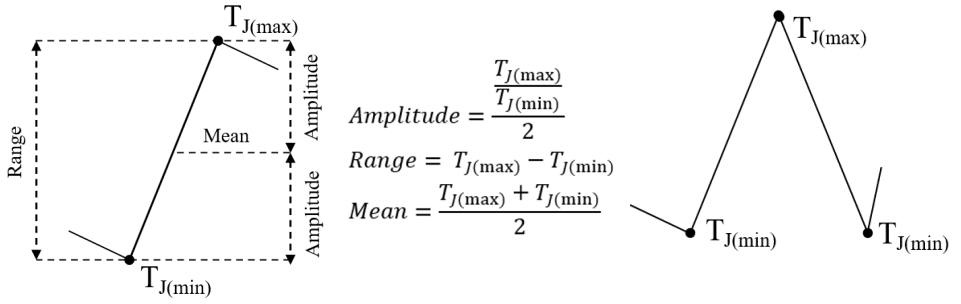

Fig. 2.24. Half-cycle (a) and full-cycle (b) of load profile, including visualization of load cycle major characteristics – amplitude, range and mean.

Fatigue is considered a failure mechanism of a particular object under observation caused by repeated cycles of stress. Fatigue analysis study accumulation of damage when the object is subjected cyclical changes in stress. Cycle amplitudes are below static material strength and given enough time cracks in the material are initiated at microscopic scale. Failure is caused as the cracks continue to propagate due to application of continuous stress, forming a cumulative and unrecoverable damage. Number of cycles until failure depends on amplitude of the cycle. Crack initiation, propagation and final fracture are stages of fatigue failure process.

Not all cyclic stress ranges are causing fatigue failure, as if the range value of cycle is below endurance limit, also called a Cutoff threshold, a material failure should not occur, and it is concluded that material is safe for operation with respect to damage. Stress values below Cutoff threshold does not further propagate existing small cracks (see Fig. 2.25).

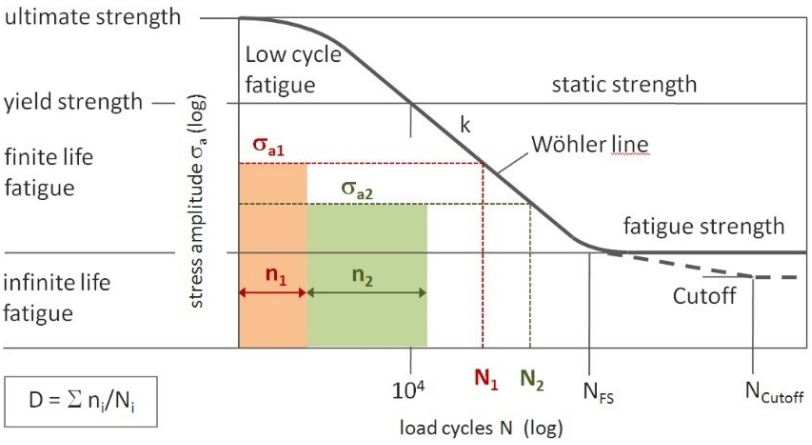

Fig. 2.25. S-N curve (stress amplitude, number of cycles) or logarithmic Wöhler curve, principles of cumulative fatigue damage of load cycle estimation, including cutoff stress [27].

Ultimate tensile strength is the maximal safely withstand able stress range exceeding which failure will occur. Stress amplitudes should be kept below endurance limit, away from ultimate tensile strength during component design phase.

As the tensile strength of material is exceeded by the applied load, material surface crack initiation occurs weakening the part and being the first stage of fatigue failure. Initial crack continues with crack growth stage. Rate of component crack propagation depends on operation conditions and environment as increased load and cyclic stress on the surface accelerates the growth. Other impact factors include load type, object size, mean and distribution of stress/strain, metallurgical factors, material properties and frequency effects. Predicting fatigue life is defined according to ASTM E-1049 "Standard Practices for Cycle Counting in Fatigue Analysis" standard as a number of stress cycles that a specimen sustains before failure.

One of methods to determine the number of loading and unloading part fatigue cycles in specific application time is "Rainflow Counting". Estimation of load change cycles as a function of cycle amplitude is provided by Rainflow counting algorithm. While simple fatigue damage calculations are done for cyclical load with constant amplitude, real world material loading profiles including number of cycles and amplitudes are not easy to determine. Typical profile is a function of force or strain versus time, eventually converted into stress time history. Range and mean of cycles are extracted through Rainflow Counting algorithm. See example of stress hysteresis loops covered by Rainflow algorithm in Fig. 2.26.

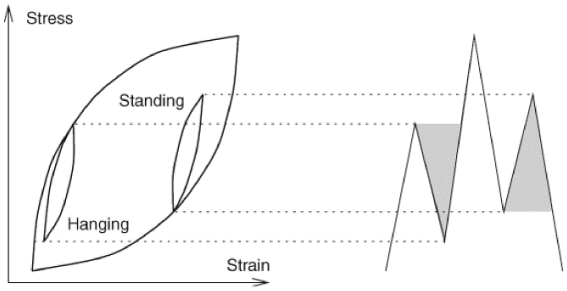

Fig. 2.26. Rainflow algorithm supporting recognition of stress hysteresis loops [28].

Filtering is required for the load data, to adjust it for stress cycle counting and calculation of fatigue damage. Local extrema of the input load profile are called turning points and are detected by the first filter. Local extrema filter is mandatory, as the sequence of turning points translated from load history is required as the input of the fatigue analysis model. Turning points or reversals are the local data points where load is changing sign.

Input junction temperature data formatting for Rainflow counting application is completed as shown in Fig. 2.27 [29]. Positive and negative peak values are sorted. Close peaks are filtered with 5 % hysteresis filter. Remaining values are discretized and arranged in data bins, and processed by Rainflow-counting algorithm. Output data are analyzed through range histograms, and further processed, to reveal lifetime consumption of the cycles and half cycles.

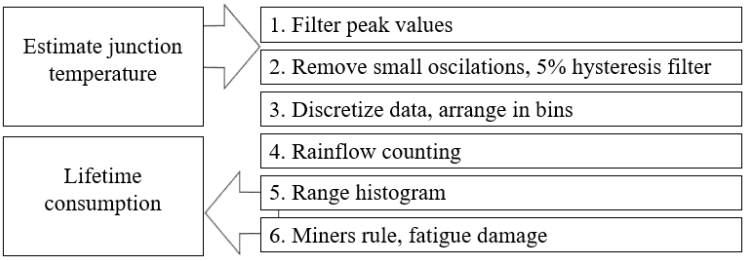

Fig. 2.27. Junction temperature data translation to lifetime consumption through Rainflow-counting algorithm and application of Miners rule.

Sample welding program was simulated including a 6-DoF industrial manipulator. Mechatronic model of robot and electrical cabinet is used to provide input data to thermal model. Output of thermal model, estimated junction temperature of KUKA Servo Pack IGBT for Axis 1 during sample welding application is presented in Fig. 2.28. Sample program duration is 13.5 seconds, it includes multiple acceleration and deceleration peaks, as the robot is navigating through the required processing points.

While detailed data of junction temperature through time provide insight in thermal processes, peak values and reversal points have the highest importance regarding damage estimation and temperature change evaluation with Rainflow-counting fatigue data analysis algorithm. Therefore, peak values are filtered from the original data set. Difference between original data set and peak values, selected for Rainflow-counting fatigue analysis algorithm is presented.

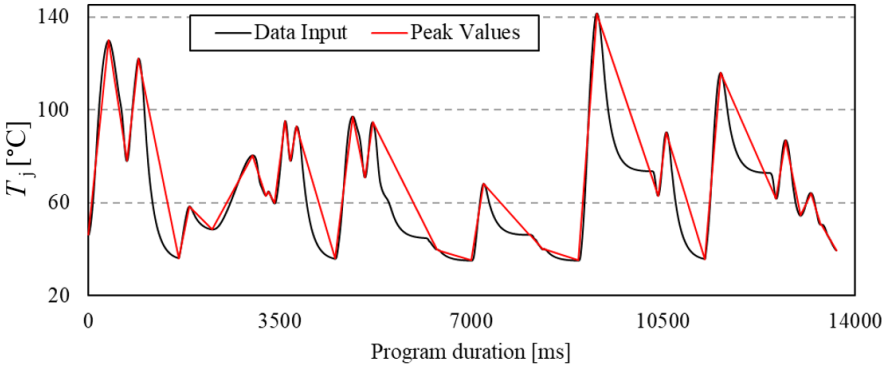

Fig. 2.28. A1 axis drive inverter KUKA Servo Pack IGBT module junction temperature estimation through duration of a sample welding application, with data filtered through local extrema filter.

Small oscillations are removed from the input load extrema data through hysteresis filter. Turning points which correspond to the range of cycles below threshold are discarded, while

increased threshold will discard higher number of turning points. Turning point quantity reduction can be beneficial for both, testing and simulation. In this model, 5 % hysteresis threshold parameter T % is applied to the load extrema data. See the output data in Fig. 2.29.

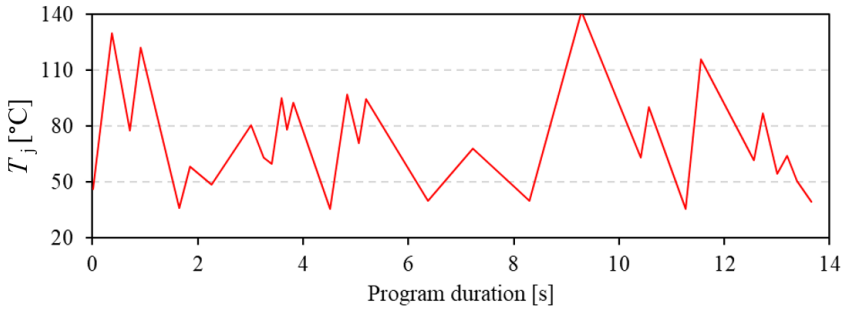

Fig. 2.29. Data before and after 5 % hysteresis threshold application.

Failure of IGBT semiconductor module is linked to mechanical deformation of internal wire-bonds. To characterize and explain this relationship and estimate cycles to failure, multiple variables are introduced:

s – characteristic life time (also, N_i),

m – Coffin-Manson exponent, has been found to be 2, not depending of the material that goes plastic deformation cycles [30],

a – proportionality coefficient of junction temperature and deformation,

C – coefficient for the life time of the technology,

c_Δ, c_T, c_0 – coefficients fitted to power cycling life time data,

ε_e – elastic deformation,

$T_{j,min}$ – minimum junction temperature during the cycles [K],

$T_{j,max}$ – maximum junction temperature during the cycles [K],

$\Delta\varepsilon$ – total deformation of the wire bond material,

$\Delta\varepsilon_e$ – elastic deformation per cycle,

$\Delta\varepsilon_p$ – plastic deformation per cycle,

ΔT_j – junction temperature cycle amplitude [K],

$\Delta T_{j,cut-off}$ – junction temperature cycle amplitude threshold for elastic deformation [K],

σ – yield strength,

E – elastic modulus.

Bond wire fatigue is caused by plastic deformation, and relationship between deformation per cycle and characteristic life time is predicted according to Coffin and Manson equation as shown in Eq. (2.52).

$$s = \left(\frac{C}{\Delta\varepsilon_p}\right)^m \tag{2.52}$$

During power cycling of IGBT module, deformation of the wire bond material is caused by significant differences in coefficient of thermal expansion of silicon (2.5 ppm/K) and aluminum (24 ppm/K). Deformation is occuring both, elastically and plastically. The assumption established and verified at [31] is that single deformation point description is sufficient to obtain life time model. Further assuming proportionality of the total deformation and junction temperature swing, according to Eq. (2.53).

$$\Delta\varepsilon = \Delta\varepsilon_{\mathrm{p}} + \Delta\varepsilon_{\mathrm{e}} = a\Delta T_{\mathrm{j}} \tag{2.53}$$

Experiments completed at [32] show that yield strength of wire bond materials is temperature dependant, as shown in Fig. 2.30 (a).

For development of this initial life time model of wire bond, yield strength relationship to junction temperature is assumed linear, and that the material shows ideal plastic behaviour. Amount of elastic deformation is calculated as shown in Eq. (2.54):

$$\varepsilon_{\mathrm{e}} = \frac{\sigma}{E} \tag{2.54}$$

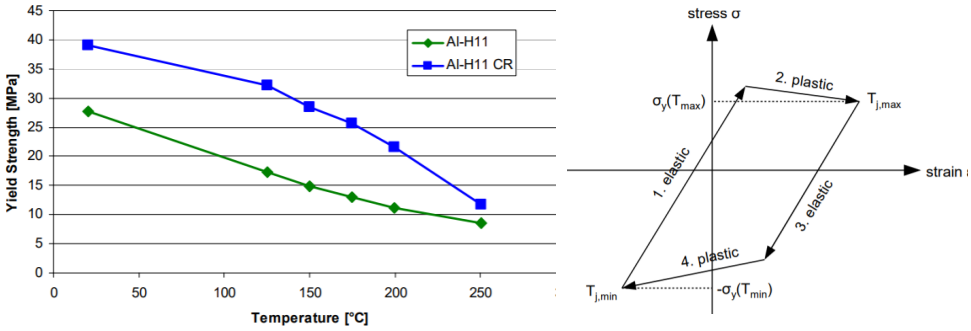

a) b)

Fig. 2.30. (a) Yield strength of two bond wire materials as a function of temperature, assumed linear relationship in this model [32], (b) one temperature cycle stress strain curve of wire bond junction temperature [31].

Stress-strain diagram for one cycle of the material is illustrated in Fig. 2.30 (b). It shows the 4 phases of material deformation, as it is heated from minimum temperature reaching yield strength. Further heating, material deforms plastically, lowering the yield strength and the stress is reduced as maximum temperature is reached. When cooling, wire bond deforms elastically until yield strength. As cooling continues, yield strength and stress increase during plastic deformation.

As the elastic amount of deformation is limited by the yield strength, plastic deformation is rewritten accordingly, see Eq. (2.55).

$$\Delta\varepsilon_{\mathrm{p}} = a\Delta T_{\mathrm{j}} - \left(\frac{\sigma(T_{\mathrm{J,min}}) + \sigma(T_{\mathrm{J,max}})}{E}\right) \tag{2.55}$$

And due to previously assumed linear dependence of temperature and yield strength, following relationship can be derived as shown in Eq. (2.56):

$$\Delta\varepsilon_{\mathrm{p}} = c_{\Delta}\Delta T_{\mathrm{j}} + c_{\mathrm{T}}T_{\mathrm{j,max}} - c_0 \tag{2.56}$$

Life time of bond wire is obtained with the updated Coffin-Manson equation as in Eq. (2.57). Initial life time coefficient is omitted, as it is included in the three coefficients c_{Δ}, c_{T}, c_0 fitted to power cycling data. Exponent m is set to 2, according to [32].

$$s = \left(\frac{1}{c_{\Delta}\Delta T_{\mathrm{j}} + c_{\mathrm{T}}T_{\mathrm{j,max}} - c_0}\right)^{m} \tag{2.57}$$

Cutoff line, where wire bond theoretical life time is infinite due to only plastic deformation, in the current model is included in model through 5 % threshold filtering, before data input in Rainflow as 5 % threshold filter, as shown in Eq. (2.58).

$$\Delta T_{\mathrm{j,cut-off}} = 0.05(T_{\mathrm{j,max}} - T_{\mathrm{j,min}}) \tag{2.58}$$

This research attempts to highlight temperature cycles due to changing mission profile as the major impact factor to IGBT lifetime estimations. In the scope of this research, changing junction temperature cycles are viewed as a variable input of IGBT thermal and damage evaluation model, while other constants and parameters remain constant, since the system itself does not change. This approach enables relative comparison of the results as a sufficient analysis method, without a mandatory requirement to determine actual remaining lifetime value. As the relative relationship is confirmed and analyzed, impact factors of relative damage can be analyzed further.

Data has been processed through local extrema and threshold filter, N equidistant bins are created splitting the load signal range and assigning remaining data points to closest bins. For example, temperature range from 40 °C to 140 °C can be discretized into 5 or 10 bins. As the load profile is unpredictable and random through the cycles, a set of contiguous intervals transform it into a discrete form. Data range from 25 °C to 145 °C is divided in 6 bins each with range of 20 °C, and data from mission profile is updated as shown in Fig. 2.31.

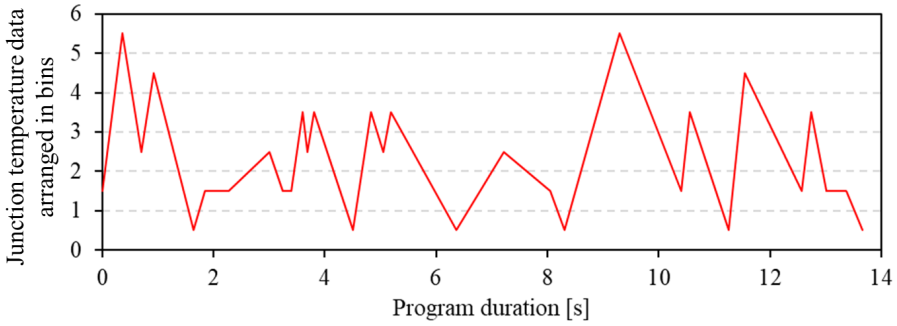

Fig. 2.31. Sample mission profile data after discretization in bins.

Calculating absolute ranges between consecutive pairs of turning points is a simple and straightforward cycle counting method known as Markov counting. It seems like a reasonable option to evaluate cycles, for example, value of absolute difference between 1st and 2nd turning point is |46-130|=84, value between 2nd and 3rd turning points is |130-78|=52, as shown in Fig. 10. A major drawback of this counting method is that large amplitude cycles, which include smaller cycles and have a significant role in fatigue damage accumulation, are not detected. There is a cycle with large amplitude between 5th and 11th turning points, however, a series of smaller cycles will be counted instead, which do not form a cycle of the same amplitude and the data of |36-95|=59 range is not detected [33], as shown in Fig. 2.32.

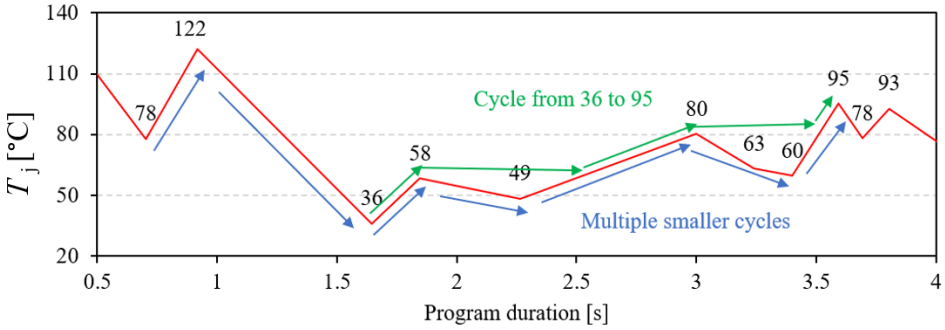

Fig. 2.32. Markov counting drawback – not detecting larger cycles which are a combination of several smaller stress cycles.

Rainflow counting method detects hysteresis loops (also called – closed cycles or full cycles) within the filtered input data. Turning points which cannot be included in the full cycles, are considered residuals (also called – open cycles or half cycles). Residual treatment may differ between various counting standards. Rainflow counting method is widely used in industry.

While Markov counting does not detect large amplitude cycles with internal smaller cycles, Rainflow counting algorithms will include such cycles in the analysis. As shown in Fig. 2.33, where two smaller amplitude cycles have been recognized between 5th and 11th turning point, and the value of largest range is not lost.

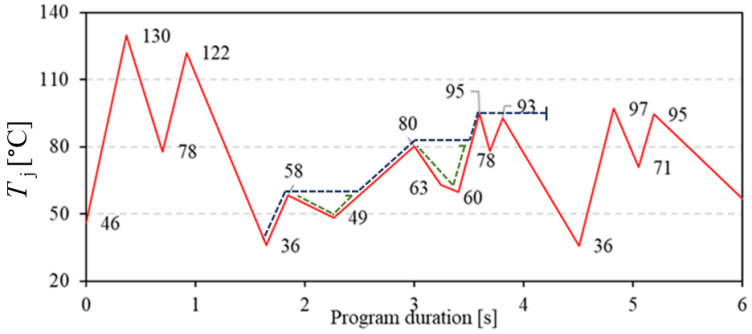

Fig. 2.33. Example of Rainflow cycle counting algorithm cycles and half cycles illustrating recognition of larger amplitudes with internal smaller load cycles.

Rainflow algorithm function (see Fig. 2.34) considers a moving reference point and a moving subset of three-points. Reference is called *Z*, group of 1st and 2nd points is called *Y*, group of 2nd and 3rd points are called *X*. Both, *X* and *Y* sorts the points from earlier to later in time, but may become not consecutive through the processing of algorithm, as the algorithm moves through peaks or valleys and full cycles are being discarded.

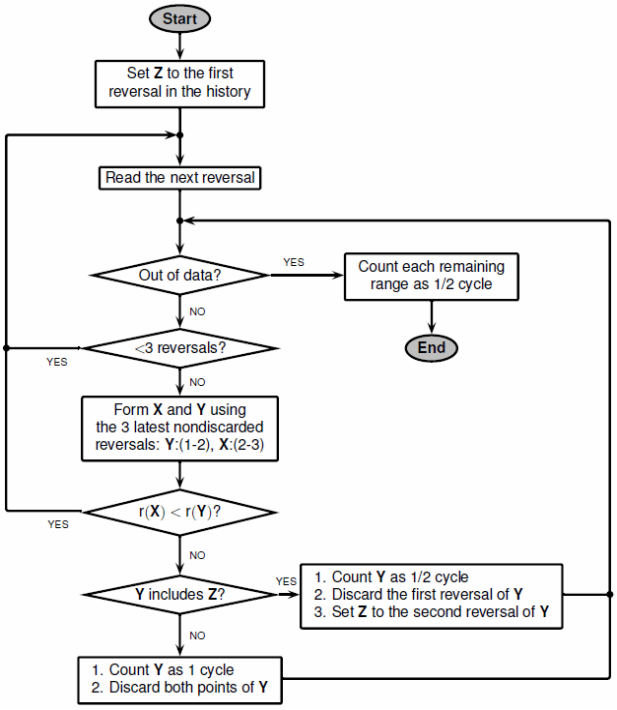

Fig. 2.34. Rainflow Algorithm data processing flowchart implemented in the current IGBT thermal model [34].

Distribution of thermal stress is represented by a 2-dimensional graph – range histogram (see Fig. 2.35). Axis of histogram corresponds to temperature cycle range and number of cycles. For example, if a load cycle contained 20 cycles of range 40, and 30 cycles of range 20, the following entries would be included in histogram – X=40, Y=20 and X=20, Y=30. Created histogram can be overlaid with a corresponding S-N curve (stress amplitude, cycles to failure), to verify that the histogram values do not exceed the curve.

Histogram of junction temperature swing cycles can be generated for each of the analyzed mission profiles. It is expected that smaller amplitude cycles will be in larger quantity, compared to high amplitude stress cycles.

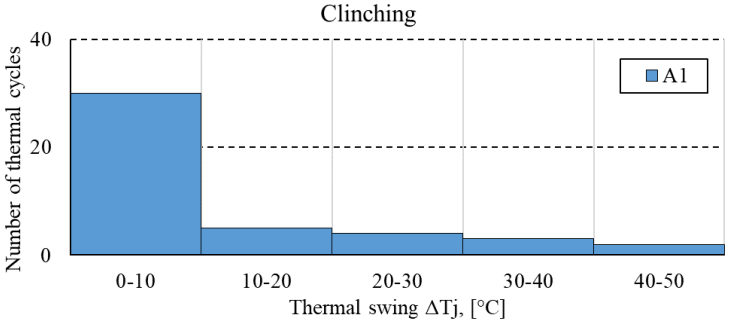

Fig. 2.35. Range histogram of Robot axis A1 inverter IGBT junction temperature swing and cycles during sample clinching operation

The total fatigue damage is estimated by Palmgren-Miner linear damage hypothesis or Miner's rule. In context of this research, damage is a ratio between service load cycles and permissible value. Fatigue damage is calculated as shown in Eq. (2.59), assuming that each cycle with the same amplitude range, consumes fraction of the total lifetime. Increase of damage is proportional to load cycle number, and reaching value 1.0 a fatigue crack is expected to appear as the device will be considered damaged.

$$D = \sum_i \frac{n_\mathrm{i}}{N_\mathrm{i}} \tag{2.59}$$

where:

D – amount of cumulative fatigue damage,

i – number of specific cycle or half cycle amplitude ranges,

j – total number of cycles or half cycles,

n_i – number of cycles with the same amplitude range,

$n[i]$ – number of the specific temperature cycles or half cycles,

$\mathrm{N}_f[i]$ – number of cycles to failure, according to Coffin-Manson law,

N_i – permissible cycle quantity or number of cycles to failure.

In further computations, damage of each fatigue cycle and half cycle is assumed for each of amplitude ranges, defined by i=1..j, as shown in Eq. (2.60).

$$D = \frac{n[i]}{N_{\mathrm{f}}[i]} \tag{2.60}$$

Total damage is computed by summing of damage fractions according to Eq. (2.61). Sum of the fractions equals D=1, or 100 % in case of failure due to damage [35].

$$D_{\mathrm{total}} = \sum_{i=1}^{j} \frac{n[i]}{N_{\mathrm{f}}[i]} \tag{2.61}$$

Drawbacks of the Miner's rule include not being able to recognize the probabilistic nature of fatigue relating rule results with the characteristics of probability distribution. Number of cycles to failure are calculated as shown in Eq. (2.62), where parameter values are obtained through bond wire fatigue damage model [36], [37] and Palmgren-Miner linear accumulation rule [38].

$$N_{\mathrm{f}} = 1.4 * 10^{11} \Delta T^{-3.597} \tag{2.62}$$

This rule does not consider the effect of a low vs high stress sequence. As the rule predicts lower than the actual value damage for high stress following a low stress, and predicted damage is higher than actual for low stress following a high stress, due to compressive residual stress.

2.3.3. Evaluation of Temperature Affecting Factors

Relationship between power consumption of industrial robot and inverter IGBT junction temperature is established and confirmed in the simulation analysis. This section attempts to evaluate how changing tool mass and robot application type affects the junction temperature of IGBT. Motor current consumption is applied as the input and scaling factor in the developed thermal model. Current consumption impact factors are assumed to impact the junction temperature.

The main focus of section 2.3.3.1. is to run the computational model, simulating operation of the same robot program with two various load weights, while section 2.3.3.2. simulates various industrial robot program types, common in automotive manufacturing environment. Junction temperature change, thermal cycles and lifetime consumption estimates are included in each of the sections.

2.3.3.1.Changing Tool Mass

Study presented in this section is expected to either confirm or deny the assumption that changing tool mass of industrial robot has a direct impact on lifetime consumption of the hardware semiconductor components. If the assumed relationship is confirmed, tool weight reduction can be confirmed as a method to improve reliability of industrial robot inverters.

In simulation study, a welding robot program of KUKA KR220 six degrees of freedom manipulator was simulated with movement path generated by RCS module. Path was analyzed

in kinematics and mechatronics model to evaluate changing the tool mass impact on current and power consumption.

Power consumption of the robot motors during welding application has been analyzed earlier with 0 kg and 180 kg load, as shown in Fig. 2.36. Difference in average power consumption is 5.9 % between the two setups. Detailed research of changing robot load weight effect on power consumption is completed at [39].

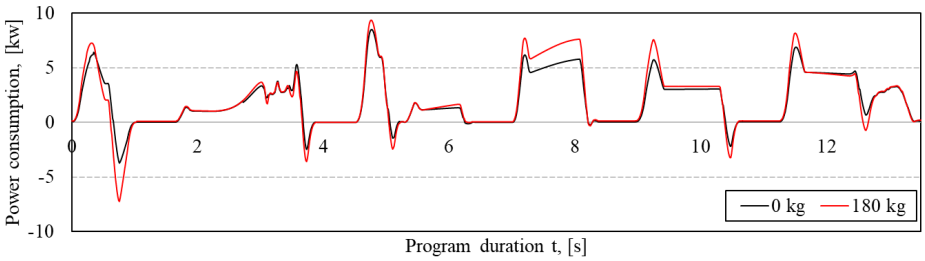

Fig. 2.36. Combined power consumption of 6 industrial robot motor power consumption during sample welding program with two load weights.

KUKA Servo Pack inverter is reviewed through the model as an integrated industrial robot application, operating in state-of-the-art robot supply and drive hardware layout, with dedicated rectifier for the common DC link and inverters for each of robot axis, connected to this link. DC link capacitance is considered, as it influences both, the current and voltage through system operation duration.

Voltage fluctuations of the DC bus during handling operation is shown in Fig. 2.37. Operation of the same sample handling program with minimum load weight and maximal load weight is simulated. In general, voltage decrease below rated DC voltage is caused by high current consumption. Upper limit of the DC bus is controlled by brake chopper resistance, which is connected through semiconductor switch to dissipate recuperated energy, generated during deceleration of robot axis motors. When current energy consumption exceeds the generation, energy stored in DC bus capacitor capacitance is discharged and voltage returns to rated value during consumption from AC grid.

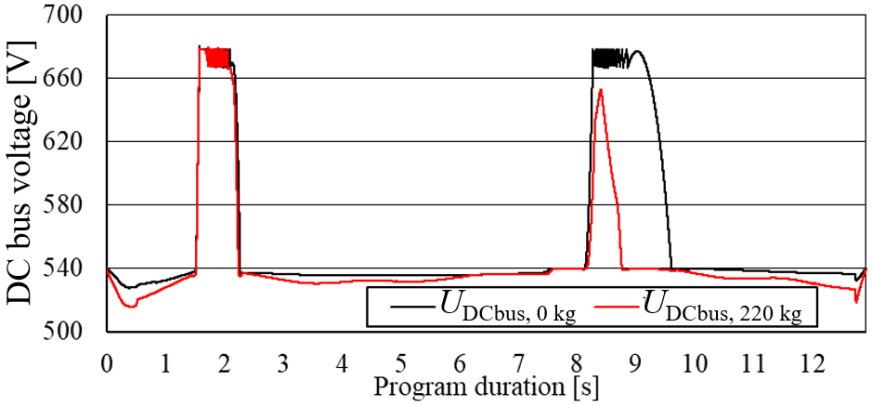

Fig. 2.37. Voltage of DC bus during handling operation with minimum and maximum load weight of the simulated 6-DoF industrial robot.

Robot acceleration and operation is supplied from the AC grid, through three phase rectifier. Current consumed from AC grid through the same handling operation is shown in Fig. 2.38. Simulation reveal, that increased tool weight results in significantly increased current consumption from the AC grid. Peak current consumption is increased especially high during acceleration. This value is combined current consumption of 6 robot motors, and efficiency losses of their drive circuit. Current is not consumed from AC grid when combined generated energy of robot motors exceed the consumed value.

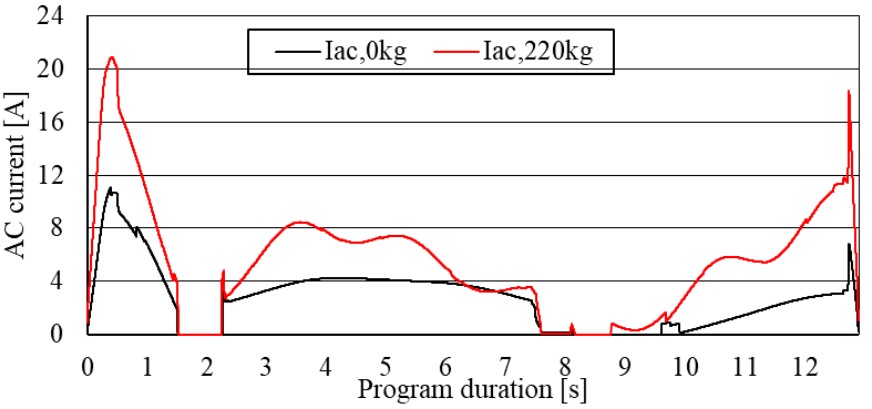

Fig. 2.38. Combined current consumed from AC grid of 6-DoF industrial robot axis motors during handling operation with two load weights.

In this study one of the simulated programs is a handling program lasting 10.5 seconds. It has a starting (home) position, two processing points, and movement between the defined points is simulated by RCS module, data being imported and analyzed in the developed mechatronic

model. Simulation model allows to separate the combined current consumption by robot axis drive units, see Fig. 2.39. See complete Axis 1-6 current consumption data in Appendix E. Six robot motors are supplied and driven through two inverters, each of which supply three robot axis. In general, axis 1-3 have higher current consumption and higher motor power than axis 4-6, as first axis must support both - the weight of the remaining axis and the load of the robot.

For purposes of the study, a handling program was simulated with no load (0 kg) and 56 % (125 kg) of the maximal load (220 kg). Analysis of the sample program motor current data of two weights confirm the expected correlation - increased robot load weight increase current consumption. It is verified by review of current maximal and minimal values through the robot program duration.

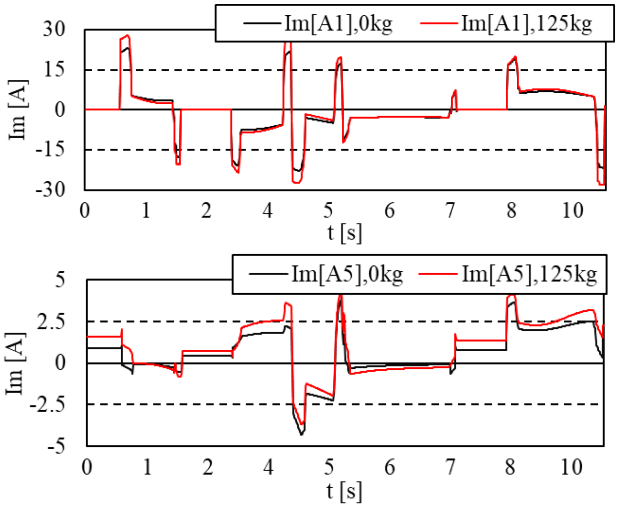

Fig. 2.39. Current consumption of each robot axis motors during handling program ("case_handling_1") simulated with two load weights - 0 kg and 125 kg.

For example, maximal current of axis A1, changed from 23.17 A to 28.08 A (21 % increase). Minimal value of the robot motor current changed from −23 A to −28.22 A (22 % increase) as well. The same principle is visible when data of other robot axis is reviewed, as shown in Table 2.2. Data confirm that in general axis A1−A3 has higher current consumption values, compared to axis A4−A6, as explained in Section 2.2.2.

Table 2.2

Axis motor current consumption − sample handling program, with 0 kg and 125 kg load

	I_{max} [A]	I_{min} [A]	$Change_{max}$	$Change_{min}$
A1(0 kg)	23.17	−23.00		
A1(125 kg)	28.08	−28.22	21 %	23 %
A2(0 kg)	18.82	−13.17		
A2(125 kg)	23.48	−18.91	25 %	44 %
A3(0 kg)	31.83	−14.96		
A3(125 kg)	38.66	−16.86	21 %	13 %
A4(0 kg)	3.62	−3.58		
A4(125 kg)	4.16	−3.93	15 %	10 %
A5(0 kg)	4.00	−4.29		
A5(125 kg)	4.55	−3.69	14 %	-14 %
A6(0 kg)	4.02	−3.92		
A6(125 kg)	4.02	−3.92	0 %	0 %

Junction temperature simulation of the inverter IGBT modules is done for the semiconductor switch and anti-parallel diode, as described earlier. Analysis of the temperature data for each of the robot axis provide detailed information during operation modes of the six permanent magnet synchronous motors of industrial robot. Data of robot motor current plotted in Fig. 2.40, are supplied as an input to thermal model, and junction temperature data for the sample handling robot program are obtained, as shown in Fig. 2.40. See data of Axis 1-3 in Appendix F.

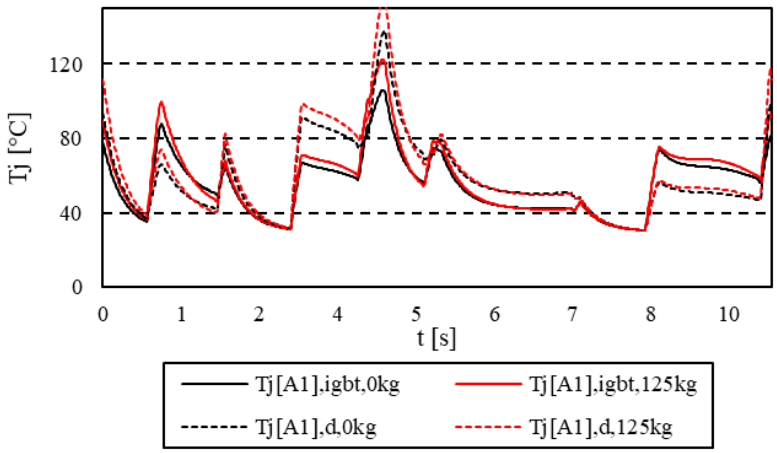

Fig. 2.40. Axis 1 inverter IGBT and anti-parallel diode junction temperature data of sample handling program, with 0 kg and 125 kg load.

Similar to current consumption data, the junction temperature increase is observed in the reviewed axis 1-3 for both, diode and semiconductor switch. Data reveal that junction temperature mission profiles between various robot axis are barely similar, therefore a high variety of data is expected. Strong acceleration profiles and levelled deceleration profiles lead to IGBT junction temperature changes and limited dynamics of diode temperature. At the same time, strong deceleration with controlled acceleration result in higher diode junction temperature, and reduced temperature IGBT temperature.

Junction temperature data analysis confirm change of maximal temperature with increased load weight. Increase of IGBT junction temperature peak value with increased tool mass and the same program is between 15−23 % for Axis 1-3, and between 9-17 % for anti-parallel diode junction temperature of Axis 1-3 inverter, as shown in Table 2.3. Load weight increase has less effect on minimal temperature peak values, as module manages to cool down sufficiently during deceleration, and during normal operation smooth deceleration profile is viewed as energy efficient practice. Minimal temperature increase for semiconductor module junction temperature is between 0-9 % for Axis 1-3, and between 0-18 % for diodes of Axis 1-3 inverter IGBT modules.

Table 2.3

Data of axis motor inverter IGBT and anti-parallel diode junction temperature through sample handling program, with 0 kg and 125 kg load.

	Setup	$T_{j,max}$[°C]	$T_{j,min}$[°C]	$Change_{max}$	$Change_{min}$
	A1(0 kg)	106.05	30.58		
	A1(125 kg)	122.11	30.59	15 %	0 %
	A2(0 kg)	106.57	34.54		
	A2(125 kg)	127.50	35.61	20 %	3 %
	A3(0 kg)	89.94	32.64		
IGBT	A3(125 kg)	110.24	35.69	23 %	9 %
	A1(0 kg)	137.86	30.67		
	A1(125 kg)	158.23	30.67	15 %	0 %
	A2(0 kg)	76.06	34.11		
	A2(125 kg)	88.71	35.33	17 %	4 %
	A3(0 kg)	77.39	32.30		
diode	A3(125 kg)	84.19	38.18	9 %	18 %

Further analysis of IGBT and diode junction temperature values reveal that both, highest peak value and amplitude from lowest and highest value has increased with higher tool mass. Study reveals that specific values and percentage of the increase depend on mass of the load. Axis 1 diode highest temperature peak has increased by 20 °C (see Fig. 2.41) due to tool mass change from 0 kg to 125 kg. Not all temperatures are changed equally, as the diode temperature highest value for the inverter semiconductor modules of Axis 3 has increased by lower value - 10 °C. Similar situation is with IGBT switches, as not only the amplitude and maximum peak

value has increased, but mean value of the junction temperature during handling operation has increased by about 20 °C as well.

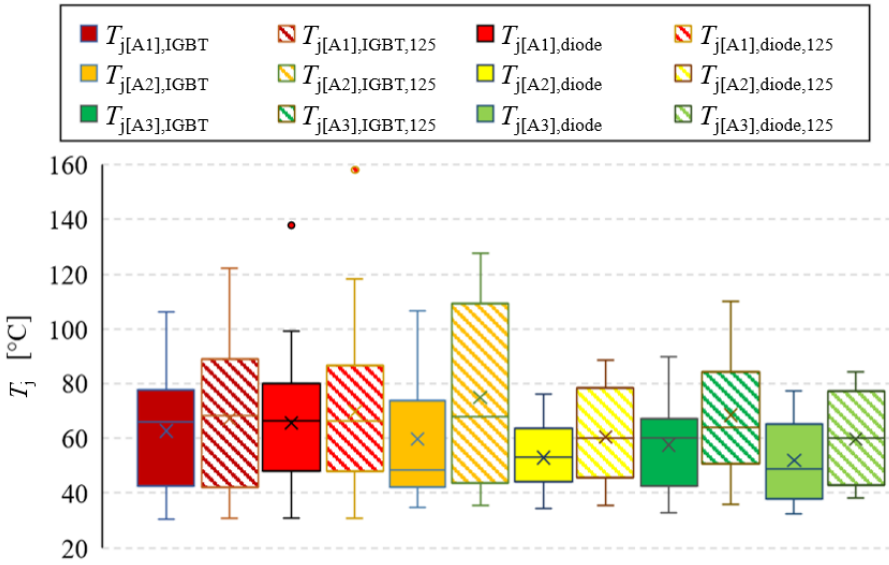

Fig. 2.41. Highest peak value, temperature change amplitude and mean value of robot axis inverter IGBT and anti-parallel diode change during sample handling program, and changing load mass.

Simplification of input data is performed to format it for fatigue and lifetime consumption analysis, where temperature change amplitude during cycles and half cycles are a critical input parameter. Turning points are filtered from the estimated junction temperature data, and 5 °C threshold filter is applied to remove temperature change ripples before the selected threshold. Threshold filter is applied on the filtered data repeatedly, as the remaining turning points may as well fit within the filtered value. See turning points of IGBT and diode junction temperature data after 5 °C threshold filter in Fig. 2.42.

Data visualization confirm that junction temperature at high turning points peaks of the mission profile has increased both, for diode and IGBT semiconductor switch. Low side turning points have barely changed, as the process is cooling down to a controlled temperature value in case of both junction temperatures and load weights.

Highest temperature peak aligns with the peak current consumption. Temperature peak value difference between simulated load weights is larger at higher value temperature peaks, since power losses and therefore temperature differences are proportional to motor current. Changing tool weight does not create new turning points, with an exception, that at higher load the previously filtered, small temperature peaks become more significant, and are not removed by threshold filter

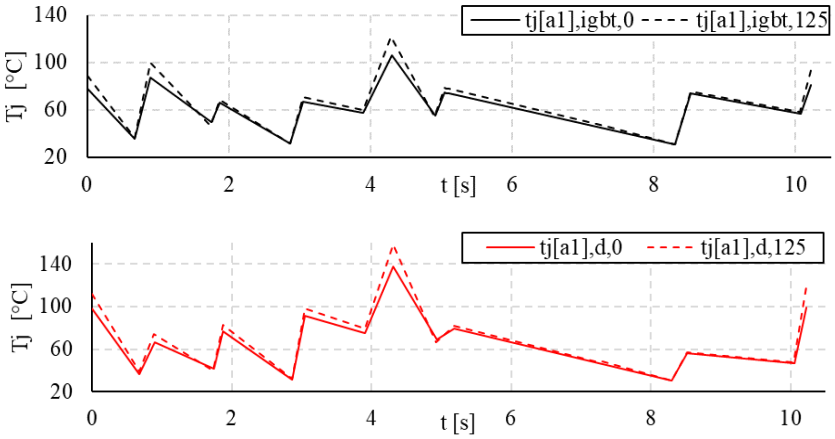

Fig. 2.42. IGBT and anti-parallel diode junction temperature profile after data turning point and 5 °C threshold filtering.

Data discretization in bins follows the threshold filtering of turning points. 10 equidistant bins are created, where first bin contains smallest turning point temperature value, and the last bin contains largest turning point peak value. In case study of handling profile and two load weights, highest and lowest turning point values are selected from the combined data of IGBT and diode profiles. For example, axis 1 IGBT temperature profile is spread across 10 bins, from 30 °C to 110 °C. Each bin covers a temperature range of 8 °C and turning point values are arranged by the recently created discrete bins.

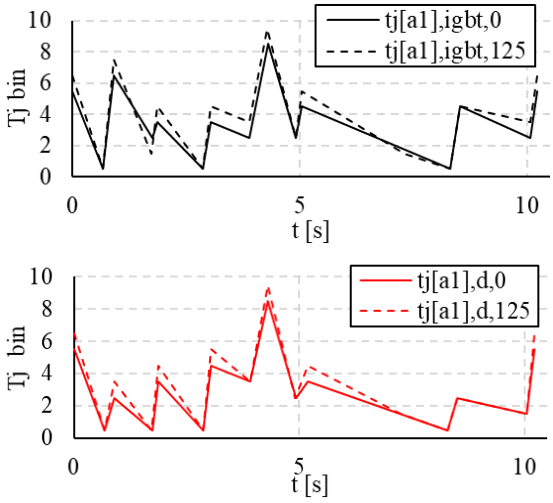

Fig. 2.43. 6-DoF robot axis 1 inverter IGBT and anti-parallel diode junction temperature data arranged in discrete bins (sample handling program) with 2 load weights, 0 kg and 125 kg.

Industrial robot axis 1 inverter IGBT and anti-parallel diode junction temperature data arranged in discrete bins are plotted in Fig. 2.43. See data for axis 1, 2 and 3 in Appendix G. Bin values are calculated for each mission profile, depending on maximal and minimal turning point value, as shown in Eq. (2.63), where $\Delta T_{\mathrm{j}_{\mathrm{bin}}}$ is the dimension of one bin, n_{bins} is the required quantity of bins, $T_{\mathrm{j}_{\mathrm{max}}}$ is the highest turning point value, $T_{\mathrm{j}_{\mathrm{min}}}$ is the lowest turning point value.

$$\Delta T_{\mathrm{j}_{\mathrm{bin}}} = \frac{T_{\mathrm{j}_{\mathrm{max}}} - T_{\mathrm{j}_{\mathrm{min}}}}{n_{\mathrm{bins}}} \tag{2.63}$$

Axis 1 IGBT temperature profile has 7 high value turning points, while Axis 2 IGBT temperature profile only has 3 turning points with 0 kg load during operation of sample handling program. Axis 3 data of the same handling program has twice as many - 8 turning points.

Mission profile data are highly variable and directly dependent on the robot program and are expected to vary between various robot programs and various load weights. Analysis of the visualized data arranged in bins confirm that with higher tool mass or load weight turning points fit in higher bin, above the same profile executed with 0 kg load weight.

Rainflow cycle counting is completed in MATLAB environment on the discretized robot axis inverter IGBT junction temperature data of the studied program, returning number of cycles, half-cycles, mean cycle value and amplitude. Value of lowest turning point value is added to input data as base value, to convert relative bin values to absolute.

From Rainflow cycle counting returned thermal cycle data of robot Axis 1-3 inverters are plotted and analyzed to evaluate effect of changing tool mass on number and amplitude of axis inverter thermal cycles, as shown in Fig. 2.44. See data for axis 1-3 in Appendix H. Amplitude of thermal swing is discrete and the resolution is defined by bins calculated earlier at Eq. (2.44).

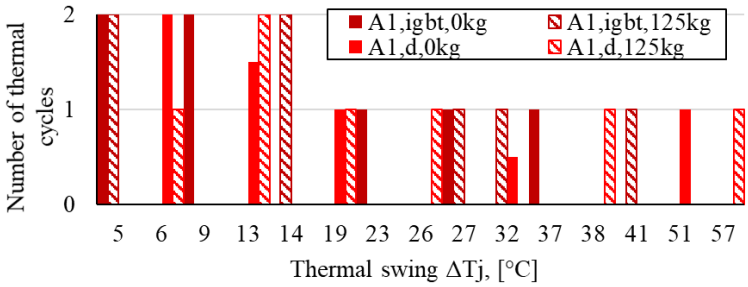

Fig. 2.44. Quantity of junction temperature cycles and half cycles for robot axis 1 after Rainflow cycle counting, sorted by thermal swing and load weight.

Data reveal that in all cases thermal swing with highest amplitude is for program with 125 kg tool mass. Programs with 0 kg tool mass have higher number of thermal cycles with smaller thermal swing, while 125 kg tool mass programs are common to have cycles with 30-50 °C thermal swings.

Translation of KRL robot program to lifetime consumption of Axis 1-3 inverter IGBT and anti-parallel diode is completed with LC data estimation, computed as described earlier in section 2.3.2. Rainflow counting output thermal swing data of analyzed robot program are processed. Lifetime consumption of data each diode and IGBT module thermal swing amplitude and quantity is estimated and plotted, as shown in Fig. 2.45. See complete data for axis 1-3 in Appendix I.

Both, highest thermal swing amplitude and lifetime consumption increase between the simulated load weights is evident for diode of Axis 1, while there is a lot smaller change in lifetime consumption of Axis 3 diode. Consumption increase (0 kg or 125 kg) of IGBT semiconductor switch lifetime for the studied sample handling program axis 1-3 is proportional, while absolute values between axis reveal significant difference. It is evident, that the largest reduction of lifetime is caused by higher amplitude temperature swings, and that the highest amplitudes are introduced by increased load weight.

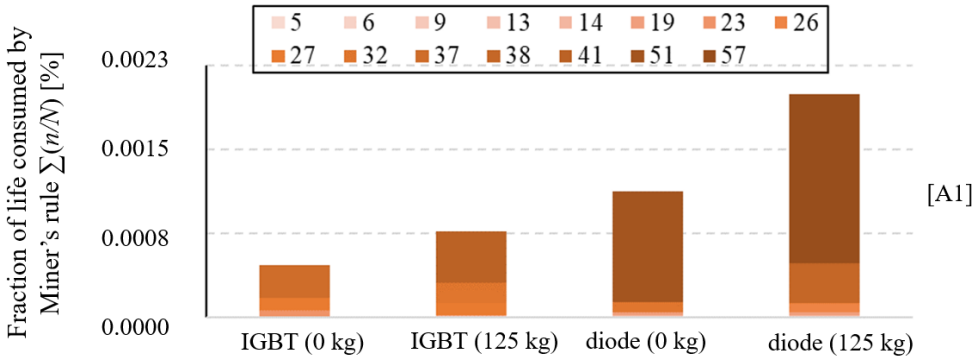

Fig. 2.45. Estimated lifetime consumption of 0 kg and 125 kg tool weight handling program, on IGBT and anti-parallel diode of A1 robot axis inverter IGBT module.

Comparison of total lifetime consumption data of all thermal swing output values reveal that estimated lifetime consumption increase between 0 kg and 125 kg load weight varies between 29 % (A3, $T_{j,diode}$) and 249 % (A2, $T_{j,IGBT}$). Average lifetime consumption increase for axis 1-3 at IGBT junction temperature is 119 %, while average lifetime consumption increase for anti-parallel diodes of axis 1-3 is 118 %, as shown in Table 2.4. However, average increase value is misleading, as the diode lifetime consumption change with tool mass increase differs from 29.6 % (A3) to 249.7 % (A2).

Table 2.4

Lifetime consumption for axis 1-3 inverter IGBT and anti-parallel diode.

	LC, 0 kg [%]	LC, 125 kg [%]	Change [%]
A1, IGBT	4.6E-04	7.7E-04	64.7
A1, diode	1.1E-03	1.9E-03	77.3
A2, IGBT	1.9E-04	6.1E-04	212.8
A2, diode	3.3E-05	1.1E-04	249.7
A3, IGBT	2.0E-04	3.7E-04	80.3
A3, diode	1.0E-04	1.3E-04	29.6

Lifetime consumption difference is expected between IGBT, which is powered through acceleration, and anti-parallel diode which reach the highest temperatures during deceleration. Due to different operation modes and characteristics, the differences between the two profiles are expected.

2.3.3.2. Changing Application Type

This section of the thesis presents the study and results, in an attempt to analyze effects of changing mission profiles to power consumption and junction temperature of inverter semiconductor modules. Lifetime consumption dependance on robot application type (handling, adhesive bonding, and others) is evaluated. If the relationship between robot application type and robot axis drive inverter power switching module lifetime consumption is confirmed, various reliability improvement options can be considered and introduced, such as program adjustment or predictive maintenance.

Several types of six degrees of freedom industrial robot programs were simulated, with following IGBT junction temperature analysis. Purpose of research is to evaluate how changing intensity and characteristics of industrial robot applications influence the temperature of IGBT module. Tool mass, average power consumption, and velocity profile description are selected as key parameters for comparison of various programs, as shown in Table 2.5.

Table 2.5

Data of Various Industrial Application Sample Robot Programs

Name	Program duration [s]	Tool mass [kg]	Average power [kW]	Description
Handling	10.25	125	3.70	High velocity
Clinching	9.31	50	2.45	High velocity, stop & go
Spot welding	13.66	180	2.65	High velocity, stop & go
Adhesive bonding	11.10	50	2.12	High approach velocity; low velocity, high precision dispensing

Handling program is designed, to change tool location from home position, to load pick-up as fast as possible, reaching highest velocity, as the main objective of handling robots is to transport to processing, or rearrange parts. In most cases access to parts is easy and without a lot of time-consuming positioning, to improve output of the production process and avoid bottlenecks.

Clinching is an agile and high velocity manufacturing process, with supported robot program designed supporting the high pace requirements. Sample clinching program has five processing spots with stop and wait commands, holding the position for clinching time, before moving itself and clinching tool to the next processing area. Clinching spots may require extensive positioning adjustment from axis 4-6, as access to parts may be difficult.

Spot welding programs are fast paced, aimed at completing the highest number of spot welds in shortest time. Movement profile is a mixture of sharp decelerations to standstill and fast accelerations, while moving to next spot weld location. Sample robot program has 6 spot welding locations. Handling program is similar in a way, as it includes steep acceleration and deceleration, but the spot-welding is expected to have higher number of processing points, standstill cycles. Spot welding program is similar to clinching.

Adhesive bonding is a speed-sensitive manufacturing process, and robot program is designed accordingly. Processing area is approached quickly, steady and process-safe velocity is maintained through adhesive application, and robot is returned to home position after application is done.

Simulation reveals that during fast paced robot programs with high velocity – handling, spot welding and clinching – junction temperature of inverter IGBT reach higher values (see Fig. 2.46). See visualization of all 4 application types in Appendix J. In temperature profile – peaks are observed during robot acceleration, temperature does not change during steady operation with set velocity and no acceleration (small changes due to inertia), and it decreases to ambient value during reduction of speed to standstill.

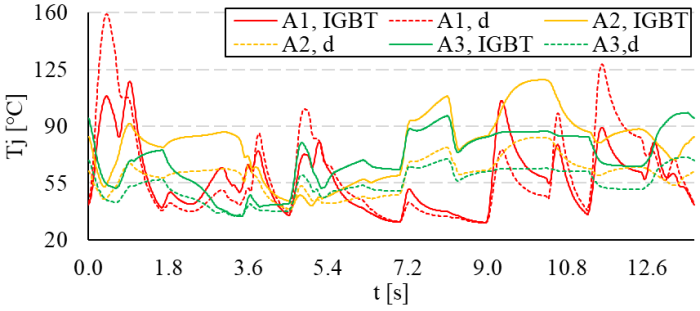

Fig. 2.46. Simulated junction temperature of robot axis 1-3 inverter IGBT modules and anti-parallel diodes, during sample welding application.

Minimal temperature change between robot applications is a lot smaller, as proved by both – amplitude of minimal temperature differences (range from 1 °C to 5 °C) and the calculated standard deviation of the simulated values (range from 0.84 to 2.30)

Analysis of temperature values (see Fig. 2.47) reveal, that both, highest peak value and amplitude from lowest to highest value has welding and handling programs. See visualization of all handling, clinching and adhesive bonding application data in Appendix K. Study reveals, that specific peak values of each axis depend on robot program, as values for handling and welding program are similar, yet different. Highest and mean value are different for each axis inverter and anti-parallel diode of the various simulated programs. Each robot application type due to specific operation characteristics is expected to have similar characteristics of the junction temperature profile.

Table 2.6

Junction temperature data of sample welding, handling, clinching and adhesive bonding robot programs.

			$T_{j,max}$ [°C]	$T_{j,min}$ [°C]	Stdev, $T_{j,max}$	Stdev, $T_{j,min}$	Amplitude $T_{j,max}$ [°C]	Amplitude $T_{j,min}$ [°C]
A1	IGBT	Welding	117.58	30.66	17.37	2.03	36.80	4.24
		Handling	125.63	31.35				
		Clinching	96.21	33.93				
		Adhesive bonding	88.83	34.90				
	diode	Welding	159.02	30.48	21.60	2.30	52.35	5.14
		Handling	129.44	31.15				
		Clinching	106.67	35.63				
		Adhesive bonding	126.42	33.01				
A2	IGBT	Welding	118.53	40.98	15.98	2.25	37.26	4.96
		Handling	110.20	39.71				
		Clinching	102.01	41.40				
		Adhesive bonding	81.28	36.44				
	diode	Welding	83.12	38.69	16.96	0.84	36.72	1.72
		Handling	83.63	38.16				
		Clinching	78.74	36.97				
		Adhesive bonding	115.46	37.09				
A3	IGBT	Welding	98.33	34.51	29.06	1.17	69.32	2.57
		Handling	119.33	35.82				
		Clinching	86.42	37.08				
		Adhesive bonding	50.01	34.75				
	diode	Welding	71.00	34.85	12.77	1.49	30.36	3.17
		Handling	84.20	38.01				
		Clinching	63.86	34.94				
		Adhesive bonding	53.84	36.38				

Largest contrast is between spot welding and adhesive bonding junction temperature profiles. Maximal values for welding temperatures are – 117.57, 159.02, 118.53, 83.12, 98.33, 70.99, while maximal values for adhesive bonding temperature profiles are about 25 % lower – 88.83, 126.41, 81.27, 115.45, 50.01, 53.83.

Lowest temperature values have just 1.1 % difference between two sample programs – spot welding (30.84, 31.17, 40.98, 38.69, 34.96, 36.56) and adhesive bonding (34.90, 33.00, 36.44, 39.95, 34.74, 36.38).

Difference between mean values of the analyzed profiles is 14 %, mean values being for spot welding (64.82, 66.75, 75.88, 59.62, 66.73, 52.79) and for adhesive bonding (53.63, 60.81, 56.48, 80.79, 43.20, 42.96).

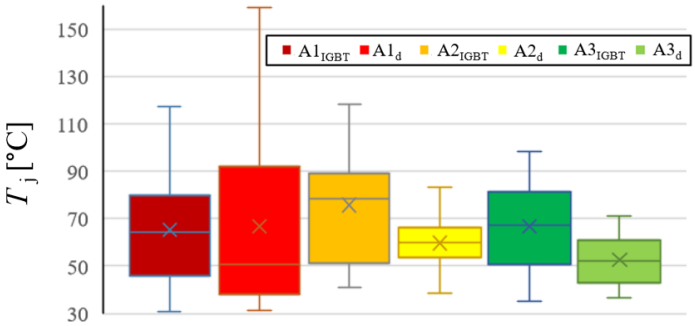

Fig. 2.47. Highest peak value, temperature change amplitude and mean value of robot axis inverter IGBT and anti-parallel diode change during sample spot welding program.

Analysis of thermal cycle and thermal swing (see Fig. 2.48) data reveal, that due to operation characteristics values observed in adhesive bonding (gluing) and clinching programs differ from welding and clinching programs. Clinching and adhesive bonding programs consist of multiple closely arranged processing points, while spot welding and handling programs are designed for few processing points and as fast movement speed. See complete visualization with data from axis 1-3 in Appendix L.

Handling and spot-welding junction temperature profile analysis confirms that more dynamic robot programs with repetitive acceleration and deceleration cycles have higher number of temperature cycles at higher amplitudes. Five out of six reviewed temperatures, highest thermal swing values were for either welding or handling programs.

Simulated clinching operation includes a series of start/stop cycles and requires high precision positioning, to reach processing points. Movement speed is highly variable, and a number of small amplitude temperature changes are introduced in this program.

Welding operation begins with a fast movement to reach beginning of adhesive application starting point, and is followed by a steady, controlled speed movement limited by process quality requirements. Robot returns to home position after adhesive application is completed.

This explains the initial several higher swing cycles, while majority of cycles is with low thermal swing.

Due to the specifics of industrial robot construction and operation, failure due to component degradation of any axis eventually means that none of the other axis can be operated as well. If the robot is not located in single robot cell, it is highly probable that the operation of production cell might have to be stopped due to IGBT or anti-parallel diode failure.

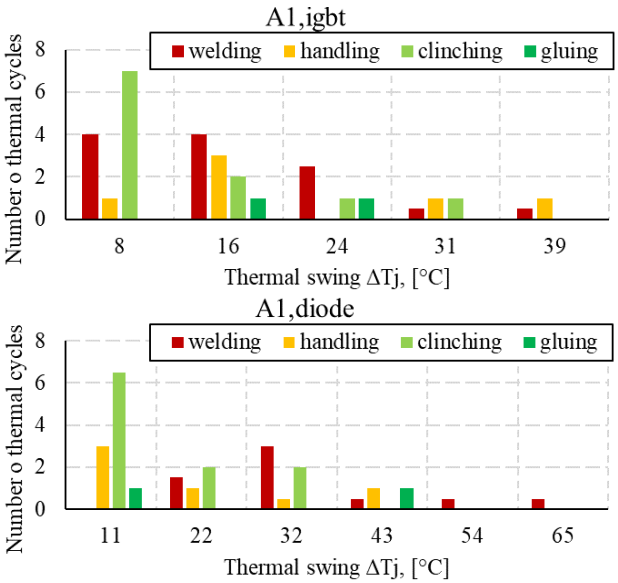

Fig. 2.48. Quantity of IGBT and anti-parallel diode junction temperature cycles and half cycles for A1 of each simulated robot program type after Rainflow counting – spot welding, handling, clinching and adhesive bonding (gluing).

.

Lifetime consumption data per IGBT semiconductor switch and anti-parallel diodes of robot axis 1-3 (see Fig. 2.49) reveal significant differences in LC data depending on robot program. See visualization of estimated fraction of life consumed for handling, clinching and adhesive bonding programs in Appendix M. The data follow trends from thermal cycle and thermal swing analysis, however, the magnitude of difference is notable for handling and welding programs with higher temperature swings.

Highest lifetime consumption is introduced to Axis 1 anti-parallel diode during operation of all simulated programs. Estimated values of LC (see Table 4) reveal that clinching and adhesive bonding programs have an order of magnitude smaller estimated degradation through one cycle of program operation. While the data for all programs follow a pattern of Axis 1 being the most demanding regarding remaining lifetime, actual values and magnitude depends on program data and mission profile.

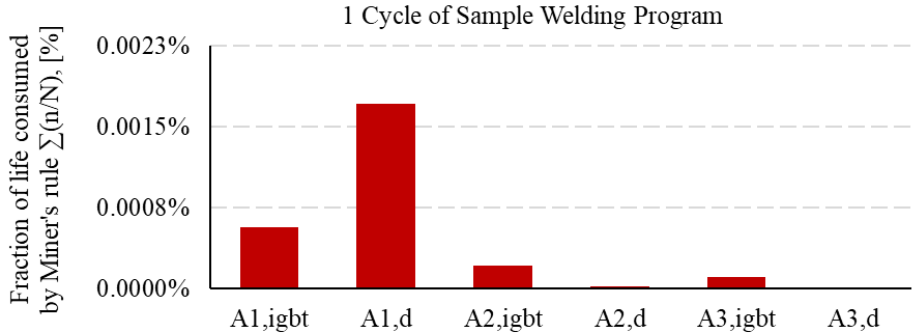

Fig. 2.49. Estimated lifetime consumption of the simulated welding robot program for IGBT and anti-parallel diode of A1−A3 robot axis inverter IGBT module.

Data in Table 2.7 are conditionally formated to minimal value being green, as it is the least damaging. Red color cells have damage above 50 % of the value difference between minimal and maximal value. Cells with green background color have damage below 50 % of minimal and maximal value difference. White cells, and cells with low opacity value are located close to middle of the value range.

Table 2.7

Estimated lifetime consumption of the simulated four robot program types for IGBT and anti-parallel diode of A1−A3 robot axis inverter IGBT module.

		welding	handling	clinching	gluing
Axis #	Duration:	13.66 s	10.25 s	9.31 s	11.1 s
A1	IGBT	5.73E-04 %	7.48E-04 %	1.40E-04 %	7.90E-05 %
	diode	1.71E-03 %	1.08E-03 %	3.55E-04 %	4.94E-04 %
A2	IGBT	2.16E-04 %	2.19E-04 %	2.32E-05 %	2.30E-05 %
	diode	2.59E-05 %	4.48E-05 %	4.91E-05 %	1.33E-04 %
A3	IGBT	1.09E-04 %	4.42E-04 %	5.05E-05 %	1.41E-06 %
	diode	1.05E-05 %	1.28E-04 %	6.99E-06 %	7.04E-07 %

Difference between estimated total lifetime consumption values of all reviewed IGBT semiconductor switches and anti-parallel diodes for Axis 1-3 of the analyzed robot programs (see Fig. 2.50) confirm the initial assumption that each robot program type has unique inverter current mission profile. Mission profile leads to wide spread in junction temperature values for robot axis inverters. The current and junction temperature difference is translated to number of thermal cycles and thermal swing amplitudes. Final result of the computation model is an order of magnitude differences of lifetime consumption estimations per each program type.

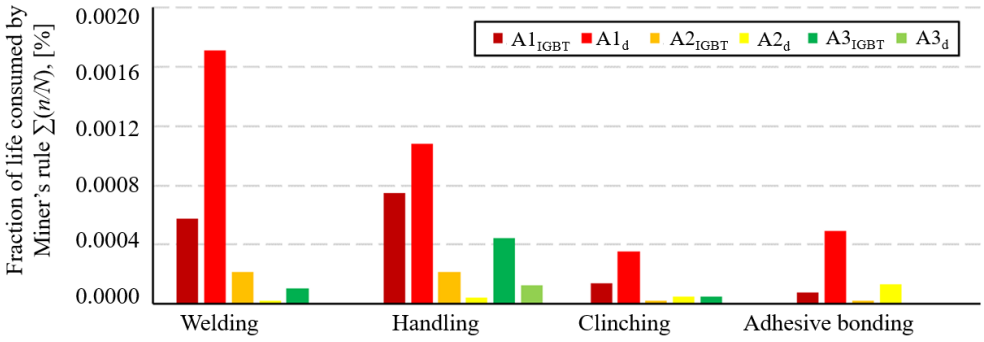

Fig. 2.50. Estimated lifetime consumption of the simulated 4 robot program types – welding, handling, clinching and adhesive bonding.

Background of the developed model, including automotive industry specifics, has been reviewed and analyzed. Added thermal and lifetime consumption estimation models have been developed and presented. Conclusions regarding operation and reliability of state-of-the-art robot hardware have been made for various robotized manufacturing scenarios, therefore study has managed to estimate junction temperature of IGBT and establish a relationship between robot hardware, robot operation and drive inverter damage.

3. ASSESSMENT OF CONTROL AND TOPOLOGY

Improvement of technology has always been driven by the need to increase efficiency, reduce costs or other factors. In similar way the efficiency of AC/DC voltage converters have increased over time [40], [41] and currently is considered sufficient for most of the applications. As the technology becomes more available and efficient, its applications in systems should be reviewed with more caution if the only possible solution is with the AC/DC converter, or is it installed as the easy choice. So the use, type and quantity of voltage rectifiers should be evaluated during system design phase.

Some of the reasons to decrease the total quantity of these voltage converters is to reduce the footprint and improve cost efficiency. In various system designs it is possible to combine DC links, which will not only help to decrease overall quantity of AC/DC converters, but will also improve system reliability often by providing redundancy of power supply.

Industrial systems require more attention as the investment, total power consumption and overall scale is larger compared to household applications. One of the examples is the most recent industrial applications recovering brake chopper energy [42] and enabling support for energy exchange within the system consumers and generators.

Currently installed power electronics systems mostly support unidirectional power flow, consist of high number of avoidable converters (both, rectifiers and inverters), still waste the excess DC bus energy in brake choppers without utilizing the storage and energy exchange possibilities at the possible common DC link.

All of this prove that there is not only room to optimise both AC/DC and DC/AC voltage converters, but to improve transmission infrastructure as well by creating DC microgrids or shared DC bus applications. As mentioned previously, sharing of DC link can improve reliability and availability of power source through redundancy of converters. An example of reliability improvement principle through power supply redudancy is illustrated in Fig. 3.1.

Fig. 3.1. DC power supply redundancy to improve reliability in industrial hardware.

Drawbacks and challenges of shared DC link systems (DC microgrids) include the required reliability evaluation, technological barriers (limited availability of hardware solutions and high specialization), as well as economic and legal barriers. Challenges include establishing DC voltage standards for various types of microgrids.

Stakeholders of developing DC microgrid systems for both - households and industry - include production site developers and operators, original industrial or household equipment

manufacturers, researchers, policy makers, investors. There are various applications and layouts of DC microgrids used throughout the industry:

a) AC Home Grid Appliances and Power Losses

Energy consumption of households is increasing with the number of available electrical devices. Introduction of Internet of Things, as well as wireless network and software availability has brought new devices and applications into the market, a lot of which are supplied with low power AC/DC power supply or charger. As the power consumption of these devices (chargers for wearables, mobile phones, robotized vacuum cleaners) is combined, so are the power losses (P_{loss}), so the total losses value is becoming significant after losses of smaller units are combined, as shown in Fig. 3.2.

When installing backup batteries for the household, or deploying an electric vehicle charging station, number of power converters is increased further. Batteries will require a rectifier for charging, and a sophisticated inverter to provide to grid when power is required. Adding alternative energy sources, such as solar panels, or fuel generator, require high quality output parameters of the inverter, to synchronize the generated sine wave voltage with the AC grid (and various safety features, such as not providing to grid, in case of voltage blackout).

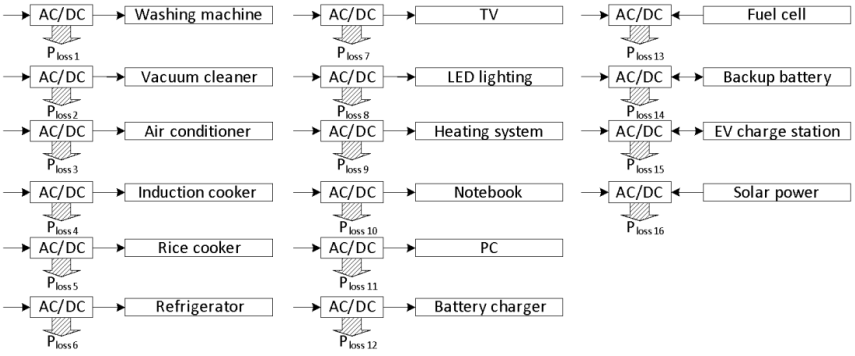

Fig. 3.2. Household electrical consumer system with 16 AC/DC converters, power losses.

However, the excessive use of AC/DC converters is not only common to household systems and consumers, it also occurs in industry, where the combined power loss is even more significant, as the devices, such as lightning and drive units are operating at high numbers and for extended period of time.

Practicality of DC micro grid remains by maintaining modularity at the same level, or is increased above one of the AC systems where system components follow parameter requirements. During the development of setup, teams focus on system operation evaluating the efficiency and use of solutions. As the efficiency of DC switches is being improved by applications of innovative materials and topologies, DC micro grid systems should be updated as well, and modular solutions allow easier upgrades. While being around for a while, DC micro grid applications still are innovative and awarded [43].

Remote households will find DC microgrids not only cost efficient, but energy efficient as well, since combined with solar or wind energy sources it can power the household and provide self-sustainable home capabilities. Energy generation and storage is supported by photovoltaic generators (see Fig. 3.3 (b)) with energy storage systems, such as batteries, likely operating more efficient if compared to alternative current system (see Fig. 3.3 (a)).

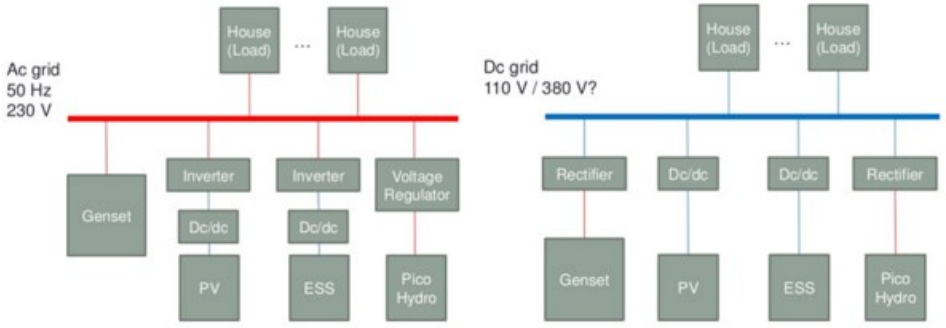

(a) (b)

Fig. 3.3. Topologies of AC (a) and DC (b) microgrid solutions including converters [44].

b) Industrial DC Grids.

Setups for industrial environment and manufacturing are less available due to smaller demand, higher capital costs and more conservative society demanding reliable and proven solutions. One of tasks is to introduce the DC microgrids and it's supported features to the manufacturing community. Several innovative projects have been completed during the last years developing DC microgrids specific for industrial environment, contributing to both - research and production.

Results of these projects reveal that facilities with specific equipment such as drives, industrial manipulators with dynamic applications can benefit from DC microgrids, and larger consumers will have proportionally increased savings from the improved efficiency, compared to scaled down home systems. For static environment and load sites without the industrial robots or other dynamic drive systems, other options such as economy from conversion to LED lightning connected to DC supply bus are available. DC microgrid modifications with renewable energy generation and storage integration, as well as systems dedicated for electric vehicles and light emitting diode (LED) street light systems are documented [45], [46].

Various DC microgrid systems have been designed for home installation and have power ratings up to 10 kW [47], [48]. Power profile of household appliances is characterized by medium load peaks repeating periodically and small parasitic consumption from stand-by mode of devices. Control methods and algorithms are not complex as the processes within this electrical system are not very dynamic.

One of the projects mentioned earlier is DC C+G, which developed and introduced an industrial DC microgrid for data center facilities. Currently widely used solutions use rectifiers

to supply the backup power uninterruptable power supply, and inverters to create voltage required for the internal grid, later being rectified for use of the data management hardware, as shown in Fig. 1.6.

One of DC microgrid developers and researchers for data center facilities throughout the years has been Intel Corporation. Their project results revealed improved energy efficiency (7-8 %), capital cost reduction (15 %), space savings (33 %) and reliability improvement (200 %) [46].

Efficiency of electricity distribution and equipment and efficiency of solar power systems has been increased by 5 % and 7 %, as reported in project funded by European Union - "DC Components and Grids" [49].

Another of DC system advantages over AC system is improved design simplicity, such as frequency coupling which is required by multiple generator AC systems, but not for DC (see Fig. 1.7). This is very practical at locations with limited space for equipment with large footprint, therefore one of test applications for DC microgrid system was ABB onboard system for vessels. Practical results of the project reveal efficiency improvement (20 %) and footprint reduction (30 %), also highlighting how easy it is to integrate various energy sources (gas, diesel, renewables) within the DC grid [50].

Analysis and review of AC and DC topologies is completed from section 3.1 through section 3.3 in terms of recovered regenerated energy, cost, availability, redundance and other parameters. Common DC link layouts, including state of the art setup with brake chopper and layout with added capacitance, are reviewed in section 3.1. Section 3.2 includes comparison of advanced DC link layouts, such as external energy storage with and without converter and layout with bidirectional rectifier for energy return to AC grid. Interconnection of multiple robot systems is reviewed in section 3.3, supplied by single or multiple rectifiers.

Results and conclusions of the analysis completed in sections 3.1 through 3.3 are combined in table shown at Fig. 3.4. Layouts are compared through different characteristics and parameters. One of the goals for this study is to improve reliability of manufacturing equipment, therefore several reliability and lifetime related parameters are evaluated as well, such as redundancy, probability of failure, consequence of failure.

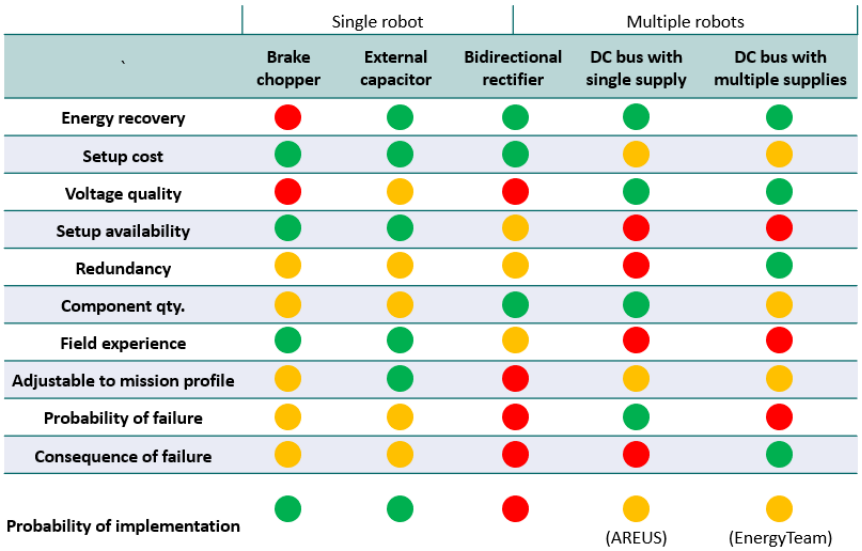

Fig. 3.4. Multiple parameter comparison of recuperative energy hardware applications.

As a general conclusion, probability of implementation is evaluated for single robot and multiple robot systems. Analysis reveal, that single robot system with state of the art hardware layout, upgraded with a additional capacitor, selected for the specific robot program, is the most recommended solution.

3.1. Common DC Link Layouts of Industrial Robot Hardware

State of the art setup with brake chopper and layout with added capacitance is reviewed in this section. Modification options are analyzed and evaluated. Section 3.1.1. is an introduction to typical hardware layout of motor drives. Section 3.1.2. evaluates the state of the art layout and section 3.1.3. the addition of capacitor to DC link is analyzed.

3.1.1. Introduction

In electric drive systems motors can and will operate as generators for certain time of operation, likely during deceleration. Typical systems of DC link frequency converter supply AC voltage from grid through the DC link (including chopper resistance unit for overvoltage control) to electric motor. When energy is generated by motor, voltage in DC bus increase and the generated energy in many cases is dissipated as heat in the previously mentioned brake chopper unit. Three phase drive power supply system with frequency converter and DC link with brake chopper is illustrated in Fig. 3.5.

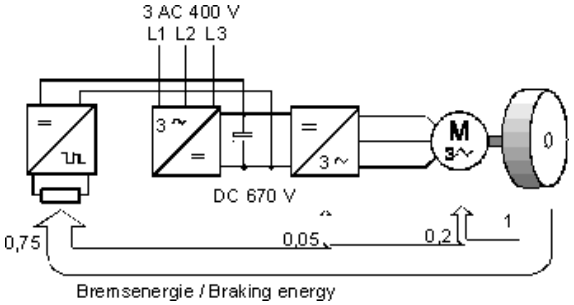

Fig. 3.5. Typical electrical drive with brake chopper setup [51].

Similar to systems with single motor, brake chopper is also common for multiple electric motor systems, such as industrial robots. Definition of robot has been declared by International Organization for Standardization, which states that "automatically controlled, reprogrammable, multipurpose manipulators, programmable in three or more axes, which can be either fixed in place or mobile for use in industrial automation applications" [52] are called robots**.** Industrial manipulators, also industrial robots, are complex mechatronic systems, consisting of a long list of parts and components, including motors, drives, controllers, actuators, communication interfaces, tools. Number and sales of industrial robots has been surging during the last several years [53].

Precision and repeatability of the industrial units is a reason for the high demand. For example, rather small industrial manipulator KUKA KR 4 R600 can repeat its movements within $<\pm 0{,}015$ mm [54]. High demand is also supported by the maximum payload, for units such as KUKA KR 1000 1300 titan PA, being able to operate with up to 1300 kg heavy load [55].

As the robots can be highly customized regarding tools, sizes and movement, they are widely used throughout the industrial environment, providing handling of materials and final products in palletizing and packaging, painting, metalworks - welding and clinching, gluing and many more.

Typical requirement for manufacturing line is to operate continuously with little or no downtimes. From one to several thousands, number of industrial robots at factory depends on several factors, such as output quantity, variety of products, cost efficiency. Large quantity of manipulators result in significant total power losses.

3.1.2. Single Robot, Current State of the Art with Chopper

KUKA, a German manufacturer of industrial robots for over 40 years, similar to other AC powered industrial robot manufacturers, supply their units from AC grid. Robot cabinet (see Fig. 3.6) is supplied through the power supply - KUKA Power Pack (KPP) which includes a rectifier R_1 and provides voltage for the DC bus. KUKA Servo Pack (KSP) is connected to the DC bus, and includes I_1, I_2 (also, input filtering capacitances C_1, C_2) transforming the energy

for electric motors. Movement of the manipulator axis is achieved by six permanent magnet synchronous motors (PMSM) which are supplied and controlled KSP. Inverters of the servo pack support two direction energy transfer, operating as rectifiers as well, during regenerative operation of the motors, where brake chopper protects DC bus from over voltage. The DC circuit present between KPP, KSP and the brake chopper Rbr is connected to the brake chopper through KPP unit, which includes switch S1 for switching of the chopper resistance. While the main power is supplied through the KPP, KUKA Power Supply (KPS) provides required 230 V for additional electronics appliances (cooling, brakes, control unit, smartpad). Flow of data within the industrial robot system is managed by Cabinet Control Unit.

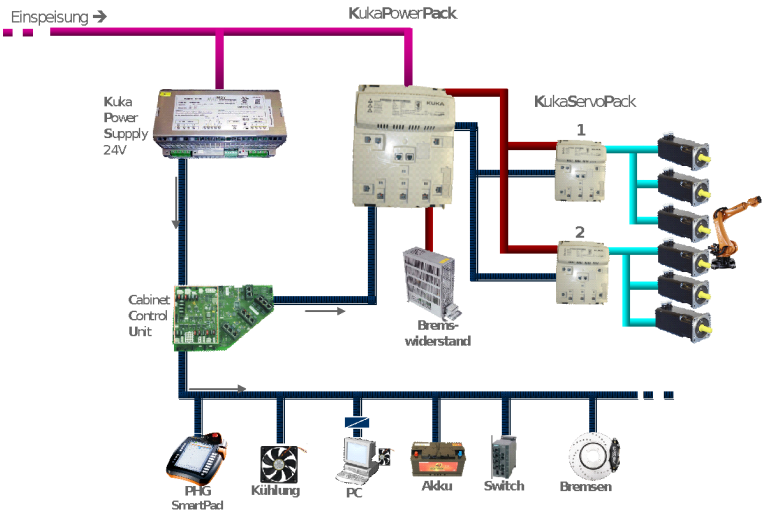

Fig. 3.6. Layout of power supply and control within cabinet of KUKA industrial robot [56].

Energy dissipated in brake chopper is linked to movement velocity of the industrial manipulator, which can reach values up to 2 m/s during handling operations. As the energy of slower movement is lower, so is the dissipated energy in brake chopper resistance. Values will vary between movement programs and robot cells. Operations which require higher accuracy and where technical process requires lower speed for the improved accuracy, also limit the velocity to less than 0.4 m/s [57], leading to smaller quantity of recuperated energy.

Sample movement profile of industrial robot state of the art layout was generated to highlight the energy losses on brake chopper - in this case, 15 % of the total value. While not efficient from an energy savings point of view, this setup is cost-effective and reliable, therefore legitimate for smaller sites and less dynamic industrial robot movements. Energy storage or exchange methods described in more detail later throughout this work absorb this brake chopper energy for re-use during acceleration.

When movement speed of industrial robot is decreasing, energy conversion from mechanical inertia to electrical is carried out at motors working as electricity generators for a

short period of time. Energy is returned to DC intermediate circuit through the rectifiers in KSP, where it is stored within the capacitance, raising the voltage to maximal allowed value. When this value is exceeded, S_1 is triggered, applying voltage to terminals of Rbr, where the recuperated energy is dissipated into heat at active resistance. As voltage drops, switch S1 is released to remain disconnected until voltage value is exceeded again. As mentioned before, small amount of this energy is stored at DC circuit capacitors, while voltage of DC link increases to required value, before switching on brake resistor, however, this capacitance C_1, C_2 is too small to store a significant amount of recuperated energy.

Sample movement profile of industrial robot was generated to highlight the energy losses on brake chopper - in this case 15 % of total value. While not efficient from energy savings point of view, this setup is cost effective and reliable, therefore legitimate for smaller sites and less dynamic industrial robot movements. Energy storage or exchange methods described in more detail later throughout this work absorb this brake chopper energy for re-use during acceleration.

Current state of the art chopper circuit provides some energy storage in DC bus capacitor capacitance, which delays the DC bus voltage increase and beginning of brake chopper switching. Power charging the capacitor is shown in Fig. 3.7 from 1.52 s to 1.58 s. Brake chopper dissipate the excess regenerated energy, but the capacitor remains fully charged, as the generated energy exceeds the possible charge. Eventually brake chopper discharge the capacitor and decrease DC bus voltage, which is recharged during chopper switch off period. The cycle continues for the duration of generated power exceeding consumed power. Chopper switching frequency is reduced with the decrease in generated power. Energy stored in DC bus capacitor capacitance is consumed during the acceleration from 2.10 s to 2.23 s (see Fig. 3.7).

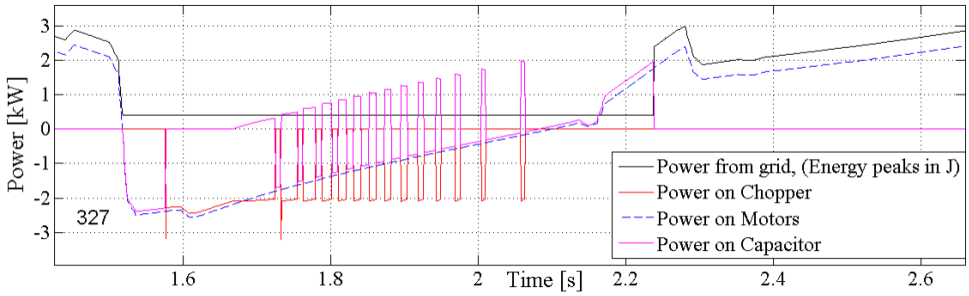

Fig. 3.7. Power change and distribution during a section of a sample robot movement program.

Energy flow including brake chopper, capacitance and total regenerated amount during one deceleration peak of the simulated sample robot program is visualized in Fig. 3.8. Initial regenerative peak is stored in capacitance (W_{cap}), with energy dissipation on brake chopper (W_{br}) beginning as soon as the DC bus voltage reaches the limit and capacitor is considered

fully charged. Ripple capacitor and brake chopper energy is caused due to partial discharge of capacitor during brake chopper switching. As shown in 2.01 s, about 25 % of the regenerated energy is stored in capacitance, while 75 % of the energy has been dissipated in brake chopper resistance.

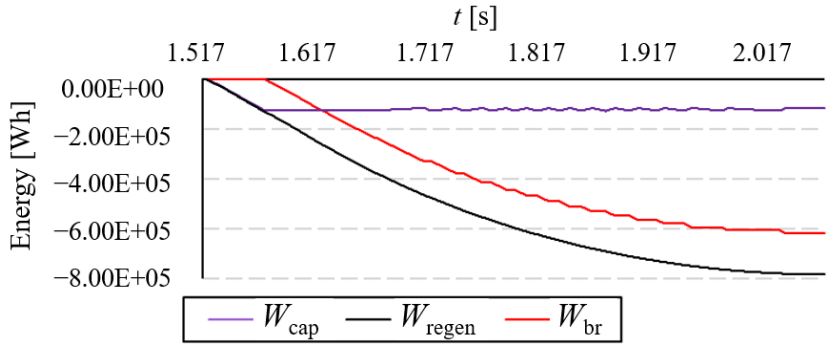

Fig. 3.8. Energy flow during deceleration of sample robot program with state of the art circuit setup.

Regarding energy recovery, current state of the art circuit is viewed as a reference layout, with majority of deceleration energy being dissipated in brake chopper resistance. Total cost of the hardware setup for the current layout is average. There are no specific elements which would either increase or decrease the hardware cost significantly. Components required by this layout are readily available in the market and they have been used widely in the industry. In the state of the art setup without external capacitor any redundancy regarding DC bus and power supply is not introduced.

The setup does not provide nor require any adjustment options to mission profiles to improve the performance. Just general energy efficient path planning rules apply, to reduce the energy consumption.

Failure probability of this circuit is considered average, as there are neither any redundancy options nor reliability bottle necks, being a single-source, single-consumer type system, not a power grid. Therefore consequence of failure is also considered average, as failure of included elements will affect a single robot.

Attempt to estimate probability of implementation for the state of the art layout reveal that it is very high. This is a straight-forward, simple solution ready for manufacturing environment. The main drawback is the extensive operation of brake chopper during deceleration, but the positive - having wide field experience and being an easy to understand, easy to repair layout, ranks this as a highly probable hardware layout.

3.1.3. Single Robot Setup with Capacitor

As mentioned earlier, during operation of currently used layout with brake chopper, small amount of energy is stored within the capacitance of DC link as the voltage increase to limit value. If the capacitance is increased, energy capacity of the DC circuit is also increased. When looking at industrial robot systems, robot motor is not capable of operating as generator for extended time period, most likely during deceleration, therefore value of available energy is known and value of capacitor can be assumed. Studies reveal that reduction of total consumed energy by up to 30 % is possible for manipulator movements in dynamic applications, which is achieved by addition of external energy storage unit to the DC link [58]. This storage unit can be but not limited to a capacitor (most likely), a battery, or a flywheel (less likely). Storage of recuperated energy within an external capacitor or a battery is reviewed throughout this work.

Within state of the art system with brake chopper and added external capacitor, recuperated energy from PMSMs of industrial manipulator is stored within the capacitor during deceleration. Energy is returned to DC bus via the KUKA Servo Pack operating as rectifier. During the following acceleration, recuperated energy from external capacitor through the KSP operating as inverter, is returned to electric drives of the robot. While not popular for industrial robot systems, external capacitor is well documented and recommended for storage of recuperated energy [59], [60], [61].

As mentioned during review of brake chopper systems, recuperated energy is movement trajectory and intensity dependent, therefore handling robot movement profiles require larger storage unit compared to painting or welding robot applications, due to movement speed differences [62]. It is recommended to either calculate capacitance of an external capacitor for each movement program, or at least choose the capacitor sizes in modular fashion, regarding movement type. Storage of recuperated energy within dedicated external storage unit is eventually more efficient approach than dissipation of this energy within active resistance of brake chopper, reviewed in previous section.

Schematic of KUKA industrial manipulator system with external capacitance for storage of recuperated energy (see Fig 3.9) includes KPP, two KSP, a dc bus, external capacitance module (C_{ext}), and six permanent magnet synchronous motors PMSMs ($M_{1.1...1.3}$, $M_{2.1...2.3}$)

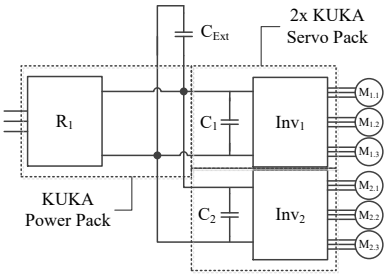

Fig. 3.9. Schematic of KUKA industrial manipulator system with external capacitance for storage of recuperated energy [63].

Often the maximal voltage of capacitors is limited below the operational voltage of DC bus and series connection of several units is required. While series connection divides the voltage to multiple units enabling safe connection, the capacitance is decreased as well. In addition, charge balancing circuit is required when multiple capacitors are connected in series, decreasing both, efficiency and financial benefits of the system [64].

Supercapacitors are one of the most energy dense capacitors being the reason why they are also researched as possible solution for storage of recuperated voltage of industrial manipulators. Technical specification of supercapacitor units declare operational voltage well below one of electrolytic capacitors. If linked to DC bus of KUKA industrial robot without a converter, 250 units would be required to create a series connection, and multiple drawbacks, such as high *ESR* value, significantly worse reliability compared to single supercapacitor as failure of single cell will result in failure of the unit, capacitance reduction, and the cost of similar layout is well too high to even consider the application.

On the other side, maximal allowed voltage of electrolytic capacitor is higher than the maximal voltage of supercapacitor unit, therefore a similar setup would require several electrolytic capacitors $C_{1.1}, C_{1.2}, C_{2.1}, C_{2.2}$ (see Fig. 3.10). As series connection reduce the capacitance, addition of parallel capacitors is used, therefore a parallel-series layout of electrolytic capacitors is introduced to compensate for the the loss and to reduce the combined *ESR* value of storage unit (as shown in Eq.3.1), where ESR_{tot} – total *ESR* of the connected capacitors, $ESR_{1,1..2,2}$ – *ESR* of the individual capacitor units in the circuit.

$$ESR_{\text{tot}} = ESR_{1,1} + ESR_{1,2} + ESR_{2,1} + ESR_{2,2} \tag{3.1}$$

Capacitance value can be increased to required and voltage requirements for connection to DC bus can be achieved. Connecting directly to DC bus without voltage level is the most common design, as it is financially reasonable and available solution.

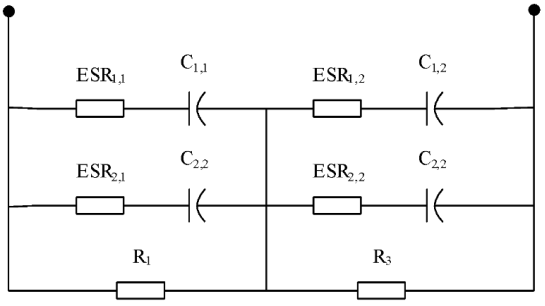

Fig. 3.10. The principal layout of parallel-series capacitors, connected without level converter or switch. A simplified version is integrated in model.

After rectification of input AC voltage, a smoothing filter placed at DC output of rectifier is required. In sample full wave diode bridge rectifier design (D_1,..,D_4) this filter includes an electrolytic capacitor C_2 (see Fig. 3.11). If capacitance of C_2 is approaching 0 uF, then output DC voltage ripple amplitude is significant and copies the input voltage. Current waveform for

such design is full sine wave pattern with no high peaks as shown in Fig. 3.11 (a). By increasing the filter capacitor value, energy is stored within the capacitor and does not fluctuate as previously, smoothing the ripple to create stable output DC voltage, as shown in Fig. 3.11 (b). However, the added capacitance creates high peak currents from charge of capacitor.

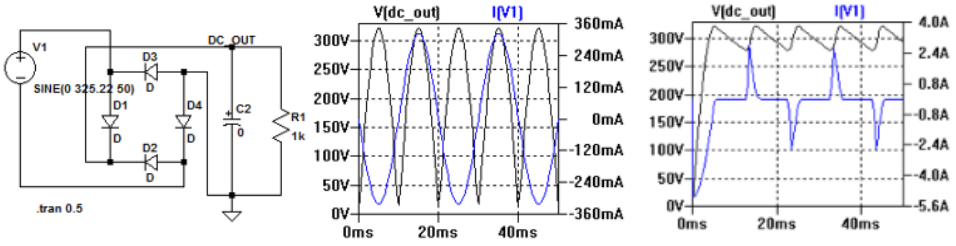

(a) (b)

Fig. 3.11. DC bus layout and simulated rectifier output voltage and current data (a) revealing effect of added capacitance on the output current and voltage (introduction of ripple and peaks)(b).

By adding an inductor in series with output of AC rectifier, a further reduction of output voltage ripple is possible, creating a low pass LC filter. Drawback of LC is the introduction of resonance frequency at specific L, C values. In layout of industrial robot cabinet, rectified voltage is supplied also from PMSM side through KSP, which also require filtering, adding high frequency pulse width modulated (PWM) voltage to to the bus together with high frequency ripple current.

While capacitance is required to smoothen the voltage ripple, higher capacitance unit is more expensive, introduces higher peak currents in circuit. By obtaining value of load current, filtering capacitor value can be obtained as shown in Eq.1.5., at which C is the required capacitance, f - ripple frequency, I - load current, ΔU - allowed ripple voltage. For full wave rectifier ripple frequency is 100Hz.

$$\Delta U = IfC \rightarrow C = If\Delta U \tag{3.2}$$

As suggested earlier, increased capacitance of DC bus will be able to store more of recuperation energy when supplied through KSP by motors. That is correct, but this will also unnecessarily increase DC output filtering capacitance during normal operation when powered from grid. Added capacitance will significantly increase AC input current peaks and inrush current during power on. Therefore a switch is recommended to connect the external capacitance temporarily during the recuperation phase, reducing number of discharge cycles and increasing time to failure. By control of current flow, it is possible to avoid a switch for energy supply from capacitor to DC bus during acceleration.

Switch is recommended to disconnect the external capacitance from DC bus during normal operation, but apart from that, connecting of external storage unit does not require additional control units or voltage converters, also the efficiency improvement is instant. If the introduced

storage unit is sufficient to store all of the generated energy, brake chopper should remain in the system for hardware safety, otherwise it is still required for use during normal system operation cycles.

Typical parallel-series external capacitor storage unit would consist of switch S_1, controlled by voltage, electrolytic capacitors C_1, C_2, passive voltage balancing circuit elements R_1, R_2, controlled discharge resistance with switch R_3, S_3, and charge current limiting circuit R_4, S_2, as shown in Fig. 3.12.

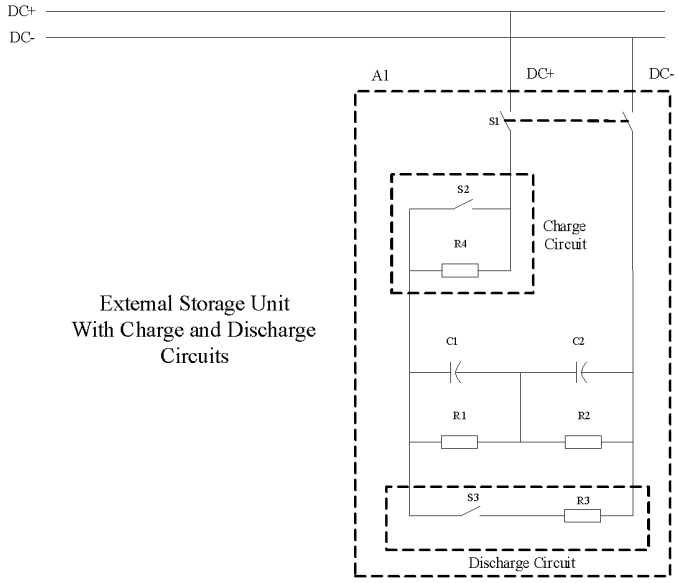

Fig. 3.12. Typical layout of capacitor based external storage unit (with charge and discharge circuits, disconnection switch) connected to DC bus of industrial robot.

As voltage in DC bus is unable to change in full range, from 0 V to maximal voltage of the capacitor, there is a charge threshold which is stored in the capacitor and not discharged during operation. This value is defined by hardware limited upper and lower voltage values, being 95.371 % of rated DC bus voltage, and 125.925 % as higher limit of rated DC bus voltage. See DC bus voltage change through an acceleration and decceleration cycle in Fig. 3.13.

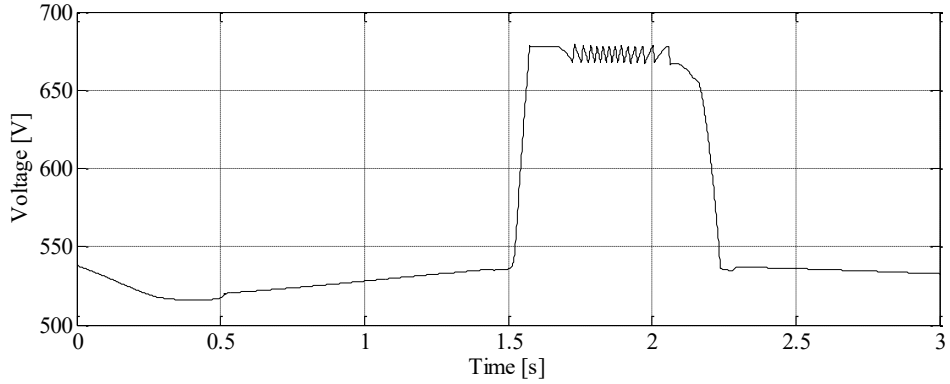

Fig. 3.13. Voltage change amplitude in DC bus as capacitor charge is changing during robot program duration.

Small or medium already constructed manufacturing sites with few industrial manipulators completing quick handling and packing tasks will find additional external capacitance upgrade useful and affordable. When looking over steps and possibilities of electrical energy consumption reduction, addition of external storage to DC link in order to decrease energy dissipated in brake chopper resistance should be considered.

Large manufacturing sites at which investments have been made to construct the line with a number of electrical drives, multiple (from several up to dozens) robots, conversion to a new hardware layout will be more expensive. Install of increased DC bus capacitor at dynamic robot movement profiles will be both - cost and energy efficient.

Disadvantages of implementing external storage system include price and information about the recuperated energy of specific movement programs, which will be equipped with the capacitor. Selection principles of optimal capacitor capacity value are suggested in this work. For rapid handling operations payback period will be smaller and for slower movements it will be longer. Another limitation is that one external storage unit can only support one industrial manipulator, as this layout does not support link of multiple robots to single capacitor.

From hardware point of view it might seem simple to add external capacitor to DC bus for energy storage, however there are some factors to consider in layout and operation, as to what effect would such change of capacitance have during normal operation of the circuit. Following section reveals how the significantly increased capacitance would change the electrical performance and suggests how to solve the upcoming issues.

Capacity of the added capacitor is selected through power consumption curve analysis. For sample program an additional capacitance of 7.3 mF (see Fig. 3.14 (a)) was calculated, providing recovery of 1.5 %. From the combined power consumption profile, energy dissipated in brake choper is used as a reference to estimate the required additional capacitance (see Fig. 3.14 (b)).

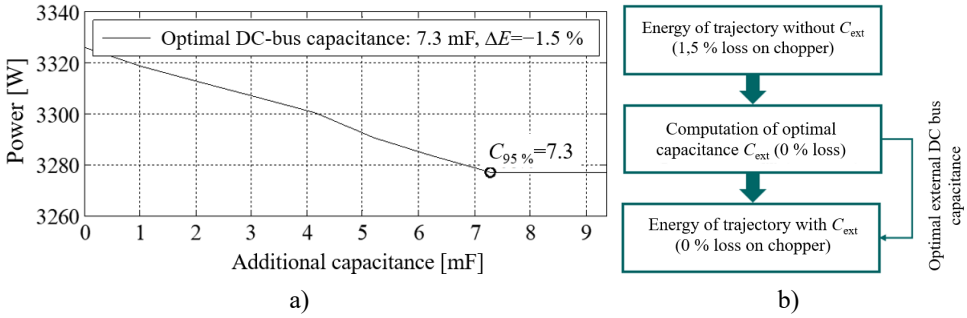

Fig. 3.14. a) Change of power consumption from AC grid through increase of additional DC bus capacitor capacitance, b) implementing optimal capacitance.

Energy flow during deceleration of the state of the art circuit with external capacitor is shown in Fig. 3.15. The capacitance value is selected to store at least 95 % of the largest dissipated brake chopper energy (W_{br}) peak of simulated program. As a result of this requirement, no energy is dissipated on brake chopper. The added external DC bus capacitor capacitance is able to store (W_{cap}) most of the regenerated energy (W_{regen}) and reuse it efficiently except for some efficiency losses. Compared to previous layout without capacitor, the energy efficiency benefit is evident - less energy is lost on chopper, however, the effect on reliability of this change is uncertain and studied later in this section.

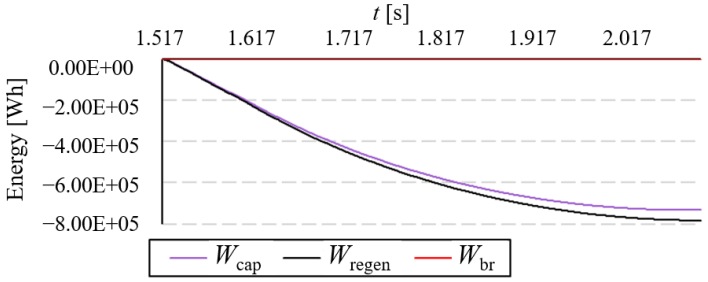

Fig. 3.15. Energy flow during deceleration of sample robot program with state of the art circuit setup and external capacitance.

To estimate life cycle consumption, inverter current is considered as the main mission profile data. It is suggested that reduced inverter current peak values improve the lifetime estimation. Motor drive and inverter current values of the sample simulated program for layouts with and without external capacitor are simulated. Robot axis 1 inverter currents are compared for the two mentioned scenarios, with absolute and relative current value difference being plotted in Fig. 3.16. As the brake energy is introduced during deceleration, the most significant difference of the current profiles is also at the decceleration

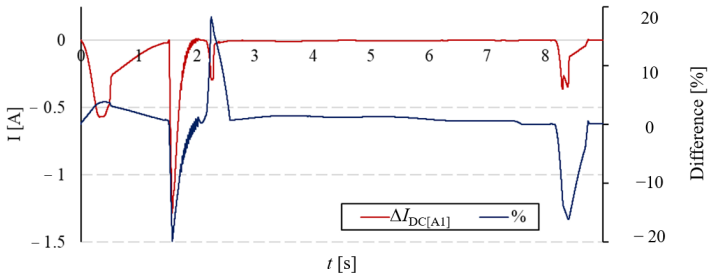

Fig. 3.16. Comparison of relatibe and absolute value differences for axis A1.

Further translation from inverter current mission profile, to IGBT and anti-parallel diode junction temperature is completed as shown in Fig. 3.17. Current to junction temperature translation is required to continue with lifetime consumption estimation for the two simulated profiles. Due to existing thermal intertia of materials temperature profile does not directly follow mission profile current, therefore current peaks are smoothened during translation calculations.

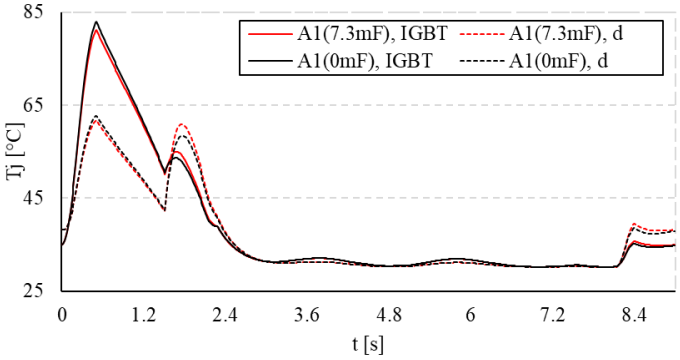

Fig. 3.17. Junction temperature estimation of IGBT and diode for A1

Data visualization reveal that highest temperature peak values at 0.6 s are for profiles without external capacitance. Values of the second temperature peak at 1.8 s are higher for profile with the added capacitance. Conclusion is that external capacitor may not reduce the junction temperature peak values through all of the operation, however, the amplitude between peak values appears being reduced.

Processing the junction temperature data through filters and Rainflow algorithm lead to lifetime consumption values for the simulated profiles. Data (Table 3.1) and visualization (see Fig. 3.18) analysis confirm the initial assumption, that addition of external capacitor of brake chopper to the DC bus might improve lifetime of the reviewed power circuit elements (IGBT, anti-parallel diode). Reduced lifetime consumption means that overall lifetime expectancy of the material has incresed.

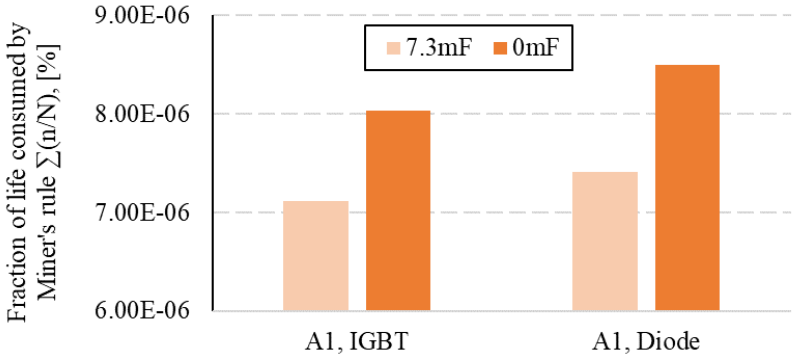

Fig. 3.18. Lifetime consumption for state of the art hardware layout without external capacitance, and with 7.3 mF added capacitance to absorb regeneration energy peaks.

Simulation data reveal more than 10 % (12.73 % for IGBT and 14.67 % for anti-parallel diode) lifetime consumption difference when comparing the two the reviewed circuits. As the general trend is confirmed, with an addition of external capacitance lifetime consumption is expected to decrease for the remaining axis of industrial robot A2-A6 as well.

Table 3.1.

Change of lifetime consumption values with and without added external capacitance.

	A1, C_{ext}=7.3 mF	A1, C_{ext}=0 mF	Change
Lifetime Consumption, IGBT	7.12E-06 %	8.03E-06 %	12.73 %
Lifetime Consumption, anti-parallel diode	7.41E-06 %	8.49E-06 %	14.67 %

According to the data, energy recovery rate for the state of the art circuit with external capacitor is very high, as barely any braking energy is lost, mostly in efficiency losses rather than direct dissipation in active resistance.

Total cost of the hardware setup is considered average, as it is more cost effective upgrade for smaller sites with agile (high velocity, multiple start-stop cycles) robot programs. It is more expensive and less cost efficient to upgrade existing sites with larger robot quantity and slower (small velocity, process without start-stop cycles).

Reviewed layout is a state-of-the-art circuit with added external capacitance, therefore majority of the layout is readily available and used widely in industry. Added external capacitance, including simple balancing circuit is either completely or mostly a passive element, easy to source and implement.

Addition of external capacitance does not introduce any redundancy regarding DC bus and power supply in the existing state of the art hardware layout.

Optimal external capacitance calculation method provide capability to adjust performance for the specific program of current robot system, in order to maximize the benefits. Sure, to reduce the energy consumption, general energy efficient path planning rules apply as well.

The inverter semiconductor switch lifetime consumption estimation results presented in this section allow concluding that the expected failure probability of a state-of-the-art circuit with additional capacitance is lower than for a system without this addition. Relative and absolute values are mission profile dependent. Drawback of this layout is that a new component (capacitor) with its own failure probability and characteristic failure modes is introduced in the system. Consequence of a failure is considered average for this layout as well, as a single source, single robot power supply circuit is reviewed.

The probability of implementation for the state of the art layout with additional capacitance is high. The demand is created by the promised energy consumption reduction of this relatively simple addition to the most commonly used hardware layout, preventing the brake chopper dissipation. Drawbacks include limited options to estimate the required capacitance before the actual implementation of the robot and several test-runs of the robot program with load, as it is not provided by the manufacturer and require robotics engineer involvement. Overall conclusion is that this is a highly probable hardware layout.

3.2. Advanced DC Link Layouts of Robots

There are limited performance (efficiency, reliability, etc) improvement options if one of the requirements limits the amount of hardware changes, therefore single robot topology assessment in this study is categorized in simple modifications (external capacitance) and advanced upgrades. Simple modifications have been reviewed in previous section 3.1, while sub-sections of 3.2, section 3.2.1 reviews the introduction of a new DC/DC converter and section 3.2.2. – an introduction of a bidirectional rectifier with inverter capabilities to return generated energy to AC grid. Characteristics of the topologies are analyzed and compared according to previously highlighted key areas, such as energy recovery, redundancy, failure probability and others.

3.2.1. DC Bus, Capacitor+Converter

In state of the art circuit with added capacitor, there is a charge threshold as described previously. Due to electrical limits, charge below threshold is not available for consumption during acceleration of industrial robot, as the voltage is unable to decrease below lower limit value (see Fig. 3.19). One of possible options to access more energy is by introduction of DC/DC converter with wide voltage range between the DC bus and capacitor.

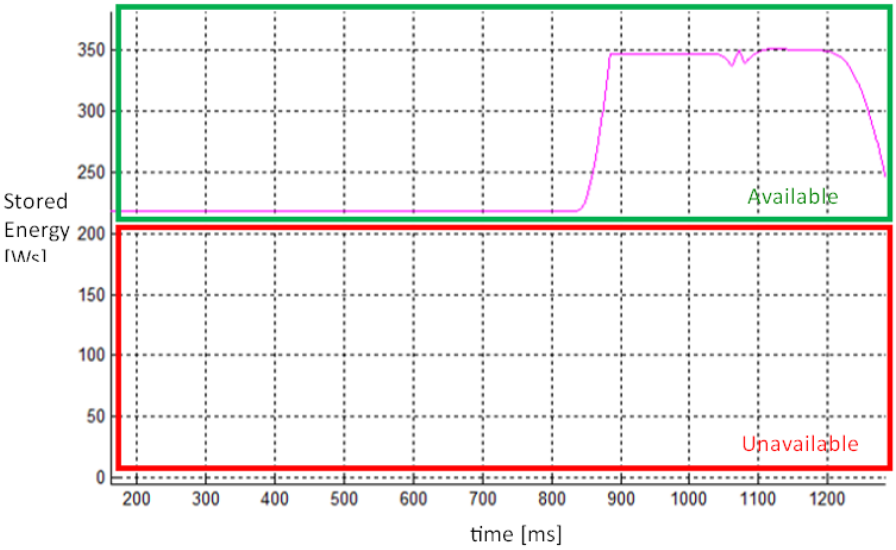

Fig. 3.19. Stored energy charge level within DC bus capacitor during robot movement without added external capacitor for optimal energy recovery.

As mentioned earlier, capacitor connection without series layout often is not technologically possible due to high maximal voltage of the DC bus, such as 540 V to 600 V DC within KUKA systems. While parallel-series layout is possible, there are several limitations to this setup, compared to systems with DC/DC voltage level converter between storage units and DC bus.

Connection of electrical storage units to high voltage DC link through voltage converter has been researched by other industries earlier, as shown in Fig. 3.20. DC/DC converter is installed between high voltage DC bus, and supercapacitor or electrolytic capacitor connection, either reducing the voltage or boosting it to the required level.

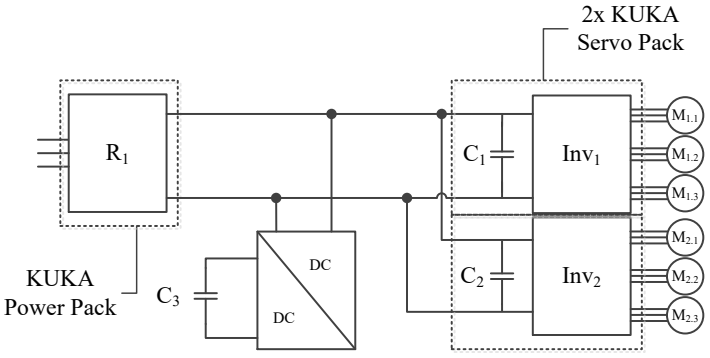

Fig. 3.20. Integrated DC bus system of KUKA industrial robot controller with an external capacitor and interfacing DC/DC converter connected to DC bus.

Throughout the operation, voltage within DC bus of KUKA industrial robot ranges from 520 V to 680 V , therefore energy is accessable through this voltage range as well, and voltage is unable to decrease below 520 V – at full discharge voltage is 23 % lower than full charge, never reaching 0 V. Energy in capacitor follows Eq. (3.1), where E – energy [Ws], C – fixed capacitance [mF] and U – change in DC bus voltage between reference and end of charge voltages [V].

$$E = \frac{1}{2} C U^2 \tag{3.1}$$

System with DC/DC converter reduces the unrecoverable energy providing the availability to manage storage side DC voltage at wider amplitude, and provides additional protection for storage capacitors, through voltage controlled switches or fuses.

Some of the benefit is lost at the power losses of the converter. Costs of the converter are added compared to parallel-series capacitor connection, but a smaller number of high voltage capacitors are required, improving energy density.

Energy recovery rate for a system with DC/DC converter is high. Similar to a direct connection, energy capacity of storage elements is selected to meet the requirements of the robot program. While the overall recovery rate is sufficient, converter introduces additional efficiency losses, which increase the amount of dissipated energy.

Cost structure is similar to previously reviewed directly connected additional capacitance layout, in terms of being more cost effective to smaller sites with agile programs, and less cost efficient upgrade to existing sites with larger robot quantity and slow cycles. Introduced converter lower the overall cost efficiency of the setup, as in general direct connection layout is capable to store sufficient charge, and converter would be the most efficient with larger stored energy capacity.

Either high voltage or low voltage energy storage solutions, both are available and used widely in industry. In addition to the passive energy storage, an active DC/DC converter hardware is introduced. Sourcing a converter to support the required voltage conversion rate and power could become difficult, therefore this layout is considered less available.

Neither direct connection nor an additional DC/DC converter does not provide redundancy regarding DC bus and power supply for full operation of the robotized equipment. The interfacing converter does enable connection of a larger stored energy capacity solutions. It enables an option to power the equipment for a period of time, for example, to return of manipulator to a safe home position.

Added external capacitance is adjusted to align with the regenerated power values of the specific program of current robot system. The increased storage capacity enables an option to support short backup or uninterruptable supply also adjustable to the requirements of the specific manufacturing equipment. In some scenarios, the introduced DC/DC converter parameters could become a technical limitation for the complete backup supply system.

As concluded earlier, in general an optimal DC bus capacitor capacitance reduces the lifetime consumption for the motor drive power electronics semiconductor switches, likely due

to the reduction of current values and more stable voltage. The same principle applies to a system with a capacitor and an additional converter, sure, absolute and relative values depend on each mission profile. Drawbacks regarding lifetime consumption are the failure probability curves and characteristic failure modes of the introduced equipment – storage elements and DC/DC converter. Failure consequence for this single source, single robot power supply circuit is considered average. If the enabled backup supply option is integrated, partial failure of the system could affect the performance of the specific robot during supply interruptions.

Probability of implementation for the state of the art hardware layout with a DC/DC converter separated additional energy storage is average. The demand for this layout is supported by the requirement to store energy previously dissipated in brake chopper, and the requirement to provide some backup power supply capabilities with larger energy storage options. Drawbacks include ones mentioned previously, that required energy capacitance estimations are complicated without the model or hardware installed and measured. Converter properties are discutable as well, as they will affect the system performance and change cost efficiency. Uninterruptable power source is a process requirement for a selection of manufacturing processes, but most processes either do not require it or would have to evaluate the cost efficiency of this application. Overall conclusion is that this is a probable option, expected to be limited to a specific applications.

3.2.2. DC bus, Bidirectional Rectifier

Concept of energy storage is based on requirement to store electrical energy until it is required for use by any consumer, such as industrial robot. If analyzing a manufacturing environment, there are a lot of high power consumers connected to the grid on site, therefore storage is not the only option for management of recuperated energy, as it can be returned to grid and consumed at the same moment. As power is supplied to robot through AC/DC converter operating as rectifier, the same converter is required to operate as inverter as well to support energy return to grid. Industrial robot system with installed bidirectional AC/DC converter R_1 consists of energy consumers, generators – PMSMs ($M_{1.1...1.3}$, $M_{2.1...2.3}$), bidirectional KUKA Servo pack AC/DC converters (Inv_1, Inv_2), filtering capacitors (C_1, C_2) as shown in Fig. 3.21.

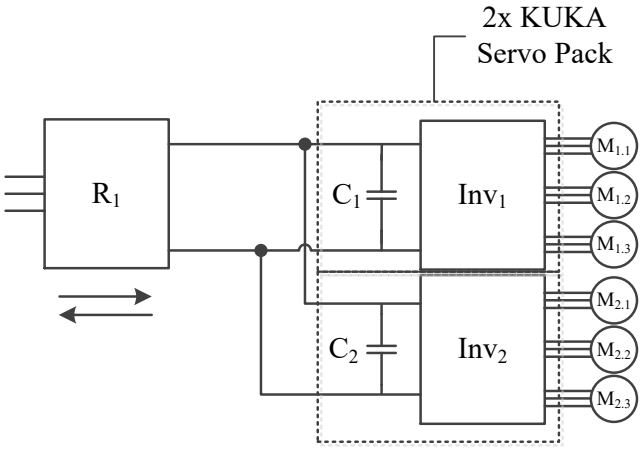

Fig. 3.21. Industrial robot electrical cabinet supplied through power supply with fully integrated inverter [63].

As long as the motors of industrial manipulator operate as electrical energy consumers, R_1 is operating as rectifier and Inv_1, Inv_2 are operating as inverters to provide required voltage for acceleration. As robot is decelerating, Inv_1, Inv_2 are returning the excess energy to DC bus operating as rectifiers, and due to voltage increase in DC bus, rectifier R_1 is switching to inverter mode and return this generated electricity to AC grid before it, turning the energy meter backwards.

While bidirectional AC/DC converter setup may seem simple, it has several major drawbacks. Power lost due to voltage conversion losses are small, but motors of industrial manipulator operate as generators for short periods of time even during handling operations. AC grid capable inverter is expensive due to sophisticated synchronisation control system, and number of power electronics semiconductor switches is increased as well. High output voltage quality standards of grid-tied inverters is another challenge for bidirectional AC/DC converter developers. There can be dozens of robots connected to one AC grid, and several hundred or even thousands within a region [65], posing “a threat to network in terms of stability, voltage regulation and power-quality issues” [66] due to distributed generation.

From a single industrial robot system point of view, energy recovery rate for a state of the art system with bidirectional rectifier is high. It is assumed that the grid has unlimited capacity to accept the energy peak generated by robot motors. Some of the generated energy is lost in efficiency losses of the involved power electronics converters. Operation of a bidirectional power supply for microgrid applications has been studied in [67].

Cost of the hardware is considered above average, as current rectifier within KUKA Power Pack is replaced with industrial AC grid capable grid-connected high power three phase bidirectional rectifier/inverter equipment, or extended with an additional inverter module. Cost-efficiency is questionable and depends on the specifics of the robot program, as less agile

programs does not establish a sufficient demand for a grid connected energy recovery system, as seen from previous examples.

While not common in robotized manufacturing environment, bidirectional energy flow in drive systems is common in other areas. Returning motor energy to grid is offered for elevator systems [68, 69], therefore the technical solutions are available. The existing systems are being provided as a separate regenerative unit connected to DC link for more flexibility, as fully integrated regenerative system limits the available use case options. State of the art robot power supply system supports the the addition of an inverter module to DC link as shown in Fig. 3.22.

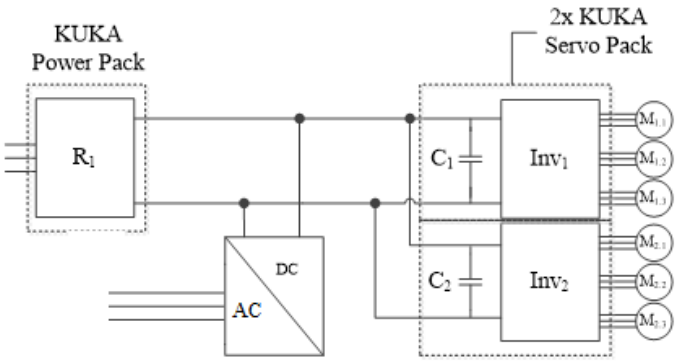

Fig. 3.22. Industrial robot electrical cabinet supplied through standard KPP power supply with an additional inverter module.

Connecting a bidirectional power supply with an inverter capability does not provide redundancy regarding operation of the connected robotized equipment, since the robot power cabinet is supplied through single power source.

Although some inverter module adjustment is possible to a specific robot program returned peak currents – it is not expected. Implementation of an inverter module with support to high rated return power peaks reduces the development cost and enables further program adjustments. Overall, this setup does not provide nor require any adjustment options to the needs of various mission profiles.

General conclusion regarding lifetime consumption of the motor drive power electronics semiconductor switches applies to a layout with bidirectional rectifier as well. Reduced current values and more stable voltage reduces the lifetime consumption. Improvement values depend on each mission profile. It applies to a system with additional inverter module as well. Drawbacks of the lifetime model – as a new hardware is introduced with their failure probability curves and characteristic failure modes, increasing the quantity of components, overall lifetime estimation is expected to worsen as the probability of failure has increased.

As the reviewed bidirectional supply layout is a single source, single robot power supply circuit, failure consequence is considered average. In case of failure, a distruption is expected

in the single robot system, with possible effect on a manufacturing cell of several robots or manufacturing line, if a extended delay is caused.

The reviewed layout has a low probability of implementation. The demand is supported by the specific requirement for a general solution to regenerated energy not involving storage elements as capacitors. Dimensioning of storage capacitor is not a problem, as the excessive generated energy is returned to grid. The addition of inverter or bidirectional rectifier provides an option to return electrical energy to AC grid, the DC link of robot cabinet supports the connection of external energy sources, such as solar panels with DC output, where energy is returned to grid when not directly consumed by the equipment. While an unlikely requirement for general consumers, some use cases are expected have this requirement.

Drawbacks of the system include limited use cases, challenges to select the converter parameters and limited options of the equipment in the market. Bidirectional rectifier includes an active converter which increase the cost and worsen the overall reliability of a system compared to state of the art layout. Cost efficiency for a single robot system with no additional energy sources is questionable, as the more popular use case for a bidirectional converter elevator systems include extended generation durations in high-rise buildings.

3.3. Multiple Interconnected Robot System Layouts

Advanced hardware upgrades to improve performance (efficiency, reliability, etc) of the single robot topology suggest an introduction of various new converters (a DC/DC converter for storage, DC/AC for return to grid) expanding the capabilities of robot cabinet DC link. This section suggests to continue the changes of existing state of the art layout and provides an initial analysis of various layouts focused on multiple robot cabinets with a shared DC link.

The main benefits and drawbacks of multiple robot connection are discussed in general at section 3.3.1. Section 3.2.2. reviews the option to supply multiple robot systems through a single rectifier. Connection of multiple state of the art systems to a shared DC bus is reviewed in section 3.3.3. Topologies are analyzed and compared to highlight significant benefits and drawbacks in the terms of energy recovery, redundancy, failure probability and others.

3.3.1. Multiple Robots, DC Link

Some of industrial robot cells (enclosed manufacturing area where robots are operating) contain several robot units, as they both participate in handling or manufacturing operations. Voltage in DC bus directly depends on the movement program of robot. If it is accelerating, then the voltage is lower and electricity is being consumed. If the robot is decelerating, the voltage is increasing and electrical energy – generated. If one of two robots accelerates at the same time, directly or soon after stopping of the other unit, some of the generated energy could be re-used.

Such multiple robot systems enable possibility to establish a DC link between DC bus of these robot power supply circuits. This enables to further improve efficiency, as one of robots can consume electricity which is generated during deceleration of the second robot (see Fig. 3.23), and the brake chopper use time as well as capacitance of the DC bus can be reduced during normal operation [58]. Connecting more industrial robots to shared DC bus can decrease the overall dissipated energy in brake chopper significantly, as probability of simultaneous acceleration and deceleration of two motors is increasing. Therefore if multiple robots are linked at DC bus, but they accelerate, decelerate simultaneously to each other, setup will not have the desired effect. Scheduling of robot movements can be planned through virtual commissioning software.

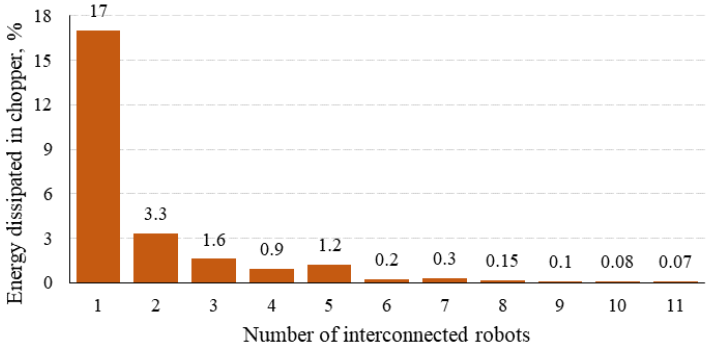

Fig. 3.23. Impact on energy dissipation in brake chopper of multiple robot electrical cabinet interconnection through DC link [66].

As the concept of joining several robot units to single DC link has been approved as effective, there are several aspects to consider regarding the power electronics hardware layout of the system. One of these aspects is choosing the power supply for the new multiple robot system, as it can be supplied either by single high power rectifier, or several redundant sources. Single and multiple power supply industrial robot DC link systems are analyzed in terms of energy recovery, redundancy, failure probability, through the following sections 3.3.2 and 3.3.3.

3.3.2. Single Rectifier, Multiple Robots, DC Link

For manufacturing facilities in planning or development where groups of robots are located in single cell, it is possible to link robots with common DC link (see Fig. 3.24), and supply the system from single, high power industrial rectifier. There are several significant drawbacks and things to consider regarding this approach, including reduced reliability (high costs for redundancy) and requirement for high combined peak power, meaning more expensive (higher

current) hardware. German patent is issued for a setup of multiple industrial manipulators powered by single, large power rectifier for Daimler AG [70]. Demo laboratory of this setup was also presented during project AREUS [1].

Sample setup of single high power rectifier and multiple industrial robots sharing a DC bus include rectifier R_1, inverters Inv_1,.. Inv_4, PMSMs 1.1,..,4.4 and operational external energy storage unit C_{ext} as shown in Fig. 3.24.

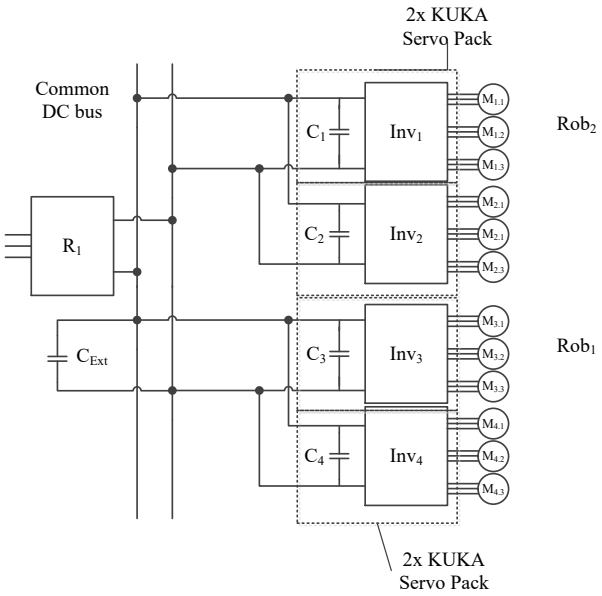

Fig. 3.24. Connection of multiple industrial robots to a shared DC bus with centralized supply and an external capacitor for additional energy storage [70].

Similar to previously discussed layouts of industrial robot power circuitry, recuperated energy is stored in capacitors or dissipated in brake chopper, connected to DC bus. Capacitance of external capacitor can be reduced as with many robots with common DC link more energy is used without storing. Brake chopper must remain connected to DC bus, as its primary function is DC bus circuit overvoltage safety switch [71].

With this being the first discussed layout of DC link within this research, the most significant advantage over previous systems is that if a manipulator linked to the same DC bus accelerate during deceleration of another robot, energy can be used before storage in capacitor, and losses are decreased further [58]. Benefit increases together with number of electrical drives connected to the common DC link, as probability of instantaneous energy exchange between robots becomes higher (actual movement dependent).

All of the power from AC grid is supplied through single rectifier, and operation of the system completely depends on its performance, which is challenge for reliability also due to

centralized component heating. Support of redundancy for high peak power, high reliability industrial system is expensive. With the increased number of robots, standby power consumption has increased as well, making it increasingly cost effective to consider connection of an alternative power source, such as solar panels to the common DC bus.

Energy recovery rate for multi-robot systems is considered high in general. To maximize the efficiency, an additional capacitor is an available option. Since the assumption of maximal energy recovery for this hardware layout considers connected robots accelerating and decelerating simulatenously for the consumption of generated peaks, scheduling of programs and movement has increasingly important role in the process. Some of the regenerated energy is lost in efficiency losses of the involved voltage converters.

Several alignment options were studied through this work to confirm the program scheduling effect on hardware lifetime consumption. Spot welding program with duration of 13.66 seconds (see Table 2.5) was selected base program, and 10.25 seconds long handling program was selected as an overlay program, changing the alignment related to welding program as shown in Fig. 3.25. Robots are simulated with a shared DC bus, supplied through centralized rectifier.

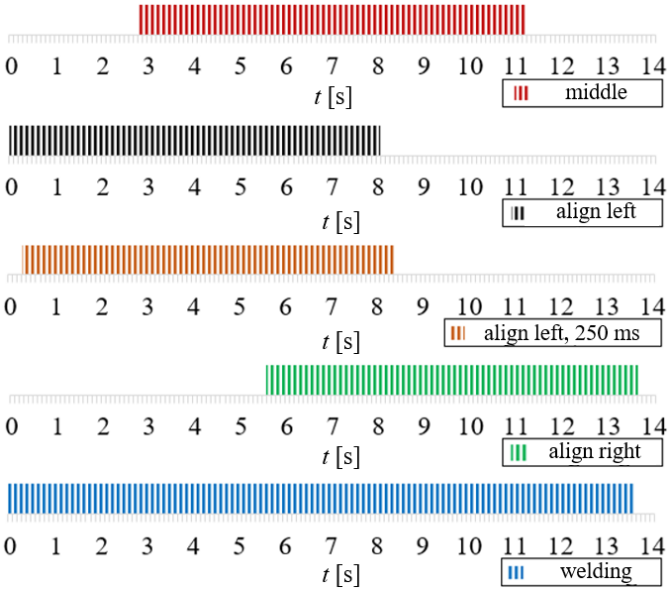

Fig. 3.25. Studied alignment options for sample handling and welding robot programs connected to a shared DC bus with centralized supply

Simulated voltage in DC bus is compared for the 4 studied scenarios of welding and handling 6-DoF KUKA industrial robot programs are shown in Fig. 3.26. Analysis confirm that scheduling scenarios of robot programs have different DC bus voltage profiles.

Compared to a single robot system, simulated setup with two connected robots has doubled the number of linked motors from 6 to 12. Energy exchange between motors has increased the current flow direction change, which affects the voltage profile. Even though the robot programs and required energy to perform movement does not change, alignment of power consumption and generation peaks is different, leading to significant differences in DC bus voltage data. The common for both scenarios is base DC bus voltage profile defined by welding program. The lowest values of DC bus voltage are caused by current consumption peaks, and the highest values (triggering the brake resistor switch) are caused by current generation peaks with no immediate consumers available.

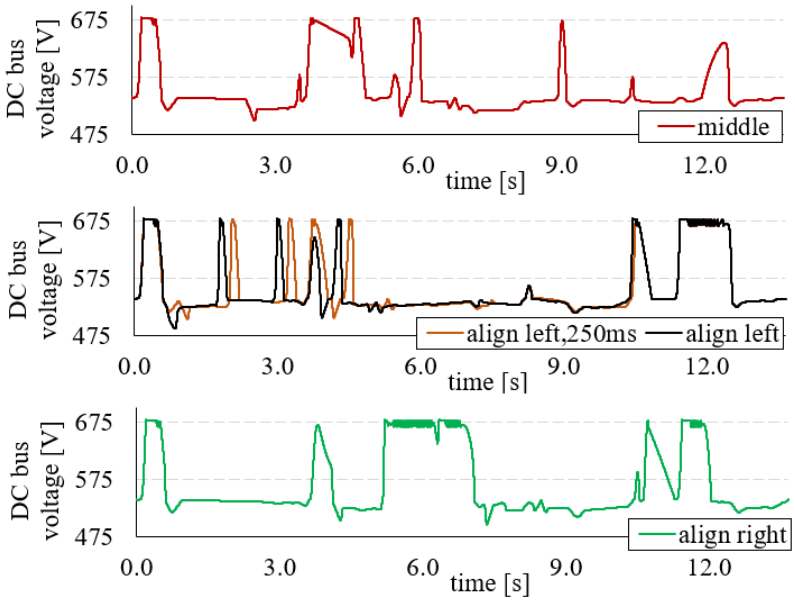

Fig. 3.26. DC bus voltage for various alignment options of the two robot programs.

Energy consumption data for the simulated profiles reveal differences in energy consumption, average power and average power on chopper values as well (see Table 3.2). Reviewed alignment differences reveal 3 % change in both, energy consumption and average power, which can be considered a significant as programs are setup for long term operation. Values of average power on brake resistance range from 0.10 kW for middle alignment, to 0.23 kW for right alignment. Data show almost no difference between left alignment and slightly offset (250 ms) program.

Table 3.2

Energy and Power Data of the Simulated Various Handling and Welding Robot Program Alignment Options (see Fig. 3.24).

Alignment	Energy [kJ]	Average power [kW]	Average power on chopper [kW]
Middle	51.90	3.80	0.10
Left	52.69	3.86	0.15
Left, 250 ms	52.67	3.86	0.15
Right	53.51	3.92	0.23

Simulated current profiles of scheduling scenarios have been compared (see Fig. 3.27). Regarding the current mission profiles, a one of major indicators is the current peak at the beginning of program when most axes accelerate to change robot position. For single robot peak value is 20 A, while combined current consumption peak values for a layout with single power source can reach 43 A. Other scheduling options still have the current consumption peak, but with lower values – at 35 A and 37 A. Left alignment with 250 ms offset reveal that the initial current demand has decreased from 43 A to two separate peaks of 20 A and 30 A.

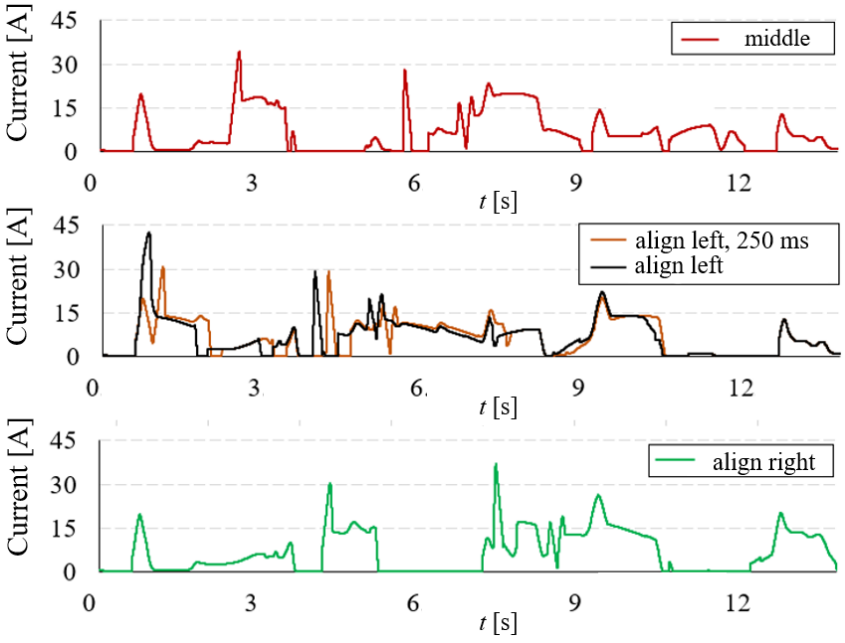

Fig. 3.27. Current consumption from AC grid through central rectifier for various alignment options of the two robot programs

Two of the scenarios (middle and right alignment) were selected for lifetime consumption analysis of the robot inverter IGBT modules for one axis, in an attempt to confirm or deny that alignment of robot programs may affect the semiconductor module lifetime, and to evaluate the possible scale of change. Middle alignment has the lowest energy consumption and average brake chopper power, while right alignment is the opposite for both values – highest energy consumption and highest average brake chopper power of the 4 studied scenarios. See comparison of the DC bus voltage for the two scenarios in Fig. 3.28. First seconds of the DC bus voltage profile during which welding robot axis are changing position are shared between the base welding movement and handling movement overlay.

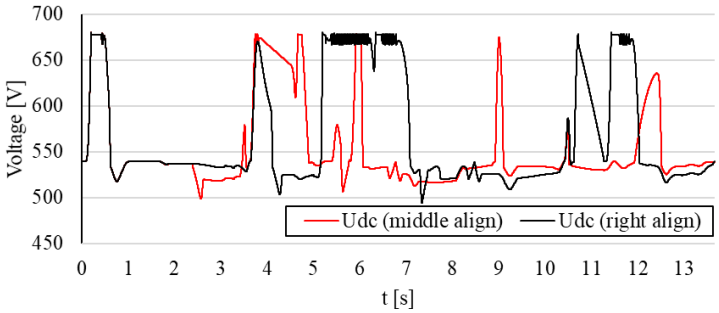

Fig. 3.28. DC bus voltages for two sample welding and handling program alignment options.

Junction temperatures of the both scenario handling robot axis 1 inverter IGBT and anti-parallel diodes are plotted in Fig. 3.29. Immediate difference is the different offset of temperatures in time, which is caused by different alignment to the base welding process, however, the different offset is not expected to have a significant impact on long term lifetime consumption.

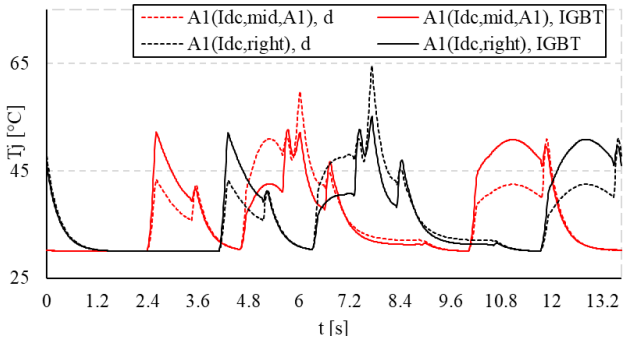

Fig. 3.29. Estimation of handling robot Axis 1 inverter IGBT and anti-parallel diode junction temperature during operation of two sample welding and handling program alignment options.

More significant parameter is the value of the highest junction temperature peak, and there is a difference between the two scenarios for both – highest value of IGBT and diode. Junction temperature at 8.0 s has peak values of 65 °C (diode, right align) and 55 °C (IGBT, right align), and at 6.0 s peak values of 60 °C (diode, middle align) and 52 °C (IGBT, middle align).

Lifetime consumption analysis for the simulated junction temperature data confirm that both alignment scenarios are not equal, as shown in Table 3.3. Results reveal that operation of robot programs in right alignment is expected to have 10.21 % more damage on IGBT, and 45.58 % more damage on anti-parallel diode of the analyzed axis drive inverter power electronics switch components.

Table 3.3.

Change of lifetime consumption values for right and middle alignment of welding and handling robot programs.

	Align middle	Align right	Decrease
Lifetime Consumption, IGBT	7.89E-06 %	8.78E-06 %	10.21 %
Lifetime Consumption, anti-parallel diode	8.68E-06 %	1.59E-05 %	45.58 %

Compared to other hardware layouts, lifetime consumption for a multiple robot system of the motor drive power electronics follow the same principles as discussed. Challenge of this layout is to manage the optimal efficiency and reduce energy dissipation in brake chopper through program and movement scheduling, as it has been confirmed (see Fig. 3.30) in the study presented in this section. Number of rectifiers is reduced which is an improvement to overall reliability, with the effect becoming increasingly significant with higher number of robots. Drawbacks of the model include introduction of a new hardware with failure probability curve and characteristic failure modes. Scaling of the central rectifier is a challenge, as rated parameters for the AC/DC converter change with each added robot unit.

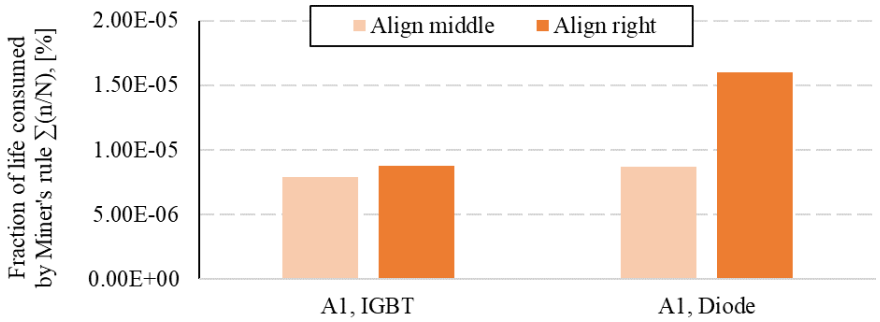

Fig. 3.30. Lifetime consumption for the power electronics switches of robot Axis 1 inverter, for two sample program alignment options.

Hardware cost for multiple robot system with a single supply is considered high. Benefits for the costs are that current KUKA rectifiers are not required. The main drawback is that the

same combined power has to be supplied through the single supply, with a very high total rated power (unless mission profile values are available from simulation). Costs are expected to be higher due to the fact that rectifier has to use increasingly expensive high power components for the support of multiple robots. If power supply redundancy is required by the specifics of manufacturing process it is financially expensive, as the backup supply must be with high rated power as well.

Multiple robot system with a central power source require a high current rectifier, with peak current value being mission profile and and number of robots dependent. A wide range of AC to DC voltage rectifiers are available in market as there are several industries that require high power conversion. One of the drawbacks regarding availability is that current robot systems are designed to control electrical cabinet of a robot including a rectifier, therefore reaching out to robot manufacturer may be required to enable hardware and software support for a centralized power source.

Connection of multiple robots with a single power source does not provide redundancy regarding operation of the robots. As mentioned earlier, redudancy options are expensive for this type of layout, therefore would be questionable in a budget-limited manufacturing environment.

Multiple robot connection to a shared DC bus require scheduled robot program timing of accelerations and decelerations for energy efficient performance, especially significant for a systems with low robot quantity. Addition of external capacitor to store the excessive regenerative energy is an option, selected to store the regenerated power values of the specific programs of current multi-robot system. Therefore multiple robot layout with centralized supply is adjustable to specific robot programs with an addition of external capacitor, and scheduling of robot programs. Example of multiple operation process and robot programs is presented in Appendix B.

Failure consequence of a multiple robot system with single power supply is high. Without a redundant power source, multiple manufacturing cells with electrically connected robot cabinets are possibily affected and expected to have production distruptions. Design of the centralized power supply should be selected to have spare parts available to avoid repair delays.

The probability of implementation for the layout reviewed in this section is average and this is not expected to be selected as a mainstream option for most sites. The demand is supplied by a requirement of the engineering team to have a DC grid in the manufacturing site. As the previously reviewed additions – additional capacitance, inverter, solar power, DC/DC converter for larger energy storage elements – are supported by the DC grid layout and are more reasonable for multiple robot systems. It is an integrated solution with a possibility to become highly effective.

Drawbacks of the layout include limited use cases due to high engineering effort required for a setup, dimensioning challenges for the specific robot profiles if electrical consumption simulation data are not available during design and development phase. As the reliability risks have increased for a single supply multiple robot system, costly redundancy should be

considered when selecting and approving the central rectifier unit (increase component derating, source higher quality materials, make sure of sufficient component cooling, etc).

While there are use cases which benefit from a single supply DC grid system, majority of manufacturing sites are expected to select state of the art hardware layout with less engineering involvement, as it allows to reduce the setup time and costs, connecting the additional inverter or battery storage elements through local inverters to the factory AC grid.

3.3.3. Many Rectifiers, Many Robots, DC Link

Single high power power supply is not the only option to supply a multiple robot system. An alternative option is to establish a multiple robot DC link by connecting multiple state of the art power supplies, that could already be installed at the manufacturing site. This could avoid a complete system redesign and large investment costs. Reviewed multiple power supply layout establish a DC link between existing state of the art robot cabinets by creating a parallel connection. It is similar to previously described system layout with single rectifier with exception that rectifier of each unit remains connected (see Fig. 3.31). Layout with multiple redundant power supply units providing energy from AC grid to common DC bus is created.

As each cabinet is designed to supply a single robot, required power of two cabinet connection does not exceed the available power capacity, and addition of the new rectifier hardware is not required. The suggested DC link is a cost-effective upgrade where investments in hardware are already made, but there is a requirement for improved energy efficiency, reliability, or other reasons. Challenges of the multiple parallel rectifier system include asymmetrical balancing of rectifiers. A working prototype of multiple robots with the shared DC bus interface has been presented earlier [66].

Similar to layout with single high power rectifier, after establishing a DC link between robot cabinets the requirement for chopper resistor remains, as a upper voltage limit still exists for circuit safety purposes. External storage is still an option as well, while the capacity can be adjusted according to the new layout and manipulator movement programs. DC link enables new system capabilities - energy sharing between the cabinets avoiding storage, which is an addition to previously discussed external storage.

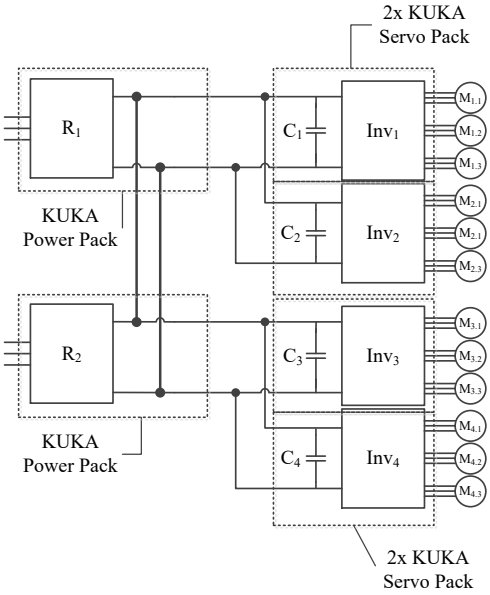

Fig. 3.31. Connection of multiple industrial robots to a shared DC bus between the existing robot power supply cabinets [57].

As mentioned before, shared DC link setup creates a connection between two or more state of the art industrial robot cabinets enabling exchange of recuperated energy during operation. DC link is connecting KUKA Power Pack rectifier KPP_1 and KPP of the second cabinet KPP_2. Inverters (KSP_n), capacitors (C_n), PMSMs (M_n), brake chopper resistances (R_{br}) with control switch (S_n) remain connected as previously. External storage (C_{Ext}) for recuperated energy with or without converter (U_{Ext}) is optional, yet recommended.

There are multiple benefits of multiple parallel rectifier layout of already existing industrial manipulator cabinets, compared to setup with single high power rectifier. Reliability of multiple rectifier setup is higher due to easier redundancy, reduced voltage ripples at output, and easier thermal management. As power is decentralized between several cabinets, components have lower current ratings [72], meaning also smaller footprint of power modules for easier handling and setup. Layout with multiple redundant rectifiers is also easier for uninterruptible power supply management and performance of active power filters [73]. See sample electrical power circuit of the DC bus interfacing module shown in Fig. 3.32.

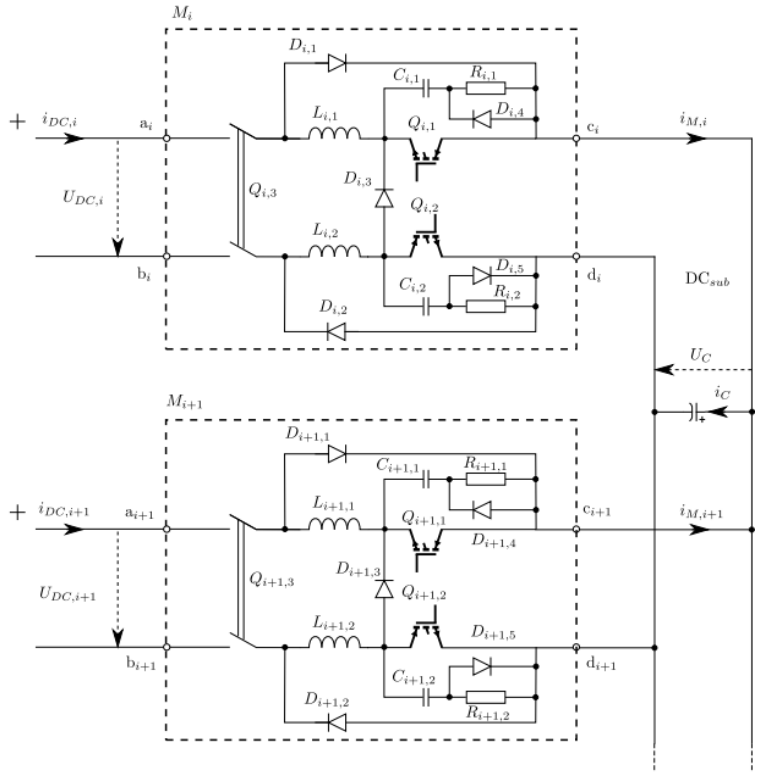

Fig. 3.32. Electrical power circuit of the DC bus interfacing module [66].

Some of the challenges for multiple redundant power supply layout include management of ground current effect [66]. High performance DC switches are required to establish and manage this DC link.

Other applications in industry with redundant high power supplies are documented at fuel cell applications [72], induction drive control [73], and used widely where high reliability is required. Daimler AG is holding a patent for both, single and parallel power supply layouts of industrial manipulator cabinets linked by DC bus [70].

Similar to previously reviewed multiple robot system with single power supply, analysis of multiple supply system lead to the same conclusions regarding energy recovery. The main factor to consider is scheduling of programs and movement, as the alignment of linked robot accelerating and deceleration cycles, as simultaneous generation rise the voltage in shared DC bus and eventually trigger the brake chopper over-voltage switch. Additional capacitor is an option to maximize the efficiency. Some of the energy is lost in efficiency of the voltage converters and interfacing hardware.

Hardware cost for the reviewed system is considered above average and the introduced equipment could be considered as an addition to the existing state of the art robot electric

cabinet. Benefit is that the interfacing enables further sharing of additional capacitance, or connection of inverter, solar panels, and that way reduce the cost of improvement per robot unit. The main drawback is the highly specific hardware that supports the interfacing between shared DC bus, and being in development the cost evaluation is difficult.

While working prototypes have been developed and confirmed in operation, a market ready hardware has not been developed, therefore an interface between DC link of multiple robot cabinets is not available without investing resources in additional research and development (for the studied KUKA system). Through the development, it may be required to reach out to robot manufacturer to enable hardware and software support for a centralized power source. As robot manufacturers create a more integrated power supply circuits, option to connect similar interfacing adapters as suggested in this layout becomes more challenging.

There are several options on how to conFig. a layout of multiple power supplies and multiple robots. Interfacing hardware may be controlled by previously defined voltage limits, either to support the exchange of generated energy (connect the DC link during energy generation), connect when a failure of other supply requires redundancy, or in other modes. While in theory multiple power supply interconnection allow redundancy, research and development process is required to, for example, reduce the ground current effect, and evaluate if the remaining supplies are able to provide the demanded amount of energy.

Reviewed layout of multiple robot multiple power supply system does not require any adjustment or dimensioning for operation of any specific robot program, as each supply is supplied by original equipment manufacturer and is designed to supply power to a single robot. From software point of view, robot movement scheduling and timing is required for the best performance and alignment of generated power peaks. If excessive energy peaks are generated with no option of direct consumption, connection of an additional capacitor is supported.

Lifetime consumption of the motor drive inverter IGBT modules during long term operation of any specific program is expected to decrease. Previous conclusion that reduction of lifetime consumption follows the reduction of brake chopper dissipated current peaks applies in this layout as well, as excessive energy is forwarded to an accelerating robot at lower voltage. Similar to one supply multi-robot system, challenge of the lifetime improvement is to arrange mission profiles accordingly. Connection of DC link interfacing hardware increases the number of components, reducing the reliability. None of the state of the art components have been removed, therefore reliability would be considered worse than the state of the art cabinet. However, if the support to redundant operation is provided, overall reliability of the robotized manufacturing system has been increased due to operation in case of failure. If supported by interfacing hardware, parallel supply and operation of the rectifiers reduce the output current of single supply through load balancing. The reviewed layouts does not provide any redundancy regarding failure of drive inverter, in case of which robot operation would be distrupted.

Failure consequence of a multiple robot system with multiple power supplies is below average. If allowed by the manufacturing process and robot cabinet layout, the remaining robot power supplies could provide power to the failed robot cabinet. Manufacturing environment

requires to analyze the process carefully, as the remaining units could have not sufficient unused power reserves through combined operation of the robots, and reducing process speed to save energy may not always be an option. Therefore additional research is required for the specific programs to utilize the redundancy feature (see Fig. 3.33), which is expected to be an issue for the fast-paced manufacturing environment.

$$R(t)_{Parallel} = 1 - [(1 - R(t)_1)(1 - R(t)_2)(1 - R(t)_3)]$$

$$R(t)_{Parallel} = 1 - \prod (1 - R(t)_i)$$

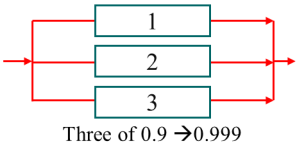

Three of 0.9 →0.999

Fig.. 3.33. Improvement of reliability through redundancy

The probability of implementation for the reviewed shared DC link layout is very low and the interfacing hardware is not expected to continue the development process to production. Upgrade is considered as an add-on for the existing state of the art hardware. The demand is supplied by requirement for a DC grid, energy efficient and reliable system layout. The main challenge is that other layout options which are readily available provide similar benefits, therefore making the presented layout challenging to implement, and a significant obstacle to implement this add-on is the previously mentioned – manufacturing sites expect a ready and complete solution with minimal engineering effort, as there is very limited time to setup and run a production line.

3.4. Start-up, Shutdown and Out of Routine Robotized System Events

Robotized manufacturing equipment integrates more applications such as additional energy storage elements or is transformed to create a micro-grid with single or multiple power sources. There are several considerations regarding operation and events of the introduced hardware and the created grids. Section 3.4 highlights some of the additional events significant to operation of the robotized system.

Startup of an industrial system with integrated DC bus is reviewed at section 3.4.1. Factors to consider during shutdown and deactivation of manufacturing equipment is reviewed at section 3.4.2. Various out of routine events are analyzed at section 3.4.3.

3.4.1. Start-up of the System

Before operation of DC microgrid in various modes is possible, power-up of the equipment is mandatory. Proportionally, much less time is spent in power-up and start-up, compared to operation, therefore it has smaller impact to overall energy efficiency of the setup. As equipment is operating in modes out of standard operation, power-up can become a reliability risk as well, if not implemented properly.

In case of industrial DC microgrid with several industrial manipulators, power and voltage rated values are high and require caution. Alignment of equipment power-up sequence has a significant role in safe initialization of the hardware. Field scenarios includes start-up after power loss, either due to grid problems or human error.

Sample industrial robot DC microgrid system as presented in Fig. 3.34. Power-up routine should begin by connection of pre-programmed and (optional) virtually commissioned control unit (PLC). Depending on system design, if logic control unit is not detected or has failed, the system should follow a logic that is not safe to power-up, and remain deactivated.

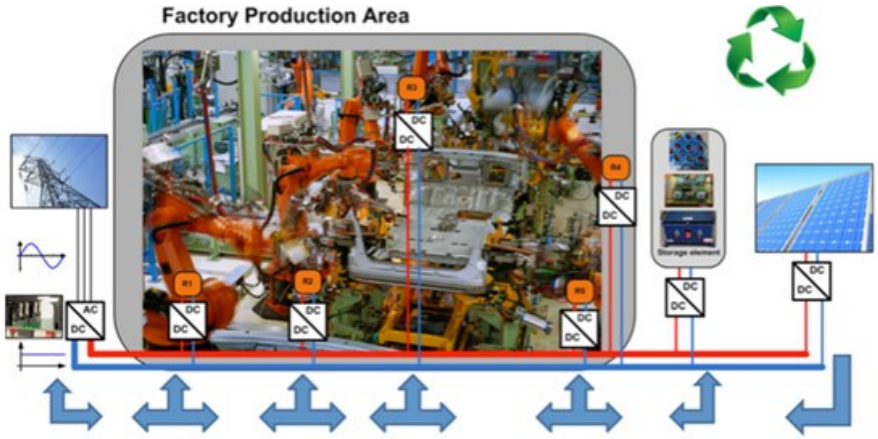

Fig.. 3.34. Field example of a centralized supply DC microgrid system with multiple robots and additional converters for backup power supply and storage [1].

Controllers within the DC microgrid are supplied either from the main DC grid (via step-down) or external 24 V power source, often supported by uninterrupted power supply, including PLC and controllers of various voltage level converters. Not only stepping down from high voltage DC bus can become complicated, often it is required for controller signals to be present before power-up of the voltage level converters, broadcasting its up status and commands to the linked devices as it is ready for operation. Controllers manage data of microgrid component statuses and may be required to boot first during system power-up. In case of main input power loss, DC microgrid may lose voltage rapidly, therefore not being reliable source for the control system power, compared to uninterruptable power supply backed up DC low voltage source.

Power-up is followed by software start-up of the system. As it is initialized, main power supply for example, active front-end rectifier, can be powered-up and started. Enabling its output, main DC link of the microgrid will be supplied with voltage. Precautions are required, due to expected current inrush peaks from charging of various capacitors connected to the common DC bus.

Connecting of possibly empty capacitor storage unit to DC bus would create a large inrush current peak, not only putting the power supply at stress, but also slightly reducing reliability

of the system. To avoid such peaks, power-on sequence should be considered, where after DC bus voltage has stabilised, soft-start mode is applied to charge the capacitors, by operating semiconductor switches with reduced PWM values. Soft-start limits the input current and is providing the initial charge of the capacitors simultaneously.

If brake chopper resistance is available within the DC microgrid, it is an option to enable it during launch of system, modulating it with PWM and using it as soft start hardware to pre-charge the capacitance of circuit [74].

Regarding other types of energy storage elements, such as batteries - they are generally considered easier to connect, as there is not the same instant inrush current as in case of capacitor. If battery storage is available, it is only recommended to not power-up simultaneously to capacitors, thus limiting the inrush current peak. After power-up, it is possible that battery will consume energy for a while, until stand-by self discharge is compensated and state returned to fully charged.

Start-up and power-up sequence of complete microgrid is recommended to be reviewed for each specific project as there may be an equipment, which requires additional start-up time for initialization, self calibration or internal start up tests. One of examples is KUKA industrial robots, which at start-up require time for safety equipment - mechanical brake tests, duration around 1 minute. Charge of the capacitor and battery is possible as a parallel process.

In case any local energy generators such as photovoltaic panels or wind generators are present at DC microgrid layout, it is recommended to connect them last, to avoid supplying yet powering-up circuit with two power sources. Several power sources might create a confusion between several operational modes and unnecessarily complicate the required control flow.

To make sure system is powered-up and initialized properly, human operator involvement in start-up and power-up procedure is an option. Through control panel operator can provide the support either as an observer, or involve with decisions and process confirmation as well.

3.4.2. Shutdown of the System

Similar as start up is a standard operation of every system, shut down is as well. Operation of manufacturing sites is often arranged to maximize output by operating in multiple shifts throughout the week and optionally scheduling shut down for weekend or holidays. While not producing any output, down time is available for any maintenance work or implementation of necessary upgrades. Regarding status of industrial DC microgrid or any other equipment during this time, it is recommended to shut down as many as reasonably possible, to avoid losses of electrical energy and reduce the impact on reliability as remaining lifetime reduction.

One of risk factors during and after shutdown is remaining charge within energy storage hardware components such as filtering capacitors and batteries. After input power disconnection, system requires a decision either to keep charge in storage elements or discharge the hazardous voltage for safety of maintenance employees. There are few reasons to keep the charge within filtering capacitors, while other electrical energy storage elements such as

supercapacitors or batteries might remain charged even through shut down, to not only to avoid decrease of charging cycles, but due to larger capacity it is more expensive to completely discharge them through the shut downs. They can be disconnected from DC grid, to avoid supply of power to other circuits.

During development phase shut down sequence should be decided. Process is usually managed by PLC through the implemented network of data transfer and communication. Regarding the sequence, various shut down scenarios are available depending on connected hardware.

A standard disconnection begins by completing the current movement profile or program, if any is still being executed. Input power supplies, any external energy storage or generation units are disconnected firstly. Other industrial hardware is safely disconnected after the voltage in DC bus is decreased, as disconnecting is started with generators and finished with loads.

At the moment of system shutdown common DC bus voltage is ranging from 300 V to 600 V, depending on system design. Along with the DC bus, voltage filtering capacitors are charged to this voltage as well, therefore circuit to discharge this bus and capacitors is required. Brake chopper resistance is an option to discharge the remaining charge of DC bus (see Fig. 3.35), however, converters of any external energy storage elements should be disconnected or powered off, or they might mistake the resistance of brake chopper as load.

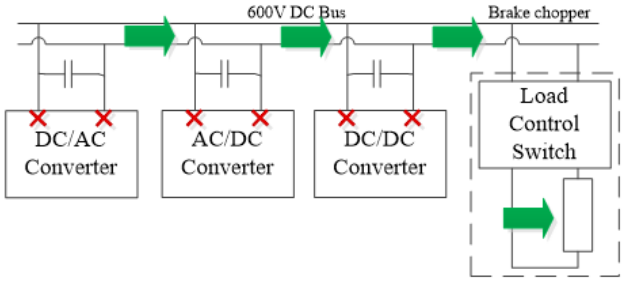

Fig. 3.35. Discharge of filtering capacitors through a connected brake chopper resistance.

To reduce risks of equipment damage and high DC voltage arcing, it is recommended to introduce semiconductor switch in series with mechanical relay to break the electrical circuit with semiconductor first, followed by disconnection of mechanical terminals within relay, to create galvanic isolation of DC grid and voltage source.

3.4.3. Out of Routine Events

At manufacturing there is a probability of various unscheduled out of routine events to happen during the manufacturing cycle. Opposite to the scheduled cycle, which is formed of very well known variables as processed parts, industrial robots executing programs, storage elements smoothing the power consumption, unscheduled events such as accidents, break down

of equipment are predicted. These events may include loose network connector corrupting the data, human entering manufacturing cell, and others.

It is common in manufacturing hardware to implement data bit for control synchronisation and acknowledgement, also called as “live bit”, indicating that PLC is operational and monitoring the system. Sample out of routine event is loss of the central control unit (disappearance of control signal) within previously presented DC microgrid system with several energy storage units, multiple industrial robots and other hardware. As PLC control is lost, equipment of the system should be able to either continue operation, complete cycle or enter safe stand by mode.

Possible hardware malfunction include either open-circuit or short-circuit failure for one of many DC microgrid components. If some of less critical system components fail open-circuit, there is a probability that operation of the system may still be effective. Short-circuit can create new current loops and pull down power supplies of various integrated microchips (IC), having critical effect on system performance.

As short-circuit event may cause damage due to over current, malfunction event should be recognized and actions should follow protecting the still operating hardware from further damage. Often choosing controllers with implemented overcurrent protection may help to avoid damage of other components, as failed controller may forward its input voltage to output.

There are several scenarios which may trigger emergency stop. Standard case is triggering emergency stop by push button near manufacturing cell. Industrial robot cells often are equipped with virtual safety wall, which trigger emergency stop event when something has entered the cell during robot operation. In some cases event may be triggered after critical error is detected somewhere within system. Signal is input at PLC which follows emergency stop routine.

During casual and scheduled shutdown equipment completes its operation, parts are processed and robot is stopped after program is completed after returning to home position. Emergency stop usually has an objective to stop manufacturing processes as fast as possible, therefore other conditions regarding robot position and equipment status after stop may apply.

Average stopping time and maximal energy generated during an emergency stop is defined by parameters of the robot and its hardware power electronics components. For example, a KUKA industrial robot would come to a standstill in an approximately 1 second, generating 97.2 kJ [63].

Multiple robots of industrial manufacturing cell could be connected to the same DC bus. In case of emergency situation in cell, all of the operational robots would supply recuperation energy to common DC bus, creating a significant peak current to dissipate at brake chopper or accumulate within energy storage elements.

While safety curtain or push button triggered emergency stop may require further operation of robots and cell equipment with manual override, for example, to open access for help to injured, in case of emergency situation triggered by electronics hardware fault, shutdown may be required according to previously described routines.

Similar to standard operation programs, it is an option to model emergency stop scenarios with system parameters such as movement speed, tool and part weight within virtual commissioning software (VCS). Mathematical model of industrial robot energy consumption throughout execution of KUKA robot language code and integration in VCS is reviewed later throughout this work.

3.5. Operation Models

Integration of programmable logic controllers enable equipment designers to adjust operation of hardware elements according to the specific needs and operation requirements. Various operation modes have been reviewed during this study with the analysis being presented in section 3.5.

Basic overview of standard operation mode of DC micro-grid is reviewed in section 3.5.1. Operation principles of energy balancing model are discussed in section 3.5.2. Power infeed dimensioning requirements are presented in section 3.5.3., while section 3.5.4. includes a review of islanding control method. Section 3.5.5. presents an application example of robotized manufacturing hardware stand-by mode.

3.5.1. Standard Operation Mode of DC Microgrid

Managing charge of capacitor according to the maximal voltage of the common DC bus (see Fig. 3.36) is one of the most common operating modes. Voltage within DC bus and charge of capacitor is controlled by brake chopper resistance and switch. PLC controls and coordinates operation between various system elements, including industrial robots, brake chopper, storage unit, others. During recuperation, increasing voltage is monitored by measurement unit and reported to controller, which either switches the external capacitor for storage, or activates brake chopper if voltage rises too high or capacitor is fully charged.

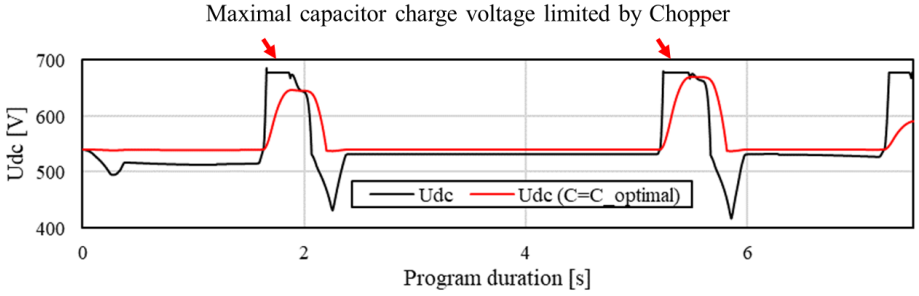

Fig. 3.36. Managing charge of capacitor according to the voltage of common DC bus

Charge management by maximal voltage of DC bus is considered rather basic control method, not requiring complex control flow, but the delivered efficiency improvement is

significant. Some of the challenges which remain within applications of this control method include primary power supply current peaks due to acceleration of industrial manipulator motors, and current peaks from tools, including welding, clinching.

3.5.2. Energy Balancing Model

When developing control method for industrial robot system, dynamic characteristics of the system should be considered. Movement of industrial robot can change rapidly from acceleration to deceleration, and together with integration of various industrial tools create a dynamic system. Sample KUKA industrial robot peak power consumption can reach 20 kW, and sample welding tool reach up to 10 kW peak values in milliseconds. Link of multiple industrial manipulators to same DC link or AC input increase the combined power consumption peak value.

Normally similar power consumption peak values put stress on the AC grid through the rectifier, while energy balancing mode is attempting to eliminate the power peak, or at least reduce it greatly. Energy balancing control method balance electrical energy in DC bus by consumed power mean value P_{average}, according to Eq. (3.1), where P_{bal} is balancing power, requiring either charge or discharge of the storage, and P_{tot} is the combined instantaneous power consumption of connected hardware.

$$P_{\text{bal}}(t) = P_{\text{average}} - P_{\text{tot}}(t) \tag{3.1}$$

As long as the subtraction of power consumption mean value Paverage and Ptot the combined instantaneous power consumption of connected hardware is negative, power is consumed from the balancing dedicated storage elements in an attempt to reduce from AC supply required power value. If the instantaneous power consumption value is below average - storage elements are charged, as shown in Fig. 3.37.

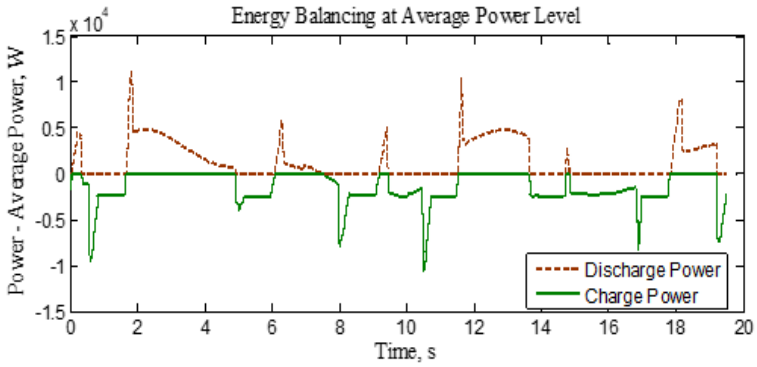

Fig. 3.37. DC microgrid energy balancing mode and power charge of storage elements.

Simulation confirmation of energy balancing controls system has been developed in MATLAB environment [75]. Model supports multi-robot, multi-storage simulation providing

from active front-end rectifier supplied power values of the system (see Fig. 3.38). As with other common DC bus systems, integration of local energy generation sources such as photovoltaic panels is possible, but the effect on performance of energy balancing system is relatively small, providing slight decrease of $P_{average}$ value.

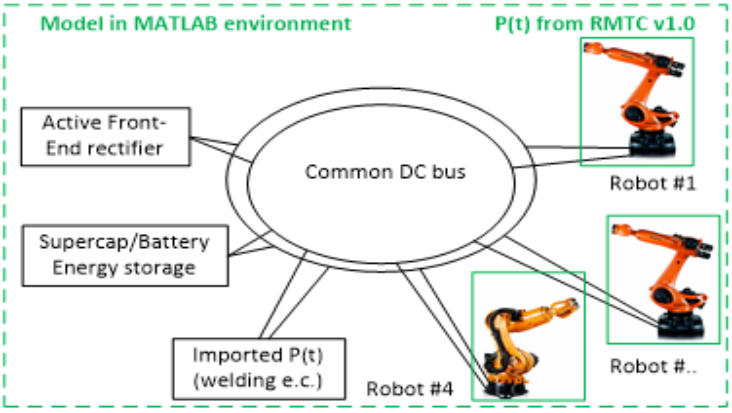

Fig. 3.38. MATLAB model of multiple robot connection to a shared DC bus supplied through single power source.

Integration of multiple robots to common DC bus system in simulation environment is an exciting improvement of previous models, as it provides information about load impact on AC voltage quality. Drawback of the reviewed model is not being able to model various trajectories of industrial manipulators, as it would provide possibility to easily schedule robots and movements in order to manipulate with combined power consumption profile. Currently, trajectories to the model are provided by utilization of model reviewed earlier in Section 2.

As mentioned earlier at analysis of various hardware layout options, DC microgrid with either single or multiple power supplies is modifiable to great extent. Industrial DC microgrid layouts can include various number and wide variety of industrial manipulators, as well as industrial tools. Robot programs depend on requirements of manufacturing process, therefore speed and rate of acceleration or deceleration may vary.

Due to high development and testing costs, hardware is more often developed modular and designed for wider use than for single, unique setup or application. Storage elements of DC microgrid are rather easy to install and integrate within the system. Some of available storage solutions include supercapacitors, various batteries, even flywheels and fuel cells. More dynamic cells will benefit more from storage than cells with less dynamic operating robots.

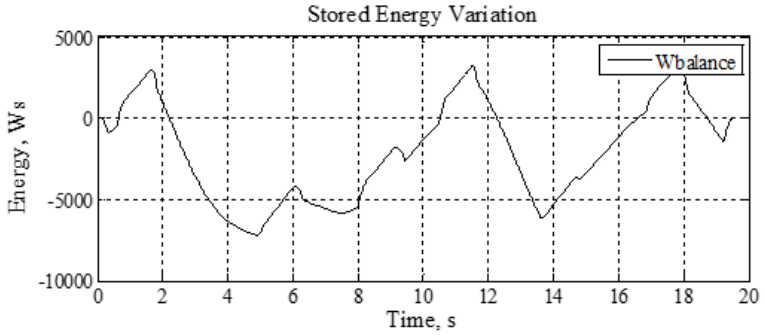

Fig. 3.39. Charge of energy storage elements operating in balancing (peak-shaving) mode.

As the energy variation throughout the time is known from the model, not considering energy efficiency losses, charge at the beginning of cycle should equal charge at the end of production cycle (see Fig. 3.39). If energy is decreasing within the plot, it is being consumed from storage, if it is increasing, the energy is being stored.

Input of capacitor energy balancing method is the power consumption before rectifier throughout the program time. Average value of power consumption P_{avg} with mean function, and power balance value P_{bal} is calculated as subtraction of instantaneous power consumption from average value. (as shown in Eq. (3.1)). Integral of balancing power values throughout time reveals energy flow throughout the process time, as shown in Fig. 3.40.

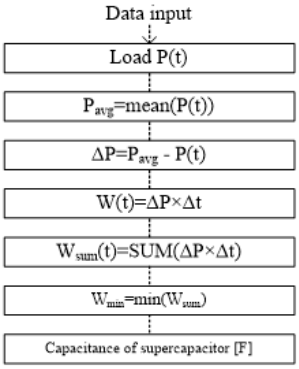

Fig. 3.40. Process flow to compute required storage capacity for energy balancing, for example, capacitance of supercapacitor.

In order to store the available energy in capacitor storage unit, having determined the largest value of energy required to be stored, capacitance of capacitor can be determined according to Eq. (3.2). C being the value of connected capacitance to store the energy peaks, W_{min} - largest of energy peaks required to be supplied by storage, U_2 is the value of highest allowed voltage and U_1 - value of lowest discharge voltage.

$$W = \frac{1}{2} C U^2 \rightarrow C = \frac{2W_{\min}}{U_2^2 - U_1^2} \tag{3.2}$$

Simulated sample movement takes 20 seconds to complete and balancing storage is required to store 7242 J. With 50 V operating range at 500 V to 550 V, a 0.2758 F capacitance will be sufficient to store the energy.

Power balancing method can help to provide the value of required storage for DC microgrid setup with several industrial robots performing different manufacturing tasks. Challenge is connecting other industrial tools to the common DC bus, as tool instantaneous power consumption may even exceed that of the robots. It is possible, that industrial spot welding tool would consume the balancing storage empty after single spot.

3.5.3. Infeed Power Dimensioning

Industrial power electronics converters are designed according to maximum power consumption requirements of the system. With a combination of multiple equipment units in a single system such approach may prove resource wasteful. For example, when combining multiple DC supplied industrial robots, main rectifier unit is designed to supply the combined maximum power consumption of all robots, even when such peak current is very unlikely due to scheduling challenges. It must be considered when designing the system power supply to avoid over-dimensioning.

Efficiency graphs of common converter topologies reveal that efficiency is not equal through the wide range from zero to rated output power. Installing high power converter in a system where average power consumption is far below the nominal power, increase power conversion efficiency challenges are expected. With the increased power rating of the supply standby power losses increase as well.

Power consumption of an industrial work cell can be predicted in both virtual commissioning software and by technical documentation. Energy consumption in production environment is cyclic and repetitive and with an access to either measured or simulated consumption data of the system, therefore assumptions regarding converter parameters can be made.

Histograms of system repetitive cycle power consumption data were created for a single robot (see Fig. 3.41 (a)) and multiple robot layout (see Fig. 3.41 (b)). There are few things to consider regarding histogram data plotting, and when using this method for converter dimensioning. For example, multiple welding points with duration 150 ms in this graph will be multiplied by number of event occurrences and total duration of 1.50 s will be displayed. A sample converter would be able to handle multiple 150 ms overload events, but one 1.50 s load would result in equipment damage. Same principle applies to high industrial robot electrical loads as well.

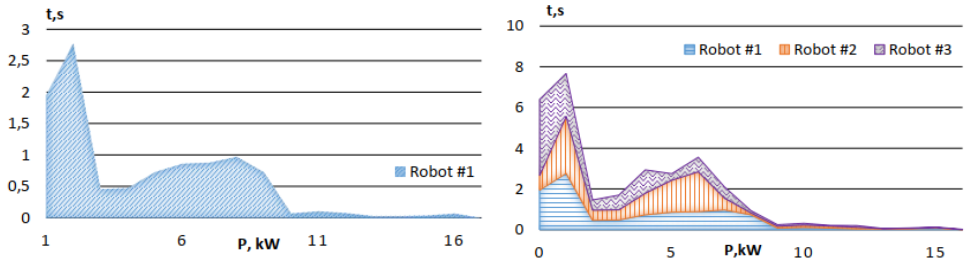

a) b)

Fig. 3.41. Power analysis results of a) single industrial robot program, b) 3 industrial robots with various programs of an industrial cycle.

One of repetitive load power consumption profile data analysis methods to estimate the infeed power rectifier uses previously recorded data from the industrial system. Parallel analysis workflow is shown in Fig. 3.42. Each electrical energy consumer is measured separated from the system and analyzed individually. Values of the power consumption data table of the equipment are then grouped according occurring frequency.

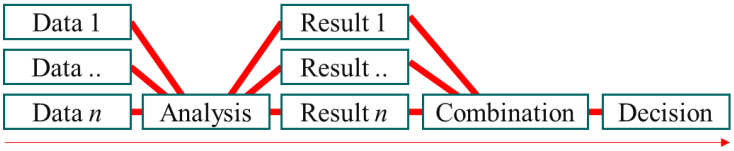

Fig. 3.42. Parallel power consumption profile data analysis [76].

For example, if all industrial robots spend most of time in standby mode, power consumption peak at standby power will be dominant. Parallel method reveals how often maximum power consumption values are reached and approximately how long the system and converter should be able to provide this amount of energy, as shown earlier in Fig. 3.43. Visualization reveals that energy consumption values during most of the sample cycle are at standby load. Power consumption value peak is around 50 % load of the system, revealing that high power converter for each consumer is required, but higher loads occur a lot less often.

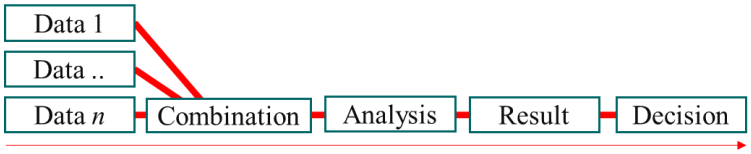

Fig. 3.43. Analysis of combined power consumption profile data [76].

Before analysis of the combined power consumption data, individual system consumers are combined in a data array, which is analyzed as previously described – visualizing frequencies

of all power consumption values of the data, as shown in Fig. 3.44. Similar to individual graphs, in case of industrial robot system, stand-by power is the most common value in data, followed by peak at around 30 % of unit rated load.

Fig. 3.44. Combined power consumption profile data with combined rated power.

In the presented example each load is rated at 20 kW and therefore combined converter rated power value is 60 kW. If robot acceleration peaks do not align, power converter is over-dimensioned and operating between 3.3 % and 10 % of the rated load. Current industrial converters for combined systems are designed assuming that there is a possibility that all loads will require rated load at the same moment. That is the main reason is 60 kW supply was selected in [1]. Practical research and modeling reveals that probability of reaching this consumption is unlikely.

Other peak current values, for example, created by welding equipment, even though with high power, last few milliseconds. Adjusting the main converter efficiency rate for such electrical loads is not cost effective. Some converters allow short lasting overload pikes without equipment damage. Capacitor should be considered, to protect the converter from damage during such demanding load. It is possible to reduce the converter maximal parameters, if during high load condition converter is supported by energy storage unit and the case study power consumption profile analysis approve that most of time converter operate with stand-by or load below 10 %.

3.5.4. Islanding Control Method of DC Bus

There have been several power loss incidents reported from major manufacturing plants worldwide, such as Volkswagen, Toshiba, others [77], [78]. While not very common, power outage can become a cause for severe financial losses, both from production down time and damaged materials.

Loss of input power can be measured and detected locally at the DC grid, therefore it is reasonable to introduce a mode to avoid damaging production materials, completing the

production cycle. By utilization of connected energy storage elements, this mode should provide the required energy to deliver system to a safe stop in case of input power loss.

Required capacitance of storage elements supporting the islanding mode are directly dependent on setup and application, considering number of robots, movement profiles and also power outage timing. If outage coincides with beginning of cell process, large amount of stored electricity will be required to complete the started process. Therefore it is reasonable to consider either large capacity power storage battery units, or design a safe return to home function which is triggered at the power outage, stopping robot and attempting to save the involved materials.

The same industrial robot movement program discussed at average power balancing method was simulated, to estimate capacitor size to supply the robot movement throughout the execution of the sample program. Through the duration of 20 seconds, an average power of 2.6 kW or 51.5 kJ is consumed (see Fig. 3.45 (a)), leading to a capacitor with 1.963 F capacitance (50 V operating range, from 500 V to 550 V), which is sufficient to supply the robot to complete its operation entirely without input power supply.

Some decelerations of robot motors throughout the profile recharge the capacitor (see Fig. 3-45 (b)), but the generated amount of electricity is not enough to dramatically reduce the size of required storage.

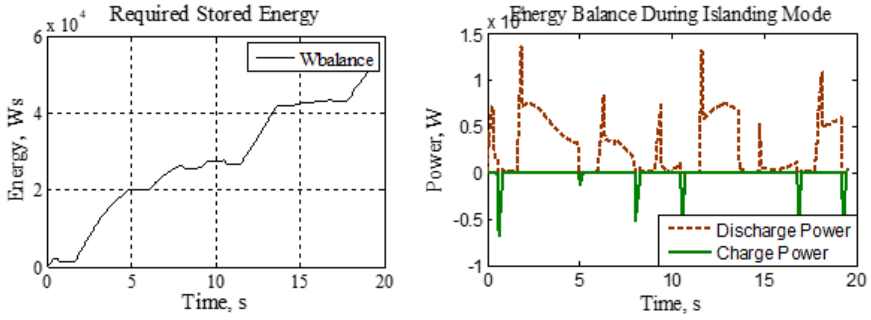

Fig. 3.45. Islanding mode operation– required energy (a) and consumed power (b).

To compare scenario of completing the program with returning to default home position, a sample movement was programmed. Trying to simulate largest required return energy, axis motors of industrial were rotated near the software limits (see Fig. 3.46 (a)). By altering home position away from default, adding heavy industrial tool or payload to robot, the power consumption of robot motors will be increased, therefore even more energy will be required to return it to home position safely.

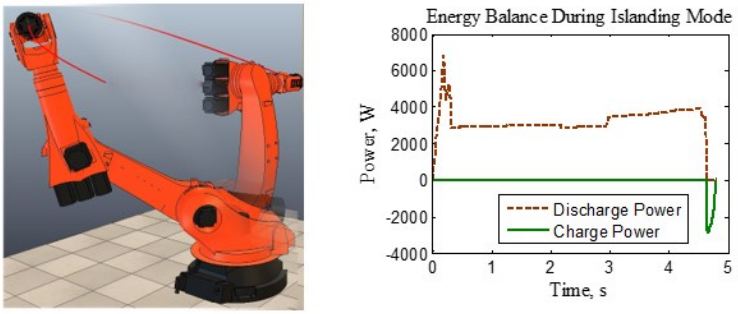

Fig. 3.46. Visualization of industrial robot returning to home position from the highest power consumption position for all axes (a) and a plot of required power from energy storage elements during this movement (b).

In the simulated movement energy of 15189 J was consumed, resulting in a 0.5789 F capacitor with 50 V operating range (500 V to 550 V). During this movement PMSM of industrial robot with highest weight load is rotated by 184 degrees, increasing value of the required energy, as shown in Fig. 3.46 (b). As home position can be altered, it can further exceed this value as well, reaching an unlikely maximum of 368 degree rotation.

As returning to home position consumes less energy than completing the production process of cell, it is more reasonable to use capacitor storage for return to home position in case of input power loss, from energy storage point of view, as capacitor with larger capacitance is more expensive. If the processed part is expensive, other storage solutions to supply production even in case of power loss are available apart from capacitors, such as battery storage, but in general they are considered more expensive than capacitor storage.

3.5.5. Utilization of Stand-By Mode

According to previous research and data of automotive manufacturers (see Fig. 3.47), instead of executing the programmed movement profile, a lot more often industrial robots are not moving at all. This also affects the energy consumption characteristics, as proportions of losses change if compared standstill to an operation, for example, brake chopper resistance is not normally connected during standstill. Analysis of about 10 thousand industrial robots from automotive production sites owned by Daimler AG, revealed that 81.1 % of year robot is not moving, compared to 18.9 % executing the programmed movement [61].

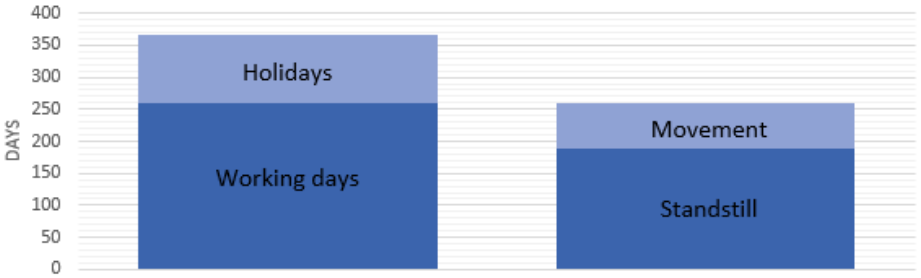

Fig. 3.47. Robot load during one year of production [61].

During standstill of industrial robot, it either has mechanical brakes open or closed. If the brakes are open, robot is able to move and standstill is managed by holding the electrical motors in one position. During this time, electrical energy is being consumed by motors. Standby electrical power consumption of KUKA industrial robot cabinet $P_{standby}$ is about 650 W. Closing the mechanical brakes transfers the load of holding robot still from electrical drive to mechanical brakes, allowing to power down the motors and reducing the power consumption. Reduced consumption, with mechanical brakes closed, is $P_{cabinet}$, which is about 275 W [61].

Attempt to transfer the electrical power consumption of standstill to financial losses, reveal about 200 € costs per one robot within 1 year. With mechanical brakes closed, 6600 Wh are consumed by the robot control cabinet during 1 day, resulting in 1.7 MWh of not efficiently used electric energy within 1 year. If these costs are multiplied according to number of robots mentioned earlier, it is clear that even slight improvement of standstill efficiency deliver great overall improvement.

If industrial DC microgrid system is reviewed, integration of additional energy generators is a considerable option to reduce the total power consumption. Photovoltaic panels, wind generators, these are some of the available options for supply of electric energy to compensate for efficiency losses when the industrial robot is not operated.

Setup of panels installed at Riga Technical University currently can supply 300 W electric power from 1 panel, therefore even a single panel can if not completely solve the cabinet power consumption problem, then at least reduce the financial impact of it. However, during analysis of the setup, it should be noted that photovoltaic panels are generators only during daylight. Wind powered generators can compensate through the night time as well.

By integrating alternative energy sources within industrial DC microgrid of industrial robot cells various operating modes become available on how to manage generated energy both, when the cells are operational and during stand still as well. These modes include exchange of energy from not operating production cells to others at operation within the same site.

Other generation operating mode is when not only some of the cells are shut down, but the entire site is not producing. Such situations are common during events as holidays. If static electrical load of factory grid such as robot cabinets is not consuming, generated energy of

photovoltaic panels becomes available. If production site has installed 400 panels, this could be about 120 kW available for management.

Energy can be returned to AC grid if it is supported by on site existing hardware (active front-end rectifiers), however the challenge of supply good quality AC voltage and current remains. To make management of this energy flow easier, separation of focused generated energy between AC network and local DC grid is an option. AC side rectifier is not required for such grid of photovoltaic panels, therefore single purpose inverter with good quality parameters is a reasonable choice.

During normal workday operation of production site, static electrical load of industrial hardware should be able to consume the generated electricity. If generated power exceeds this load, then other options such as site lightning and other building equipment can be supplied from local generators.

3.6. Control System Types

Upgrading layout of hardware within cabinet of industrial manipulator by itself does not deliver energy efficiency improvement, as software which support the operation of hardware is required. After connecting multiple industrial robots to create DC microgrid or addition of external storage capacitor, well-thought out control methods and operation algorithms throughout all operation modes provide the reliability and efficiency required.

Several control organization methods are available, being categorized by level of decision making centralization. Either the main programmable logic controller (PLC) is responsible for system operation, or voltage level converters of DC microgrid can operate central controller independent. It is also possible to develop a hybrid setup, separating control between main PLC and converter.

Various control modes should be considered, such as the most common - normal operation mode, power-averaging operation mode, emergency stop operation mode, start-up operation mode others.

With single unit control input data, controller manages this data from sensors and applications individually, monitoring the cell status and following its operation, as current industrial robot system contains a DC bus as well. Addition of multiple industrial robot units and various energy storage units to the common DC bus system requires well thought out system control and management process. These added system elements not only introduce new input data to central unit, but can require modification of operation flow within system in various scenarios, requiring monitoring of performance and operational status. Efficient data link between the connected system components has a significant role to of DC grid management.

Several control methods are suggested and analyzed (see Table 3.4) such as centralized, decentralized, hybrid.

Table 3.4

Various System Decision and Control Sources

Operation	Decentralized	Centralized	Hybrid #1	Hybrid #2
Emergency Disconnection	MCU	PLC	MCU	MCU
Energy flow direction control	MCU	PLC	PLC/MCU	PLC/MCU
...	...	...	...	..

Decentralized control systems of the connected equipment are reviewed in section 3.6.1., while centralized control methods are reviewed in section 3.6.2. Hybrid control method with elements from both, centralized and decentralized control is reviewed in section 3.6.3.

3.6.1. Decentralized control system of converters

Units of decentralized control system require either little or even not any external data or control to operate, as shown in Fig. 3.48. Typical examples of decentralized control are controllers of switching voltage level converters, which often support just 1 external input for "enable" signal, and by feedback controlled output voltage does not depend on input voltage directly. With larger and more sophisticated systems, this sample "enable" command could be provided by PLC. Advantages of decentralized system include efficient control developed by manufacturer and good response time to input or output parameter change. In some cases, commands may be executed faster, as controller is directly next to switching hardware without network adapters which support the communication between PLC and system elements. Limitations of the decentralized control include lack of customization and limited possibilities as more complex systems often require extended control such as output adjustment by voltage data feedback from consumer and dynamic current control.

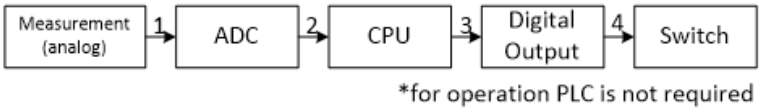

Fig. 3.48. Decentralized operation and decision control.

3.6.2. Centralized control system of converters

Units of centralized control system depend on extensive communication with central processing unit (CPU), PLC or other external control unit, as shown in Fig. 3.49. in an example from industrial manufacturing environment. Examples of centralized control devices include power circuit switches, often being able to measure DC bus voltage, provide the measured value to external controller and depend on its returned commands, either to change state of switch or not. External control can detect both, undervoltage or overvoltage and decide to protect circuit by opening switch. Other examples may include providing PWM values for control of metal-

oxide-semiconductor field-effect transistors of LED lightning, or other hardware, from external source.

Advantages of centralized control system include high integration ability, depending on hardware characteristics and design requirements. Previously mentioned voltage switch may be used in various circuits, with various operation timing and level requirements, as operation of switch is triggered externally.

Limitations include increased response time, as network adapters and communication supporting hardware is introduced with additional delays. This delay can become significant in various unexpected and unscheduled events, where early detection and disconnection of hazardous voltage values could save the connected equipment. Centralized control equipment will report the measured value to main controller, which process the data and evaluate the situation and decide accordingly, returning output data from PLC to hardware being operated possibly at dangerous voltage levels.

Exchange of data between industrial hardware through AnyBus module and Profinet, might require additional 20ms, not including the data processing time at both sides, this time being the drawback of centralized decision making.

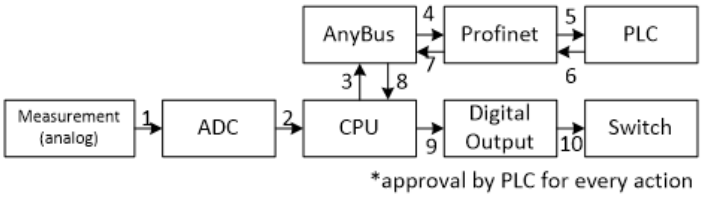

Fig. 3.49. Centralized operation and decision control synchronized with main PLC.

3.6.3. Hybrid control system of converters

As hardware units become more complex, a hybrid control system helps to solve the communication drawback for time sensitive commands, while providing the external control customization benefits. One of many hybrid control examples is QCA6410 MAC/PHY Transceiver (see Fig. 3.50), to some extent it is able to operate external control independent, as it has its own memory controller and CPU.

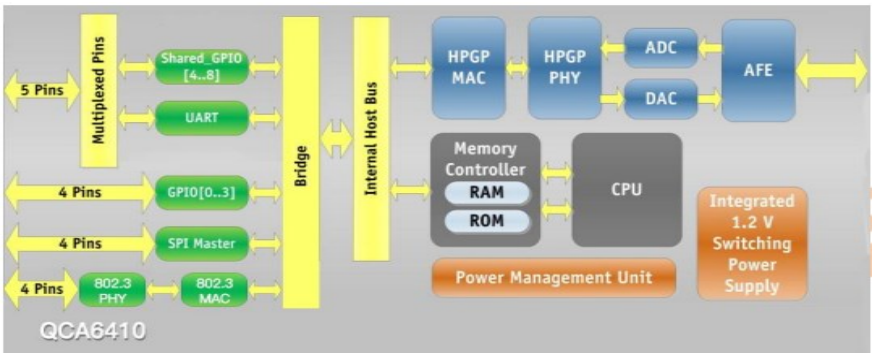

Fig. 3.50. Hybrid operation example of local control hardware [79].

Further integration of QCA6410 within other hardware is advised and supported through available communication interfaces, creating products such as MikroTik PL6411-2nD (see Fig. 3.51).

Example from power electronics field is a power switch with embedded measurement and data processing capabilities. Hybrid control system is able to take action and change state of output depending on measured input data, protecting the hardware from damage or undesired scenarios. Switch is able to handle critical situations and override input commands, yet rely on these external source commands during standard operation.

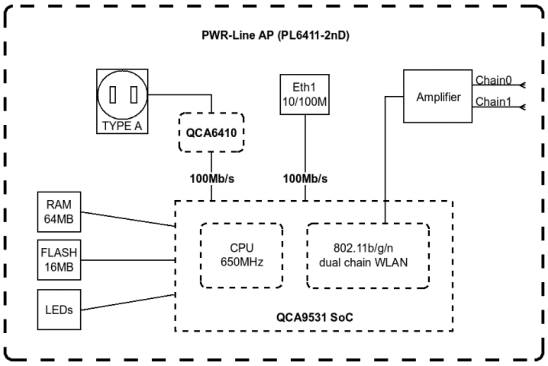

Fig. 3.51. Hybrid operation and decision control with optional synchronization through ethernet link throgh power line communication [80].

In other scenarios automatic execution of default programmed operating mode is possible, until override signal from external control is received. It could change PWM values depending if they are from internal source, or external, allowing option for remote control if required, yet being able to operate without external control.

3.7. Comparison of Layouts and Conclusions

Robotized manufacturing power supply topologies have been reviewed from through sections 3.1 to 3.7. Regenerated energy, failure probability and consequence of failure have been compared, including systems of both, single and multiple robot layouts. Single robot systems include state of the art layout, layout with added storage elements, and a layout with inverter to AC grid. Multiple robot systems with single or multiple power sources have been included in the study.

Table 3.5

Comparison of industrial manipulator hardware layout type by several parameters, with suggested ranking and substantion

Indust. manipulator HW layout type	Rank	Comparison parameter, ranking and comment
Efficiency of regenerated energy re-use		
State of the art w/ brake chopper	5	High amount dissipated at chopper, some stored internally
State of the art w/ external capacitor	2	Energy storage size limitation, leftover is dissipated
Bidirectional AC/DC converter	1	AC grid is capable to accept all regenerated energy
DC link w/ centralized rectifier	3 / 4	Higly depends on robot scheduling
DC link w/ redundant rectifiers	3 / 4	Higly depends on robot scheduling
Cost of purchase & install		
State of the art w/ brake chopper	1	Available from robot manufactuers, no additional costs
State of the art w/ external capacitor	2	Add-on to state of the art, DC/DC converter is optional, not directly available, more development is involved
Bidirectional AC/DC converter	4	Expensive per robot, enables further grid add-ons
DC link w/ centralized rectifier	3	High peak power of the central rectifier is a challenge
DC link w/ redundant rectifiers	5	Not available in market, requires development
Probability of failure and consequence		
State of the art w/ brake chopper	4	Average, lifetime depends on robot program type
State of the art w/ external capacitor	1	Less lifetime damage, introduced capacitor failure mode
Bidirectional AC/DC converter	2	Less lifetime damage, introduced inverter failure mode
DC link w/ centralized rectifier	5	Single rectifier is a risk, lifetime depends on scheduling
DC link w/ redundant rectifiers	3	Power source redundancy, introduced interfacing hardware failure modes, lifetime depends on scheduling
Average score − probability of implementation		
State of the art w/ brake chopper	3	3.33 − available, cost effective, but not efficient
State of the art w/ external capacitor	1	1.66 − available, more expensive, more efficient
Bidirectional AC/DC converter	2	2.33 − questionable cost efficiency and practicallity
DC link w/ centralized rectifier	4/5	3.83 − rectifier is dimensioning & reliability challenge
DC link w/ redundant rectifiers	4/5	3.83 − still in development, therefore expensive

Detailed comments and analysis of the discussed layouts are included in the relevant sections. More concise conclusions with a short comment and comparitive relative rank rating for some of the key areas is shown in Table 3.5. Probability of implementation is rated as a general conclusion for single and multiple robot systems.

State of the art single robot system is the most commonly installed layout, as it is provided by manufacturer. If energy efficiency improvements are required and demanded, single robot state of the art system with a capacitor upgrade, simulated for the specific robot program, has the highest probability of implementation. It has been confirmed through this study that capacitor reduces lifetime consumption of the robot drive hardware through industrial operation cycles. Lifetime of the introduced capacitor must be considered. Multiple robot systems linked with DC bus have higher initial development costs and benefits are robot program dependent. Some of the required hardware (interfacing hardware between existing robot DC links) has not been transferred from research to production environment.

4. DEVELOPMENT AND TESTING OF ROBOT HARDWARE

In the electronics industry, reliability is a characteristic of electronic system or a device, defined commonly as “the probability that a piece of equipment operate under specified conditions shall perform satisfactorily for a given period of time”, with a numerical value between 0 and 1, predicting whether item is able to operate for the required time period. It is a time function of frequency of equipment failures. Specific failures can be forecast rarely, therefore it contains a lot of engineering uncertainty. One of reliability engineering objectives is to apply various methods in order estimate reliability of designs and analyze reliability data, which is the focus of this work.

Assessment of power electronics product service life characteristics and the role of reliability testing is investigated, reviewing the main principles of accelerated life tests, stress screening, practical testing and defects. Discussion about reliable assembly of power electronics hardware is continued by analysis of failure modes and defects detected during practical application of various electrical, mechanical or thermal stress. Benefits of stress testing integration in development and production process are evaluated.

Outline of the reliability in product development, testing and production environment is reviewed in section 4.1. Section 4.2. introduces a more detailed view of design for reliability principles in product development environment. Various stress testing methods and causes of defects are analyzed in section 4.3. Section 4.3 of this study reviews principles of a reliability-oriented control of final product assembly. Burn-in principles and practical considerations, including lifetime consumption simulations with the developed extension are reviewed in Section 4.4.

4.1. Program for Development and Manufacturing

While development cost increase rapidly with more engineering effort to increase reliability, cost of replacement parts, maintenance staff and spare equipment decrease (see Fig. 4.1). From end-user point of view, equipment with the least total life cost is desired, therefore reliable equipment increase the lifetime, decreasing the total cost, up to a point where further increase of item reliability is with no economic benefit. There is a demand for methods and techniques for design of more reliable systems from existing components [81].

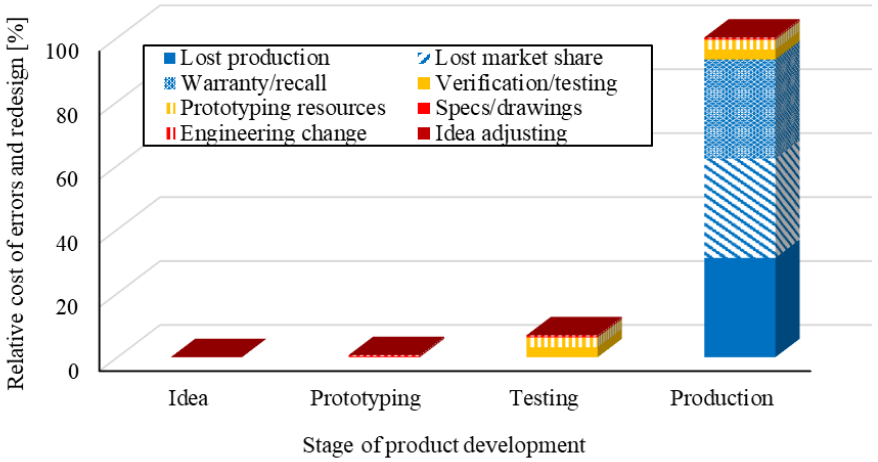

Fig. 4.1. Visualization of costs due to reliability and engineering errors at various discovery stages [82].

The consequences of underestimating importance of reliability can be dramatic. In the worst scenario, unreliable products can mean loss of market share, resource demanding recalls and warranty repairs, lost or scrapped production materials, wasted verification and testing time, as well as prototyping materials, engineering effort and idea phase.

During the development and production process, engineering team must guarantee electrical performance by choosing components, materials, boundary limits and geometry. Also, electromagnetic compatibility and power losses must be accounted. During initial and advanced testing temperature characteristics and first reliability tests, related to mechanical stress, damage and life assessment are made. Related PCBA failure mechanisms (solder fatigue, component wear e.g.) must be evaluated as well early in the development, due to significant increase in losses if reliability error is discovered late.

Transition to production stage requires implementation of engineering solutions, reducing manufacturing dimension and material quality deviations. Continuous audits of component suppliers and PCBA manufacturers are required, to guarantee their quality management system performance and reduce risks of mass production errors. Postproduction service is required to monitor product life, customer complaints and repair quantities, especially significant during the first production batches, helping to discover deviations and errors ahead of the next productions. Some of the expected failure categories are illustrated in Fig. 4.2.

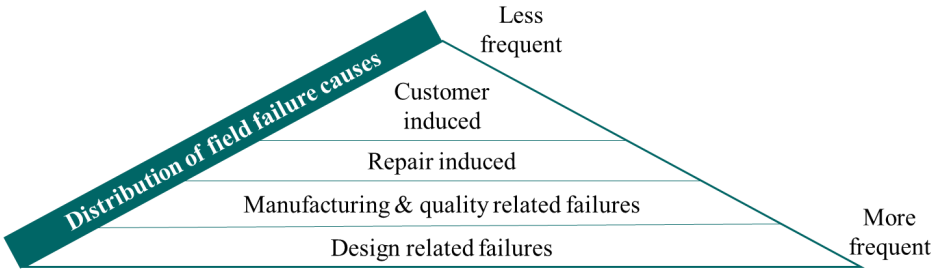

Fig. 4.2. Generalized structure of field failures for electronics applications.

This study introduces the significance of Design for Reliability topic. During the development, testing, manufacturing and even after sales design for reliability provides guidelines for high quality products and increased product lifetime. It can prove to be very time and resource demanding to complete all the required tasks and procedures, required for reducing reliability risks, however, critical errors and reliability issues can prove to be even more expensive. Implementation of design for reliability principles often requires sophisticated equipment and wide knowledge of electronics components, materials and manufacturing techniques.

Complex systems are expected to have complex failure mechanisms, including multiple failure modes which can be simulated. Thermal fatigue is very common, leading to fatigue of solder joints and plated through holes. Boards must be kept clean of contamination and moisture. Field failures are unavoidable and must be taken into product life considerations. Cost of unreliability must be assessed, as it defines product reliability target.

Objectives and tasks for reliable product design and development include evaluation of the best practices and requirements of design for reliability, including testing. Audit electronic suppliers, be sure of their quality management programs and core people. Lot of qualification tests are required. Monitor performance for the product life and acting to discover deviations and errors early.

Testing for quality is a part of manufacturing for reliable products. It includes both – design and development tests (such as accelerated life testing), as well as tests during manufacturing (such as environmental stress screening)). Test methods include vibration testing, temperature testing, functional testing, shock tests (thermal, mechanical, electrical) and others. Some of the discovered failures include defects of plated through holes, solder fatigue, short circuits, corrosion, environmental contamination and others. In general, discovered failures are not always indicative, due to competing failure modes, and fact that complex systems often have complex failure modes.

Market analysis of electronics contract manufacturers [83] reveal that more companies are launching various hardware products. It is not difficult to enter market with new devices and power electronics solutions, but without field-experience, due to the available manufacturing

outsourcing options. Data confirms that printed circuit board assembly outsourcing is common by a start-up company [84], [85] for cost optimization.

Wearable electronics, tablets, home devices and smartphones are some of the hardware with increasingly high demand and supply. Stimulus to introduce new budget-class products is supplied by business opportunities at the emerging markets. Demand for performance improvements of currently produced equipment is another factor at the core of new product development [86]. Introduction of new technologies often include new engineering and hardware solutions and challenges, increasing a risk of various failures due to the adoption period of the new hardware.

To meet the customer expectations, a common concept of the electronics hardware development is the reduction of development time to accelerate the time to market. Product development team has to balance between product reliability and product launch window limitations, as profit and market cap are affected by delayed launch [87]. Various testing tools and methods [88] are available to reduce the risks from the accelerated development process. See flowchart of sample product development stages for reliability in Fig. 4.3

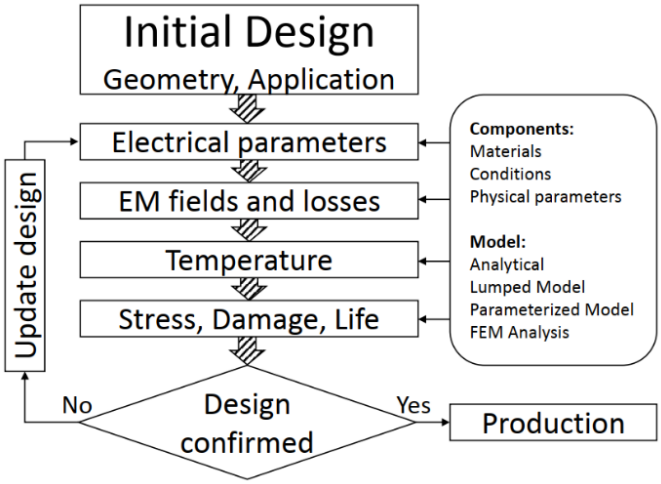

Fig. 4.3. Flowchart of product development stages for reliability [89]. Reliability improvement feedback loop returns to design phase and production.

Since the problem solving of quality and reliability issues recognized late in the process (for example, in warehouse, or after field failure) is resource demanding and expensive [90], the requirement for a well-established process with eliminated failures is not only based on ethical determination. Automotive, aerospace, military – some industries require proof of reliability and often also system redundancy due to operation critical applications.

Reliability program of a development and production cycle includes series of tests during all product life cycle stages [91]. Tests are introduced both at single product and batch level as well, to confirm that quality of the product does not deviate during production, and to verify that the initial requirements are achieved through development. Tier 4 data center facilities are one of the example applications for high reliability electronics equipment.

Feasibility, development, qualification and launch - multiple significant stages of the reliability program are illustrated in Fig. 4.4. Reliability and expected service life data are obtained during the tests. A basic understanding of the physics of failure is a requirement and a preventive measure, with field failures providing valuable feedback to the team. Design changes or new suspected failure modes are confirmed through reassigned life tests. Electrolytic capacitors and cooling fans are some of the expected failures to consider.

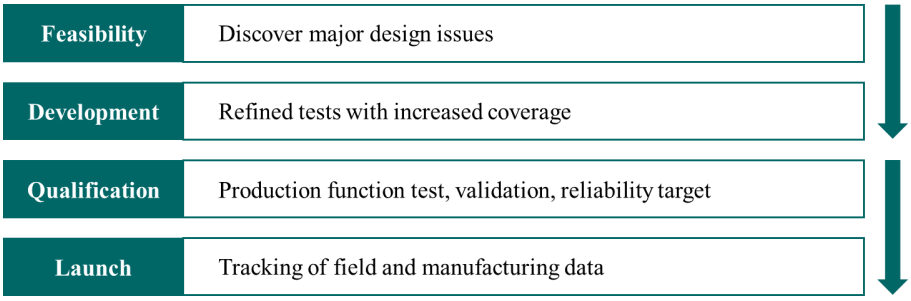

Fig. 4.4. Stages of reliability testing thorough product development.

To provide reliability data to the engineering team and customer, life testing is implemented for working prototypes as early as possible and optionally for each product revision. After the first mass production order, life testing of printed circuit board assembly is recommended to reveal early failure mechanisms [92]. Audit type selective sampling through standard production confirms that the final product meets the reliability requirements defined earlier [93]. Data from particular sampled products are used to establish generalized conclusions about the product population.

Test results provide confidence and proof of quality data of the developed product, such as fault-tolerant telecommunications equipment power converter for Tier 4 data center, where operation without downtime is critical.

Life testing within specification stress levels is impractical due to the required time to trigger relevant failure modes, therefore conditions of increased stress are introduced to accelerate damage and provide a more practical test duration [94]. Revealing failure modes is a requirement during the development and design verification phase, as late discovery is more expensive. Two categories of life assessment tests are considered - qualitative and quantitative research, focusing either on the trigger of failure mechanisms (qualitative) or data analysis and screening (quantitative).

Extensive function tests after assembly are motivated by early detection of defects, reduction of field failures and therefore warranty return. Marginal products are revealed by implemented by one of the following manufacturing tests – power on, function test, burn-in or run-in, environmental stress screening, highly accelerated stress screening or audit. Causes of failures are linked to soldering or assembly defects, a single faulty component or an entire batch.

One of the test methods to confirm that the operation of assembled units is within specification limits is called Burn-in, including electrical and optional thermal stress factors. This test method is applied to either sampled batch or the entire order. The same sampling principle is applied to Environmental stress screening. Environmental factors - changes in ambient temperature, temperature cycling, the addition of vibration stress, and humidity, are controlled and increased during this testing method up to the maximum value of the specification limit [95]. When subjected to increased stress during testing, a number of discovered failures is expected to increase, therefore decreasing the number of field failures.

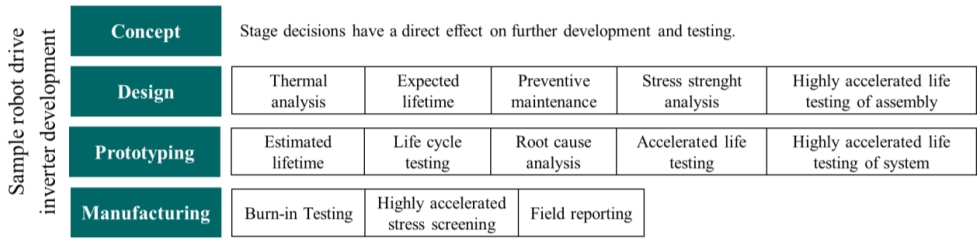

Fig. 4.5. Reliability improvement methods during sample robot drive inverter product development, with highlighted milestones reviewed through this work.

Sample robot drive inverter reliability program and improvement methods are illustrated in Fig. 4.5 and discussed in this section of the thesis. Development is categorized into concept, design, prototype and manufacturing phases. Major milestones for each phase create a basis for the continuous progress to the next phase. Basic principles of accelerated life testing have been reviewed in [96].

If required to exceed the specification, values of environmental and electrical stress test limits are increased during the highly accelerated stress screening, as well as the option to change test values and conditions. Rapid thermal cycling and transition, as well as vibration step stress and vibration mode change, are introduced [97]. The scale and product sampling principle of stress screening depends on the implemented reliability program, either to screen through a selection of units or an entire production batch. Highly accelerated stress screening during the manufacturing phase is intended to reveal failures, which would stay hidden during standard function tests [91].

When selective sampling is applied, the method is identified as a highly accelerated stress audit as the purpose is different. Instead of a complete screening process, a deviation detecting audit is introduced. The audit is expected in high volume production depending on several

factors, preferred for products with a requirement for low manufacturing price and low demand for reliability at mission-critical applications [91]. Testing and screening methods of highly accelerated processes are reviewed in [97]. IPC-SM-785 provides guidelines for evaluation of the results and extrapolation to the field use environment [98].

Stress testing of electronics during the manufacturing phase consumes the useful lifetime and therefore reliability of an individual unit is decreased. The reliability of the entire batch is increased as marginal products with defects are discovered. This is a drawback or a side effect of stress testing during manufacturing.

4.2. Stress Testing and Failure Modes

One of the root causes for early life product failures are variables of the material manufacturing and component assembly process – changes in soldering, components or handling. Failures are not necessarily product design related. A batch of poor-quality components can lead to an increased rate of early life failures. It is usually not equally distributed through the life cycle of printed circuit board assembly, as shown in Fig. 4.6, revealing that the printed circuit board assembly solder joints might break due to fatigue before any of the assembled components. Increasing, constant and decreasing failure rates are reviewed in Section 4.4.

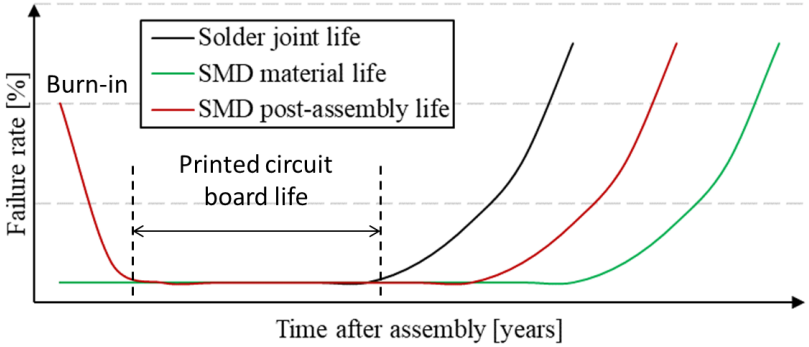

Fig. 4.6. Stages of printed circuit board assembly life cycle.

Stress testing through the implementation of a reliability program is discussed in more detail in this section. Expected failures and some of the most common defects are reviewed. See the comparison of simulation and real-life ball grid array package fatigue solder joint failure in Fig. 4.7 (a). Expanding and shrinking of materials caused solder fatigue and cracking as shown in Fig. 4.7 (b). Solder joint failure resulting in a vertical lift of the quad-flat no-lead package component is shown in Fig. 4.7 (c). Differences in characteristics of qualitative and quantitative testing are highlighted in this section.

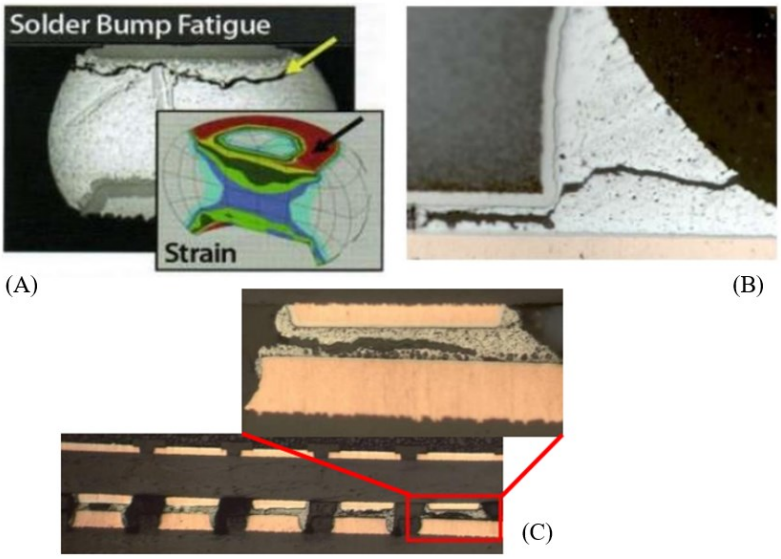

Fig. 4.7. (a) Simulation and real-life results of typical ball grid array solder failure due to fatigue [99], (b) surface mount resistor solder fatigue and failure due to damage (expanding and shrinking) of repetitive thermal cycling [100], (c) quad flat no lead chip package vertical lift during soldering leading to bad solder [101].

Stress testing principles and applications of qualitative and quantitative methods are reviewed in detail and compared in the following section 4.2.1, including examples of hardware, stress profiles and unit sampling. Some of the most common failure mechanisms including a review of defects and stresses revealed during testing are highlighted in section 4.2.2. Interpretation of results is discussed in section 4.2.3.

4.2.1. Qualitative and Quantitative Stress Testing Methods

There is a significant value of the attention to detail during the development stage, as extensive testing is an initial requirement to achieve stable results with reduced fail rate during stress testing methods of the manufacturing phase. Results from stress testing may become unstable or misleading due to issues supposedly solved during development, such as printed circuit board design for manufacturing issues, or thermal management errors. The scale of testing is often defined considering product reliability requirement, cost efficiency, and data of expected sales.

Development stage reliability and long-term performance testing have various possible variations. Specialized equipment is required for successful implementation of the mentioned stress tests – thermal cycling and shock chambers, vibration table, reviewed thoroughly at [102],

[103], [104]. Discovery and confirmation of product limits are completed through qualitative testing methods, such as highly accelerated life testing.

Thermal cycling is a commonly used reliability testing method for lead-free systems. Information about the expected life of the product is assumed by the application of Coffin-Manson (see Eq.4.3), Arrhenius (see Eq.4.1) and power law (see Eq.4.2) [105]. Models to express the exponential dependence of time to failure on applied stress are shown in Table 4.1.

Table 4.1.

Lifetime assumption methods

Arrhenius	$TF = Ae^{-\gamma\xi}e^{-E_a/k_BT}$	(4.1)
Power Law	$TF = B\xi^{-n}e^{-E_a/k_BT}$	(4.2)
Coffin-Manson	$Cycles\ to\ failure = (\Delta T)^{-q}$	(4.3)

Where TF – time to failure, A – reaction constant, γ - exponential stress parameter, ξ - generalized stress parameter, T is temperature, k_B is Botzlmann constant, E_a – activation energy. N is the exponent of the power-law and q is the material constant, exponent. ΔT temperature changes during dormant or active states of the assembly [106]. Lifetime estimation provides information to determine the duration of reliability tests such as burn-in, and to define the stress testing limit values, avoiding under or over-testing.

The most common accelerated life testing and screening combines multiple stress factors (temperature, humidity, vibration, others) [104]. Thermal testing is often complemented with vibration fatigue testing [105], including sine or random vibration, resonance search, dwell, vibration endurance and other test methods.

One of the stress testing method categories is qualitative testing methods. This type of research provides an insight into the reasons and causes of the revealed failures. Further ideas and thesis for research are established from the qualitative testing method results. Results may be misleading due to various effects discussed later in this section. Revealing realistic field failures is one of the method's advantages.

Qualitative accelerated life testing applications include highly accelerated life tests and highly accelerated stress screening. Focus on the development of a physical degradation model is expected in which input data are provided from accelerated degradation. The testing principle is to provoke the failure modes and to develop required enhancements based on the revealed weak areas. Prediction of product service life with stress values within specification limits is not made, as identification of failure modes and providing feedback to the product development team is the main objective. Several samples are tested until destruction at extreme stress, leading to highly accelerated life tests referred to as Elephant tests, Provocation tests or other names.

Incremental application of various environmental stresses beyond the operational limits is introduced during highly accelerated life testing. These stress factors include but are not limited to [107]:

- environmental (temperature, vibration, humidity)
- electromagnetic (electromagnetic sensitivity, electrostatic discharge)
- chemical (corrosive, cleaners, acid)
- pollution (dust)
- radiation (ultraviolet, infrared).

Sample testing equipment is a thermal chamber, capable of various 6 degrees of freedom vibration modes, as shown in Fig. 4.8.

Fig. 4.8. VTC-36 stress screening or highly accelerated life testing chamber manufactured by CONTROLTECNICA [108].

It is assumed that failure mechanisms revealed during the testing with increased stress will repeat after a long exposure duration to lower stress values within specification and operation limits [109].

However, the assumption is not always correct, as the relation with field failures often is not present [110]. Applied stress levels are exceeding the specification limits and unrealistic failure modes can be triggered. Different stresses can expose the same failure mode because of the crossover effect, therefore test and field failures can differ. Vibration could be assumed as the main stress factor causing failure, while in field failure thermal or humidity factors contribute more. Focus on misleading stress causes to lose an opportunity to strengthen the design for actual field failure modes [93]. An example of a stress testing profile with incremental thermal and vibration stress during highly accelerated life testing is illustrated in Fig. 4.9.

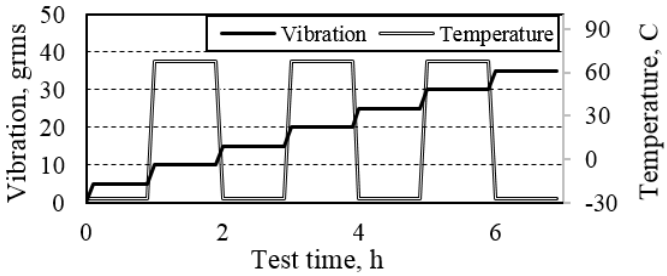

Fig. 4.9. Sample thermal and vibration stress testing profile during highly accelerated life testing of a power electronics assembly [111]

The solder joint of a dual row quad flat no-lead package component could fail due to mechanical stress during assembly, vibration, or thermal cycling. Strengthening the assembly to endure mechanical stress does not improve the product thermal cycling endurance of the same failure mode. One of the options is to shift focus from initial stress factors to failure mode.

Design weakness is identified during testing and the development team evaluates improvement options. The next design weakness is reviewed and improved, in theory, until no more possible causes for field failures are revealed through extensive testing and application of stresses. One of the practical application options is a comparison of design and materials, such as GaN to Si field-effect transistors.

Following the research during highly accelerated life tests, multiple environments over stress tests evaluate the product within previously determined destruct limits. Similar to the previous testing, relevant stresses are applied individually and in combination to reveal failure modes and expose problematic areas of the design [93].

As reviewed in [110], a significant effort is required to develop effective multiple environments overstress test. According to the testing methodology, all of the tested samples should fail before the last of the incremental stress steps scheduled from the operational limit up to the destruct limit (see Fig. 4.10). Multiple environments overstress testing does not operate at destruct limit as highly accelerated life testing does. Maximal practical overstress is revealed during this testing method [112], therefore destruct, specification and operational limits can be derived from the results.

This testing method is primarily qualitative, similar to highly accelerated life testing, and interaction of combined environment stress factors is involved compared to single stress testing [113]. Primarily applied during the development phase, the device under test in most cases has uncertain failure modes and times. A small sample size is reasonable with expensive or limited availability samples, such as prototypes.

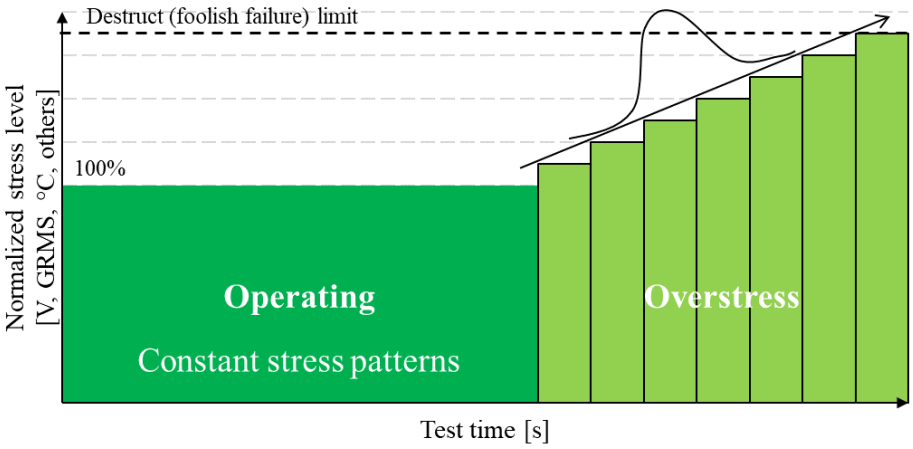

Fig. 4.10. Incremental overstress testing profile and distribution of failures from operational limit to destruct limit [114].

Foolish failure limit – is another name for destruct limit. A limit at which a product is permanently damaged is best determined for each environment separately. Products during operational life will not be subjected to such stress levels. During development testing at destruct limit provides little information on expected operational range failures, yet damages the valuable samples. Problem is that failure at destruct limit does not relate to field failure, such as melting of the plastic case at 190 ºC or cracks in printed circuit board during testing at 10 g_{rms} [113]. g_{rms} is a value defining vibration signal addressed both at source and measured signal [115] – a root mean square of continuously varying, pseudorandom, broad-spectrum vibration signal.

As there is a risk to trigger failure modes unrelated to field failures of the application, stress values are not increased to destruct level for all tested environments. Normalized and equal increments of stress and time are required to plot failure data on the Weibull plot (stress, time) [113].

Numerical data and statistics are generated and applied to research the problem in quantitative testing [116]. Research patterns are uncovered and facts are formulated through generalized results from the large sample analysis and definition of variables.

Product service life within operational limits is predicted through quantitative accelerated life testing methods, as the time to failure is decreased through accelerated usage rate. Failures are being provoked due to which products fail by their failure mechanisms, and extrapolation of the quantitative testing results provides expected service life data [117]. Destruct limit is not reached, but static or dynamic overstress values can be applied. Product life in operational conditions is predicted and the probability density function is constructed from the extrapolated data, representing the relationship between the tested hardware age and reliability.

Similar to qualitative testing, quantitative methods apply single or multiple stress types incrementally, recording the time to failure of each sample. If operational conditions are expected at 20 ºC, accelerated life tests are expected to include test points at 30 ºC, 40 ºC, 50 ºC, where stress type is thermal, and stress levels are each of the temperature steps [117].

Thermal, humidity, and vibration are some of the environmental stress factors applied in quantitative testing as well to stimulate degradation and lead to accelerated failure [118]. Based on data from qualitative testing and technical experience from field failures of similar assemblies, the team decides which stress types should be accelerated. Various failure modes can be accelerated revealed by the application of vibration stress, as reviewed in gathered data gathered [101] and illustrated in Fig. 4.11.

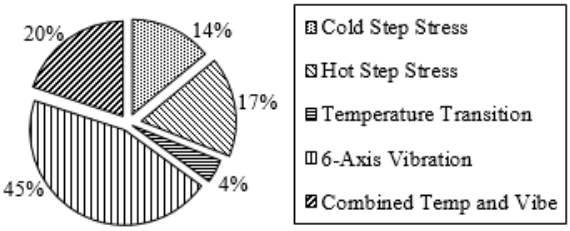

Fig. 4.11. Distribution of revealed defects after analysis of various accelerated stress tests

Some of the product types such as motor drive inverters reach operational limits rarely, mostly operating well below them. It is common to accelerate degradation during qualitative testing by simulation extended periods of operation at operational limits [117].

Acceleration of usage rate is common in a manufacturing environment. Also, in a form of an increased rate of mechanical wear. Service life durability of mechanical press buttons is tested through repetitive interaction, wear of connectors is tested through repetitive plug tests, and wear of automotive electric windows control and drive system is tested through repetitive opening and closing.

Life-stress relationship model is chosen to fit the analyzed data type. Any measure expressed as a function of stress is required to extrapolate the probability distribution function. If Weibull distribution is applied, η - scale parameter, considered stress-dependent, is assigned to the model. Accuracy is critical as data processing errors will offset the expected field life values due to the life-stress relationship.

Some of the available models to process data for one stress type, such as thermal - Arrhenius, Eyring, and inverse power law [117]. Mathematical models to analyze stress type pairs include a combination of Arrhenius and inverse power law (thermal & non-thermal) or a variation of Eyring (thermal & humidity). A higher number of stresses are supported by general log-linear or proportional hazard mathematical models. A cumulative model is an option if the applied stress varies between overstress or operational stress limits [119].

Based on Lipson equality [120], several of the final assembly units may be selected for a function test with an extended duration, which according to the parametric binomial approach [121] can be considered a batch life test. To decrease the number of tested samples a test method [122] allows to extend the test duration instead, explaining how fewer samples are tested for a longer duration. It is assumed that a proportionally small batch of the manufactured quantity being tested for an extended duration allows generalizing reliability of the not tested units.

Both, qualitative and quantitative testing methods have been reviewed in this section. See a description of the main characteristics of the methods in Table 4.2.

Table 4.2

Description of Qualitative and Quantitative Testing Methods

Qualitative testing	Quantitative testing
Understanding reasons and causes	Numerical data, statistics, failure rates
Developing ideas, failure modes	Formulates facts, uncovers patterns
Focus on failure modes not stress	Predict life at normal use conditions
Might be misleading due to crossover effect	Obtain expected life data in shorter time
Less useful for predicting service life	Accelerated usage rate
Destructive (foolish failure) limit	Not reaching destruct limit
Design robustness determination	Age and reliability relationship function
Highly accelerated life test	Stress applied at carefully increased levels
Few days	Few weeks
Engineering experience	Analytical models, Weibull, Arrhenius
Detailed product knowledge	

Qualitative testing is performed in general to provide an understanding of reasons and causes. Its focus is on failure modes to determine design robustness, therefore it is less useful to predict service life. Results of the qualitative testing may become misleading due to the crossover effect. Quantitative testing uncovers patterns and operates with numerical data and statistics to determine age and reliability relationship function. Stress is applied carefully to accelerate the usage rate. Failure mechanisms uncovered by the two testing types are reviewed further in the following section.

4.2.2. Related Failure Mechanisms

Printed circuit board assembly contains a lot of components in various package types. These are complex systems with different responses to stress, making the transfer of reliability from a single device to assembly a challenging task. The reliability of some of the package types such as the assembly of PBGA199 is evaluated in [123]. In general, through-hole assembly parts are considered more robust. In partial it is solved by focusing on physical models specific to applications - logic integrated circuits, insulation, and power modules [124]. See some of the popular surface mount component failure mechanisms in Fig. 4.12.

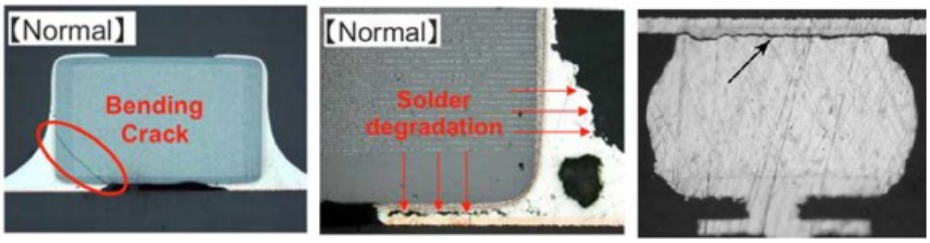

Fig. 4.12. Sample failure types of a surface mount component – bending crack, solder degradation and ball grid array solder failure.

In case sourced parts are already tested by a supplier, reliability tests of the final assembly expect to reveal failure modes of the assembly process and complete system. Stress during drop-test, thermal stress due to temperature differences, and electrical stress during power-on - are just some of the expected wear-out mechanisms of the printed circuit board assembly. If a simplified mathematical model is created by the combination of the individual parts data, assembly introduced failures such as solder joint defects and interaction of the components are not considered.

Thermal management of the design is a major consideration for reliability, not only due to the thermal management but the assembly as well. Thermal and electromagnetic interference management can involve heatsink with surface or through-hole soldering leads, often custom made and with high thermal and mass inertia. In general, heatsink assembly is a risk area - either attached by adhesive, screws, brackets or soldering.

Solder fatigue or break due to the mechanical assembly, screws loosening and causing short circuits, detached brackets or heatsink components - are some of the defects revealed at vibration testing. Revealed defects include - incorrect mounting of components, stacked resonances, wire breaking due to excessive bending, and wire or printed circuit board damage due to sharp flash residues from die casting or injection molding.

Table 4.3.

Defect Examples Revealed by Thermal Cycling and Vibration Testing

Thermal cycling:	Vibration:
Poorly matched thermal expansion coefficients	Mounting and assembly issues
Plated through-hole defects	Stacked resonances
Printed circuit board defects	Wires not protected from sharp corners
Assembly issues	Loose connections, not fixed connectors

Most of the defects revealed at thermal cycling and thermal shock have root cause at poorly matched thermal expansion coefficients [125], similar to the printed circuit board, plated through-hole defects. See sample defect types revealed during thermal cycling and vibration testing in Table 4.3.

Several types of non-destructive research equipment are used to investigate and analyze the testing results. Multimeter, microscope, caliper, strain measurement, and function testing - are some of the most common equipment. Solder and mechanical defects are viewed through X-ray and acoustic microscopy [123], [125]. Various data logging options are used to gather and plot the life span solder joint data, done using Weibull [102].

The mentioned equipment is capable to identify surface mounted multilayer ceramic capacitor failures as well. The most common failure mechanisms include flex, firing or handling cracks [125] (see Fig. 4.13). Damage due to poor design practice or during improper handling such as placing in the test jig, inserting in mechanical case, attachment of heatsinks or careless mounting of connectors are some of the surface mount capacitor failure causes revealed during accelerated life tests.

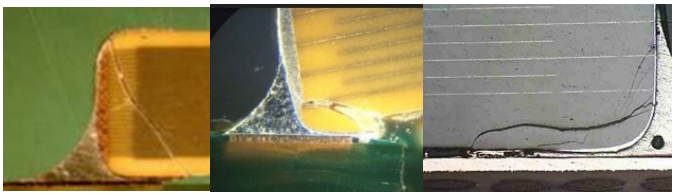

Fig. 4.13. Close up of surface mount multi-layer ceramic capacitor damaged during vibration stress or printed circuit board flex [107], [126], [127].

As reviewed earlier, higher thermal stress is expected to reveal defects earlier. It helps to sort out components such as defective electrolytic capacitors, which at specification limit will fail earlier than at normal operational parameters. Arrhenius equation, popular for thermal damage generalization, suggests that the failure rate is doubled for an increase of every 10 ºC, although this approach is criticized as too inaccurate [128]. The sample being tested at 70 °C is expected to fail sixteen times earlier, compared to a sample tested at 30 °C. This conclusion is supported by the time to failure results of samples tested in various temperatures (see Fig. 4.14), plotted according to the Weibull distribution and maximum likelihood estimation method.

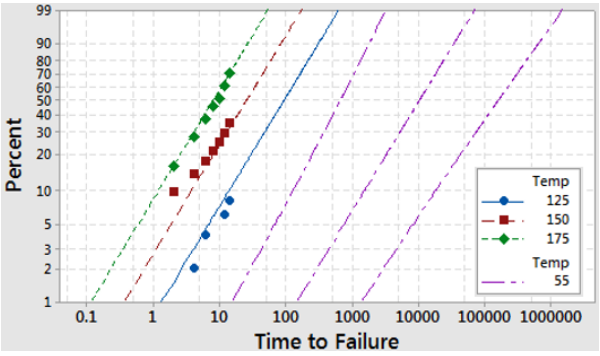

Fig. 4.14. Time to failure of samples, tested in various temperatures [129].

One of the common multilayer ceramic capacitor manufacturing defects initiated occurred earlier is oxygen defect. It is a defect revealed in long term operation. Oxygen vacancies are encapsulated in the crystal structure of the material after the firing of ceramics, see Fig. 4.15. Vacancies are expected to accumulate gradually at the cathode, leading to cracks in the ceramics body, accelerated by high temperature and voltage, therefore accumulation of oxygen vacancies at the cathode determines the lifetime of the component [130].

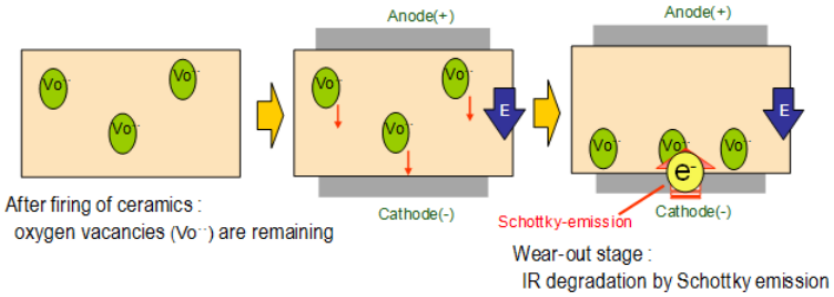

Fig. 4.15. Accumulation of oxygen vacancies in ceramic material of multilayer ceramic capacitors [130].

It is possible to estimate service life in operating conditions as the model supports voltage and temperature [103]. Estimation of values is done with the following empirical equation:

$$A_{\mathrm{L}} = \frac{L_{\mathrm{N}}}{L_{\mathrm{A}}} = \left(\frac{V_{\mathrm{A}}}{V_{\mathrm{N}}}\right)^{n} * 2\,\frac{(T_{\mathrm{A}} - T_{\mathrm{N}})}{\theta} \tag{4.4}$$

Where A_{L}, acceleration factor, θ and n - temperature and voltage acceleration constants, L_{N}, T_{N}, V_{N} - lifetime, temperature and voltage in standard conditions, L_{A}, T_{A}, V_{A} - lifetime, temperature and voltage in accelerated conditions. Temperature and voltage acceleration constants vary from the material [103].

In the case of the previously illustrated oxygen defects, an equivalent field lifetime consumption of 41 years can be consumed during an endurance test of 41 days with increased temperature and voltage. While considerably shorter, test duration of 41 days is still a challenge for the manufacturing environment. The accuracy of the extrapolation must be considered.

Multi-layer ceramic capacitors are process temperature and assembly stress-sensitive [131]. Currents of stress testing are capable to reveal the expected early field failures - damaged or malfunctioning components.

Inrush current exceeding the rated load current is possible during the initial charging of capacitors. In an operational environment, this could be observed during power cycling after longer disconnection periods. If the circuit has not considered this current peak, it can cause unwanted voltage fluctuations. Current capability for connectors and printed circuit board traces is limited and mechanical stress, as well as operational limits of any series devices, should be considered. Overcurrent involves mechanical stress and the probability of permanent damage [132].

Failures revealed during stress testing of printed circuit board assembly include, but are not limited to:

1) damage during the fabrication process,
2) overheating due to manufacturing mistakes [133],
3) component package defects (such as inductor ferrite cracking),
4) oxidation visual defects, related poor solder joint quality, ionic contamination [134],
5) other solder defects - voiding, too less solder, incorrect solder paste stencil openings,
6) assembly errors of the case or cabling - not installed properly or damaged [132].

Socket failures, connector displacement, component damage, potentiometer misplacement, cracking of plastic parts or cases at a stress point, printed circuit board damage from a broken trace, as well as software or firmware failures - are some of the failures expected to be revealed through stress testing.

The human factor is a significant contributor to early failures in the reliability function. The requirement for a high degree of workmanship likely will have an effect on reliability with a higher rate of mistakes. Simplified and intuitive assembly is a benefit [89]. Overheating and trigger of thermal protection during testing are caused by assembly problems such as missing or incorrectly assembled heatsink.

Wear out failure mechanisms of thermal stress include diffusion, evaporation, and thermal ageing. Acceleration models apply for these mechanisms. Acceleration models do not apply for the overstress failures, which include melting, freezing, and boiling. Wear out and overstress failure mechanisms for other common stress types are illustrated (see Table 4.4).

Table 4.4.

Common Overstress Failures and the Applied Stress [135]

Stress	Wear out failure mechanisms (acceleration models apply)	Overstress failure mechanisms (acceleration models do not apply)
Temperature	Diffusion, evaporation, thermal ageing	Melting, freezing, boiling, explosion, T_g transition
Humidity	Sorption, corrosion	Condensation
Vibration	High cycle fatigue	Mechanical overload, microphony, rattling
Thermal cycling	Low cycle fatigue	Same as for “Temperature”, mechanical overload
Voltage	Time dependent dielectric breakdown	Electrical overstress, electrostatic discharge
Current	Electromigration	Electrical overstress
Others	Creep, wear, ultra-low cycle fatigue	Impact
Combined	Fretting corrosion, migration, corrosion, time dependent dielectric breakdown, electromigration	Same as all the failure mechanisms above

For other types of stress such as humidity, vibration, current - overstress failures include condensation, mechanical overload, and electrical overstress. Stress values this high are reasonable for qualitative testing when an overall understanding of failure modes and relevant stresses has to be determined. They have no value for the analysis of quantitative testing results, as acceleration models do not apply on overstress failures.

Analysis of the accelerated testing results is integrated into the product reliability program and includes a comparison to expected reliability goals, evaluation of observed failure mechanisms, and evaluation of the overall design [136].

4.2.3. Interpretation of Results

Accelerated life tests do not increase the total product development and confirmation time significantly. It provides failure data to the engineering team before the product is delivered to the customer, therefore any corrective actions and design changes are implemented early. Reliability testing during design and manufacturing allows to install the equipment in uptime critical applications, and results from the destructive lifetime testing reveal destruct design and specification limits.

Data of accelerated testing and field failures is not a perfect alignment due to differences in sample sizes and failure mechanisms – Arrhenius, Coffin-Manson equations are assumed to align with field data, but the field failure mechanisms may differ. A confidence level of 60-95 % is considered for the data calculated from the accelerated stress testing results. Lifetime predictions from the accelerated testing do not consider degradation during storage or manufacturing, such as humidity penetrating moisture sensitive devices. Failure rate during the beginning of the service life can exceed the predictions due to not considered failure modes, being different from typical earlier failures and adding more uncertainty [89].

It is challenging to assume quantitative correlation from qualitative testing data, as qualitative accelerated tests are applied mostly to research the physics of failure. Field modelling performed on the returned products supports the comparison of quantitative failure data and maximum failure quantity according to accelerated testing, presented in the case study at [89].

Previous studies which have reviewed and verified field data and accelerated testing correlation include the expectation of battery field life at various stress levels, fatigue of solder joints, and others. Results from the accelerating testing and analysis results allow to change parameters as possible and reduce time to market. A more conservative temperature range could be extended, while an overly wide range with failures at higher values could be narrowed.

A part of the product reliability program is the processing flow of the accelerated testing results in the manufacturing environment, as results are analyzed and instructions for further actions according to pre-defined failure rate acceptance quality level, for example, how to proceed if several units have failed during the accelerated stress screening.

One of the methods applied in the analysis of the development and production testing results is failure modes effects and criticality analysis - "a disciplined method of product, process analysis, conducted to identify potential failures that could affect the customer's expectations of product quality or process performance" [137]. Information gathered through testing is considered [138]. Possible quality improvements are analyzed and implemented if possible and reasonable by the engineering team to reduce the future failure rate. A stable process with a reduction of revealed failures through manufacturing orders can lead to a reduction in the number of tested samples.

4.3. Stress Screening During Mass Production

The role of the outgoing quality control program is to assure that the manufactured product meets the specification requirement and functions properly and that the quality does not decline over time. Stress screening is one of the tools, applied to eliminate early failure rate by decreasing the service life of each production unit, in order to improve the reliability of the produced batch.

The printed circuit board assembly process includes subjecting to normal, worst-case, or other specific operational environment conditions, where IPC-9701 provides the guidelines for durability evaluation of electronics assembly surface mount solder attachments [139], [140].

While testing during product development is mostly qualitative and intended to reveal product destruct limit, and gather data about performance limits [141], the same testing concept is not directly transferable to the production environment. While degradation of product to reveal defects is acceptable, the damage must be controlled as the product must remain functional. Different testing methods are implemented to achieve the goals of the output quality control program. To avoid testing during manufacturing, a requirement for sourcing stress screened components is an option, for example, integrated IGBT modules.

During the service life, the initial failure rate decreases the overall reliability for the first years due to various assembly or manufacturing defects [134]. An example of an integrated electronics assembly failure rate is illustrated in Fig. 4.17. A number of wear-out failures begin to increase late in the operational lifetime.

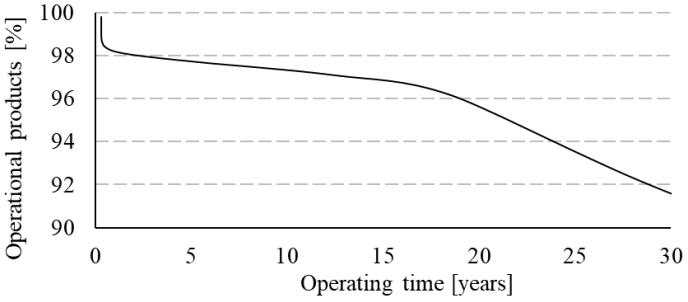

Fig. 4.17. The lifetime of operational products through time

The concept of stress screening is to simulate 2 years of field operation of all the products. Service life is reduced, but being at a manufacturing site, early field failures are revealed early before installation in an actual field application (see Fig. 4.18). On average, the operational life of the remaining production parts is increased. Development of the screening process involves the maximum probability of mission success after the screening, and maximum mean residual life [142].

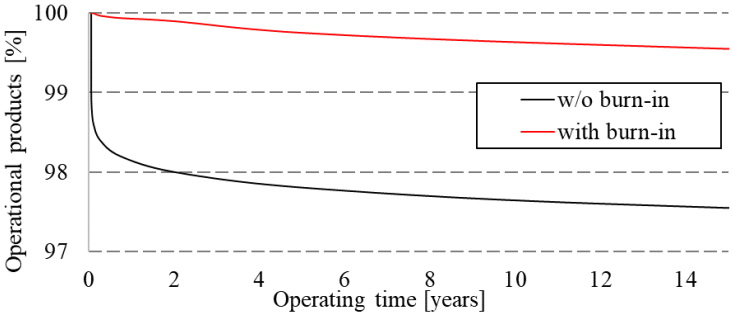

Fig. 4.18. The lifetime of operational products with and without stress test (burn-in) through time

MIL-HDBK-217 handbook contains data for the failure rate of passive and active elements such as resistors, transformers, and field effect transistors [143], and according to this document, most of the electronics can be modelled by exponential distribution [144]. This handbook reveals that failures in all applications are not revealed through stress testing, therefore it is not always practical, depending on the failure rate.

Production stress testing samples with increasing or constant failure rate ($\beta>1$, $\beta=1$) will not provide the desired result - a decrease of early failures. The average reliability of the batch is decreased instead, compared to the not tested samples. Early field failures are not eliminated during production stress testing of samples with $\beta\geq1$ as early failures are not common. Instead, the service life is decreased [134]. For efficient stress testing a failure rate of the sample product which decreases over time ($\beta<1$) is required [144]. The failure rate with decreasing failure rate of Weibull distribution is shown in Fig. 4.18

The time frame of manufacturing defects is not defined and is application dependent, for example, the electronics integrated circuit industry has observed failures driven by manufacturing or assembly caused defects up to 10 years in field operation [134]. Fig. 3. reveal failure distribution of electronic assemblies, processors or graphics processing units.

Burn-in, environmental stress screening, highly accelerated stress screening, and highly accelerated stress audit - are some of the applied accelerated stress testing methods. Condition monitoring is an option to consider as a cost-effective alternative for production stress testing, being a currently discussed topic in the power electronics industry.

Benefits of stress testing - a decreased rate of field failures and a reduced number of products not functional on arrival have been discussed since 1988 according to [145].

Latent design issues and manufacturing units not detectable in basic function tests are revealed by the subjection of controlled thermal, simultaneous mechanical, or other product specific stress during accelerated stress screening with managed profiles as shown in Fig. 4.19. Substitution of a component with an alternative, property drift and misalignment of dimension and parameter tolerances - are some of the root causes for quality and reliability deviation.

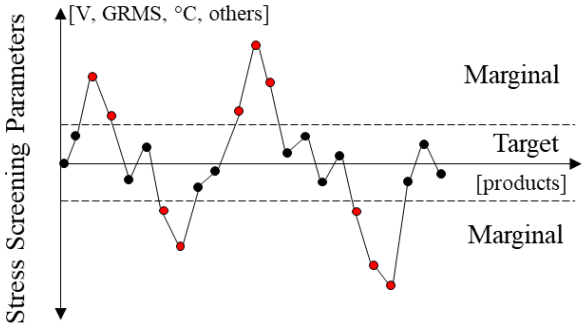

Fig. 4.19. Differences in quality of produced units, detected by stress screening

Field data reveal that by revealing various failures after implementation of accelerated degradation there is a possible up to 90 % reduction of warranty returns, for example, from 5 % to 0.5 % as in [146].

Multiple electronics assemblies are tested in the same chamber to increase the output capability of stress testing, the duration of which is from one to several hours [147].

Recommended for power supplies and other electronic assemblies with high-reliability requirements, an additional benefit of the highly accelerated stress screening process is monitoring changes in process and early notice of critical process or material quality errors [148]. The engineering team involved in the accelerated stress testing design and analysis should include highly experienced members for the selection of the right stress parameters and interpretation of the results [149].

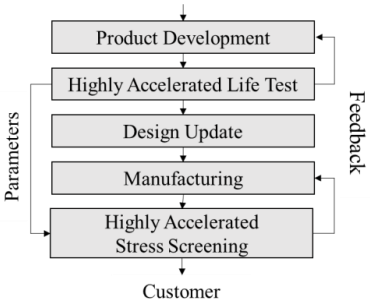

Fig. 4.20. Role of highly accelerated life testing and stress screening through product development and manufacturing

Screening reports is feedback which leads the design and manufacturing engineering teams to improve the process and implement upgrades if reasonable, as shown in Fig. 4.20 [150]. Complete elimination of manufacturing defects is challenging in some cases due to fundamental limitations of the manufacturing [151] for example, as the nucleation eventually leads to a failure.

Sampling principles of devices for stress screening during manufacturing is discussed in section 4.3.1. Fixtures, chambers and some of the issues caused by testing hardware are reviewed in section 4.3.2. Limits of stress values considered in stress screening are discussed in section 4.3.3. Section 4.3.4. provides focus on burn-in as one of the stress screening methods for mass production. Practical considerations and lifetime consumption simulations are analysed in section 4.3.5 to evaluate on-site burn-in of robot motor drive inverters with the developed thermo electrical model. The study's summary and conclusions regarding stress screening in mass production are presented in section 4.3.6.

4.3.1. Quantity of Devices Under Test

There are several available options for how to select samples for stress testing, and it depends on the selected method, test duration, and expected output - testing either all of the production units, the first units from current production, or select samples from current production in a random pattern. As mentioned earlier, tested samples can be selected through analysis of acceptance level tables, which output the number of tested samples and a number of allowed defects from the input shipment size. It is considered that both factors - test method and product quantity - contribute to the testing outcome.

Time or testing duration is the third major parameter, being highly specific and it varies for each testing setup and product, depending on the failure rate. The testing duration of isolated gate bipolar transistors is directly affected by junction temperature, which also defines the functionality of the transistor. Some of the devices are expected to reach thermal runaway and

become defective, resulting in a short circuit or open loop, caused by variations in the processing of the devices.

The major parameters - test method, product quantity, and test duration - should be decided as early as possible [91]. These tests are integrated in general product reliability or quality program, considering warranty costs, estimated service life, and other relevant data.

4.3.2. Hardware Setup

Regarding testing equipment, challenges include capital requirements to cover direct expenses such as test equipment and fixture purchase, design or manufacturing. Production time is extended therefore costs are higher than without stress testing. In addition, there is a demand for floor space to place the testing equipment.

Historically chamber and testing equipment has been designed impractical, dedicated to one product type. Easily modifiable equipment with the support of multiple product types has been introduced to reduce cost and floor space issues of the stress testing, addressing ergonomics, mistake proofing, cables and fixtures [94].

Equipment similar to accelerated life testing of the development phase, modified chambers and fixtures are used in stress screening in the manufacturing environment [152], [153]. Modifications include quick-release bolts and increased capacity of devices under test.

While continuously monitoring performance, electrical and mechanical stress is applied simultaneously, exposing the sample to rapid temperature change with high peak values. Vibration response from 20-10 kHz GRMS is generated by impactor pistons.

Due to differences in the setup parameters and requirements of the specific products it is challenging to test multiple types of products in the same chamber, instead of testing chamber is loaded with the same type of products to slightly increase the tested sample size.

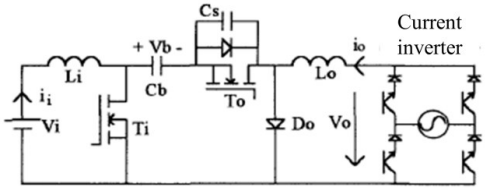

Fig. 4.21. Energy recycling Ćuk converter topology for stress testing of power supplies [154].

During the manufacturing of power electronics devices, a load current is required for stress testing. While possible to neglect this consumption during the manufacturing of small power devices, mass production of 500 W or 20 kW devices demands equipment to reduce power consumption caused by simultaneous operation at rated power for the stress testing duration. Problem is solved by energy recycling and various methods have been discussed, approved and implemented by the industry. Energy recycling systems typically is a system of the rectifier,

inverter and the device under test, connected in a sample topology - capacitive idling converter (see Fig. 4.21) [154].

Together with the device under test, a whole stress screening fixture assembly must endure the stress testing cycles repetitively. Problems caused by cable length, electrical load, environment monitoring, and fatigue of fixtures and accessories are some of the challenges to consider. Excessive cable length leads to signal degradation, voltage loss, and pick up transient external events. Testing fixture failures due to bending fatigue or friction cable damage to insulation is common. To improve the results of the stress testing:

a) locking mechanisms are required to strengthen the latch of connectors,

b) keep the cables short, supported and shielded with small radius bends [149].

c) inconsistencies in airflow and thermal distribution should be considered,

d) clamping management should be considered to change vibration inconsistencies,

e) maintenance schedule for fixtures, testers, cables, chambers due to the subjected stress,

f) reduce the electrical interference.

False, weak, noisy or biased signals are unwanted as they contribute to misleading results and time consumption of the engineering team. Interference with test results can be caused by the introduction of complex impedance as well.

Spare parts such as cables or components should be ready for replacement, as vibration causes wear-out of the fixture as well, causing loose connectors to generate electrical noise or transient connections.

Fixture mapping is recommended to distribute mechanical and thermal stress equally between devices under test. Environment monitoring is achieved through thermocouples, and accelerometers, assigned and located individually. Equal loading of fixture matters for comparability of test results, as vibration characteristics could differ for completely loaded and partially loaded fixtures. Signals are monitored and logged through data loggers for later analysis of the events by the engineering team.

4.3.3. Limits Considered in Stress Screening

Before the introduction of stress screening, highly accelerated life tests and the following improvements are required to solve weak links of the design early and provide feedback to the team accordingly. In addition to the informative background to target specific failure modes during screening, it is required to reduce the number of marginal products before the start of production and to determine product destruct limits. As shown in sample thermal stress testing (see Fig. 4.22), the amplitude of stress values ranges from lower operating limit to upper operating limit.

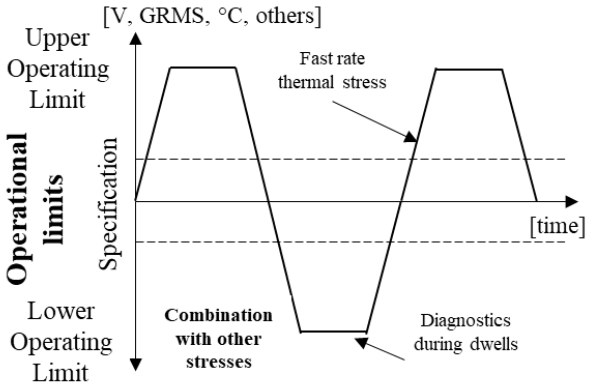

Fig. 4.22. Profile amplitude of fast rate thermal stress testing application [91].

Functional tests, performance tests and power cycling are three of the routines common in highly accelerated stress screening [155]. Functional testing is performed by automated testing equipment monitoring the performance of the device under test to verify the operation of the critical elements - solder joints, connectors, and fans. Performance testing includes monitoring the performance while loading the internal nodes to achieve the highest performance - deploy of maximum traffic or consuming maximal electric load [149].

Product limits determined during accelerated life testing define the stress limits during the screening process. Depending on the selected method, stress values are selected between specification, operational and destruct limits. Amplitude is selected between operating and destruct limit, with diagnostics being performed during temperature dwells.

An operational limit is a limit above which a product does not function properly but is not damaged [156]. This also called soft failure limit is identified during highly accelerated life testing. Being an empirical method to determine limit values, accelerated life testing does not reveal the distribution of operational or destruct limits due to insufficient sample size.

Devices can be categorized by either wide or narrow operating limits. See sample amplitudes of various stress testing types such as highly accelerated stress screening, burn-in, and environmental stress screening related to products with wide operating limit specification, operating and destruct limits in Fig. 4.23 (a). Precipitation screening values exceed the soft failure limit for products with narrow operating limits (illustrated in Fig. 4.23 (b)).

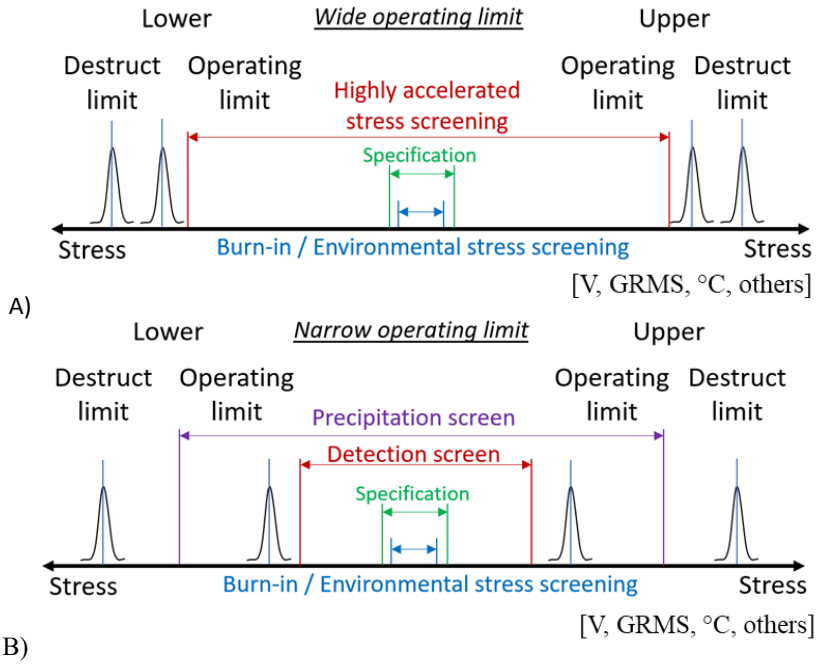

Fig. 4.23. Product limits (narrow (a) or wide (b) operating limits) and expected stress values during various stress screening options.

Regarding the reliability of product operation according to specification, specification limits are further from the operating limit for wide operating limit devices, reducing the risk of failure.

To remove less than 5 % of product life during stress testing, generalized reduction guidelines for translation from destruct to operational limit values are 50 % for vibration and 80 % - 85 % for temperature [157-161]. To confirm the remaining 95 % of service life after stress screening, the unit is tested increasing screening duration by 20 times, expecting the device under test to fail eventually.

In a sample scenario with operating limit of 100 °C, the temperature for stress screening should equal 85 °C. The temperature margin between ambient temperature (25 °C) and the operational limit is 75 °C, of which 80 % is 60 °C. After the addition of ambient temperature, the upper-stress limit for stress screening is determined.

Different stress testing profiles are selected for wide and narrow operation limits, with the integration of fast thermal rate stress to achieve degradation of wide operation limit products (see Fig. 3). Over-stress is unlikely, as in general operational limits are not exceeded. In the case of narrow operation limits, calculated stress limit values (see Fig. 4) may require adjustment if acceptable values are exceeded. Fast rate and slow rate thermal cycling is to adjust the applied stress.

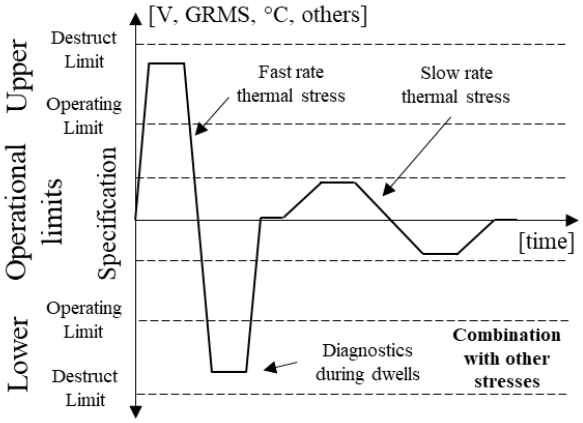

Fig. 4.24. Profile of fast and slow rate thermal stress testing during precipitation screening (above operating limit) and detection screening (below operating limit) [91].

Sample precipitation and detection stress screening method mixed stress profile is shown in Fig. 4.24 [161], where devices are tested without and with functional testing accordingly. Detection screening does not exceed the operational limits, while precipitation screening operates in the range between operational and destruct limits. As mentioned earlier, test limits are updated and adjusted to avoid over-stress caused by decreased product life or an increase in warranty returns due to under-stressed devices.

After testing hardware is installed and limits are known, a proof of screen or safety of screen [147] test is performed to confirm that stress testing does not damage the device under test beyond the required margin and that the estimated decrease of service life is achieved. The screening process is repeated at least 15 times on the same device under test to double confirm the degradation level is below destruct limit. Stress levels are adjusted through analysis of failures and improved understanding of evident failure modes and improved accuracy of calculations. The reference value of the lifetime is calculated through standard lifetime assumption methods [162].

4.4. Burn-in as a Reliability Improvement Tool

This section reviews the role of burn-in testing in production reliability improvement programs, discussing its benefits and challenges, compared to other stress screening methods. Burn-in testing is a post-assembly testing method capable to reveal electronics hardware (fans, power supplies, converters) assembly defects, process issues, and non-conformities [163]. In some sources, burn-in testing is also called run-in [164]. See sample burn-in testing hardware setup of consumer-grade power supplies with electrical stress in Fig. 4.25.

Fig. 4.25. Equipment of consumer grade power supply burn-in testing [165].

Being a rather common stress testing method, it has been discussed in several standards, such as MIL-STD-750 and MIL-STD-883, for semiconductor devices and microcircuits, and others, such as MIL-PRF-38534 for hybrid microcircuits. The mentioned standards define requirements for test conditions of electronics components before assembly and are not directly applicable for completed assemblies.

Burn-as a stress screening method is reviewed in detail at section 4.4.1. Practical considerations of implanting this method including lifetime consumption simulations with the developed extension are reviewed in Section 4.4.2.

4.4.1. Application Principles

In the simplest form burn-in testing is a power-up test of a product, operating stand-by for the required time. Voltage and temperature are increased optionally to accelerate degradation [166]. Efficiency is questionable, due to the small number of nodes being tested. Revealed defects include mixed polarity assembly of electrolytic capacitors (if test time is sufficient to trigger failure), and other defects due to which the product is unable to power on. The test is efficient for simple electronics assemblies, interface adapters, and extension boards with a small number of active components. A sample of an effective burn-in testing application for power supply assembly includes increased ambient temperature and a combination of power cycling with extended uptime periods, as shown in Fig. 4.26.

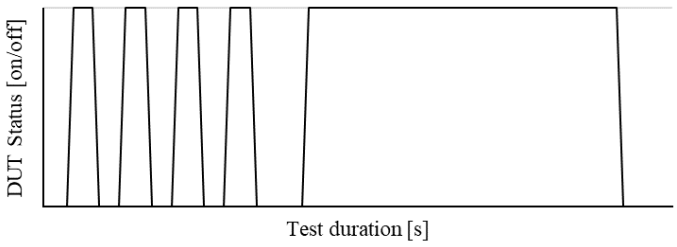

Fig. 4.26. Electric and thermal stress screening with changing power cycling and constant load periods [144].

To further accelerate degradation, a combination of three stress parameters is introduced. Electric, thermal and mechanical stress are three of the most common stress screening options. See sample stress testing profile in Fig. 4.27. Short power cycling periods are combined with longer operating cycles. The same dynamic stress testing profile is applied to both, electrical and vibration stress.

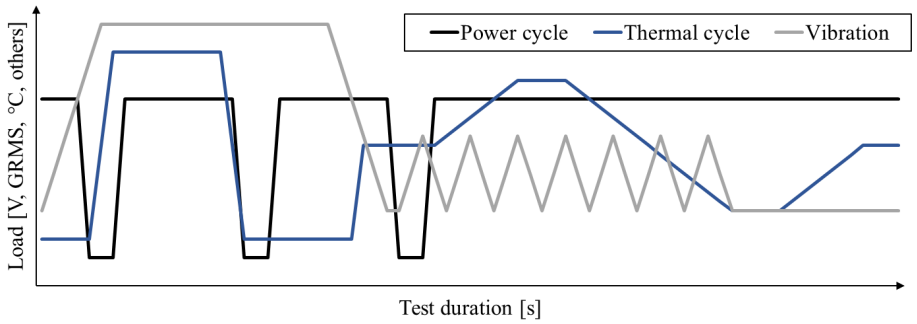

Fig. 4.27. Mixed electric, thermal and vibration stress profile during highly accelerated stress screening, including power cycling, vibration and thermal cycling.

Burn-in requirement for hardware is simple - chambers, stands, racks, and some automated testing equipment to monitor the performance and log the results [167, 168]. Sockets for power and data connection are integrated if required. Test stands with simultaneous burn-in of 30 - 50 pcs devices under test are common. A balance between the 3 major test parameters (stress level, test duration, and the number of tested samples) is required. An increase in stress level further accelerates degradation and reduces the failure period by multiple times, due to higher inrush current from power cycling and the increased thermal stress [168]. Test effectiveness is improved by the reduction of No Fault Found orders.

A complete failure analysis process is required to evaluate the root cause - an assembly or manufacturing defect or caused by a wear-out process. This can be time consuming and confusing, especially when starting a new production until data and knowledge is gathered.

The decision to integrate burn-in testing in production flow is supported by factors such as the number of components on printed circuit board assembly and their type - active and passive, including semiconductor components each with its own unique early failure rate. After assembly, the failure rates are considered regarding the functionality of the assembly.

It is possible to avoid burn-in testing if components have passed burn-in testing of their own production individually. Positive is that individually at the designated production site it is easier to stress test each component for effective results. The drawback is that the failure modes introduced during the assembly process, and failure modes due to poor complete assembly design, will not be tested. Complex assemblies with a requirement for reliability can be burn-

in tested at the actual operating site if the test conditions are reasonable [133]. After successful burn-in testing products are allowed to continue production, after failed test - either returned for analysis, reworked or scrapped.

Static and dynamic are two of the available general burn-in stress testing categories. During static testing device under test is placed in the chamber and tested in elevated temperatures or other types of stress, without external biases that make it less effective for complex systems [167]. An obvious limitation of static testing is that identification of failure is only possible during follow-up functionality tests after the device has been removed from the chamber and the exact time of failure is not known. Device response during the test is not tracked.

Dynamic testing has the same limitation. Maximum stress rate limited by burn-in chambers is applied to the device under test during dynamic burn-in, with added input stimuli to electrically stress test the internal nodes of the devices. The output of the device is not monitored.

Dynamic burn-in with a test is the third stress testing category, monitoring device outputs. The test can last up to several days, while the product is powered and functional tests are performed in changing test chamber internal temperatures. Burn-in testing in thermal cycling chambers is often a required proof of product durability margin for the automotive industry [169]. Dynamic burn-in with test enables monitoring of the product modules (central processing unit, random access memory, fans) through a combination of burn-in stress and input node stimuli with output data logging.

Installation might be required before testing to receive the expected output data, and the short power-on during installation and functional testing is not considered a burn-in. While defects are revealed, these are not classified as infant mortality. Burn-in is a manufacturing stress screening method, scheduled after printed circuit board assembly (see Fig. 4.28).

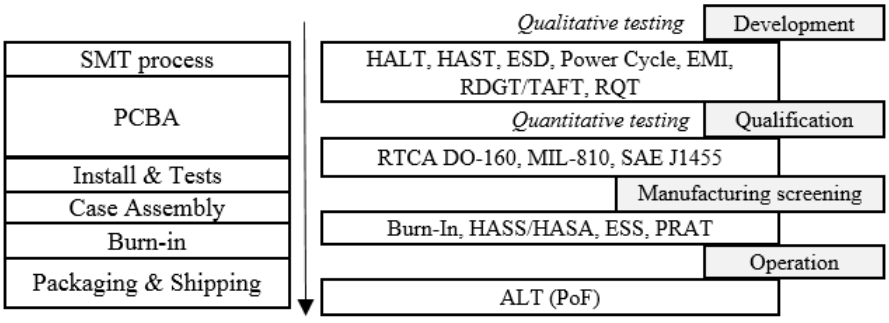

Fig. 4.28. Burn-in testing in mass production of electronic devices

After a successful test, the product continues the manufacturing process to packing. Determined by testing requirements considered earlier in the development process, burn-in equipment is selected - closed chambers or other testing stands.

It is reasonable to burn in recently assembled products, as the previously mentioned defects are revealed and sorted out, and repaired. Determination of burn-in testing duration is a compromise between production costs and reliability goals. Costs to consider include the cost of burn-in, cost of warranty returns, cost of lost items, cost of failure, cost of rework, and others. Cost-reduction objectives are often required due to business purposes and are being applied through development and manufacturing. A decision is made, on whether production tests are required, optional, or too expensive for the target price.

In some cases, the burn-in test may be skipped to reduce costs and the number of testing equipment if the part is tested after printed circuit board assembly as well, combining multiple tests in one. The drawback is that expenses of rework after burn-in are increased, and the test efficiency should be considered as well - is it possible to equally stress test the module after assembly.

When estimating testing costs - fixtures and chambers, software, duration and sample quantity are considered. Approximate rework costs and the number of failed products with their scrap rate and costs, as well as warranty replacements are included. All of the previously mentioned compared numbers of estimated burn-in test and field failures allow computing optimal test duration regarding cost-efficiency.

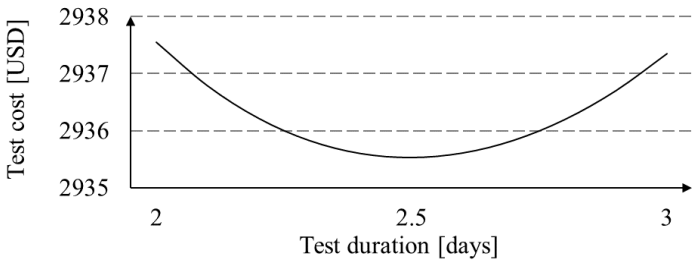

Fig. 4.29. Burn-in cost of power electronics assembly considering multiple input parameters such as warranty return and cost of the product

In the sample scenario, optimal burn-in duration is calculated at 2.3 days and the balance of the expected costs at 2935.52 USD, if warranty replacement costs are 4000 USD, one burn-in testing day costs 70 USD, revealing a failure cost of 500 USD [170], as shown in Fig. 4.29. Balancing cost value is selected as a compromise considering the cost and failure rate inputs mentioned earlier. For the sample scenario, if burn-in duration approached 0, the cost would approach 4000 USD, as it would be increasingly more likely to fail during warranty.

If the cost of a field failure is higher than burn-in test failure, burn-in testing is financially reasonable. Lost market share, decreased customer satisfaction, not returning for second purchase - not directly measurable, but considerable effects affected by early field failures.

4.4.2. Practical Considerations for Burn-in of Robot Inverter

As mentioned earlier, burn-in after assembly and delivery to customers is one of the stress testing options. Burn-in of robot motor drive inverter while performing the robot specific program after installation in manufacturing site is evaluated in this section.

Previously obtained lifetime consumption data of diode and IGBT of the inverter for 4 robot applications (welding, handling, clinching, adhesive bonding) is provided as an input for the required computation.

Stress testing of industrial robot axis drive inverters is simulated and analyzed. The developed thermo-electrical and lifetime consumption model of inverter IGBT module allows estimating the damage of hardware through one cycle of operation. Following the intention of stress testing to accelerate wear and damage, multiple repetitive cycles of the specific robot program are scheduled and simulated. The objective is to evaluate stress testing of robot drive hardware after assembly and after installation at the manufacturing site.

Acceleration of 6 degrees of freedom industrial robot welding program wear of drive inverter IGBT module through repetitive program application is simulated from 1 hour to 72 hours. Damage accumulation for Axis 1-3 inverter IGBT and anti-parallel diode after 1 hour, 24 hours and 72 hours of accelerated testing is shown in Fig. 4.30. Testing profile does include a delay of 5 seconds after each cycle but does not include a realistic schedule such as technical break, changing of workshop shifts, lunch break, or other operation interruptions.

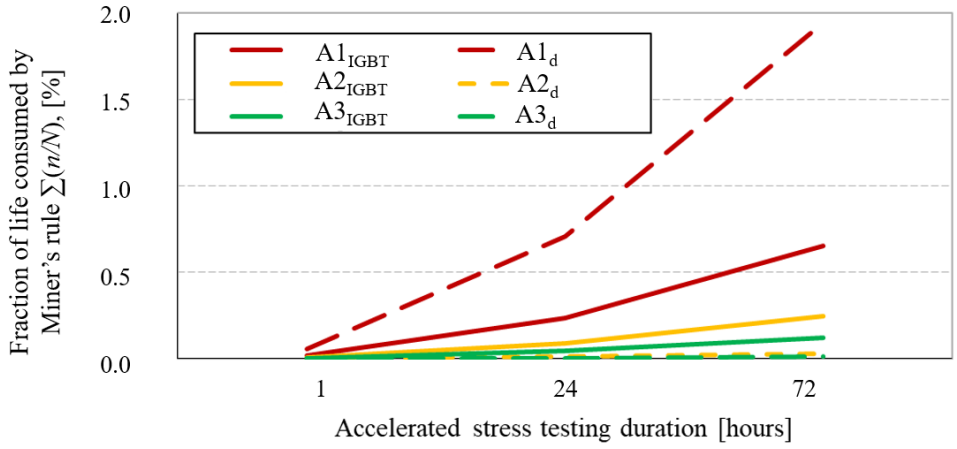

Fig. 4.30. Accumulation of robot axis 1-3 inverter IGBT and anti-parallel diode lifetime consumption through cycling of welding program for 1 h up to 72 h.

Simulation results reveal a significant difference in wear highlighted at the increased test duration. In general, estimated lifetime distribution is equal for all robot axis connected to the same inverter. Uneven loading during stress testing is a challenge if the objective is to achieve equal lifetime consumption for all of the 6-robot axis inverter hardware.

In the results of welding application cycling Axis 1, IGBT relative damage is at 0.02, while Axis 2 is about 0.0025 or 0.0015 for Axis 3. If a sample lifetime consumption of 0.002 is selected as a threshold, testing times to reach this threshold are significantly different for each robot axis. While for Axis 1 24-hour testing is sufficient, wear of the other axis is below the target value.

A comparison of normal and accelerated wear for the welding program after 72 hours of operation is shown in Fig. 4.31. The number of cycles during normal wear is decreased compared to accelerated wear. It includes an estimated coefficient to consider longer delays, realistic operation schedules such as technical breaks, changing of workshop shifts, lunch breaks and other operation interruptions.

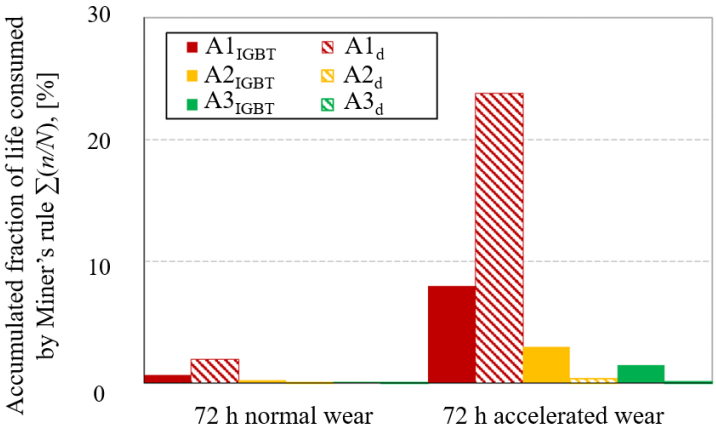

Fig. 4.31. Estimated lifetime consumption accumulated through 72 hours of normal and accelerated robot welding program cycling.

Power consumption and therefore mission profile for each robot program are different. This transfers to lifetime consumption as well. Stress testing of other robot programs such as adhesive bonding (see Fig. 4.32), handling or clinching (see Appendix N) for 72 h were simulated. Lifetime consumption compared to the welding program reveal lower peak values. While 72-hour testing lifetime consumption has decreased, consumption of axis 2 and 3 is proportionally smaller as well. Uneven loading is evident for other robot programs.

-

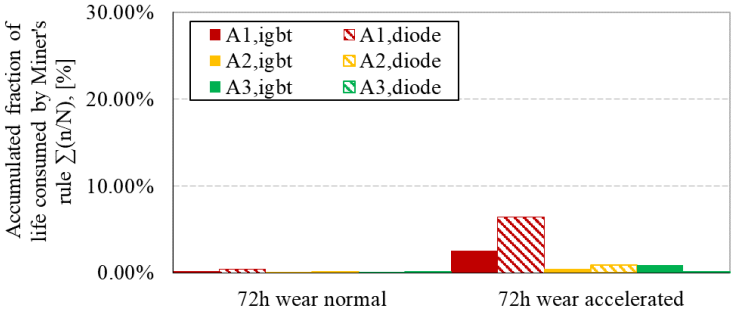

Fig. 4.32. Estimated lifetime consumption accumulated through 72 hours of normal and accelerated robot adhesive bonding program cycling.

Four robot programs were simulated with normal and accelerated loading for 72-hour period, evaluating the lifetime consumption values. Estimated damage for IGBT and anti-parallel diode for axis 1-3 of each robot program is shown in Fig. 4.33. The highest damage is accumulated during the handling program, followed by the welding program. Clinching and adhesive bonding programs have lower accumulated lifetime consumption values.

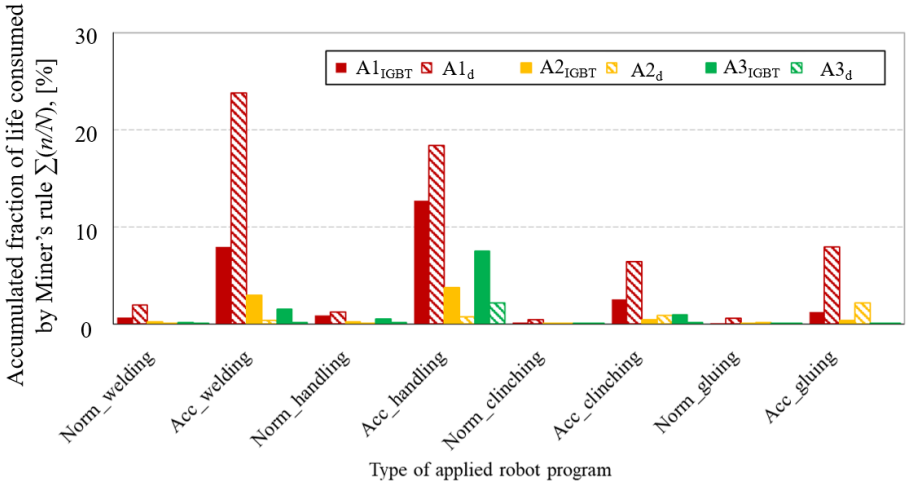

Fig. 4.33. Simulation of normal and accelerated lifetime consumption after 72 hours of robot program cycling – welding, handling, clinching, adhesive bonding programs.

An alternative to burn-in after installation is burn-in testing at the drive inverter assembly site. The load of robot axis drive electronics hardware is simulated by imitation with an electric

load. In the controlled environment, it is possible to achieve equal degradation of axis hardware through a stable process.

4.5. Conclusions

Various production environment screening methods are introduced due to reliability risks introduced by the accelerated development process. Development stage tests are destructive and applied to determine performance margins - not useful for production screening. While the remaining lifetime of each device is reduced during stress testing, the quality of the overall production is improved by eliminating early failures.

Located in a mass production site and part of the standard manufacturing process - burn-in is one of the stress screening options, with an application of ambient or increased temperature, power cycling or constant electrical load. Target costs including warranty returns and test duration, as well as reliability are considered while selecting the most effective testing methods for acceleration of early failure mechanisms. Major challenges are capital costs of the setup, reduction of pass yield and increase in overall production costs, while benefits include decreased risk of early failures and higher customer satisfaction.

Stress screening can improve the quality of mass production units by a decrease of the delivered defects, warranty costs and early failures or by reducing the quality if applied without the required considerations and causes over-stress. Degradation level is confirmed during proof of screen. Design improvements are possible since technical weaknesses are revealed through registering detailed data and root cause analysis of failed devices. The impact scale of various stress types on the specific product is evaluated during accelerated life testing, and implemented in stress screening. General stress screening challenges include keeping the number of tested devices as high as possible. With test chambers, fixtures and profiles being designed for a specific product type, increasing the scale of burn-in through the entire product lineup is resource-demanding.

A lifetime model of 6 degrees of freedom industrial robot drive inverter IGBT modules was simulated to evaluate the accumulation of lifetime consumption through normal and accelerated cycling of the robot program. Results reveal that the wear of electronics is program dependent and that robot axis hardware wears out unevenly due to differences in an applied stress profile. Suitability to local stress screening of robot hardware after assembly at the manufacturing site is low since equal lifetime consumption is required. Burn-in during manufacturing of inverter is recommended as a specific application designed for electrical stress testing is expected to achieve the objective more efficiently.

CONCLUSIONS

1. While the number of industrial robots and DC system applications is increasing, maintaining the initial functionality of industrial hardware is required to provide sustainability and continuity for the manufacturing processes, creating a demand for reliability data of the DC microgrid solutions.
2. Robot tool weight has a direct impact on motor drive inverter IGBT lifetime, increasing motor current and thermal swing. Studied application of robot program repetition with 0 kg and 125 kg tool revealed an increase in the estimated fraction of consumed lifetime for power electronics components between 29-249 % per cycle.
3. Analysis method of robot motor drive inverter IGBT with anti-parallel diode junction temperatures and estimated consumed fraction of lifetime allow to identify and evaluate the contribution of robot load weight, application type, layout type, to temperature changes within the hardware of robotized equipment. High peak temperatures of less dynamic (adhesive bonding) programs are up to 25 % lower, compared to sample spot welding or handling programs.
4. Various robot programs have differences up to 10 times in cumulative lifetime consumption values per cycle, comparing dynamic (welding, handling) and less dynamic (adhesive bonding) robot programs, with the anti-parallel diode of Axis 1 having the highest fraction of consumed lifetime.
5. Energy consumption model with a robot program code input is verified on the industrial robot, therefore introduced thermal and lifetime computations are expected to align with the realistic field data, with the accuracy losses introducing predicted misalignment. The model provides an opportunity to test various remaining lifetime improvement concepts quickly, and highlight impact factors - tool mass, stop to standstill cycles, program velocity, average current consumption, and others.
6. Focus of previous studies has been on DC microgrid layout energy efficiency improvements, therefore analysis and comparison of suggested and not yet reviewed robotized manufacturing system layout and control improvements considering reliability is a valued addition to previous work.
7. Addition of an optimal capacitance capacitor (7.3 mF) to the state-of-the-art single robot hardware layout has the highest probability of implementation, as it reduced the computed fraction of life consumed by Miner's rule by 12.73 % for IGBT, and 14.67 % for the anti-parallel diode in the robot motor drive inverter power electronics circuit.
8. Peak value of current consumption from the AC grid in a multiple robot-single supply layout can be decreased from 43 A to 30 A (30.2 % decrease) for the same combination of two robot programs, by changing the starting time for each program.

9. In a multiple robot-single supply layout, less likely to be implemented due to higher initial development costs and some technology not being transferred to a production environment, two studied robot program alignment options revealed a decrease in the computed fraction of life consumed of 10.21 % in IGBT, and 45.58 % in the anti-parallel diode of the studied axis drive inverter power electronics switch components.
10. Development methods to supply highly reliable robotized manufacturing hardware capable to operate for as long as possible have been reviewed and presented, including the deployment of a reliability program to improve through the elimination of failure modes and early failures.
11. Stress testing reduce the reliability of an individual unit as its useful lifetime is consumed, but the reliability of the batch is increased after the elimination of marginal products. Duration of burn-in stress testing considers the reduction of pass yield, warranty returns and other costs, while benefits include reduced risk of early failures.
12. To achieve a minimum of 0.2 % fraction of lifetime consumption (robot axis drive inverter IGBT) during burn-in testing of sample welding program field operation, test duration varies from 24 hours (Axis 1) to 100 hours (Axis 3).
13. Inverter IGBT modules wear out unevenly between robot axis, depending on the stress profile of the robot program, therefore burn-in of the inverter is recommended at the supplier site with equal and controlled lifetime consumption.
14. Mission profile analysis provides data for on-site adjustment of predictive maintenance schedule depending on the robot program type, tool weight, and other impact factors.

Future Vision

Further development options include a possible increase of available inverter options by manufacturer, reducing costs and increasing market share with lower cost, reduced lifetime versions. Equipment with low lifetime consumption value has an indicator of impractical use of resources, as equipment cost can be reduced by reducing overrating of components.

A further extended digital model of production at virtual commissioning software with the developed innovative energy consumption, junction temperature and long-waited lifetime consumption module provides application-specific data for predictive maintenance and other research purposes. The developed model supports further integration in virtual commissioning software.

BIBLIOGRAPHY

1. Project AREUS. *Automation and Robotics for EUropean Sustainable manufacturing* [online]. [Viewed February 2022]. Available from: https://cordis.europa.eu/project/id/609391
2. Aldrete, S. *Video Demos: New Process Simulate and RobotExpert Functionality* [online]. Place: Siemens, 2019 [viewed December 2021]. Available from: https://blogs.sw.siemens.com/tecnomatix/video-demos-new-process-simulate-and-robotexpert-functionality/
3. European Commission. *World Robotics Report 2020 by International Federation of Robots* [online]. [viewed December 2021]. Available from: https://ec.europa.eu/newsroom/rtd/items/700621/en
4. Dassault Systemes. *Assembly Robot Programmer* [online]. [Viewed November 2020]. Available from: https://www.3ds.com/products-services/delmia/disciplines/industrial-engineering/
5. ABB. *RobotStudio®* [online]. [Viewed November 2020]. Available from: https://new.abb.com/products/robotics/robotstudio
6. KUKA AG. *KUKA.Sim* [online]. [Viewed November 2020]. Available from: https://www.kuka.com/en-gb/products/robotics-systems/software/simulation-planning-optimization/kuka_sim
7. Bormanis, O. Development of energy consumption model for virtual commissioning software. In: *2015 56th International Scientific Conference on Power and Electrical Engineering of Riga Technical University (RTUCON) Proceedings, Riga, 2015*. Place: IEEE, 2015, pp. 1-4. ISBN 978-1-5090-0334-1. e-ISBN 978-1-4673-9752-0. Available from: doi:10.1109/RTUCON.2015.7343139
8. Gurgul, M. *Process Simulate: Virtual commissioning* [online]. [Viewed March 2018]. Available from: https://www.slideshare.net/mgurgul/robotics-virtual-comisionning-in-process-simulate
9. Corke, P. *Robotics Toolbox for MATLAB®* [online]. Place: PeterCorke.com, 2020 [viewed November 2020]. Available from: https://petercorke.com/toolboxes/robotics-toolbox/
10. Corke, P. *Robotics Toolbox 10 for MATLAB®* [online]. Place: Robotics Toolbox, 2020 [viewed November 2020]. Available from: https://petercorke.com/download/27/rtb/1050/rtb-manual.pdf
11. Hansen, C., Öltjen, J., Meike, D., Ortmaier, T. Enhanced approach for energy-efficient trajectory generation of industrial robots. In: *2012 IEEE International Conference on Automation Science and Engineering (CASE) Proceedings, Seoul, 2012*. Place: IEEE, 2012, pp. 1-7. ISBN 978-1-4673-0429-0. e-ISBN 978-1-4673-0430-6. ISSN 2161-8070. e-ISSN 2161-8089. Available from: doi: 10.1109/CoASE.2012.6386343
12. Illinois Capacitor, Inc. *Voltage balancing resistors* [online]. [Viewed May 2021]. Available from: http://www.lintronicstech.com/index%20pdf/voltage_balancing_resistors.pdf

13. Infineon Technologies AG. *AN2008-01. Technical Information. IGBT Modules. Definition and use of junction temperature value* [online]. [Viewed May 2021]. Available from: https://www.infineon.com/dgdl/Infineon-AN2008-1_Definition_of_junction_temperature-ApplicationNotes-v01_00-EN.pdf?fileId=db3a304320896aa201208a8f68d00038
14. Gebreel, Abd Almula G. M. *Simulation and Implementation of Two-Level and Three-Level Inverters by Matlab and RT-Lab.* Master thesis. Ohio, 2011
15. Bormanis, O., Ribickis, L. Power Module Temperature in Simulation of Robotic Manufacturing Application. *Latvian Journal of Physics and Technical Sciences*. 2021, vol.5., no.4, pp.3-14. ISSN 0868-8257. e-ISSN 2255-8896. Available from: doi:10.2478/lpts-2021-0029
16. Pigazo, A., Liserre, M., Blaagjerg, F., Kerekes, T. Robustness analysis of the efficiency in PV inverters. In: *IECON 2013 - 39th Annual Conference of the IEEE Industrial Electronics Society Proceedings, Vienna, 2013*. Place: IEEE, 2014, pp. 7015-7020. ISBN 978-1-4799-0225-5. e-ISBN 978-1-4799-0224-8. ISSN 1553-572X. e-ISSN 2577-1647. Available from: doi: 10.1109/IECON.2013.6700296
17. Infineon Technologies AG. *AN2015-10. Transient thermal measurements and thermal equivalent circuit models* [online]. [Viewed May 2021]. Available from: https://www.infineon.com/dgdl/Infineon-Thermal_equivalent_circuit_models-ApplicationNotes-v01_02-EN.pdf?fileId=db3a30431a5c32f2011aa65358394dd2
18. Sintamarean, C., Blaabjerg, F., Wang, H., Iannuzzo, F. Reliability oriented design tool for the new generation of grid connected PV inverters. *IEEE Transactions on Power Electronics*. 2015, vol.30, no.5, pp.2635–2644. ISSN 0885-8993. e-ISSN 1941-0107. Available from: doi: 10.1109/TPEL.2014.2361918
19. Zhou, S., Zhou, L., Liu, S., Sun, P., Luo, Q., Wu, J. The Application of Approximate Entropy Theory in Defects Detecting of IGBT Module. *Active and Passive Electronic Components*. 2012, vol.2012, pp.1-7. ISSN 0882-7516. e-ISSN 1563-5031. Available from: doi:10.1155/2012/309789
20. Huang, H., Mawby, P.A. A lifetime estimation technique for voltage source inverters. *IEEE Transactions on Power Electronics*. 2013, vol.28, no.8, pp.4113– 4119. ISSN 0885-8993. e-ISSN 1941-0107. Available from: doi:10.1109/TPEL.2012.2229472
21. Ciappa, M. Selected failure mechanisms of modern power modules. *Microelectronics Reliability*. 2002, vol.42, no.4-5, pp.653–667. ISSN 0026-2714. e-ISSN 1872-941X. Available from: doi: 10.1016/S0026-2714(02)00042-2
22. Bayerer, R., Hermann, T., Licht, T., Lutz, J., Feller, M. Model for power cycling lifetime of IGBT modules - various factors influencing lifetime. In: *5th International Conference on Integrated Power Electronics Systems Proceedings, Nuremberg, 2008.* Place: VDE, 2011, pp. 1–6. ISBN 978-3-8007-3089-6.
23. Scheuermann, U., Hecht, U. Power cycling lifetime of advanced power modules for different temperature swings. In: *PCIM Proceedings, Nuremberg, 2002*. Place: PCIM, 2002, pp.59-64.

24. Lee, W.W., Nguyen, L.T., Selvaduray, G.S. Solder joint fatigue models: Review and applicability to chip scale packages. *Microelectronics Reliability*. 2000, vol.40, no.2, pp.231–244. ISSN 0026-2714. e-ISSN 1872-941X. Available from: doi: 10.1016/S0026-2714(99)00061-X
25. Infineon Technologies AG. *AN2019-05. PC and TC Diagrams* [online]. [Viewed May 2021]. Available from: https://www.compel.ru/wordpress/wp-content/uploads/2020/02/infineon-an2019-05_pc_and_tc_diagrams-applicationnotes-v01_00-en.pdf
26. Abuelnaga, A., Narimani, M., Bahman, A.S. Power electronic converter reliability and prognosis review focusing on power switch module failures. *Journal of Power Electronics*. 2021, vol.21, pp.865–880. ISSN 1598-2092. e-ISSN 2093-4718. Available from: doi: 10.1007/s43236-021-00228-6
27. CAE Simulation Solutions. *Finite Life Fatigue Strength* [online]. [Viewed December 2021]. Available from: https://www.cae-sim-sol.com/en/limit-stress-evaluation/finite-life-fatigue-strength
28. Dewesoft d.o.o. *Fatigue Analysis, Damage calculation, Rainflow counting* [online]. [Viewed December.2021]. Available from: https://training.dewesoft.com/online/course/fatigue-analysis
29. Bormanis, O., Ribickis, L. Mission Profile based Electro-Thermal Model of Robotic Manufacturing Application. In: *2021 23rd European Conference on Power Electronics and Applications (EPE'21 ECCE Europe) Proceedings, Ghent, 2021.* Place: IEEE, 2021, pp. 1-6. ISBN 978-1-6654-3384-6. e-ISBN 978-9-0758-1537-5. Available from: doi: 10.23919/EPE21ECCEEurope50061.2021.9570547
30. McPherson, J. W. *Reliability Physics and Engineering*. New York City: Springer Cham, 2010, 165 p. ISBN: 978-3-319-93682-6.
31. Kovaltchouk, T., Aubry, J., Multon, B., Hamed, H.B. Influence of IGBT Current Rating on the Thermal Cycling Lifetime of a Power Electronic Active Rectifier in a Direct Wave Energy Converter. In: *2013 15th European Conference on Power Electronics and Applications (EPE) Proceedings, Lille, 2013.* Place: IEEE, 2013, pp.1-9. ISBN 978-1-4799-0114-2. e-ISBN 978-1-4799-0116-6. Available from: doi: 10.1109/EPE.2013.6631903
32. Milke, E., Mueller, T. High temperature behaviour and reliability of Al-Ribbon for automotive applications. In: *2008 2nd Electronics System-Integration Technology Conference Proceedings, Greenwich, 2008*. Place: IEEE, 2008, pp. 417-422. ISBN 978-1-4244-2813-7. e-ISBN 978-1-4244-2814-4. Available from: doi: 10.1109/ESTC.2008.4684384
33. Siemens Digital Industries Software. *Rainflow Counting* [online]. [Viewed October 2021]. Available from: https://community.sw.siemens.com/s/article/rainflow-counting
34. The MathWorks, Inc. *Rainflow counts for fatigue analysis* [online]. [Viewed October.2021]. Available from: https://se.mathworks.com/help/signal/ref/rainflow.html

35. Munk-Nielsen, Stig. *Lifetime estimation of IGBT power modules.* Master thesis. Aalborg University, 2013
36. Musallam, M., Johnson, M., Yin, C., Lu, H. and Bailey, C. Real-time life expectancy estimation in power modules. In: *2008 2nd Electronics System-Integration Technology Conference, Proceedings, Greenwich, 2008.* Place: IEEE, 2008, pp.231-236. ISBN 978-1-4244-2813-7. e-ISBN 978-1-4244-2814-4. Available from: doi: 10.1109/ESTC.2008.4684355
37. Chamund, D., Rout, C. *Reliability of High Power Bipolar Devices* [online]. Place: Dynex Semiconductor Limited, 2009 [viewed February.2021]. Available from: https://www.dynexsemi.com/Portals/0/assets/downloads/DNX_AN5948.pdf
38. Musallam, M., Johnson, C.M. An Efficient Implementation of the Rainflow Counting Algorithm for Life Consumption Estimation. *IEEE Transactions on Reliability*. 2012., vol.61, no.4, pp.978-986. ISSN 0018-9529. e-ISSN 1558-1721. Available from: doi: 10.1109/TR.2012.2221040
39. Paugurs, A., Senfelds, A., Ribickis, L. Impact of industrial robot tool mass on regenerative energy. In: *2017 19th European Conference on Power Electronics and Applications (EPE'17 ECCE Europe) Proceedings, Warsaw, 2017*. Place: IEEE, 2017, pp. 1-6. ISBN 978-1-5386-0530-1. e-ISBN 978-90-75815-27-6. Available from: doi: 10.23919/EPE17ECCEEurope.2017.8099185
40. Barbara, S. *No Moore?* [online]. Place: The Economist. Science and Technology, 2013 [viewed February 2022]. Available from: http://www.economist.com/news/21589080-golden-rule-microchips-appears-be-coming-end-no-moore
41. Briere, M., ACOO Enterprises LLC. *GaN-based power devices offer game-changing potential in power-conversion electronics* [online]. EE Times, 2008 [viewed February 2022]. Available from: http://www.eetimes.com/document.asp?doc_id=1272514
42. Ruthardt, J., Blank, F., Wölfle, J., Tröster, N., Roth-Stielow, J. Power supply with active energy storage to reuse the braking energy for servo drives. In: *2017 19th European Conference on Power Electronics and Applications (EPE'17 ECCE Europe) Proceedings, Warsaw, 2017*. Place: IEEE, 2017, pp. 1-9. ISBN 978-1-5386-0530-1. e-ISBN 978-90-75815-27-6. Available from: doi: 10.23919/EPE17ECCEEurope.2017.8099002
43. Wood, E. *22 intriguing microgrid projects to watch in 2022* [online]. Microgrid Knowledge, 2022 [viewed February 2022]. Available from: https://microgridknowledge.com/22-intriguing-microgrid-projects-watch-2022/
44. Hew, W.P. *Feasibility of DC-microgrid For Off-grid Communities Electrification* [online]. Place: University of Malaya, 2015 [viewed March 2018]. Available from: https://www.slideshare.net/e4sv/kuching-2g34-off-grid-dc-microgrid-che-hang-seng
45. Shentai, R. *DC Microgrids and the Virtues of Local Electricity* [online]. IEEE Spectrum, 2014 [viewed February 2022]. Available from: http://spectrum.ieee.org/green-tech/buildings/dc-microgrids-and-the-virtues-of-local-electricity

46. Melton, P. *A Surge of Popularity for Efficient DC Power* [online]. BuildingGreen.com, 2011 [viewed February 2022]. Available from: https://www2.buildinggreen.com/article/surge-popularity-efficient-dc-power
47. Schneider Electric India, *0.5 kW to 10 kW prepaid DC Micro Grid solution with centralized generation and distributed storage* [online]. [Viewed February 2022]. Available from: http://www.schneider-electric.com/products/in/en/8600-access-to-energy-collective-solutions/8610-villaya-collective-solutions/62210-dc-micro-grid/
48. Alternate Energy Company. *Renewable Energy Projects* [online]. [Viewed February 2022]. Available from: https://alternateenergycompany.com/
49. DC Components and Gris. *DCC+G* [online]. [Viewed February 2022]. Available from: https://cordis.europa.eu/project/id/296108
50. Almeida, R.. *Exciting Times in Marine Engineering – A Look at the Evolution and Future of Electrical Power* [online]. Place: gCaptain, 2012 [Viewed February 2022]. Available from: http://gcaptain.com/exciting-times-engineering-evolution/
51. KIMO® Industrial Electronics GmbH, *KIMO Drive Technology. Braking choppers* [online]. [Viewed March 2022]. Available from: https://www.kimo.de/en/braking-choppers/
52. International Organization for Standardization. *International Standard ISO 8373 Third edition 2021-11. Robotics - Vocabulary* [online]. [Viewed January 2022]. Available from: https://cdn.standards.iteh.ai/samples/75539/1bc8409322eb4922bf680e15901852d2/ISO-8373-2021.pdf
53. Xuequan, M. *Global industrial robot sales reach record level in 2018* [online]. Place: Xinhua, 2019 [viewed March 2020]. Available from: http://www.xinhuanet.com/english/2019-09/18/c_138402462.htm
54. KUKA Roboter GmbH. *KR 4 R600* [online]. [Viewed April 2022]. Available from: https://www.kuka.com/event/media?itemId=A1E271AD96B64015946635714B6CD3DA
55. KUKA Roboter GmbH. *KR 1000 1300 TITAN PA* [online]. [Viewed April 2022]. Available from: https://www.kuka.com/event/media?itemId=815499F8EF864D549A788487EA80AD54
56. Meike, D. *Energy Efficient Robotics, Present state, options, ideas* [PowerPoint slides]. Place: Daimler AG, Sindelfingen, 2010.
57. Meike, D., Ribickis, L. Analysis of the Energy Efficient Usage Methods of Medium and High Payload Industrial Robots in the Automobile Industry. In: *10th International Symposium Topical Problems in the Field of Electrical and Power Engineering. Doctoral School of Energy and Geotechnology II Proceedings,* Pärnu, 2011. Place: Eesti Moritz Hermann Jacobi Selts, 2011, pp. 62.-66.lpp. ISBN 9789985908945.
58. Raņķis, I., Meike, D., Šenfelds, A. Utilization of Regeneration Energy in Industrial Robots System. *Power and Electrical Engineering*. 2013, vol.31, pp.95-100. ISSN 14077345.
59. Meike, D., Ribickis, L. Recuperated Energy Savings Potential and Approaches in Industrial Robotics. In: *2011 IEEE International Conference on Automation Science and Engineering*

Proceedings, Trieste, 2011. Place: IEEE, 2011, pp. 299-303. ISBN 978-1-4577-1730-7. e-ISBN 978-1-4577-1732-1. ISSN 2161-8070. e-ISSN 2161-8070. Available from: doi: 10.1109/CASE.2011.6042435

60. Hoffmann, A. *Micro Power System with LVDC Link* [online]. [Viewed February 2022]. Available from: http://www.studentaward-germany.com/idea.php?id=75
61. Meike, Dāvis. *Increasing Energy Efficiency of Robotized Production Systems in Automobile Manufacturing*. Doctoral Thesis. Rīga: RTU Press, 2013
62. Meike, D., Ribickis, L. Energy Efficient Use of Robotics in the Automobile Industry. In: *2011 15th International Conference on Advanced Robotics (ICAR) Proceedings, Tallinn, 2011*. Place: IEEE, 2011, pp. 507-511. ISBN 978-1-4577-1158-9. e-ISBN 978-1-4577-1159-6. Available from: doi: 10.1109/ICAR.2011.6088567
63. Bormanis, Oskars. *Improvement of Industrial Robots Energy Efficiency by Energy Storage Applications.* Bachelor Thesis. Riga, 2014
64. Markoff, J. *Skilled Work, Without the Worker* [online].Place: The New York Times, 2012 [viewed February 2022]. Available from: http://www.nytimes.com/2012/08/19/business /new-wave-of-adept-robots-is-changing-global-industry.html?pagewanted=all&_r=0
65. Singh, M., Khadkikar, V., Chandra, A., Varma, R.K. Grid Interconnection of Renewable Energy Sources at the Distribution Level With Power-Quality Improvement Features. *IEEE Transactions on Power Delivery*. 2011, vol.26, no.1, pp.307-315. ISSN 0885-8977. e-ISSN 1937-4208. Available from: doi: 10.1109/TPWRD.2010.2081384
66. Meike, D., Senfelds, A., Ribickis, L. Power converter for DC bus sharing to increase the energy efficiency in drive systems. In: *IECON 2013 - 39th Annual Conference of the IEEE Industrial Electronics Society Proceedings, Vienna, 2013.* Place: IEEE, 2014, pp. 7199-7204. e-ISBN 978-1-4799-0224-8. ISSN 1553-572X. Available from: doi: 10.1109/IECON.2013.6700329.
67. Šenfelds, A., Bormanis, O., Paugurs, A. Modelling of AC/DC Power Supply Unit for DC Microgrid. In: *2015 IEEE 3rd Workshop Advances in Information, Electronic and Electrical Engineering (AIEEE 2015) Proceedings, Riga, 2015.* Place: IEEE, 2016, pp. 1-4. ISBN 978-1-5090-1202-2. e-ISBN 978-1-5090-1201-5. Available from: doi: 10.1109/AIEEE.2015.7367294
68. Mitsubishi Electric. *Elevators & Escalators* [online]. [Viewed December 2021]. Available from: https://www.mitsubishielectric.com/elevator/modernization/elevator_index.html
69. Magnum Elevators & Co. *Magnum Elevators-Green Energy* [online]. [Viewed December 2021]. Available from: http://magnumelevators.com/green_energy.php
70. DAIMLER AG. *Robotersystem.* Michael Lebrecht, Thomas Schneider. Germany. Int. Cl.: B25J 9/10 (2006.01).
71. ABB. *Technical guide No. 8 Electrical braking* [online]. [Viewed April.2021]. Available from: https://library.e.abb.com/public/20be376000f34dd6b9c513580cf56423/ Technical_guide_No_8_3AFE64362534_RevC.pdf

72. Thounthong, P., Davat, B. Study of a multiphase interleaved step-up converter for fuel cell high power applications. *Energy Conversion and Management*. 2010, vol.51, no.4, pp.826-832. ISSN 0196-8904. e-ISSN 1879-2227. Available from: doi: 10.1016/j.enconman.2009.11.018
73. Ramesh, V., Anjappa, P., Dhanamjaya, P. Two Parallel Single Phase Rectifiers by Using Single Phase to Three Phase Induction Motor. *International Journal of Research in Engineering and Technology*. 2013, vol.2, no.10, pp.441-452. ISSN 2321-7308. e-ISSN 2319-1163. Available from: doi: 10.15623/ijret.2013.0210067
74. Thanyaphirak, V., Kinnares, V., Kunakorn, A. Soft starting control scheme for three-phase induction motor fed by PWM AC chopper. In: *2014 17th International Conference on Electrical Machines and Systems (ICEMS) Proceedings, Hangzhou, 2014.* Place: IEEE, 2015, pp. 92-95. e-ISBN 978-1-4799-5162-8. Available from: doi: 10.1109/ICEMS.2014.7013460
75. Senfelds, A., Vorobjovs, M., Meike, D., Bormanis, O. Power smoothing approach within industrial DC microgrid with supercapacitor storage for robotic manufacturing application. In: *2015 IEEE International Conference on Automation Science and Engineering (CASE) Proceedings, Gothenburg, 2015.* Place: IEEE, 2015, pp. 1333-1338. e-ISBN 978-1-4673-8183-3. ISSN 2161-8070. e-ISSN 2161-8089. Available from: doi: 10.1109/CoASE.2015.7294283
76. Šenfelds, A., Bormanis, O., Paugurs, A. Analytical Approach for Industrial Microgrid Infeed Peak Power Dimensioning. In: *2016 57th International Scientific Conference on Power and Electrical Engineering of Riga Technical University (RTUCON 2016) Proceedings, Riga, 2016.* Place: IEEE, 2016, pp. 1-4. ISBN 978-1-5090-3732-2. e-ISBN 978-1-5090-3731-5. Available from: doi: 10.1109/RTUCON.2016.7763140
77. Clark, D. *Power Blip Jolts Supply of Gadget Chips* [online]. Place: The Wall Street Journal, 2010 [viewed April 2020]. Available from: http://www.wsj.com/articles/SB10001424052748703766704576009071694055878
78. Cremer, A. *VW says power loss cut German plant output more than expected* [online]. Place: Reuters, 2014 [Viewed April 2021]. Available from: http://europe.autonews.com/article/20140310/ANE/140319991/vw-says-power-loss-cut-german-plant-output-more-than-expected
79. Dropbeats Technology Co.,Ltd. *DB2021ECB Wideband PLC DB2021ECB Module Specification 1.0.4* [online]. [Viewed February 2022]. Available from: http://www.dropbeats.com/zh/images/pdf/DB2021ECB.pdf
80. SIA Mikrotīkls. *PL6411-2nD Block Diagram* [online]. [Viewed January 2022]. Available from: https://i.mt.lv/cdn/product_files/PL7411-2nD_181220.png
81. Constantinides, K., Mutlu, O., Austin, T.M., Bertacco, V. A Flexible Software-Based Framework for Online Detection of Hardware Defects. *IEEE Transactions on Computers*. 2009, vol.58, no.8., pp:1063-1079. ISSN 0018-9340. e-ISSN 1557-9956. Available from: doi: 10.1109/TC.2009.52

82. Blattau, N. *HALT and Sherlock Automated Design Analysis Software* [PowerPoint slides]. Place: DfR Solutions, Beltsville, 2014.
83. Grand View Research, Inc.. *Electronic Contract Manufacturing And Design Services Market Report, 2030* [online]. [Viewed January 2021]. Available from: https://www.grandviewresearch.com/industry-analysis/the-global-electronic-contract-manufacturing-services-market
84. Mark Evans Consulting. *How Much Of A Startup's Operations Should Be Outsourced?* [Online]. Place: Marketing Spark, 2016 [viewed March 2018]. Available from: http://www.markevans.ca/2016/08/23/
85. Evans, M. *6 Key Areas To Outsource When Starting A Business* [online]. Place: Forbes, 2015 [viewed March 2018]. Available from: https://www.forbes.com/sites/allbusiness
86. Loo, W.T. *The Next Big Thing in Consumer Electronics is Already Here* [online]. Place: Euromonitor International, 2014 [viewed March 2018]. Available from: https://www.euromonitor.com/article/the-next-big-thing-in-consumer-electronics-is-already-here
87. Initial State Technologies, Inc. *Late-to-Market Calculator* [online]. [Viewed January 2022]. Available from: https://www.initialstate.com/latecalc/
88. Keithley Instruments, Inc. *Fundamentals of HALT/HASS Testing* [online]. Place: Tektronix, 2000 [viewed January 2022]. Available from: https://download.tek.com/document/HALT_HASS_WP.pdf
89. Hobbs, G.K. *Accelerated Reliability Engineering: HALT & HASS*. Denver: Hobbs Engineering Corporation, 2005, 229 p. ISBN: 978-0615128337.
90. Song, Y., Wang, B. Survey on reliability of power electronic systems. *IEEE Transactions on Power Electronics*. 2012, vol.28, no.1, pp.591–604. ISSN 0885-8993. e-ISSN 1941-0107. Available from: doi:10.1109/TPEL.2012.2192503
91. Silverman, M. *Design for Reliability (DFR) Seminar* [PowerPoint slides]. Place: Ops A La Carte LLC, 2011. Available from: https://www.slideshare.net/fms95032/design-for-reliability-dfr-seminar-13813404
92. Verbitsky, D.E. Improving aerospace electronics by systemic early failure analysis during development and modification. In: *2015 IEEE Aerospace Conference, Big Sky, 2015.* Place: IEEE, 2015, pp. 1-15. ISSN 1095-323X. Available from: doi: 10.1109/AERO.2015.7118892
93. Meadowsong N., Kyser, E.L., Cisco Systems. *The Benefits and Costs of Overstress Testing* [online]. Place: Electronic Design, 2003 [viewed November 2020]. Available from: https://www.electronicdesign.com/home/article/21200807/benefits-and-costs-of-overstress-testing
94. Rhoads, J.M. *Design for Reliability Handbook*. Maryland: US Army Materiel Systems Analysis Activity, 2011. Available from: https://www.scribd.com/document/453673418/Design-for-Reliability-Handbook-TR-2011-24

95. Das, D. *ESS and HASS: Concerns with the Practices and Standards* [PowerPoint slides]. Place: Center for Advanced Life Cycle Engineering, 2016. Available from: https://www.slideshare.net/HPERERA/ess-and-hass-concerns-with-the-practices-and-standards
96. Bormanis, O., Ribickis, L. Accelerated Life Testing in Reliability Evaluation of Power Electronics Assemblies. In: *2018 IEEE 59th International Scientific Conference on Power and Electrical Engineering of Riga Technical University (RTUCON 2018), Proceedings, Riga, 2018.* Place: IEEE, 2019, pp. 1-5. ISBN 978-1-5386-6904-4. e-ISBN 978-1-5386-6903-7. Available from: doi: 10.1109/RTUCON.2018.8659911
97. McLean, H. *HALT, HASS and HASA Explained: Accelerated Reliability Techniques*. Milwaukee: ASQ Quality Press, 2000, 194 p. ISBN: 978-0-87389-766-2.
98. Koschmieder, T. *FSL Product Package Mechanical Reliability Testing FTF-ENT-F0557* [PowerPoint slides]. Place: Freescale Semiconductor, Inc., 2011. Available from: https://www.nxp.com/files-static/training_pdf/WBNR_FTF11_ENT_F0557.pdf
99. MacDiarmid, A. *Thermal Cycling Failures* [online]. Place: RIAC Journal, 2011 [viewed January 2022]. Available from: https://permanent.fdlp.gov/gpo155271/RIACjournalJAN11_WEB.pdf
100. Reid, P. The Impact of Lead-Free Processing on Interconnect Reliability. *Printed Circuit Design & Manufacture*. 2007, vol.24, no.3, pp.37-39. ISSN 1543-6527. e-ISSN 1543-6527.
101. Steinberg, D.S. *Vibration analysis for electronic equipment.* Hoboken: John Wiley & Sons, 2000, 414 p. ISBN: 978-0471376859.
102. Integrated Service Technology Inc. *PCBA/System Level Reliability Test* [online]. [Viewed March 2018]. Available from: http://www.istgroup.com
103. Amphenol Mobile Consumer Products. *Capabilities* [online]. [Viewed March 2018]. Available from: http://www.amphenol-tm.com/
104. Adaptertek Technology Co., Ltd. *Reliability Test Equipment* [online]. [Viewed March 2018]. Available from: http://www.adaptertek.com.tw/
105. Mi, J., Li, Y-F., Yang, Y-J., Peng, W., Huang, H-Z. Thermal Cycling Life Prediction of SN-3.0Ag-0.5Cu Solder Joint Using Type-I Censored Data. *The Scientific World Journal*. 2014, vol.2014, no.9, pp.1-11. ISSN 2356-6140. e-ISSN 1537-744X, Available from: doi: 10.1155/2014/807693
106. McPherson, J. W. *Reliability Physics and Engineering*. New York City: Springer Cham, 2010, 165 p. ISBN: 978-3-319-93682-6.
107. Maxwell, J. *Capacitor Cracks: Still with Us after All These Years* [online]. Place: Johanson Dielectrics Inc., 2006 [viewed November 2020]. Available from: http://www.johansondielectrics.com/
108. Qualmark. *What is HALT HASS testing?* [online]. [Viewed November 2020]. Available from: https://www.qualmark.com/whatishalthass

109. CONTROLTECNICA. *Cámaras Halt & Hass serie VTC* [online]. [Viewed December 2021]. Available from: https://www.controltecnica.com/test/producto/camaras-halt-hass-serie-vtc/
110. Bergès, C., Chung, S. Innovative methodology in automotive semiconductors for statistical correlation study between reliability accelerated stress tests and real field applications. In: *2017 IEEE 24th International Symposium on the Physical and Failure Analysis of Integrated Circuits (IPFA) Proceedings, Chengdu, 2017.* Place: IEEE, 2017, pp. 1-6. ISBN 978-1-5386-1780-9. e-ISBN 978-1-5386-1779-3. ISSN 1946-1550. e-ISSN. Available from: doi: 10.1109/IPFA.2017.8060098
111. Bullema, J. E. *Accelerated testing: ALT, HALT and MEOST* [PowerPoint slides]. Place: TNO, 2017. Available from: https://www.slideshare.net/JanEiteBullema/2017-accelerated-testing-alt-halt-and-meost
112. Bhote, K.R., Bhote, A.K. *World Class Quality: Using Design of Experiments to Make it Happen*. New York: AMACOM, 2000, 512 p. ISBN: 978-0814404270.
113. TDK Corporation. *Flex Crack Countermeasures in MLCC (Multilayer Ceramic Chip Capacitors)* [online]. [Viewed November 2020]. Available from: https://product.tdk.com/info/en/products/capacitor/index.html
114. Kreucher, J. *Multiple Environment Over Stress Testing (MEOST). A Primer with Examples from an Automotive Component Supplier* [PowerPoint slides]. Place: Delphi Powertrain, 2011. Available from: https://static1.squarespace.com/static/515082bbe4b0910b244269db/t/516d6c79e4b0f84b6313bb9e/1366125689604/MEOST+Webinar.pdf
115. Doertenbach, N. *The Calculation of Grms* [online]. Place: Electronic Products, 2014 [viewed November 2020]. Available from: https://www.electronicproducts.com
116. Babbie, E.R. *The Practice of Social Research*. 14th ed. Belmont: Cengage Learning, 2010, 592 p. ISBN: 978-1305104945.
117. HBM Prenscia Inc. *Quantitative Accelerated Life Testing Data Analysis* [online]. [Viewed November 2020]. Available from: http://www.weibull.com/basics/accelerated.htm
118. Jayatilleka, S., Okogbaa, G. *Accelerated Life Testing (ALT)* [PowerPoint slides] Place: Minneapolis, 2014.
119. Mettas, A., Vassiliou, P. Modeling and Analysis of Time-Dependent Stress Accelerated Life Data. In: *Annual Reliability and Maintainability Symposium. 2002 (Cat. No.02CH37318) Proceedings, Seattle, 2002.* Place: IEEE, 2002, pp. 343-348. ISBN 0-7803-7348-0. ISSN 0149-144X. Available from: doi: 10.1109/RAMS.2002.981665
120. Lipson, C., Sheth, N. *Statistical Design and Analysis of Engineering Experiments*. New York: McGraw-Hill Book Company, 1973, 448 p. ISBN: 978-0070854475.
121. Edward, V. T. *A Statistical Perspective on Highly Accelerated Testing* [online]. Place: Sandia National Laboratories, 2015 [Viewed November 2020]. Available from: https://www.osti.gov/servlets/purl/1170512

122. Misra, K.B. *Handbook of Performability Engineering*. London: Springer, 2008, p. 539 p. ISBN: 978-1848001305.
123. Danto, Y., Deletage, J.Y., Verdier, F., Fremont, H. *Evaluation of Reliability Assessment in PCB Assemblies*. In: SBMICRO - XVI International Conference on Microelectronics and Packaging Proceedings, Pirenopolis, 2001.
124. Wenting, L., Jiang, L., Zongyou, X., Guangping, Q., Hu, Z. Step-stress accelerated life testing to predict service life for space vehicle electrical system. In: *2016 IEEE Chinese Guidance, Navigation and Control Conference (CGNCC) Proceedings, Nanjing, 2016*. Place: IEEE, 2017, pp. 1120-1125. ISBN 978-1-4673-8319-6. e-ISBN 978-1-4673-8318-9. Available from: doi: 10.1109/CGNCC.2016.7828945
125. CALCE Electronic Products and Systems Center. *Design and Process Guidelines for Use of Ceramic Chip Capacitors* [online]. [Viewed November 2020]. Available from: http://www.ieca-inc.com/technicalexpertisecapabilitiesservices.html
126. ZVEI. *Handbook of Robustness Validation* [online]. [Viewed November 2020]. Available from: https://www.zvei.org/fileadmin/user_upload/Presse_und_Medien/Publikationen/2013/Oktober/Handbook_for_Robustness_Validation_of_Automotive_Electrical/Robust-Validation-EE-Modules.pdf
127. Fujitsu Quality Laboratory Ltd. *Services Reliability* [online]. [Viewed November 2020]. Available from: https://www.fujitsu.com/us/about/local/corporate/subsidiaries/fai/reliability/services/
128. O'Connor, P. Arrhenius and Electronics Reliability. *Quality and Reliability Engineering International*. 1989, vol.5, no.5, pp.255. ISSN 0748-8017. e-ISSN 1099-1638. Available from:10.1002/qre.4680050402
129. Minitab Inc. *Example for Accelerated Life Testing* [online]. [Viewed November 2020]. Available from: https://support.minitab.com
130. Murata Manufacturing Co., Ltd. *Reliability of electronic components (Chapter 2: How do you estimate the lifetime of components?)* [online]. [Viewed November 2020]. Available from: https://www.murata.com/en-us/products/emiconfun/
131. Murata Manufacturing Co., Ltd. *Failure mode & its cause of MLCC* [online]. [Viewed November 2020]. Available from: https://www.murata.com/-/media/webrenewal/support/faqs/products/capacitor/ceramiccapacitor/qlty/0015/failuremodecauseofmlcc.ashx?la=en-sg&cvid=20180115054747448400
132. Kaknevicius, A., Hoover, A. *Application Report SLVA670A Managing Inrush Current* [online]. Place: Texas Instruments, 2015 [viewed November 2020]. Available from: https://www.ti.com/lit/an/slva670a/slva670a.pdf?ts=1666686750380
133. ReliaSoft Corporation. *How Long Should You Burn In a System?* [online]. Place: Reliability HotWire, 2006 [viewed November 2020]. Available from: https://www.weibull.com/hotwire/issue69/relbasics69.htm

134. Kuo, W., Chien, W.-T.K., Kim, T. *Reliability, Yield, and Stress Burn-in: A Unified Approach for Microelectronics Systems Manufacturing & Software development*. Berlin: Springer Science+Business Media, 1998, 420 p. ISBN: 978-0792381075.
135. Electronic Environment. *Examples of common wear out or overstress failure mechanisms* [online]. [Viewed April 2020]. Available from: https://www.electronic.se/wp-content/uploads/2015/03/skarmavbild-2015-03-09-kl.-14.35.09-572x600.png
136. IPC International, Inc. *IPC-SM-785. Guidelines for Accelerated Reliability Testing of Surface Mount Solder Attachments* [online]. [Viewed April 2020]. Available from: https://www.scribd.com/document/467143203/IPC-SM-785
137. ReliaSoft Corporation. *Quantifying Optimum Burn-in Period* [online]. Place: Reliability HotWire, 2005 [viewed November 2020]. Available from: https://www.weibull.com/hotwire/issue58/hottopics58.htm
138. Warwick Manufacturing Group. *Product Excellence Using Six Sigma. Section 12. Failure Modes, Effects & Criticality Analysis* [online]. Place: University of Warwick, 2007 [viewed November 2020]. Available from: https://fdocuments.net/document/failure-modes-effects-criticality-analysis.html?page=1
139. IPC International, Inc. *IPC-9701A. Performance Test Methods and Qualification Requirements for Surface Mount Solder Attachments* [online]. [Viewed April 2020]. Available from: https://standards.globalspec.com/std/641918/IPC-9701
140. McNally, L. *Application Report, SPRABY2-March 2015, Board Level Reliability Primer for Embedded Processors* [online]. Place: Texas Instruments, 2015 [viewed April 2020]. Available from: https://www.ti.com/lit/an/spraby2/spraby2.pdf?ts=1666762775505
141. Cheon, S., Jeong, H., Hwang, S.Y., Hong, S., Domblesky, J., Kim, N. Accelerated Life Testing to Predict Service Life and Reliability for an Appliance Door Hinge. *Procedia Manufacturing*. 2015, vol.1, pp.169–180. ISSN 2351-9789. e-ISSN 2351-9789. Available from: doi: 10.1016/j.promfg.2015.09.082
142. Narayanan, P., Mini, V.P. Study on Energy Efficient Burn-In Techniques for Power Supplies. In: *2014 International Conference on Advances in Green Energy (ICAGE) Proceedings, Trivandrum, 2014.* Place: IEEE, 2015, pp. 204-209. e-ISBN 978-1-4799-8050-5. Available from: doi: 10.1109/ICAGE.2014.7050166
143. Kececioglu, D., Sun, F.B. *Burn-In Testing, Its Quantification and Optimization*. New Jersey: Prentice Hall, 1997, 704 p. ISBN: 978-0133242119.
144. Lasance, C. *Temperature and reliability in electronics systems – the missing link* [online]. Place: Electronics Cooling Magazine, 2001 [viewed April 2020]. Available from: https://www.electronics-cooling.com/2001/11/temperature-and-reliability-in-electronics-systems-the-missing-link/
145. Hobbs, G.K. *The History of HALT and HASS* [online]. Place: Sound & Vibration Magazine, 2002 [viewed April 2020]. Available from: http://www.sandv.com/oct02.shtml

146. Gray, K.A., Paschkewitz, J.J. *Next Generation HALT and HASS, Robust Design of Electronics and Systems.* Hoboken: John Wiley and Sons, 2016, 267 p. ISBN: 978-1118700235.
147. Delserro Engineering Solutions. *HALT & HASS: Accelerated Life Test, Accelerated Stress Screening* [online]. [Viewed April 2020]. Available from: https://www.desolutions.com/blog/2013/02/halt-hass-informational-guide/
148. TT Electronics-IMS. *HALT, HASS and ESS* [online]. [Viewed January 2018]. Available from: http://www.ttelectronics-ims.com/testing/halt-hass-and-ess
149. McLinn, J.A. HALTs from Hell. In: *2015 Annual Reliability and Maintainability Symposium (RAMS) Proceedings, Palm Harbor, 2015*. Place: IEEE, 2015, pp. 1-7. ISSN 0149-144X. Available from: doi: 10.1109/RAMS.2015.7105191
150. ESPEC North America, Inc. *Why HASS works* [online]. [Viewed January 2018]. Available from: https://www.qualmark.com/whatishalthass/whyhassworks
151. Liu, D.D., Sampson, M.J. Some Aspects of the Failure Mechanisms in BaTiO3-Based Multilayer Ceramic Capacitors. In: *CARTS International 2012 Proceedings, Las Vegas, 2012.* Place: Curran Associates, Inc., 2013, pp. 49-61. ISBN 978-162748136-6.
152. Thermotron Inc. *AST for HALT/HASS Testing* [online]. [Viewed January 2018]. Available from: http://thermotron.com/equipment.html
153. Weiss Technik. *SIGMA HALT-HASS Test Chambers* [online]. [Viewed January 2018]. Available from: http://weiss-uk.com/products
154. Vendrusculo, E.A., Pomilio, J.A. High-Efficiency Regenerative Electronic Load Using Capacitive Idling Converter for Power Sources Testing. In: *PESC Record. 27th Annual IEEE Power Electronics Specialists Conference Proceedings, Baveno, 1996.* Place: IEEE, 2002, pp. 969-974. ISBN 0-7803-3500-7. ISSN 0275-9306. Available from: doi: 10.1109/PESC.1996.548699
155. Cooper, J. Introduction to HALT – making your product robust. In: *2017 Pan Pacific Microelectronics Symposium (Pan Pacific) Proceedings, Kauai, 2017.* Place: IEEE, 2017, pp. 1-5. ISBN 978-1-5090-4342-2. e-ISBN 978-1-944543-01-3.
156. Bahret, A. *ESS and HASS* [online]. Place: Apex Ridge Reliability, 2016 [viewed January 2018]. Available from: https://apexridge.com/blog-37/
157. Mao, W. *An introduction to HALT, HASS HASA, and CALT* [online]. [Viewed March 2018]. Available from: https://pt.slideshare.net/WinsonMao/alt-51413823
158. Doertenbach, N. Highly accelerated life testing - Testing with a different purpose. *S V, Sound and Vibration*. 2001, vol.35, no.3, pp.18-23. ISSN 0038-1810.
159. Honeywell, Inc. *Highly Accelerated Life Testing and Highly Accelerated Stress Screening (HALT/HASS) Guidelines*. Place: Minneapolis.
160. Technology Training, Inc. *Accelerated Testing: ESS, HALT & HASS, Course No.240* [online]. [Viewed March 2018]. Available from: https://ttiedu.com/course_outline?tid=34

161. Peterson, C. *HALT and HASS, HALT testing, HASS test* [online]. Place: Environmental & Technical Services Ltd., 2007 [viewed January 2018]. Available from: https://www.ets.co.uk/previous-features/1007.php
162. HALT & HASS Consulting Nz Ltd. *HASS Testing Introduction* [online]. [Viewed January 2018]. Available from: http://www.halthass.co.nz/library-and-useful-resources/halt-and-hass-information/hass-testing-introduction/
163. Bormanis, O., Ribickis, L. Review of Burn-In for Production of Reliable Power Electronic Applications. In: *2019 IEEE 60th International Scientific Conference on Power and Electrical Engineering of Riga Technical University (RTUCON 2019) Proceedings, Riga, 2019.* Place: IEEE, 2020, pp. 1-7. ISBN 978-1-7281-3943-2. e-ISBN 978-1-7281-3942-5. Available from: doi: 10.1109/RTUCON48111.2019.8982357
164. Hnatek, E. R. *Practical Reliability of Electronic Equipment and Products*. Boca Raton: CRC Press, 2002, 472 p. ISBN: 978-0824708320.
165. Dongguan Rico Electronic Co., Ltd. *Burn In Test Area* [online]. [Viewed April 2018]. Available from: http://www.rico-electronic.net
166. Parasrampuria, M., Jain, S. *Burn-in 101* [online]. Place: AspenCore Inc., 2014 [viewed April 2018]. Available from: https://www.edn.com/design/integrated-circuit-design/
167. Thomas Publishing Company. *Burn-In Systems* [online]. [Viewed April 2018]. Available from: https://www.thomasnet.com/articles/
168. Keithley Instruments, Inc. *Burn-in Testing Techniques for Switching Power Supplies* [online]. Place: Tektronix, 2014 [viewed April 2018]. Available from: https://download.tek.com/document/TestingTechniques_SwitchingPwrSupplies.pdf
169. Benbow, D., Broome, H. *The Certified Reliability Engineer Handbook*. 2nd ed. Milwaukee: ASQ Quality Press, 2013, 360 p. ISBN: 978-0873898379.
170. Kececioglu, D., Sun, F.B. *Burn-In Testing, Its Quantification and Optimization*. New Jersey: Prentice Hall, 1997, 704 p. ISBN: 978-0133242119.

APPENDICES

A: Abbreviations

Abbreviation	Term
2D	Two Dimensional
3D	Three Dimensional
A1,…, A6	Number of Robot Axis 1 to 6
AC	Alternating Current
ADC	Analog-Digital Converter
AG	Aktiengesellschaft (German), Public Limited Company
API	Application Programming Interface
AREUS	Automation and Robotics for European Sustainable Manufacturing
CPU	Central Processing Unit
DC	Direct Current
DOF	Degrees of Freedom
FEM	Finite Element Method
HALT	Highly Accelerated Life Test
IGBT	Isolated Gate Bipolar Transistor
KPP	KUKA Power Pack
KRL	KUKA Robot Language
KSP	KUKA Servo Pack
KUKA	Keller und Knappich Augsburg, KUKA Roboter GmbH
LC	Lifetime Consumption
MEOST	Multiple Environment Overstress Test
PCBA	Printed Circuit Board Assembly
PLC	Programmable Logic Controller
PMSM	Permanent Magnet Synchronous Servo Motor
PWM	Pulse Width Modulation
RCS	Robot Control Simulation
RRS	Realistic Robot Simulation

B: Multiple Robot System Example

For research purposes 60 seconds were chosen as duration for the simulated production process of 4 industrial manipulator (R_1, .., R_4) movement and tool operation in a hardware layout with centralized power supply. As shown in Fig. 5.1, welding operation with 5 interactions was added to robot R_2, clinching operation with 5 interactions was performed by robot R_4, and gluing operation lasting 6 seconds was performed by robot R_3.

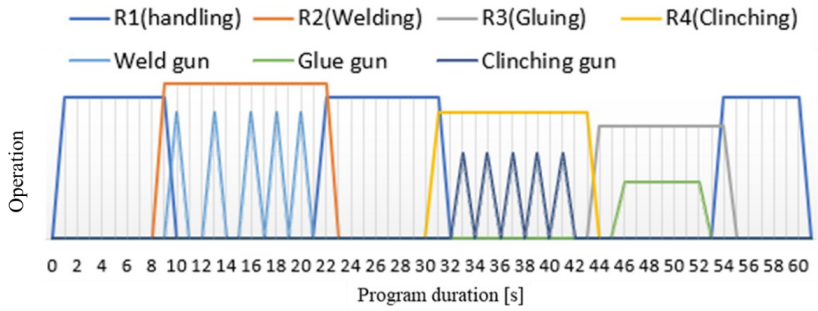

Fig. 5.1. Illustrative timetable of process scheduling in modeled industrial cell.

Process starts by handling of part by robot R_1. It inserts and positions part at the cell. Average power consumption throughout the first operation with assumed load weight of 125 kg is 3.82 kW. Part is positioned and after 3 seconds robot returns to home position.

Robot R_2 equipped with spot welding tool reaches to five programmed welding operation positions. Average power consumption throughout the operation of robot R_2 is 2.65 kW with assumed load weight of 180 kg, movement duration of 13.66 seconds, and welding points at seconds: 1, 4, 5, 6, 8, 11.

Before clinching at 5 positions is carried out by robot R_4, position of part is changed by handling robot R_1 in 10.25 seconds long movement. Average power consumption is 3.70 kW with decelerating to standstill at seconds 2 and 7, simulating pick up and pick down of part.

Movement of clinching robot R_4 is scheduled to last 12.54 seconds with a tool weight of 150 kg. Robot stops at 5 points throughout the movement, with an average power consumption of 2.11 kW. From programming point of view, clinching is similar to spot welding.

Glue application is supported by robot R_3, and part is moved to output of production cell by R_1 as soon as the gluing process lasting several seconds is completed. Movement of R_3 lasts 11.10 seconds, and average power consumption throughout the operation of robot R_3 is 2.12 kW. Glue application is a movement speed sensitive operation, therefore robot is programmed to decrease speed after approach to part is complete for improved quality.

Movement of processed part to output of production cell by R_1 lasts 7.16 seconds, and average power consumption is 3.28 kW. There are two scheduled stops, one at part pick up and one at release. Part weight remains 125 kg as previously, but it could increase as well after welding operations.

C: Data of KUKA Industrial Robot Motor Drive Inverters

Table 5.1

Voltage, power, frequency and efficiency data of KUKA KSP 600-3x40

KUKA KSP 600-3x40	Cable layout	Voltage type	Rated		Rated power [kW]	Frequency range	Efficiency
			Voltage	Current			
Input	2/PE	DC	565/675 V	25 A			
Output	2/PE	DC	565/675 V	25 A	14/17		
3x Output AC	3/PE	AC	400/480 V	30 A	12/14	0-500 Hz	94 %

Table 5.2

Voltage, power, frequency and efficiency data of KUKA KSP 600-3x20

KUKA KSP 600-3x20	Cable layout	Voltage type	Rated		Max Current	Rated power [kW]	Frequency range
			Voltage	Current			
Input	2/PE	DC	565/675 V	25 A			
Output	2/PE	DC	565/675 V	25 A		14/17	
3x Output AC	3/PE	AC	400/480 V	9 A	20 A	6/7	0-500 Hz

D: Torque of Robot Axis

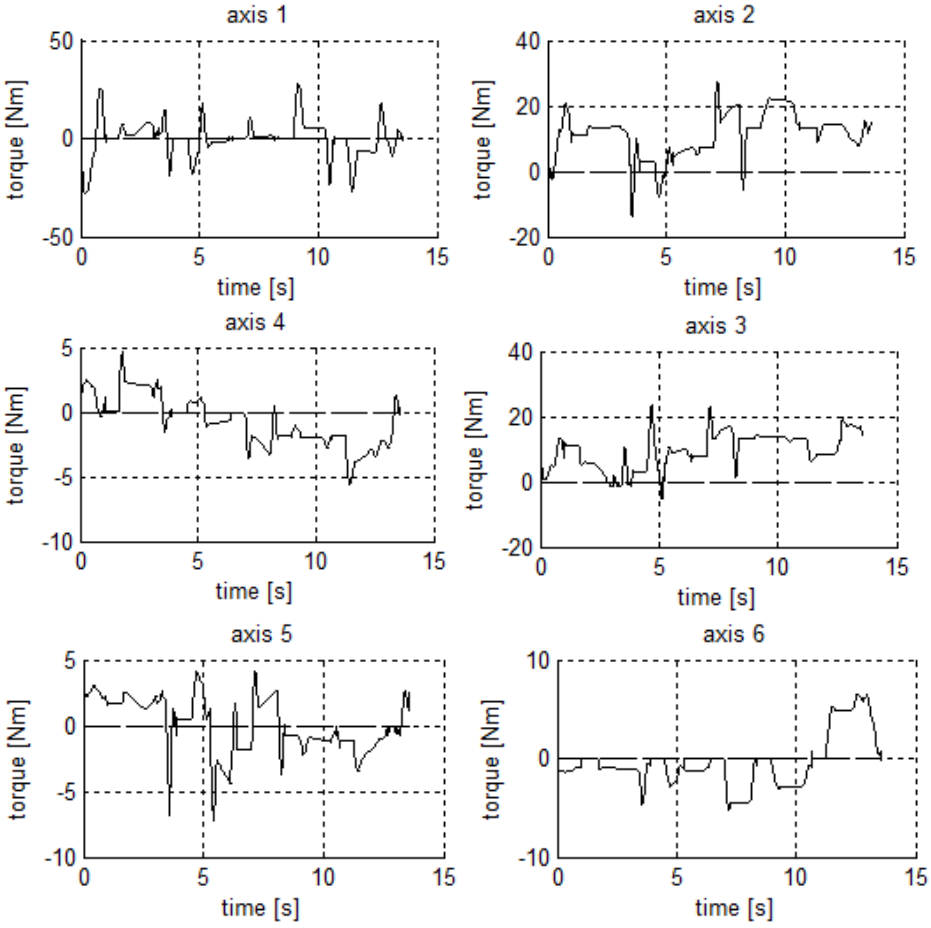

Fig. 5.2. Torque translation for each of six degree of freedom industrial robot servo motors through simulated sample welding program.

E: Current Consumption of Axis 1-6 Motors

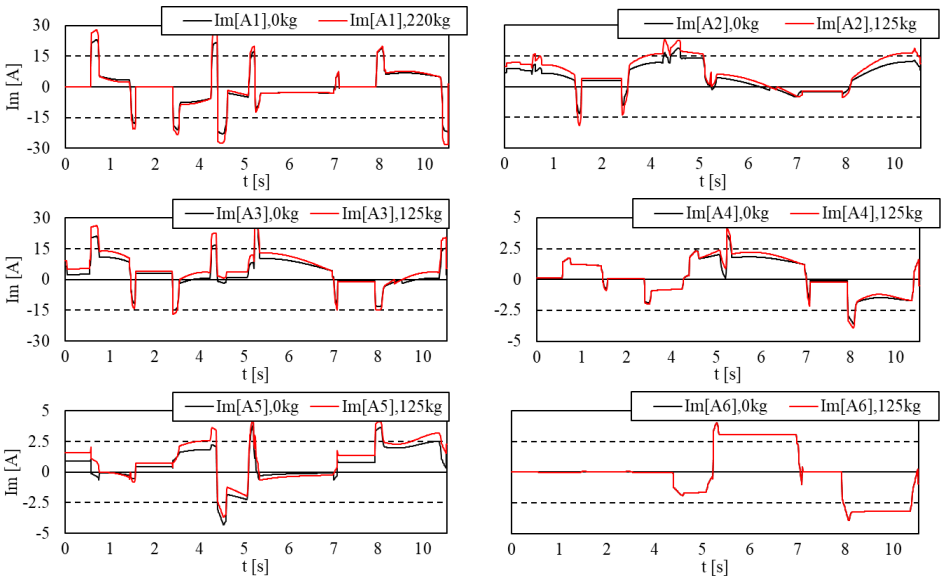

Fig. 5.3. Current consumption of each robot axis motors during handling program ("case_handling_1") simulated with two load weights - 0 kg and 125 kg.

F: Junction Temperature of Axis 1-3 Inverter Power Transistors

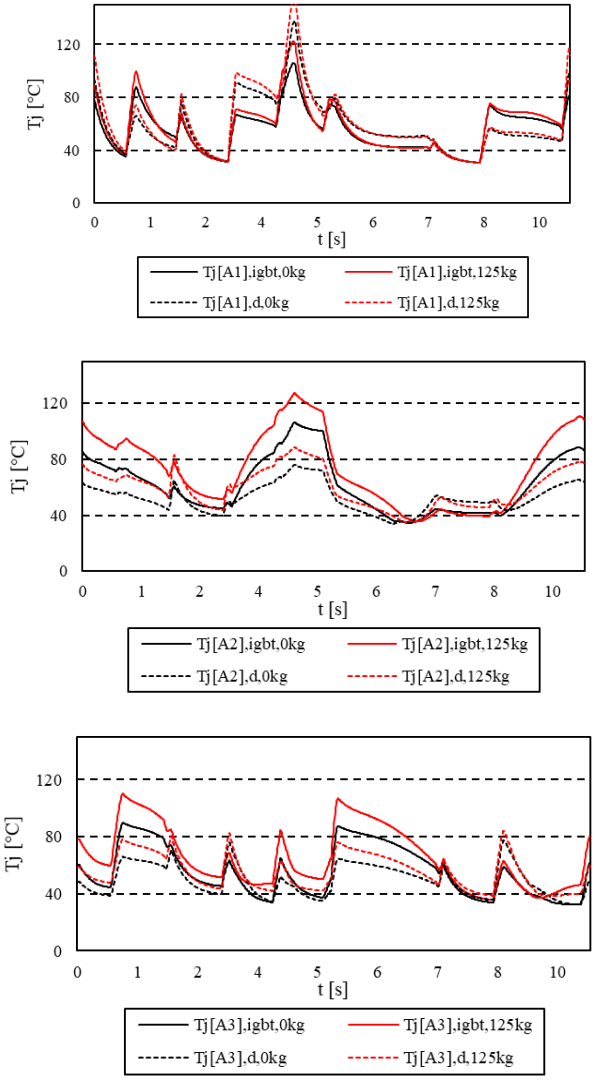

Fig. 5.4. Axis 1-3 inverter IGBT and anti-parallel diode junction temperature data of sample handling program, with 0 kg and 125 kg load.

G: Filtered Junction Temperature Data Arranged in Bins

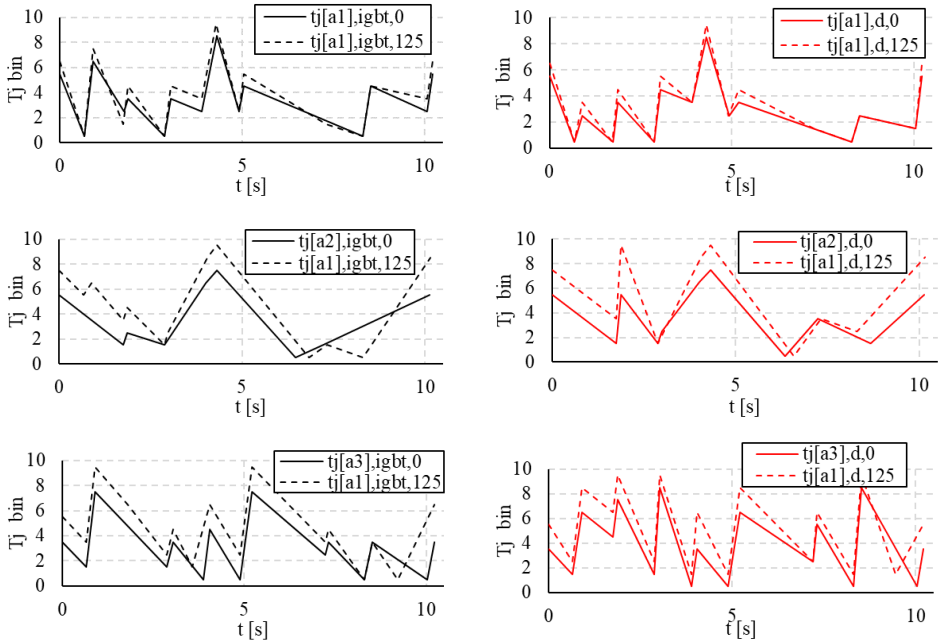

Fig. 5.5. 6 degree of freedom industrial robot axis 1-3 inverter IGBT and anti-parallel diode junction temperature data arranged in discrete bins of the sample handling program with two load weights, 0 kg and 125 kg.

H: Number of Cycles and Half Cycles After Rainflow Counting

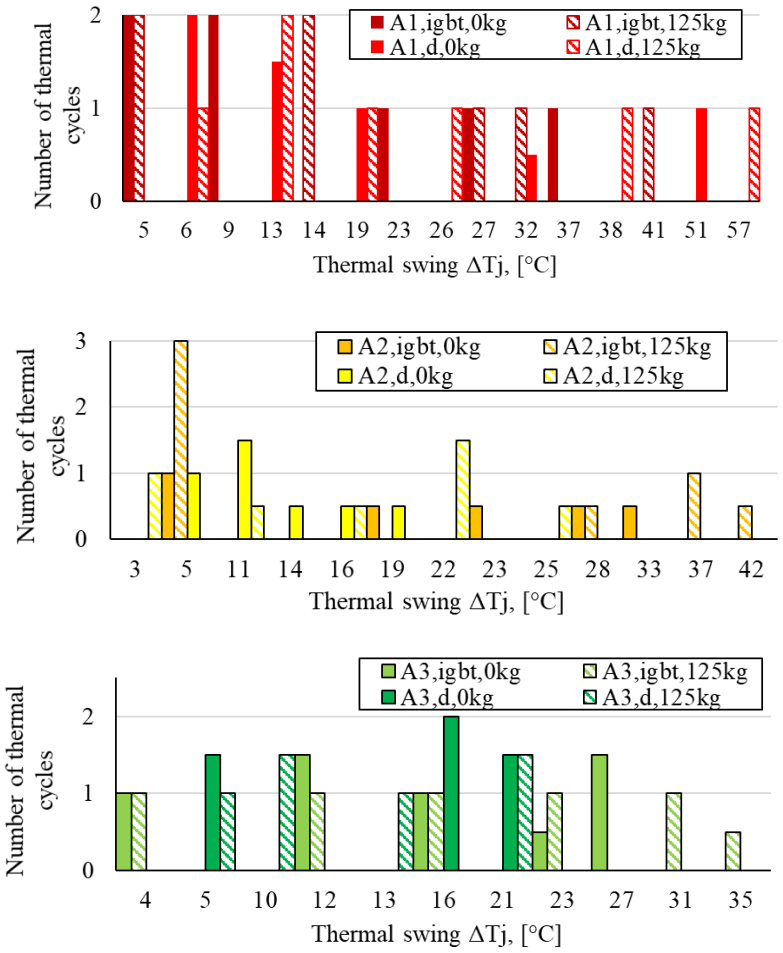

Fig. 5.6. Quantity of junction temperature cycles and half cycles for each robot axis after Rainflow cycle counting, sorted by thermal swing and load weight.

I: Estimated Lifetime Consumption of 0 kg and 125 kg Tool Weight

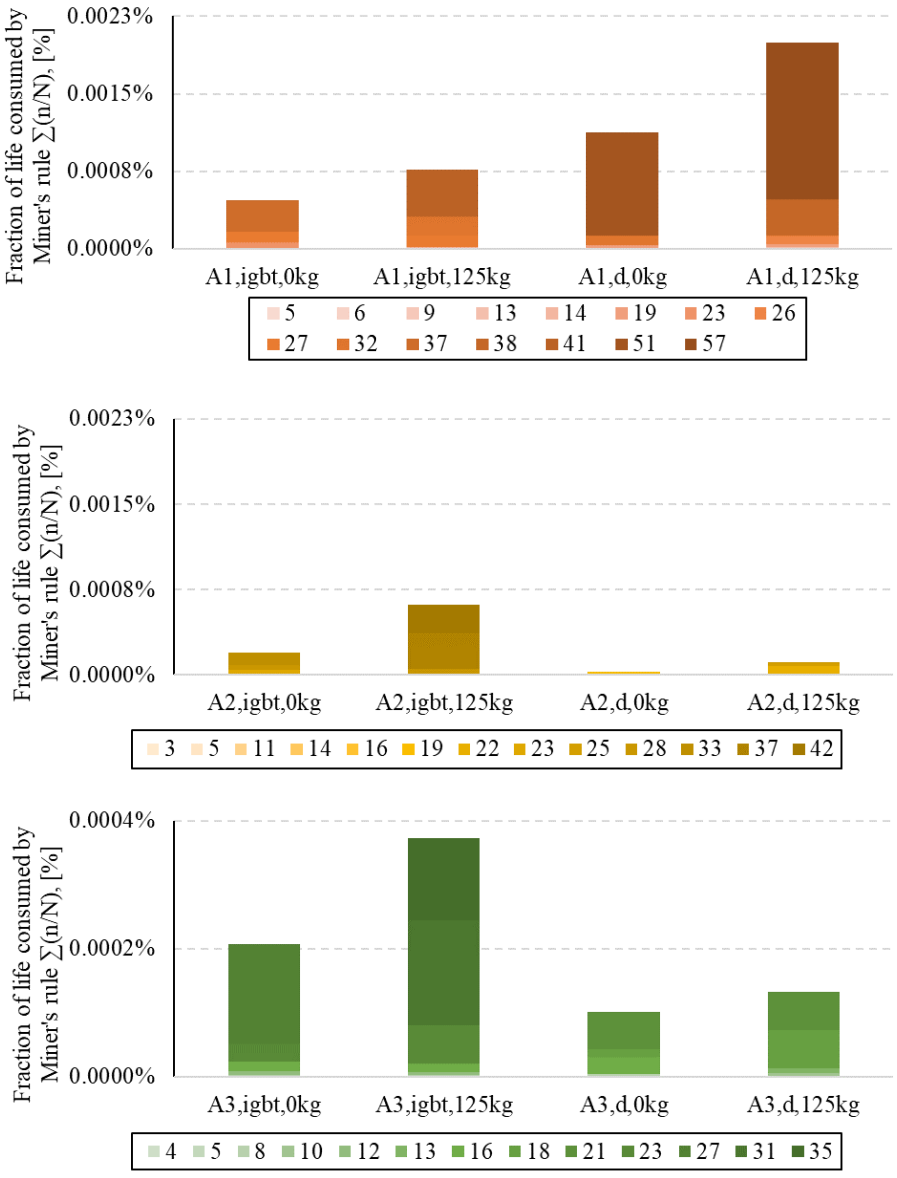

Fig. 5.7. Estimated lifetime consumption of 0 kg and 125 kg tool weight handling program, on IGBT and anti-parallel diode of A1−A3 robot axis inverter IGBT module.

J: Junction Temperature of Sample Robot Applications

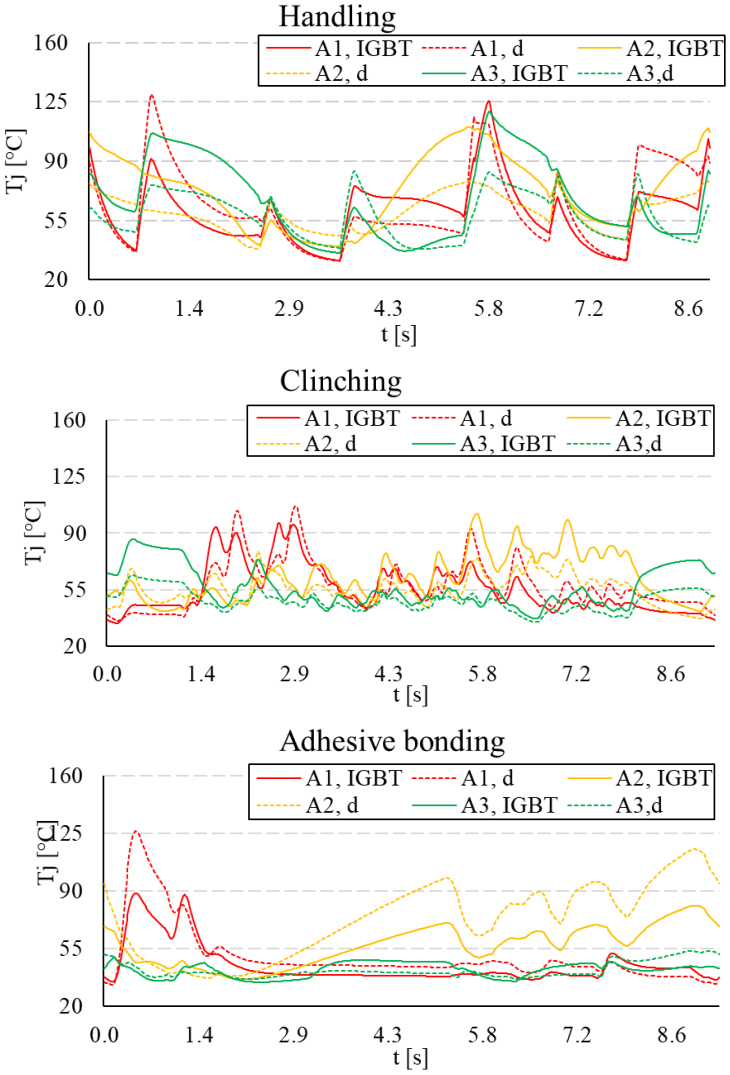

Fig. 5.8. Simulated junction temperature of robot axis 1-3 inverter IGBT modules and anti-parallel diodes, during sample welding, handling, clinching and adhesive bonding applications.

K: Junction Temperature Change Data for Sample Robot Applications

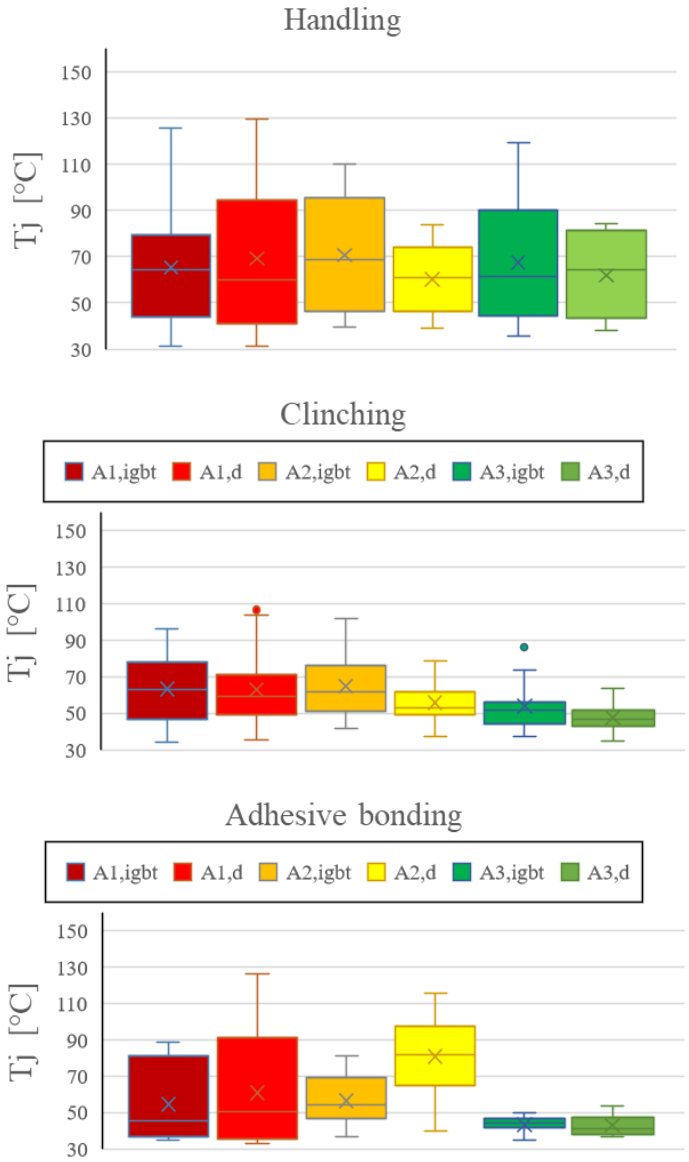

Fig. 5.9. Highest peak value, temperature change amplitude and mean value of robot axis inverter IGBT and anti-parallel diode change during sample spot welding, handling, clinching and adhesive bonding programs.

L: Thermal Cycle and Thermal Swing Data for Sample Applications

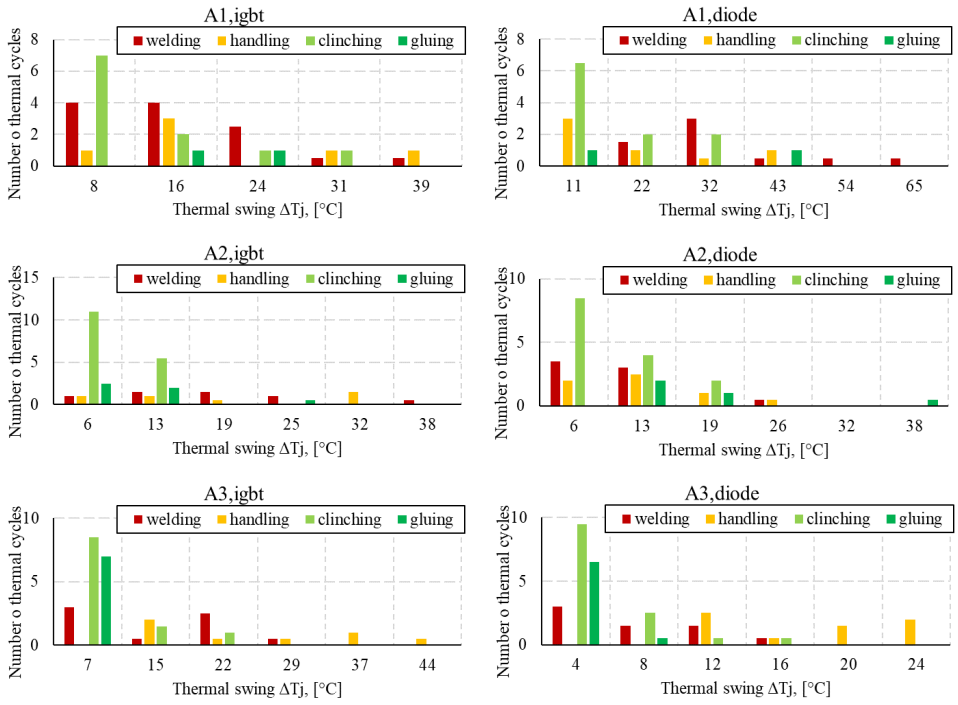

Fig. 5.10. Quantity of IGBT and anti-parallel diode junction temperature cycles and half cycles for each simulated robot program type after Rainflow counting – spot welding, handling, clinching and adhesive bonding (gluing).

M: Lifetime Consumption of Sample Robot Applications

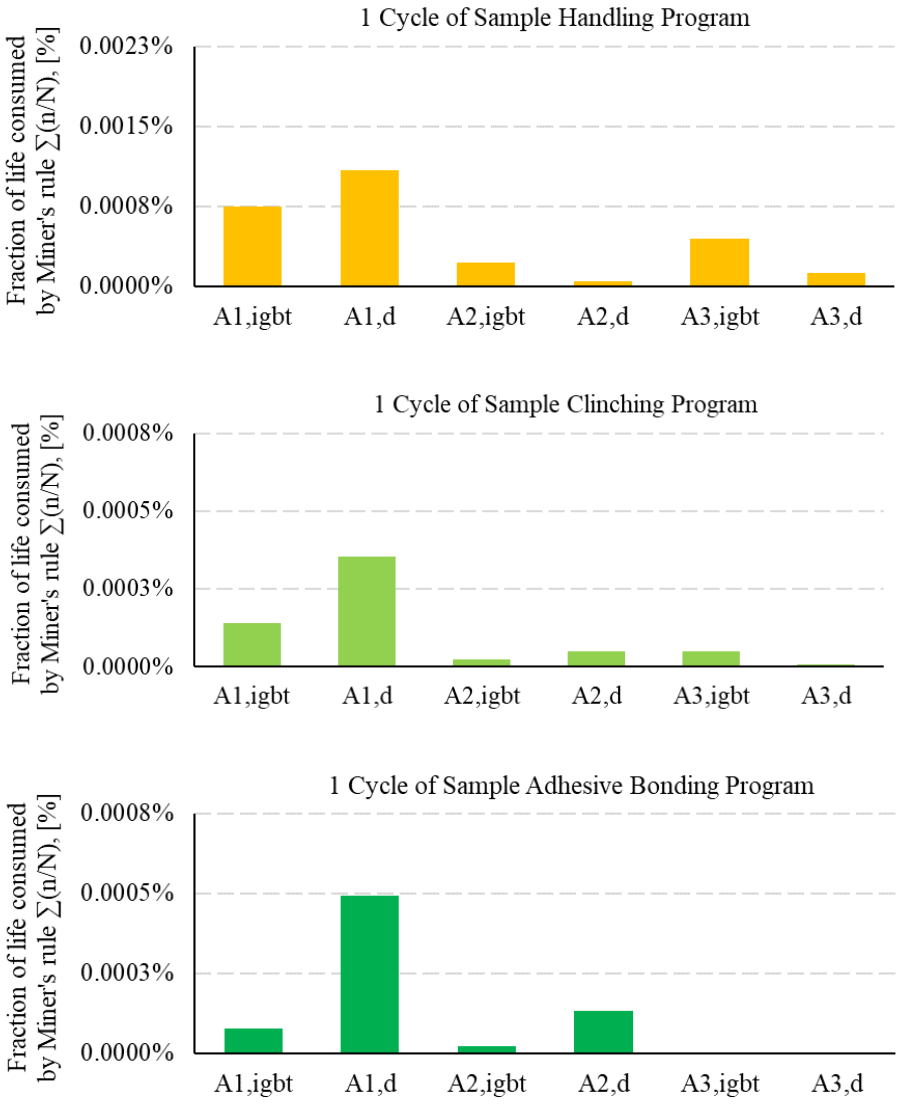

Fig. 5.11. Estimated lifetime consumption of the simulated four robot program types for IGBT and anti-parallel diode of A1−A3 robot axis inverter IGBT module.

N: Accumulation of Lifetime Consumption for Handling and Clinching

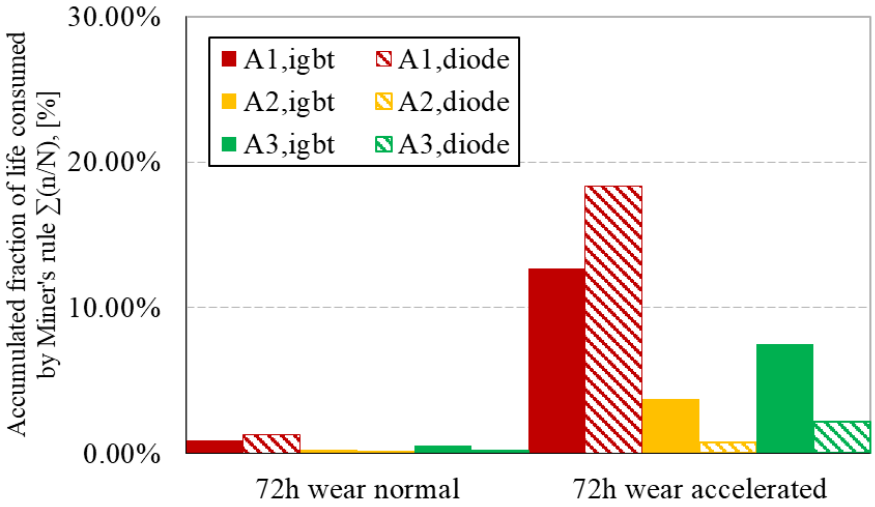

Fig. 5.12. Estimated lifetime consumption accumulated through 72 hours of normal and accelerated robot handling program cycling.

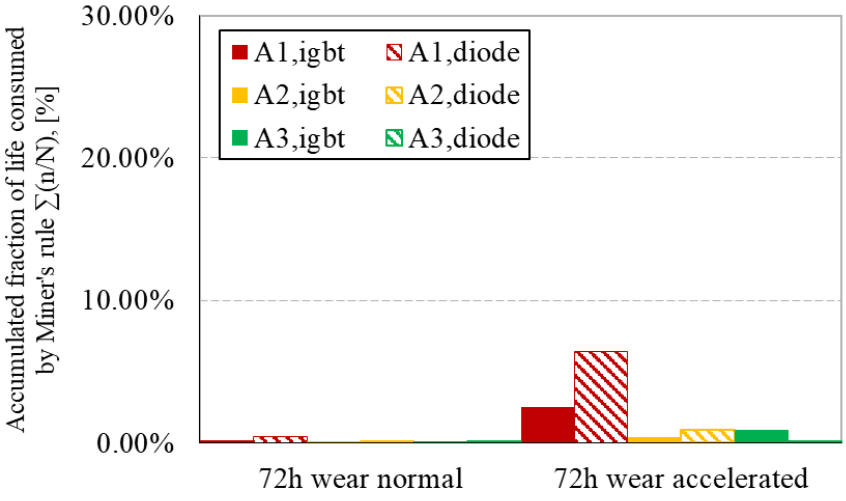

Fig. 5.13. Estimated lifetime consumption accumulated through 72 hours of normal and accelerated robot clinching program cycling.